An experimental investigation of fragmentation occurrence and outcome in the context of rockfall

Davide E. Guccione MSc (Parma)

A thesis submitted in fulfilment of the requirements for the degree of Doctor of Philosophy in Civil Engineering

December 2020

Priority Research Centre for Geotechnical Science and Engineering
Faculty of Engineering and Built Environmental
University of Newcastle
Callaghan, 2308, AUSTRALIA

THE UNIVERSITY OF NEWCASTLE AUSTRALIA

Statement of Originality

I hereby certify that the work embodied in the thesis is my own work, conducted under normal supervision. The thesis contains no material which has been accepted, or is being examined, for the award of any other degree or diploma in any university or other tertiary institution and, to the best of my knowledge and belief, contains no material previously published or written by another person, except where due reference has been made. I give consent to the final version of my thesis being made available worldwide when deposited in the University's Digital Repository, subject to the provisions of the Copyright Act 1968 and any approved embargo.

Davide E. Guccione

19 December 2020

I hereby certify that the work embodied in this thesis contains published papers of which I am a joint author. I have included as part of the thesis a written declaration endorsed in writing by my supervisor, attesting to my contribution to the joint publications.

By signing below, I confirm that Davide E. Guccione contributed substantially to the paper/publication entitled:

- Dodo, M., **Guccione, D.E.,** Thoeni, K., Giacomini, A., Bertrand, D., Bourrier, F. (2018). *Discrete Element Modelling of fragmentation with the open-source framework YADE*. Paper presented at the 3rd Australasian Conference on Computational Mechanics (ACCM), Geelong, Victoria, 12-14 February 2018.
- **Guccione D.E.,** Fityus S., Gregg N., Giacomini A., Buzzi O. (2019). *Experimental study on influence of impact angle on fragmentation of brittle blocks upon dynamic impact*. Paper presented at the 13th Australia New Zealand Conference on Geomechanics, Perth, Western Australia, 1-3 April 2019.
- **Guccione D.E.,** Thoeni K., Fityus S., Buzzi O., Giacomini A. (2019). *Development of an apparatus to track rock fragment trajectory in 3D*. Paper presented at the Rock Mechanics for Natural Resources and Infrastructure Development - Full Papers: Proceedings of the 14th International Congress on Rock Mechanics and Rock Engineering (ISRM 2019), CRC Press, 1622–1629.
- **Guccione D.E.,** Thoeni K., Giacomini A., Buzzi O., Fityus S. (2020). Efficient multi-view 3D tracking of arbitrary rock fragments upon impact. *ISPRS - International Archives of the Photogrammetry, Remote Sensing and Spatial Information Sciences XLIII-B2-2020*, 589–596. https://doi:10.5194/isprs-archives-XLIII-B2-2020-589-2020.
- **Guccione D.E.,** Thoeni K., Fityus S., Nader O., Giacomini A., Buzzi O. (2021). An experimental setup to study the fragmentation of rocks upon impact. Accepted with minor revisions at *Rock Mechanics and Rock Engineering.*
- **Guccione, D. E.,** Buzzi, O., Thoeni, K., Fityus, S., & Giacomini, A. (2021). Predicting the fragmentation survival probability of brittle spheres upon impact from statistical distribution of material properties. International *Journal of Rock Mechanics and Mining Sciences, 142,* 104768. https://doi.org/10.1016/j.ijrmms.2021.104768.

Principal Supervisor: Prof. Anna Giacomini

19 December 2020

Acknowledgements

I am sincerely grateful to my supervisors, Prof. Anna Giacomini, Prof. Olivier Buzzi, Prof. Stephen Fityus and A/Prof. Klaus Thoeni for giving me the opportunity to take part in this research project. Thanks for your constant support and encouragement, your endless knowledge has been for me inspiring. This work would not have been possible without you.

I would like to thank the staff of the Laboratory of Civil Engineering of the University of Newcastle which helped me during the set-up of the experimental apparatus. My gratitude goes in particular to Dr Michele Spadari whose patience, professional expertise and personal support have been precious in this project. Thanks also to Rose Gibson, Mick Goodwin, Ian Jeans, Andy Sullivan and Lachlan Bates for the technical support received. A special thanks to Juan Correa for his help during the material preparation.

I acknowledge the staff of PRCGSE centre, especially the past coordinator Ms Kirstin Dunncliff who preciously assisted me with always her best efforts and professionalism. Your efficiency and prompt help have been invaluable.

My gratitude goes to the international students who worked with me through the course of this research: Tomà Canessi, Giuseppina Ciccone, Eleonora Marangoni, Nathan Fourcade, Michela Caccia and Jules Ulrich. Thanks also to Luke Zelinski for the help received the series of tests conducted at the Forum.

To my friends and colleagues Dr François Nader and Dr Marina Santise, thank you for your valuable comments, time and support throughout my PhD research and more.

Thanks to the fellow PhD students who shared with me this journey, in particular Dr Davide Casagrande, Dr Peter Newton, Dr Esmaeel Bayat, Michael Jeffery, Dr Khosro Ghobadi, Barbara Do Nascimento, Guilherme Barros.

My appreciation extends to my friends and family in Italy that encouraged me unconditionally over the years.

Thank you to my mother, father and to my sister for their understanding, patience and infinite support and love.

Last but not least, thank you to my wonderful and loved partner Roberta which following me to other side of the globe. Thanks to be brave, for your encouragements and to be tolerant. Finally, thank you to Bianca for filling my life with a lot of joy.

Abstract

Rockfall research has made significant progress since the 1980s, with considerable improvements made in terms of design of protection measures, invention of new systems such as self-cleaning meshes, draperies and attenuators, and of rockfall trajectory modelling. The latter is a key step of the design of rockfall protection structures and hazard assessment, as it provides information about impact energy and possible trajectories of blocks. After a rockfall event, breakage of rocks is often observed. Rock fragmentation is one aspect of rockfall that is still poorly understood and usually not modelled because the current state-of-the-art knowledge is not sufficient to predict it or model it adequately. Indeed, it is a complex phenomenon influenced by many factors, such as rock strength, presence and properties of discontinuities in the block, stiffness of the ground, block shape and impact conditions.

In this thesis, an innovative experimental fragmentation cell is presented to produce high-quality fragmentation data that will advance fragmentation knowledge. The cell was designed to conduct controlled vertical drop tests and record key impact parameters including impact force, impulse, impact duration, translational and rotational velocities (of the block before impact and its fragments after impact) and all energy components pre-impact and post-impact. The cell is equipped with four high-speed cameras and two mirrors providing six views, used for the accurate reconstruction of 3D trajectories of blocks and fragments, in translation and rotation.

An extensive campaign of drop tests using artificial rock spheres of different diameter (50, 75 and 100 mm) and different mortar strength was carried out. More than 360 spheres were dropped with different impact energy in order to investigate the survival probability of spheres at impact, size frequency distribution of fragments, trajectory of fragments, fragmentation patterns, distribution of energy amongst fragments, key energy dissipation mechanisms, and more.

The device was first validated using several series of drop tests and its ability to reconstruct 3D trajectories, including rotation was verified. Then, it was found that the survival probability of spheres upon drop tests follows a linear distribution, opposed to a Weibull distribution as often observed for breakage of particles. It is also shown that the survival probability is size dependent: the larger the spheres, the more energy is required to initiate fragmentation.

For the testing conditions considered, it was found that the amount of energy dissipated in fragmentation represents about 3% of the kinetic energy at impact and can be considered constant in the range of 5 to 10 m/s. The extensive fragmentation data clearly indicates that the assumption kinetic energy can be distributed to fragments proportionally to their mass (often made in fragmentation models) is not valid. More research is required to understand the process of kinetic energy distribution amongst fragments.

A key point of this research was to tackle the fragmentation phenomenon from a stochastic point of view. The natural variability in material properties and block shape (albeit using the same material) implies that the amount of energy required to fragment a rock is not a unique value but a probability distribution. A novel model was proposed to predict the survival probability of brittle spheres upon impact based on the statistical viability of material strength. The model is based on theoretically derived conversion factors used to convert the critical work required to fail mortar cylinders in indirect tension (i.e. by Brazilian test) into the critical kinetic energy at failure in drop tests. The conversion factors account for the shape and size of the specimens tested and the increase of strength under dynamic loading (strain rate effect). The model was satisfactorily validated (relative errors of less than 15%) for three different sphere diameters and two mortar strengths. This model constitutes the first step into the prediction of survival probability of natural blocks. As far as the author knows, this model is the first of its kind.

Table of Contents

List of Figures

List of Tables

Nomenclature

$a_{z,L\&HPF}$	Raw signal from accelerometer after applying high and low pass filter
$a_{z,raw}$	Raw signal from accelerometer
AC	Accelerometer
A_j	Area of new surfaces generated by fragmentation
c	Dimensional viscosity damping coefficient
C_{Shape}	Shape conversion factor
$C_{Shape-F}$	Shape conversion factor for force
$C_{Shape-\delta}$	Shape conversion factor for displacement
C_{Size}	Size conversion factor
C_{Rate}	Rate conversion factor
C_{Rate-F}	Rate conversion factor for force
$C_{Rate-\delta}$	Rate conversion factor for displacement
$CD(\sigma)$	Cumulative distribution corresponding to a stress value of σ
CoR_d	Theoretical coefficient of restitution due to elastic-perfectly plastic deformation of a sphere impacting a plate
$\overline{CoR_d}$	Measured coefficient of restitution due to elastic-perfectly plastic deformation
CoR_E	Coefficient of restitution defined as square root of the ratio of the total kinetic energy after E_k^a and before impact E_k^b
$\overline{CoR_E}$	Measured coefficient of restitution defined as square root of the ratio of the total kinetic energy after E_k^a and before impact E_k^b
CoR_N	Coefficient of restitution defined as ratio of the normal component of the rebound and impact velocity

CoR_T	Coefficient of restitution defined as ratio of the tangential component of the rebound and impact velocity
CoR_v	Coefficient of restitution defined as ratio of the rebound velocity and impact velocity
CoR_w	Coefficient of restitution for elastic wave propagation
d	Diameter of the disc used for the Brazilian test
D	Diameter of spheres used for drop tests
d_{cr}	Characteristic particle size (or Weibull scale parameter)
$E_{k(D)}^{b}$	Kinetic energy of sphere of diameter D before dynamic impact
$E_{k(D)}^{cr}$	Critical value of kinetic energy of sphere of diameter D before dynamic impact
E_k^b, E_k^a	Total kinetic energy before and after impact
$E_{k,i}^a$	Total kinetic energy after impact of the fragment i
E_{kt}^b, E_{kt}^a	Translational component of kinetic energy before and after impact
$E_{kt,i}^a$	Translational component of kinetic energy after impact of the fragment i
E_{kr}^b, E_{kr}^a	Rotational component of kinetic energy before and after impact
E_{kr}^a	Rotational component of kinetic energy after impact of the fragment i
f	Impact force frequency
f_d	Damped natural frequency
f_n	Undamped natural frequency
F	Force
F_1, F_2, F_3	Forces recorded from the three load cells under the slab
$F_{BT(d)}$	Force required to reach failure of a mortar disc of diameter d under quasi static indirect tension (Brazilian test)
$F_{BT(d)}^{cr}$	Critical value of force required to reach failure of a mortar disc of diameter d under quasi static indirect tension (Brazilian test)
$F_{DYN(D)}$	Force required to reach failure of a mortar sphere of diameter D under dynamic impact
$F_{DYN(D)}^{cr}$	Critical value of force required to reach failure of a mortar sphere of diameter D under dynamic impact

F_{impact}	Estimated impact force
$\overline{F_{impact}}$	Impact force recorded from the top load cell
$F_{SC(d)}$	Force required to reach failure of a mortar sphere of diameter d under quasi static compression
$F_{SC(D)}$	Force required to reach failure of mortar spheres of diameter D under quasi static compression
$F_{SC(D)}^{cr}$	Critical value of force required to reach failure of mortar spheres of diameter D under quasi static compression
F_T	Transmitted force corresponding to the sum of the three forces recorded from the load cells under the slab
G	Gradient of the cumulative Weibull curve
h	Thickness of the disc used for the Brazilian test
h_s	Thickness of the slab
ISR	Increase in strain rate between quasi static tests and dynamic impact
I_I, I_{II}, I_{III}	Moments of inertia for the principal axes
$I_{I,i}, I_{II,i}, I_{III,i}$	Moments of inertia for the principal axes of the fragment i
J	Impulse
J_c	Impulse at maximum compression (i.e. at the point where the normal velocity is temporary equal to zero)
J_{impact}	Estimated total impulse (i.e. at the end of the impact when the body rebounds and separates from the surface)
$\overline{J_{impact}}$	Impulse computed using top load cell data
k	Stiffness of the system composed by the slab and three bottom load cells
K	Stress intensity factor
K_{Ic}	Fracture toughness
LC1, LC2, LC3	Load cells
m	Mass of the impacting object (sphere)
m_i	Mass of fragment i
m_s	Mass of the slab
m_{tot}	Sum of the masses of all fragments

M1, M1*, M2, M3	Mixtures of mortar
n	Number of fragments
N	Number of tests performed, for a given impact energy, to ascertain a given value of survival probability
N_f	Number of tests that resulted in fragmentation of sphere, for a given impact energy
p	Momentum
R_1, R_2	Radius of the sphere and the slab
$\tilde{R}$	Equivalent radius
SP	Survival probability
SP_{fit}	Fitted survival probability
t	Time
t_{BT}	Average time required to fail mortar discs in indirect tension (Brazilian test)
t_c	Period of the elastic compression
t_{impact}	Average duration of impacts for the drop tests
v	Absolute translational velocity
v_{filter}	Velocity of the slab after filtering
v_i	Absolute translational velocity of fragment i
v_{imp}	Impact velocity
$v_{imp(D)}$	Impact velocity of a sphere of diameter D
$v_{imp(D)}^{cr}$	Critical value of impact velocity of sphere of diameter D upon dynamic impact
$v_{imp,N}$	Normal component of the impact velocity
$v_{imp,T}$	Tangential component of the impact velocity
v_p	Propagation velocity of quasi-longitudinal waves in the slab
v_{reb}	Rebound velocity
$v_{reb,N}$	Normal component of the rebound velocity
$v_{reb,T}$	Tangential component of the rebound velocity
v_{xy}	Horizontal component of the translational velocity
$v_{xy,i}$	Horizontal component of the translational velocity of fragment i

v_y	Yield velocity
v_z	Vertical component of the translational velocity
$v_{z,i}$	Vertical component of the translational velocity of fragment i
V1, V2, V3, V4	Physical viewpoints
V5, V6	Virtual viewpoints
VH	Visual Hull
$W_{SC(d)}$	Work required to fail a sphere of diameter d in quasi static compression
$W_{SC(D)}$	Work required to fail a sphere of diameter D in quasi static compression
$W_{BT(d)}$	Work required to fail a disc of diameter d in quasi static indirect tension (Brazilian test)
$W_{BT(d)}^{cr}$	Critical value of work required to fail a disc of diameter d in quasi static indirect tension (Brazilian test)
Y_m, Y_s, Y_c	Elastic modulus of the mortar, steel and concrete slab (referred as system slab plus load cells), respectively
$\tilde{Y}_{mc}, \tilde{Y}_{ms}$	Equivalent elastic modulus of the mortar-concrete slab (referred as system slab plus load cells) and mortar-steel platens, respectively
$z, \dot{z}, \ddot{z}$	Displacement, velocity and acceleration of the slab
z_{filter}	Displacement of the slab after filtering
$z_{filter,HPF}$	Displacement of the slab after filtering and after applying high pass filter
z_{slab}	Max displacement of the slab
α	Proportion of total deformation of the sphere/slab system upon dynamic impact that corresponds to the deformation of the sphere
β	Non-dimensional viscous damping coefficient
γ	Surface energy per unit area (or so-called strain energy release rate)
$\delta_{BT(d)}$	Reduction in diameter (deformation) of a mortar disc of diameter d at failure under quasi static indirect tension (Brazilian test)
$\delta_{BT(d)}^{cr}$	Critical value of reduction in diameter of a mortar disc of diameter d at failure under quasi static indirect tension (Brazilian test)

δ_c	Deformation of an infinitesimal particle at the maximum compression
$\delta_{DYN(D)}$	Reduction in diameter of a mortar sphere of diameter D at failure under dynamic impact
$\delta_{DYN(D)}^{cr}$	Critical value of reduction in diameter of a mortar sphere of diameter D at failure under dynamic impact
δ_f	Final deformation of an infinitesimal particle after impact
$\delta_{SC(d)}$	Reduction in diameter of a mortar sphere of diameter d at failure under quasi static compression
$\delta_{SC(D)}$	Reduction in diameter of a mortar sphere of diameter D at failure under quasi static compression
$\delta_{SC(D)}^{cr}$	Critical value of reduction in diameter of a mortar sphere of diameter D at failure under quasi static compression
ΔE_d	Energy loss in elastic-plastic deformation
ΔE_{fr}	Energy loss to create the fracture surfaces
ΔE_{slab}	Energy loss associated to the elastic displacement of the slab
ΔE_{tot}	Total energy loss associated with the impact
ΔE_w	Energy loss in elastic wave propagation
Δt	Theoretical impact duration
Δt_i	Direct measurement of the impact duration by the pressure sensor
$\Delta t_{i,LC}$	Direct measurement of the impact duration by the top load cell
Δt_{ti}	Transmitted impact duration recorded from the load cells under the slab
θ_i	Impact angle
θ_r	Rebound angle
ϑ_y	Ratio of mean indentation pressure (assumed fully plastic) to uniaxial yield stress
λ	Inelasticity parameter
μ	Weibull shape parameter
μ_{BT-F}	Weibull shape parameter pertaining to the distribution of maximum force for quasi static indirect tension tests (Brazilian test)

μ_{BT-W}	Weibull shape parameter pertaining to the distribution of work required to fail discs under quasi static indirect tension test (Brazilian test)
μ_E	Weibull shape parameter pertaining to the survival probability of the drop tests, expressed in terms of kinetic energy
μ_{SC-W}	Weibull shape parameter pertaining to the distribution of work required to fail spheres in compression
μ_v	Weibull shape parameter pertaining to the survival probability of the drop tests, expressed in terms of impact velocity
ν_m, ν_s, ν_c	Poisson's ratio of the mortar, steel and concrete slab (referred as system slab plus load cells), respectively
ρ_1, ρ_2	Density of the mortar sphere and the concrete slab (referred as system slab plus load cells)
σ	Stress
σ_c	Unconfined compressive strength
σ_{cr}	Weibull scale parameter for the stress σ, also called critical value of σ
σ_t	Tensile strength
σ_y	Yield stress of the impacting material (sphere)
Ψ_s	Slope angle
ω	Absolute rotational velocity
ω_{ref}	Reference absolute rotational velocity
$\omega_I, \omega_{II}, \omega_{III}$	Rotational velocities around the 3 principal axes
$\omega_{I,i}, \omega_{II,i}, \omega_{III,i}$	Rotational velocities around the 3 principal axes of fragment i

1 Introduction

1.1 Background

Since the 1980s, significant progress has been made on rockfall protection systems, with a significant increase of system capacity (impact energy up to 10 MJ can be successfully dissipated by some systems) and the invention of innovative solutions such as self-cleaning systems, draperies and attenuators (Turner and Schuster 2013).

Designing rockfall protection structures requires the estimation of the trajectory and energy of rocks falling down a slope. Starting from an initial energy potential defined by the block's mass and initial elevation, a falling rock gains kinetic energy as it falls and loses energy at each impact with the slope. Although trajectory modelling has also seen significant improvements over the years (e.g. advanced 3D modelling), there remains one aspect of rockfall that has largely been left unaddressed and is still poorly understood: rock fragmentation upon impact. Fragmentation is often observed post rockfall events (Agliardi and Crosta 2003) and it is recognised as critical for adequate rockfall risk management (Jaboyedoff et al. 2005; Volkwein et al. 2011). It is a very complex phenomenon influenced by the presence of discontinuities in the block including their persistence, shape and orientation at the moment of the impact; the intact and jointed rock strength; the impacting energy; stiffness of the ground; impact angle and impact velocity (Giacomini et al. 2009; Wang and Tonon 2011).

Fragmentation should be accounted during rockfall protection design for a number of reasons:

- If fragmentation occurs, a significant amount of energy will be dissipated in breakage upon impact, which reduces the final impact energy that the protection structure should be designed for (see Figure 1-1a). In other words, the system capacity is likely to be over-designed, which comes at a cost.

- The height and position of a protection structure are governed by the trajectory of the falling blocks. Fragments could have a very different trajectory to that of an intact block. In particular, there is a risk of a small fragment "flying" above a given protection structure.
- The mechanism of energy distribution among fragments post fragmentation is unknown. If a small fragment possesses a high kinetic energy, there is a risk of barrier failure due to mesh perforation as per Figure 1-1b.

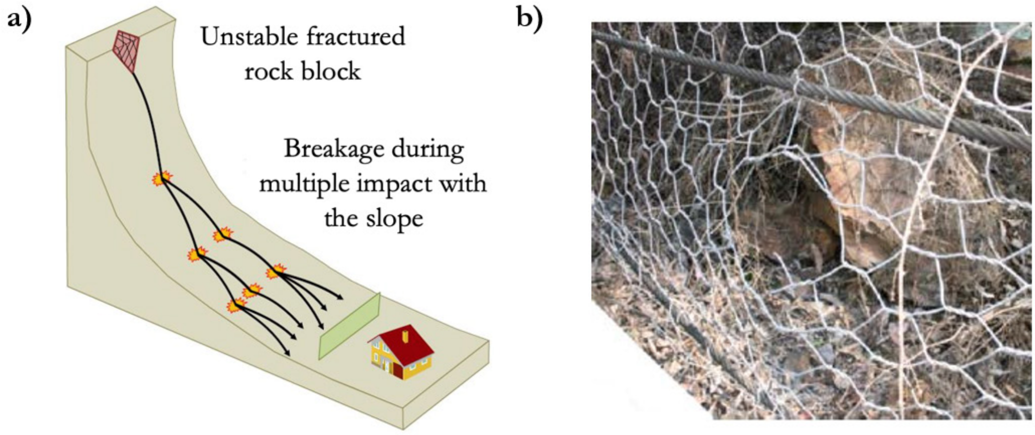

Figure 1-1: (a): Fragmentary rockfall phenomenon (modified after Matas et al. (2017)). (b): Damage to a rockfall barrier done by a high energy rock fragment (NSW)

It is hence important to deepen our understanding of rock fragmentation upon impact in order to optimise the design of protection structures.

The development and calibration of adequate fragmentation models is currently hindered by a lack of comprehensive fragmentation tests and data. Rockfall models that claim to predict fragmentation are often based on inadequate assumptions, such as the idea that fragmentation is a threshold phenomenon, an assumption contradicted by Giacomini et al. (2009).

1.2 Objectives of the research

This PhD research aims to provide high quality fragmentation data in order to improve our fundamental knowledge on the phenomenon. More specifically, the research conducted aims at providing elements of answers to the following questions:

1. In a rockfall event, for a given geological setting, is fragmentation likely to occur?
2. If fragmentation occurs, what is the outcome of fragmentation? This includes the number and distribution of fragment sizes, the partition of energy amongst fragments and fragment trajectories.

Given the complexity of the problem and the large number of significant factors, this PhD work focuses on a detailed study of the impact of brittle spheres on a concrete slab and aims at:

- Designing and assembling a specific fragmentation study apparatus.
- Producing high-quality experimental data of brittle fragmentation of spherical blocks, pertaining to survival probability, fragmentation patterns, fragment size distribution, trajectories before and after impact and energy balance.
- Developing and validating a model that can predict the survival probability of brittle spheres upon dynamic impact based on the statistical variability of block strength properties.

1.3 Structure of the thesis

The work presented in this thesis is organised in seven chapters, including this introduction (Chapter 1).

Chapter 2 provides a review of the literature, covering impact mechanics and impact modelling in rockfall, elements of fracture mechanics and significant numerical and experimental studies on fragmentation.

Chapter 3 presents the experimental setup designed to capture fragmentation of blocks upon impact. A detailed description of the developed apparatus and testing methodology is given.

Chapter 4 presents the derivation of a novel model to predict the impact survival probability of brittle spheres upon impact from statistical distribution of material properties.

In Chapter 5, the material used and the experimental program are presented.

Chapter 6 then covers the main results of this research. First, the extensive material characterisation and the setup validation are presented. Then, attention is focused on the experimental outcomes of fragmentation tests and the application of the novel model to predict the observed impact survival provability of brittle spheres upon impact. Finally, the test results are analysed in terms of energy dissipation mechanisms and the partition of energy between fragments.

The thesis concludes with Chapter 7, which contains conclusions and recommendations for future research.

2 Literature review

This chapter includes in two main sections. The first focuses on the literature review on impact modelling and impact mechanics in the context of rockfall. Note that, a detailed review of rockfall hazard and risk assessment methodologies and type of rockfall protection structures proposed in the scientific literature is not considered in this section as out of the scope of the thesis. A comprehensive reviews of these topics can be found in Peila and Ronco (2009), Volkwein et al. (2011), Turner and Schuster (2013), Thoeni et al. (2014), Wyllie (2014b), Ferrari et al. (2016), Effeindzourou et al. (2017), Corominas et al. (2019), Volkwein et al. (2019), just to name a few. The second section covers the principles of fracture mechanics and the most significant experimental and numerical studies conducted on fragmentation over the last few decades.

2.1 Impact modelling

Four main motion models are generally considered to characterise the fall of a block along a slope: free fall, bouncing, rolling, sliding, or a combination of the four motions. In early 60s' Ritchie (1963) proposed to relate the type of rockfall motion to the slope angle, Ψ_s (see Figure 2-1). The steepest the slope, the higher is the tendency of the block to move from a rolling motion to a bounce and then free fall motion. Generally speaking, the freefall mode can be mostly observed on the upper part of a scarp and when the slope angle varies between 90° and 70°. For lower angle values, the block tends to bounce or move with a combination of bouncing and rolling motions. At impact, a significant amount of energy is usually lost, partially within the impacted soil/rock layer and partially as rebound energy and/or fragmentation energy for the block. If the slope gradient decreases downward to about 45°, the motion is generally transformed into a pure rolling motion. Sliding mainly occurs at the initial stages of the fall or near its stopping point.

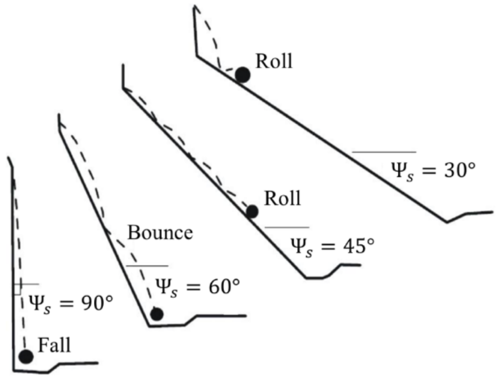

Figure 2-1: Relation between motion type and slope angle (modified after Ritchie (1963))

Trajectory modelling is generally used to assess rockfall hazard and to estimate the impact energy for design of protection measures (Volkwein et al. 2011). Existing rockfall trajectory simulation models can be grouped according to the trajectory's spatial domain:

1. Two-dimensional (2D) models simulate the rockfall trajectory along a user-defined slope profile in a spatial domain defined by two axes (Azzoni et al. 1995).
2. 2.5D or quasi-3D trajectory models consider the direction of the rockfall trajectory in the x-y domain independent from the kinematics of the falling rock; in fact, the latter evolves in the vertical plane (Volkwein et al. 2011).
3. 3D trajectory models define the trajectory in a 3D plane (x, y, z). Models in this group include EBOUL-LMR (Descoeudres and Zimmermann 1987), STONE (Guzzetti et al. 2002), Rotomap (Scioldo 2006), DDA (Yang et al. 2004), STAR3-D (Dimnet 2002), HY-STONE (Crosta et al. 2004) and Rockyfor3-D (Dorren et al. 2004), RAMMS: Rockfall (Christen et al. 2007), etc. The major advantage of 3D models is that they consider the slope topography and therefore they allow for more realistic trajectories within the 3D space. Nevertheless, 3D models require spatially explicit parameter maps which may involve significant time-consuming activity in the field.

A main aspect of rockfall trajectory modelling resides in the modelling of the rebound of the block upon impact with the slope, which can be very challenging. Two approach are commonly considered for this purpose: the lumped mass approach and the rigid body approach (Giani 1992; Hungr and Evans 1988). Lumped mass methods consider the interaction of the point (in which the mass of the block is concentrated) with the slope without accounting for the shape of the blocks (Guzzetti et al. 2002; Hoek 1987; Hungr and Evans 1988; Piteau and Clayton 1977; Ritchie 1963; Stevens 1998). Instead, the rigid body methods use the fundamental equations of dynamics, including the rotation, to model the motion of the block along the slope (Azzoni et al. 1995; Cundall 1971; Descoeudres and Zimmermann 1987; Falcetta 1985). Other numerical tools are based on an hybrid approach that considers a lumped mass approach in the free fall trajectory phase and accounts for geometrical and mechanical characteristic of the block and the slope at impact (Azimi and Desvarreux 1977; Bozzolo and Pamini 1986; Crosta et al. 2004; Dorren et al. 2004; Jones et al. 2000; Kobayashi et al. 1990; Pfeiffer and Bowen 1989; Rochet 1987).

Most of the existing rockfall trajectory models use coefficients of restitution (normal and tangential) to account for the rebound at impact with the slope surface and a friction coefficient to model the rolling motion. An overview of typical values considered for the coefficients of restitution can be found in Scioldo (2006) and the concept of the coefficient of restitutions is further described in Section 2.1.1.

The rolling of a boulder along a slope can be represented by a sequence of short bounces and low flying parabolas. Rolling motion is usually well defined for spherical, cylindrical or discoid blocks for which the velocity of the boulder is low, and the boulders are moving on a medium to low terrain gradient with limited surface roughness. However, a pure rolling motion of a rock can be considered an abstraction as natural blocks do not have typical geometric shapes and the impacted surface is never completely flat (Azzoni et al. 1995; Bozzolo and Pamini 1986; Dorren 2003; Giacomini et al. 2010; Guzzetti et al. 2002). As previously mentioned, sliding is mostly limited to the initial stage of a rockfall and the motion is characterised by low velocity and high loss of energy due to the frictional interaction with the slope surface. For large boulders, sliding may also occur at impact, with significant loss of energy. The distinction between rolling and sliding models is quite difficult since a combination of the two movements can occur very rapidly (Descoeudres 1997; Giani 1992).

2.1.1 *Empirical approach: coefficient of restitution in rockfall engineering*

The accurate modelling of the rebound of a block at impact is one of the most difficult tasks in rockfall analyses. Several studies showed that the rebound of the block at impact with the slope surface is affected by both slope and block characteristics (Table 2-1).

Numerous experimental investigations were carried out in the field (Asteriou et al. 2012; Azzoni and De Freitas 1995; Azzoni et al. 1992; Berger and Dorren 2006; Bozzolo et al. 1988; Broili 1977; Evans and Hungr 1993; Ferrari et al. 2013; Fornaro et al. 1990; Giacomini et al. 2009; 2010; 2012; Giani 1992; 2004; Kirkby and Statham 1975; Kobayashi et al. 1990; Lied 1977; Pfeiffer and Bowen 1989; Ritchie 1963; Spadari et al. 2012; Statham and Francis 1986; Teraoka et al. 2000; Urciuoli 1996; Wu 1985; Wyllie 2014a; Yoshida 1998) and in the laboratory (Ansari et al. 2015; Asteriou et al. 2012; Asteriou and Tsiambaos 2018; Azimi and Desvarreux 1977; Azimi et al. 1982; Bourrier 2008; Buzzi et al. 2012; Camponuovo 1977; Chau et al. 1998a; 1998b; 1999a; 2002; 1999b; Heidenreich 2004; Imre et al. 2008; Ji et al. 2019; Kamijo et al. 2000; Kawahara and Muro 1999; Masuya et al. 2001; Murata and Shibuya 1997; Statham 1979; Ushiro et al. 2000; Wong et al. 1999; 2000; Ye et al. 2019b) to investigate the mechanisms occurring during impact and to quantify the influence of the parameters listed in Table 2-1.

Table 2-1 Parameters assumed to influence the bouncing phenomenon (Labiouse and Descoeudres 1999).

Slope characteristics	Rock characteristics	Kinematics
Strength Stiffness Roughness Inclination	Strength Stiffness Weight Size Shape	Velocity (translational and rotational) Incidence angle configuration of the rock at impact

Bouncing is significantly affected by the transfer of energy between the block and the slope. The kinetic energy of the block at impact is converted into rebound kinetic energy, energy diffusion and energy dissipation into the slope. Some elastic deformation also occurs for the slope material, but it is generally neglected (Volkwein et al. 2011). The energy diffusion is related to elastic wave propagation at the impact point (Bourrier et al. 2008; Giani 1992), while energy dissipation is mostly related to frictional (plastic) processes inside the slope material (Bourrier et al. 2008; Bozzolo and Pamini 1986; Giani 1992; Heidenreich 2004) and block and/or soil particle fragmentation (Azimi et al. 1982; Fornaro et al. 1990; Giani 1992). The magnitude of energy dissipation is assumed to be mainly governed by the ratio between the block size and the size of the slope particle (Bourrier et al. 2008; Statham 1979), the slope characteristics (slope hardness, roughness, slope composition/material) (Ansari et al. 2015; Asteriou et al. 2012; Asteriou et al. 2013b; Azzoni and De Freitas 1995; Azzoni et al. 1992; Chau et al. 1998a; Giokari et al. 2015; Paronuzzi 2009; Wyllie 2014a) and the block characteristics (shape, size/mass, Schmidt hardness, etc.) and its kinematic characteristics (slope/impact angle, incident velocity, rotational velocity, etc.) (Ansari et al. 2015; Asteriou et al. 2013a; Asteriou and Tsiambaos 2018; Buzzi et al. 2012; Chau et al. 1999a; 2002; Falcetta 1985; Ferrari et al. 2013; Giani et al. 2004; Heidenreich 2004; Ji et al. 2019; Ushiro et al. 2000; Wong et al. 2000). Energy diffusion and dissipation processes are also strongly dependent on the kinetic energy of the block before impact, which is related to its mass m and its impact velocity (v_{imp}), i.e., $E_k^b = 1/2 \cdot m \cdot v_{imp}^2$ (Asteriou et al. 2013a; Jones et al. 2000; Pfeiffer and Bowen 1989; Urciuoli 1996; Ushiro et al. 2000). The dissipation of energy at impact is generally represented by two coefficients of restitution CoR_v and CoR_E (also called, e_v and e_E, k_v and k_E, or R_v and R_E). CoR_v represents the formulation in terms of velocity loss and CoR_E is the ratio of the total kinetic energy after E_k^a and before impact E_k^b:

$$CoR_v = \frac{v_{reb}}{v_{imp}} \quad CoR_E = \sqrt{\frac{E_k^a}{E_k^b}} \tag{2-1}$$

Two alternative parameters related to the normal and tangential velocity of the block after and before impact are also commonly used for this purpose, CoR_N and CoR_T.

$$CoR_N = -\frac{v_{reb,N}}{v_{imp,N}} = \left|\frac{v_{reb,N}}{v_{imp,N}}\right| \quad CoR_T = \left|\frac{v_{reb,T}}{v_{imp,T}}\right| \tag{2-2}$$

where $v_{imp,N}$ and $v_{reb,N}$ are the normal components which always have opposite signs and $v_{imp,T}$ and $v_{reb,T}$ are the tangential components before and after the impact (Figure 2-2)

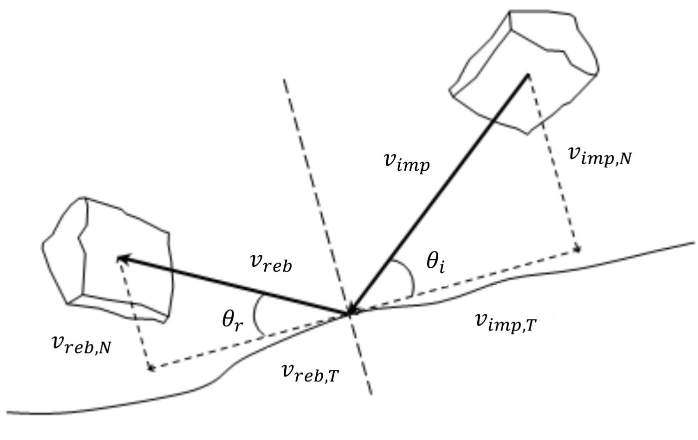

Figure 2-2 Block velocities before (v_{imp}) and after impact (v_{reb}) with normal and tangential components. θ_i represents the impact angle while θ_r is the rebound angle (modified after Giacomini et al. (2010)).

A common range of values for the coefficients of restitution is between 0.50 and 0.85 for CoR_T and 0.20 and 0.50 for CoR_N respectively (Volkwein et al. 2011). Labiouse and Heidenreich (2009) showed that CoR_T is unaffected by the slope angle, while the lower the slope angle, the lower CoR_N (as show Table 2-2). The authors also demonstrated the decrease of CoR_N, CoR_T and the ratio of the total energy before and after the impact with an increasing of the impact energy.

Recent research conducted at the University of Newcastle (Buzzi et al. 2012; Spadari et al. 2012) also showed that values of CoR_N can be higher than 1 as a partial transfer of translational kinetic energy to rotational kinetic energy at impact can occur for low values of impact angle, θ_i (angle between the tangent to the block's trajectory before impact and the slope surface, see Figure 2-2). More recently, these findings were confirmed by Wyllie (2014a). The author investigated the relationship between impact angle and normal coefficient of restitution for several rockfall field testing campaigns conducted in North America and Japan and studied the rockfall impact phenomenon according to the principles of impact mechanics. In particular, the study showed a strong correlation between the values of the normal coefficient of restitution and the impact angle (Figure 2-3) with coefficients of about 0.1 to 0.2 for normal impact (θ_i = 50 - 90°) and values often greater than 1.0 for shallow impacts (θ_i = 10 - 25°).

The impulse theory has been used to account for the change of momentum of the block during the compression and restitution phases of the impact (Bozzolo et al. 1988; Descoeudres and Zimmermann 1987; Dimnet 2002; Dimnet and Fremond 2000; Frémond 1995; Goldsmith 1960; Stronge 2000). As this aspect of the study is significantly correlated with the research presented in this thesis, the theory will be further discussed in Section 2.1.2.

	Parameter	CoR_N	CoR_T	CoR_E	Ground material	reference
Block	Block mass ↗	↘			Concrete, rock	Ushiro et al., 2000
	Angularity ↗ (shape changing from sphere to angular block)	↘	↗ (slightly)	↘	Granite	Wong et al., 2000
		30°< θ<60°: - 15°< θ<30°: ↗	↘ (slightly)	↘ (slightly)	Plaster	Chau et al., 1999a
Ground	Young's Modulus ↗	↗	↗		Natural slopes	Pfeiffer and Bowen, 1989
		↗	↗		Natural slopes	Fornaro et al., 1990
		↗	↗		Plaster, rock, soil	Chau et al., 2002 Wu, 1985
	Dry density ↗	$w < w_{opt}$: ↗ $w > w_{opt}$: ↔	$w < w_{opt}$: ↗ $w > w_{opt}$: ↔	$w < w_{opt}$: ↗ $w > w_{opt}$: ↔	Soil, plaster	Chau et al., 1999b
Kinematics	Impact angle θ ↗ respectively Slope angle β ↘ (θ + β = 90°)	↘	↗ (slightly)		Wood, rock	Wu, 1985
		↘ (slightly)			Granite, shotcrete	Wong et al., 2000
		↘			Plaster, soil	
		↘ (slightly)	↔	↘	Granite, shotcrete	Chau et al., 2002
		↘	↔	↘	Plaster, soil	
	Drop height H ↗ respectively Impact velocity ↗	↘	↘	↘	Limestone	Urciuoli, 1988
		↘ (slightly)	↔		Concrete, rock	Ushiro et al., 2000

Table 2-2 Factors affecting the coefficients of restitution CoR_N and CoR_T identified in the (modified after Labiouse and Heidenreich (2009)). CoR_E is the ratio of the total energy before and after impact.

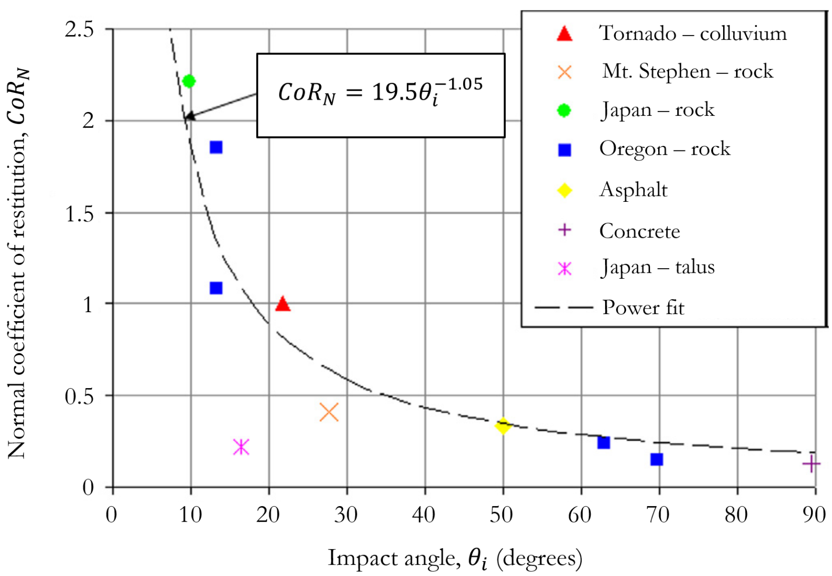

Figure 2-3: Relationship between the impact angle θ_i and the normal coefficient of restitution CoR_N for the rockfall sites describe in Wyllie (2014a).

It is important to highlight that, laboratory and field tests that measure the coefficient of restitution (CoR) have been typically conducted under the assumption of no fragmentation of the block at impact (Asteriou and Tsiambaos 2018; Giacomini et al. 2012; Kamijo et al. 2000). Very few studies investigating the evolution of damage and cracks at impact and the energy dissipation mechanisms during rock fragmentation can be found in the scientific literature. Studies in the fields of material science and material processing tend to focus on the size distribution of fragments produced (Carmona et al. 2008; Khanal et al. 2008; Shen et al. 2017; Tomas et al. 1999; Wu et al. 2004). In the area of rock mechanics, several studies have investigated the effect of cumulative damage under repeated impacts on the rebound characteristics for normal impacts (Chau et al. 2002; Imre et al. 2008; Labous et al. 1997; Seifried et al. 2005; Ye et al. 2019b). In particular, Ye et al. (2019b) developed an experimental setup to drop spheres of marble and record the coefficient of restitution during multiple rebounds via an acoustic sensor. The authors showed the existence of different energy dissipation mechanisms related to the progressive development of macrocracks with increasing impact energy. Asteriou and Tsiambaos (2018) also observed a reduction of the normal coefficient of restitution with impacting velocity (under single impact), which can be explained by the existence of damage upon impact.

As far as theoretical analysis is concerned, most of the current research on rockfall collisions is based on elastic–plastic theory (Heidenreich 2004). Contact constitutive models of elastic-perfectly plastic spheres (Brake 2012; 2015; Chang et al. 1987; Ghaednia et al. 2014; Jackson et al. 2010; Stronge 2000; Thornton 1997) based on Hertzian elastic contact theory (Hertz 1882) have established a correlation between the CoR_N and impact velocity (v_{imp}). Viscoelastic contact theories can also be found in the literature and they have been successfully applied to describe the CoR_N values of particles for various materials (Alizadeh et al. 2013; Kuwabara and Kono 1987; Ye and Zeng 2017). According to Ye et al. (2019b), the application of viscoelastic contact theory could be considered as a valid approach to describe the complex velocity and size dependence of CoR_N at impact.

2.1.2 Principles of normal impact mechanics

The theory of impact mechanics (Goldsmith 1960; Stronge 2000), which builds on early work by Sir Isaac Newton (Newton 1687) and other ground breaking researchers such as Poisson and Hertz in the 19th century is used in several fields of science and engineering to characterise impact between colliding bodies. The impacting bodies are typically made of different materials, possibly of unequal masses, and can be translating and/or rotating in a three-dimensional space. In the case of rockfall, the impact conditions involve a stationary slope characterised by an infinite mass and some roughness being impacted by blocks of irregular shape. Such conditions render the analysis of impact quite complex.

This section explores the application of the theory of impact mechanics based on the work of Stronge (2000) and Wyllie (2014b) to the rockfall phenomenon. The reviews cover only the normal impact of a nonrotating rigid body on a rigid surface as it represents the only test condition explored in this study. More details on the case of a rotating body impacting a rough and inclined rigid surface can be found in *Chapter 4* and *6* of Wyllie (2014b).

Compared to other fields in science and engineering involving impact of projectiles or car crashes, it can be said that impacts in rockfall typically occur at low velocity (i.e. less than about 40 m/s). Also, for impacts involving rock on rock, the impact duration is relatively short so that the impact induces high stress concentration in relatively small areas and generates minor deformations. With no significant interpenetration or adhesion between impacting objects, the impact is qualified as a "low compliance" impact.

In the case of a rigid body impacting a rigid surface, the impact area can be assumed to be equivalent to a short and stiff spring, or an infinitesimally small and deformable particle (Figure 2-4) (Wyllie 2014b). The impact includes a compression phase, where the particle (or spring) is compressed and the impacting object loses energy, followed by a restitution phase where the compressed particle returns the energy accumulated during the compression to the block, which in turn moves away from the slope. In such impact with infinitesimal deformation, the block position is considered constant and the weight of the block can be ignored, as it is much lower than the impact force.

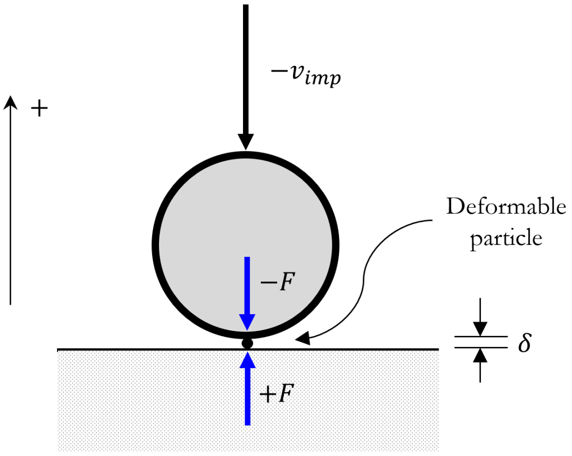

Figure 2-4: Forces (F) generated at the contact point during normal impact of a block with a rigid surface (modified after Wyllie (2014b)). v_{imp} is the impact velocity of the block and δ represents the deformation of the deformable particle.

The impacting body is characterised by its mass (m) and its impact velocity (v_{imp}) which can be used to define the momentum of the object ($p = -m \cdot v_{imp}$) and its kinetic energy before impact ($E_k^b = 1/2 \cdot m \cdot v_{imp}^2$). Analysing the change in momentum and energy during the impact involves Newton's second and third laws of motion, expressed as:

- *Second Law*: the momentum of a body (p) has a rate of change with respect to a time that is proportional to, and in the direction of, any resultant force (*F*) acting on the body:

$$F = \frac{dp}{dt} \tag{2-3}$$

- *Third Law*: two interacting bodies have forces of action and reaction that are equal in magnitude, opposite in direction and collinear.

During the impact illustrated in Figure 2-4, the compressed infinitesimal particle generates equal and opposite impact forces ($F, -F$) parallel to the direction of movement, which produces a change in momentum and therefore, a change in velocity during the impact. Note that the mass of the rigid body can be considered constant.

The impact intensity can be quantified in terms of impulse $J(t)$, which is related to the contact force $F(t)$ and the change of momentum by:

$$J(t) = \int_{t=0}^{t} F(t)\, dt = \int_{t=0}^{t} dp = \int_{t=0}^{t} m\, dv \tag{2-4}$$

Noting $v_{imp,N}$ the impact normal velocity at impact and $v_{reb,N}$ the normal velocity when the block separates from the impacted surface at rebound, the relative normal velocity at any time ($v_N(t)$) during the impact can be obtained by integration:

$$v(t) = \int_{t=0}^{t} \frac{1}{m} dJ \tag{2-5}$$

$$v(t) = v_{imp} + \frac{J(t)}{m} \quad \text{where} \quad v_{imp} < 0 \tag{2-6}$$

Eq. (*2-6*) can be used to:

- find the impulse at maximum compression J_c at the point when the normal velocity is temporarily equal to zero:

$$J_c = -m \cdot v_{imp} \quad \text{where} \quad v_{imp} < 0 \tag{2-7}$$

- find the total impulse J_{impact} at the end of the impact when the body rebounds and separates from the surface:

$$J_{impact} = m\left(v_{reb} - v_{imp}\right) \quad \text{where} \quad v_{imp} < 0 \tag{2-8}$$

These two values of impulse reflect the fact that normal force increases to a maximum value during the compression phase of the impact and then reduces during the restitution phase until the block separates from the impacted surface.

The changes in the normal contact force F during impact are illustrated in Figure 2-5a where the force (F_{impact}) and deformation (δ_c) are at the maximum compression phase, followed by partial recover (δ_f), for inelastic impact, at the end of the restitution phase. The compression and restitution phases are also characterised by changes of kinetic energy: some energy is lost during the compression phase and some energy is recovered during the restitution phase.

Figure 2-5b shows the change in the normal contact force as a function of time. The area under the $t - F$ curve up to time equal to t_c is the impulse J_c generated during the compression phase and represents the kinetic energy of relative motion that is converted into internal deformation. The area between times t_c and Δt is the change in impulse ($J_{impact} - J_c$) which represents the energy recovered during the restitution phase. For perfectly elastic materials, the energy lost in compression is fully recovered during the restitution phase

($CoR_N = 1$). In contrast, for perfectly plastic materials, the energy absorbed during the compression phase is not recoverable ($CoR_N = 0$). For elasto-plastic materials, the impact energy is partially recovered ($0 < CoR_N < 1$).

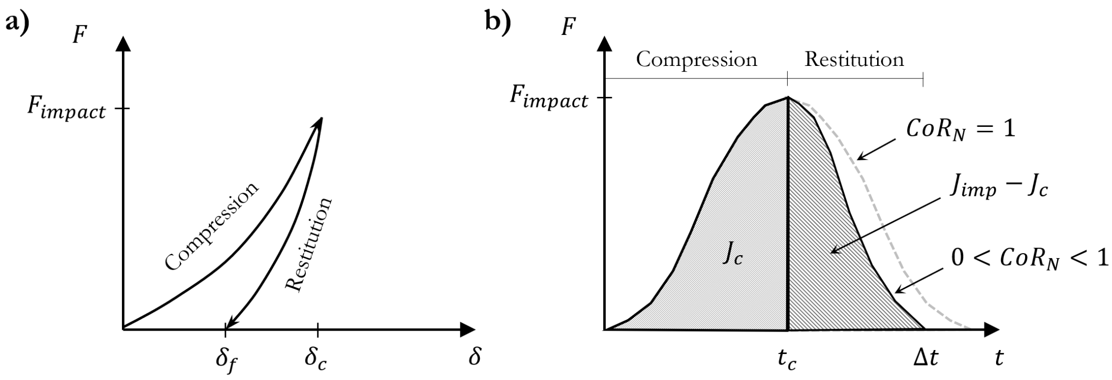

Figure 2-5: Variation of force F during impact: (a) relationship between force and deformation at the impact point; (b) change in force and impulse over time during impact; J_c is the impulse generated up to the time of maximum compression ($t = t_c$); $J_{impact} - J_c$ is the impulse generated during the restitution phase of impact ($t = t_c$ to $t = \Delta t_i$).

Using Eq. (2-2) (normal coefficient of restitution CoR_N) to express v_{reb} in Eq. (2-8) the impact impulse can be written as:

$$J_{impact} = m\left(-CoR_N \cdot v_{imp} - v_{imp}\right) = -m \cdot v_{imp}(1 + CoR_N) \tag{2-9}$$

and using Eq. (2-7) it can be further simplified to:

$$J_{impact} = J_c(1 + CoR_N) \tag{2-10}$$

By rearranging Eq. (*2-10*) the normal coefficient of restitution can be expressed as:

$$CoR_N = \left(\frac{J_{impact}}{J_c} - 1\right) \tag{2-11}$$

It is possible to use Eq. (2-11) to calculate the net energy loss during impact as:

$$\Delta E_{tot} = \frac{1}{2} m \cdot v_{imp}{}^2 \left(1 - CoR_N{}^2\right) \tag{2-12}$$

For a normal impact, the coefficient of restitution CoR_N is at maximum equal to 1, which corresponds to a perfectly elastic case.

2.2 Fragmentation of brittle materials

2.2.1 Elements of Fracture Mechanics

Fracture mechanics relates to the study of stress concentration due to sharp-tipped flaws and the propagation of these flaws within the body. Fracture mechanics originates from two seminal contributions by Griffith (1920) and Irwin (1958), which recognise the role of a crack as a stress concentration that influences brittle fracture.

The analysis of crack propagation in fracture mechanics has its origins in the attempts to understand the failure of glass, the stability of metal engineering structures in service, and, recently, the fracture properties of engineering ceramics. More recently, fracture mechanics has been also widely applied in the study of rock material behaviour and geophysics problems (Atkinson 1987).

The current research intends to deepen the understanding of dynamic fragmentation upon impact by experimental observations. Although the intent is not to use fracture mechanics to predict the occurrence of fragmentation or its outcome, the state of the art of fracture mechanics provides a valuable framework to interpret some of the experimental results on intact and controlled materials (e.g. quantify the amount of energy required to form new fracture surfaces in an intact material). Therefore, some key aspects of fracture mechanics, namely fracture modes, crack propagation, fracture toughness, dynamic fracture strength and the prediction of fragment size and distribution upon dynamic loading are discussed in the following paragraphs.

In the scientific literature, the term fracture refers to the appearance of a discontinuity surface called "crack", that locally separates a solid in two different parts (Atkinson 1987). There are three fundamental modes of crack propagation (or displacement) named as mode-I (Figure 2-6a), mode-II (Figure 2-6b) and mode-III (Figure 2-6c) referred as tensile, in-plane shear and anti-plane shear, respectively. In problems involving crack loading, the superposition of these three fundamental modes is sufficient to describe the most general case of fracture deformation and stress field (Atkinson 1987). For example, assuming a linear and elastic crack tip propagation and stress field on the plane $z = 0$, the following condition occurs for each of the three modes (see Figure 2-7 and Eqs. (*2-13*), (*2-14*) and (*2-15*)):

$$\text{For mode-I} \qquad \sigma_x \neq 0,\ \ \sigma_y \neq \sigma_z \neq 0,\ \ \tau_{xz} = 0 \tag{2-13}$$

$$\text{For mode-II} \qquad \tau_{xz} \neq 0,\ \ \sigma_y = 0 \tag{2-14}$$

$$\text{For mode-III} \qquad \tau_{yz} \neq 0, \;\; \sigma_y = 0, \;\; \tau_{xz} \neq 0 \tag{2-15}$$

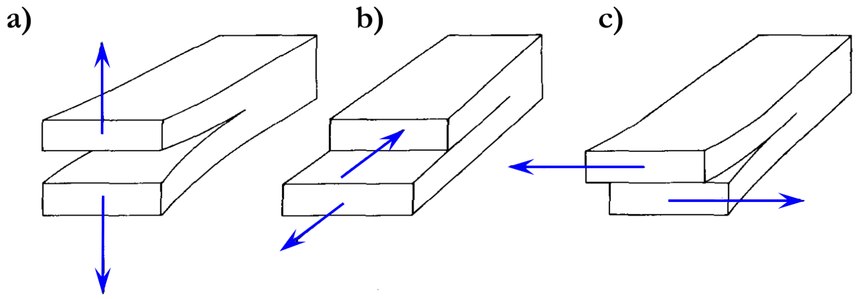

Figure 2-6: Schematic sketches illustrating the three fundamental modes of fracture: (a) mode-I, tensile or opening mode; (b) mode-II, in-plane shear or sliding mode; (c) mode-III, anti-plane shear tearing mode. (modified after Atkinson (1987)).

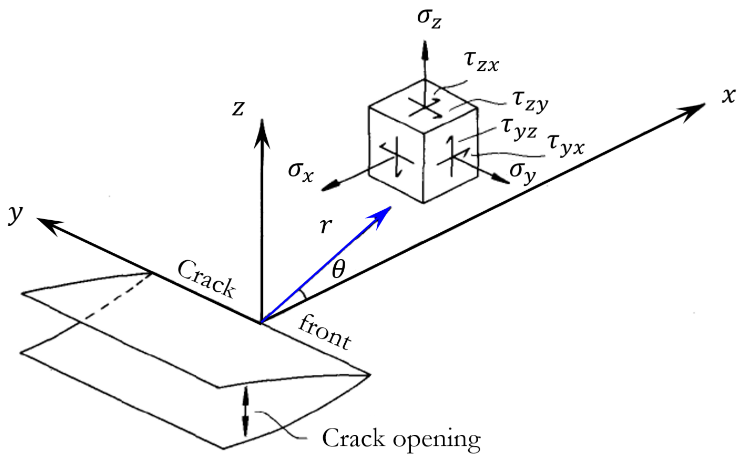

Figure 2-7: Example of the elastic stress field for fracture mode-I. Rectangular and polar reference system are centred at the crack front. Note that the opening of this crack is exegeted to be more visible. (modified after Atkinson (1987)).

Stress intensity analysis is used to measure the real force applied to a crack tip, which determines whether the crack grows or remains stable. The classical linear elasticity theory can be applied to study the fracture behaviour of the rock material, under fracture modes I, II and III. The stress intensity factor (K) is used to predict the stress state close to the tip of a crack or "notch" cursed by a remote force or residual stress (Anderson 2017). The stress intensity factor depends on the shape of the body, the length of the crack and it is directly proportional to the applied load. If a very sharp crack, or a V-notch can be made in a specimen with a defined geometry (Kuruppu et al. 2014), the minimum value of K_I, which corresponds to the critical value of stress intensity required to propagate the crack, can be determined experimentally. This critical value determined for mode-I loading in plane strain is named critical fracture toughness (K_{Ic}) of the material.

The critical fracture toughness can be used to determine the energy loss per unit of new crack separation area formed during an increment of crack extension (also called "strain energy release rate"). In quasi-static condition, it can be calculated for each fracture mode using the well know Irwin's correlation (Atkinson 1987; Zhang and Zhao 2014a):

$$\gamma_I = \frac{K_I^2(1-\nu^2)}{Y} \tag{2-16}$$

$$\gamma_{II} = \frac{K_{II}^2(1-\nu^2)}{Y} \tag{2-17}$$

$$\gamma_{III} = \frac{K_{III}^2(1+\nu)}{Y} \tag{2-18}$$

where Y is the Young modulus and ν is the Poisson ratio of the material.

Indeed, the response of a single crack to quasi-static or impulsive loading has been studied over the past several decades and it is reasonably well understood. It is also known that material properties and fracture behaviour of rock are highly affected by loading rate, and in particularly if it exceeds a critical value (Atkinson 1987; Backers et al. 2003; Bažant et al. 1993; Cadoni 2010; Hoek and Bieniawski 1965; Kipp et al. 1980; Zhang and Zhao 2014a; Zhang and Zhao 2014b). Researchers have attempted to explain the effect of loading rate on fracture strength by the existence of inherent flaws (Curran et al. 1977) and by considering the dynamic response of isolated cracks (Chen and Sih 1977). These two approaches capture different physical features of the transient fracture process observed in the dynamic fracture of rock and both lead to a theoretical description of the dynamic fracture strength of rock (Grady and Kipp 1987). For more detail about the two approaches consult Grady and Kipp (1987).

Prediction of fragment size and distribution in dynamic fragmentation

The fragment (or particle) size distribution produced in a fragmentation event has drawn the attention of researchers in various fields of science, especially if related to impulsive fracture applications. Several aspects of fragmentation, such as the resulting fragment distribution, are indeed significant in numerous explosive or percussive rock breakage applications, such as in deep drilling (Varnado and Stoller 1978), explosive or propellant stimulation of gas and oil wells (Warpinski et al. 1979), and mining and construction blasting (Langefors and Kihlström 1978). Similarly, the aspects are relevant for natural events such as the explosive eruption of a volcano or the catastrophic impact of a major meteorite (Melosh 1984; O'Keefe and Ahrens 1976) in which debris can be distributed through the earth's atmosphere.

Various approaches have been developed to predict the average fragment size and/or describe the fragment (or particle) size distribution. For the prediction of the average fragment size, both theories described in the previous section (fracture activation due to interaction of existence of inherent flaws or by considering the dynamic response of isolated cracks) have been successfully used to account for high loading rate fracture events (Costin and Grady 1984; Grady 1982; Grady and Benson 1983; Grady and Kipp 1980; Grady and Kipp 1987; Shockey et al. 1974).

The predominantly statistical nature of fragmentation was recognised in early studies of the phenomenon and standard distributions such as Poisson (Bennett 1936; Lienau 1936), binomial (Gaudin and Meloy 1962), log normal (Kolmogorov 1941), and Weibull (Rosin and Rammler 1933) have been successfully used to characterise fragment size distribution over the last century. Theoretical geometric studies have also been conducted to assess and model fragment size distribution, such as the random partitioning of lines, areas or volumes into the most probable distribution of sizes. In a one-dimensional case, the topic has been discussed by several authors (Gaudin and Meloy 1962; Gilvarry 1961; Grady and Kipp 1985; Lienau 1936), while it has been mutually agreed that in 2 and 3 dimensional spaces, the solution cannot be achieved without strong assumptions on the random partitioning of areas close to the boundaries. Therefore, the applicability of any geometrical statistical fragmentation model is not straight forward. In addition, statistical approaches ignore the dynamics of the fragmentation event like growing, propagating, interacting cracks and fractures or energy consuming, which strongly influence the fragment size statistics. Some of the main statistical distributions considered in the literature for the modelling of the fragment size distribution resulting from catastrophic fracture events (i.e. explosion) are discussed next.

Theories on the prediction of the fragments size distribution have been proposed since the early 1930s' and started with the fundamental hypothesis of a randomly cracked body (Figure 2-8). Concepts of Poisson statistics have been pivotal to the works proposed by Bennett (1936), Lienau (1936) Gilvarry (1961) and Mott and Linfoot (1943).

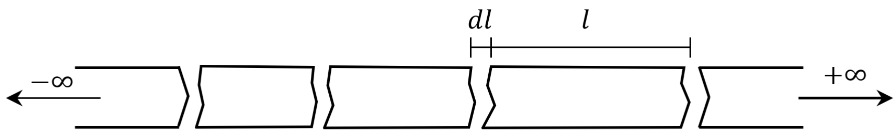

Figure 2-8: Poisson process - Random one-dimensional fragmentation (modified after Grady and Kipp (1987)).

Considering an infinite one-dimension line or bar along which random fractures occuring with an average rate N_0 fractures per unit length (as illustrated in Figure 2-8), the propability of finding n fractures within the length l, $P(n, l)$, is given by:

$$P(n, l) = \frac{(N_0 l)^n e^{-N_0 l}}{n!} \tag{2-19}$$

The most probable distribution in fragment size is found by observing that the probability of finding no fractures whithin a length l is:

$$P(0, l) = e^{-N_0 l} \tag{2-20}$$

while the probability of finding one fracture within a length, dl is:

$$P(1, dl) = N_0 \, dl \tag{2-21}$$

Thus the probability of finding a fragment of length l within a tolerance of the increment dl can be written as:

$$dP(dl) = P(0, l)P(1, dl) = N_0 \, e^{-N_0 l} \, dl \tag{2-22}$$

Integration of Equation (2-22) leads to:

$$N(l) = N_0 \, e^{-N_0 l} \tag{2-23}$$

A major difficulty to extend the one-dimensional problem to the two-dimensional geometric fragmentation of an infinite sheet, resides in the randomly partition of the area.

Mott and Linfoot (1943) proposed a linear nominal measure of the fragment size, proportional to the fragment area, a. The authors proposed a cumulative fragment number distribution:

$$N(a) = N_0\, e^{-\sqrt{2N_0 a}} \tag{2-24}$$

where N_0 is the number of fragments per unit area. This distribution was particularly successful to describe fragmentation during rapid experiments conducted on spherical and cylindrical shells. However, the method may be hardly applicable for dynamic fragmentation of rocks, as shown by experimental observations (Grady and Kipp 1985; Grady and Kipp 1987). Alternatively, Grady and Kipp (1985) suggested using a scalar measure of the fragment area, a, as a Poisson variable to represent dynamic fragmentation data:

$$N(a) = N_0\, e^{-N_0 a} \tag{2-25}$$

This "linear exponential" distribution was successfully used to represent dynamic experimental fragmentation data (Grady and Kipp 1985), and it was also expressed in terms of volume, V, as per Eq. (2-25):

$$N(V) = N_0\, e^{-N_0 V} \tag{2-26}$$

Another classical statistical formulation commonly used to describe the fragment size distribution is the Weibull distribution. The latter considers a flexible two-parameter analytical formula and it has been used in several engineering applications involving fragmentation and to describe fragmentation data (Rosin and Rammler, 1933, Grady and Kipp, 1987). Bennett (1936), Gilvarry (1961) and Kuznetsov and Faddeenkov (1975) put significant efforts to provide a reliable theoretical framework for the application of the Weibull description to fragmentation. However, the valid applicability of the distribution for fragmentation purposes has yet to be demonstrated, as theoretical issues related to divergence from fragment number and fragment surface area at the end of the distribution have been observed for such applications.

According to the Weibull representation of fragmentation, the cumulative distribution of fragment mass fraction (or volume fraction) finer than size x, is:

$$\frac{m(< x)}{m_{tot}} = 1 - e^{\left(-\frac{x}{m_{cr}}\right)^{\mu}} \tag{2-27}$$

where $m(< x)$ is the cumulative mass of fragments less than x, m_{tot} is the total mass of fragments and m_{cr} is related to a characteristic particle mass (or scale parameter) and μ is a Weibull shape parameter.

Grady and Kipp (1987) suggested that the shape parameter should range from about 0.5 to 6 as a function of the type or method of fragmentation. A theoretical upper limit of μ equal to 6 was suggested by Grady and Kipp (1985). Mock and Holt (1983) and Weimer and Rogers (1979) showed values of μ for a large body of fragmenting munitions ranging between 4 and 6, while direct impact fragmentation experiments showed a range between 2 and 3 (Shockey et al. 1974). In split Hopkinson pressure bar tests the shape parameter varies from about 1.2 to 1.8 (Costin and Grady 1984; Grady 1981). More diverse cases of fragmentation data, such as for ball milling comminution of mineral (Rosin and Rammler 1933), or explosive crushing experiments on glass spheres (Bergstrom et al. 1962), have shown distributions of μ close or equal to 1.

To summarise this section, studies conducted over the last century show that the energy consumed to create fractures can be estimated by knowing the fracture toughness of the material (estimated from standard toughness tests). However, the fracture behaviour of rock materials is significantly influenced by loading rate and is strongly correlated to the presence of imperfections or flaws. Various statistical distributions have been used in the literature for the modelling of the fragment size distribution resulting from catastrophic fracture events and an overview of the most well know statistical distributions and approaches has been provided as background for the research work presented here.

2.2.2 Experimental studies on fragmentation upon impact

The experimental study of breakage of rocks or particles of brittle materials is a challenging research field. The intrinsic shape variability of a natural rock represents one of the most important aspects to account for when designing and performing experimental investigations. However, it also brings an additional level of complexity to the problem. To simplify, spheres or discs have been generally used in comminution research to study the breakage by compression or impact, and theoretical solutions for linear elastic behaviour have been proposed to calculate the stress field developed upon breakage (Schönert 2004). The following sections provide further insights into the most recent experimental studies on brittle material conducted to investigate the static and dynamic response of spherical samples and intend to provide a useful background for the experimental work presented in this thesis.

2.2.2.1 Quasi static loading

The compression of spheres, either statically or dynamically, between two flat rigid platens, is one of the most popular experimental tests (Chau et al. 2000). In quasi-static conditions, crushing of spheres between two flat platens has been used to assess the deformability of elastic materials, the hardness of ductile materials and crushing strength of brittle materials. The test is also used to estimate the tensile strength of brittle spheres (Hiramatsu and Oka 1966; Jaeger 1967; Wynnyckyj 1985; Yoshikawa and Sata 1960). The static compression of spheres between two flat rigid platens has been applied to test the performances of various materials such as glass (Arbiter et al. 1969; Bergstrom and Sollenberger 1961; Bergstrom et al. 1962; Cheong et al. 2003; Gilvarry and Bergstrom 1961a; 1961b; Gorham et al. 2003; Kschinka et al. 1986; Schönert 2004; Shipway and Hutchings 1993c) ceramics (Wong et al. 1987), granulates (Antonyuk et al. 2005), sand concrete (Arbiter et al. 1969; Khanal et al. 2008), plaster (Chau et al. 2000; Wu et al. 2004), quartz sand (Breval et al. 1987), agglomerates (Meyers and Meyers 1983; Schubert 1975; Shinohara and Capes 1979; Wynnyckyj 1985), minerals, coals (Sikong et al. 1990), and rocks (Jaeger 1967; Santurbano 1994). A rather comprehensive review on the compression test of spheres is given by Darvell (1990).

Stress field and fragmentation pattern

The breakage of spheres (or particles) under compression has been explained by taking into consideration the pressure distribution and stress field developed upon loading (Antonyuk et al. 2005; Schönert 2004; Wu and Chau 2006). Analytical solutions have been proposed to describe the phenomenon: Hertz (1882) derived the ellipsoidal pressure distribution in a sphere during its contact deformation; Huber (1904) presented the stress field inside an infinite elastic half-space; Lurje (1963) calculated the spatial stress distribution in the whole sphere. One of the most popular model was proposed by Hiramatsu and Oka (1966) which obtained an analytical solution for isotropic spheres under diametral point load.

Similar solutions can also be found in Sternberg and Rosenthal (1952) and Dean et al. (1952). The solution by Hiramatsu and Oka (1966) was further extended by Wei and Chau (1998), Chau and Wei (1999) and Chau et al. (2000).

The typical failure pattern observed for spheres (or particles) under static compression shows two cones close to the contact points, which determine the splitting of the sphere (due to tensile stress) along one or more meridian fracture planes. In other words, spheres tend to split in two or three slices (like the shape of orange slices) with two conical fragments detaching from the contact zone (Figure 2-9). This fragmentation pattern was observed by Arbiter et al. (1969), Chau et al. (2000), Antonyuk et al. (2005), Gorham et al. (2003), Schönert (2004), Wu et al. (2004), Khanal et al. (2008) and Russell et al. (2015).

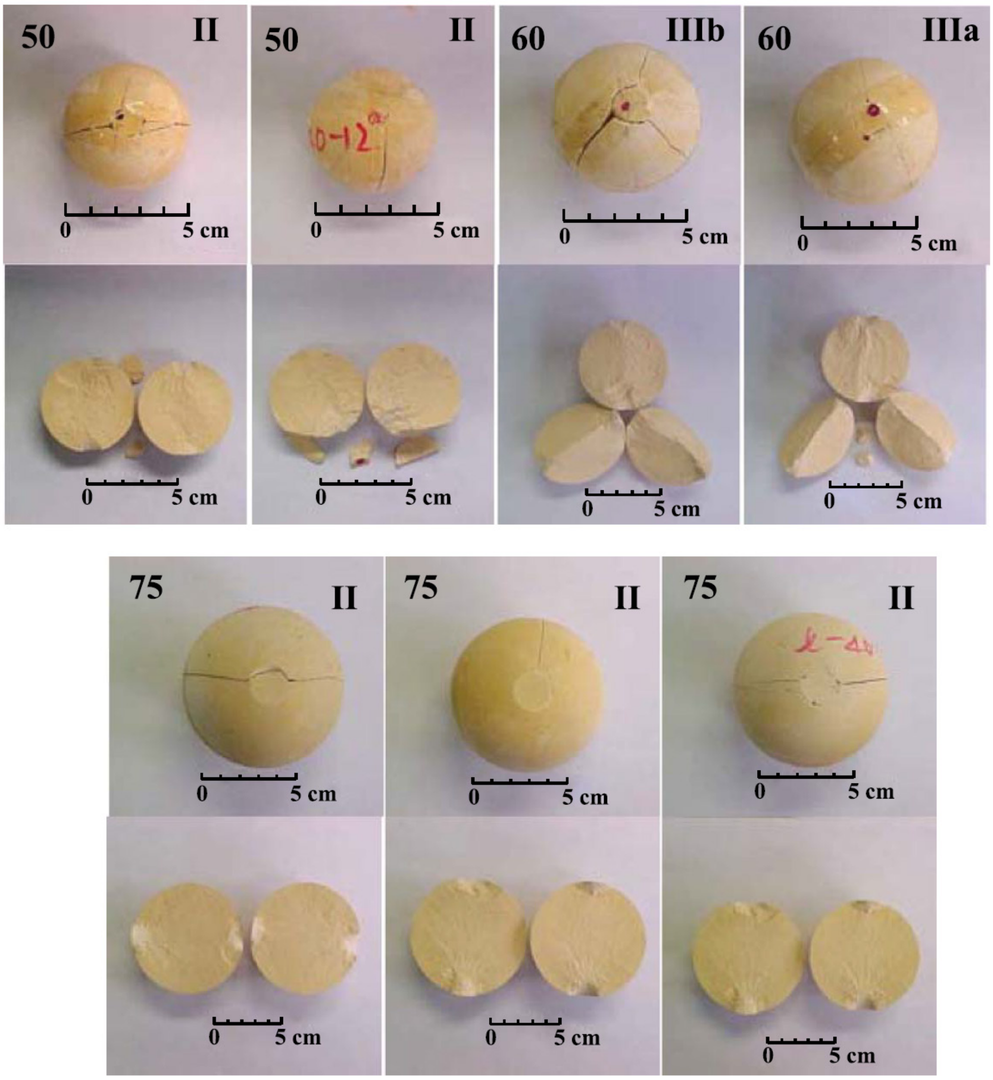

Figure 2-9: Typical failure mode of Plaster spheres under quasi-static compression for three diameters (50, 60 and 75 mm) observed by Wu et al. (2004). The Roman numeral indicates the failure mode: II indicates two slices, IIIa three unequal slices and IIIb three equal slices.

Survival probability and size effect

It is commonly recognised that for a given set of tests conducted on a series of samples (e.g. grains, spheres or particles) made of the same material, the stress measured at failure shows some variability between specimens. Even for homogeneous and identical samples, the material strength can be affected by differences in microstructure, distribution and orientation of granular bonds, defects, and pores size distribution. The survival probability (SP) of a sphere subjected to compressive stress loading is commonly described by a Weibull distribution (Frossard et al. 2012; Huang et al. 2014a; McDowell and Amon 2000; Nakata et al. 1999; Wang et al. 2015; Weibull 1951):

$$SP(\sigma) = 100 \cdot e^{-\left(\frac{\sigma}{\sigma_{cr}}\right)^{\mu}} \tag{2-28}$$

where σ is the stress applied to the spheres; $SP(\sigma)$ is the survival probability of the spheres under stress σ; μ is the distribution shape parameter corresponding to the slope of the central part of the Weibull distribution; and σ_{cr} is the scale parameter, also called critical value of σ, corresponding to a survival probability equal to $1/e \sim 37\%$. An example of survival probability with different Weibull shape parameters is given in Figure 2-10. Note that this formula can be also expressed in term of force or energy required to break the sample.

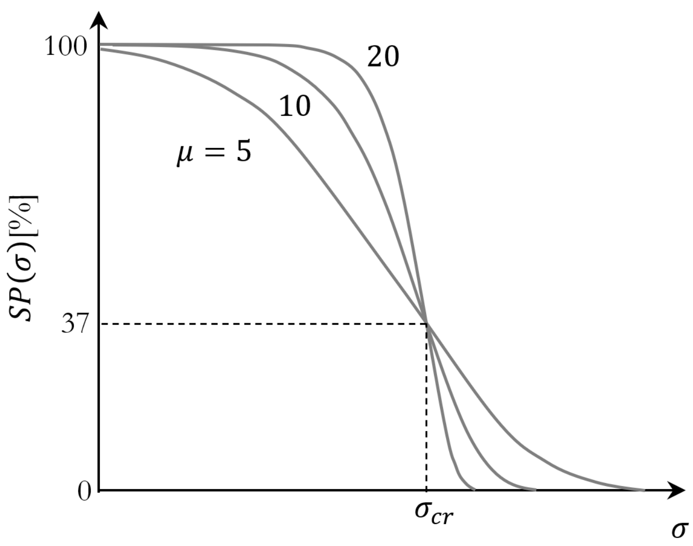

Figure 2-10: Example Weibull distribution with different Weibull shape parameter μ.

One of the most important aspects to consider in the study of quasi-static compression of spheres, is the size effect. This latter can generally be described as the dependence of a material intrinsic property on a characteristic sample dimension (e.g. volume or diameter). The size effect for the compression of spheres can be expressed by the statistical decrease of the intrinsic strength of a sample with its increase in size (Bažant and Planas 1997). Relevant experimental studies on the investigation of the size effect on breakage of grains or particles have been conducted by Yashima et al. (1987), Nakata et al. (1999), McDowell and Amon (2000), Antonyuk et al. (2005), Frossard et al. (2012), Ovalle et al. (2014), Huang et al. (2014a) and Wang et al. (2015) to name a few.

2.2.2.2 Dynamic loading

Considerable effort has been devoted to the study of the failure of a single sphere of rock caused by compressive forces, and several laboratory techniques have also been developed to investigate the phenomenon. Beside the quasi-static loading compression method (see Section 2.2.2.1), experimental testing of rock spheres under dynamic loading conditions is generally conducted by single impact or double impact (see Figure 2-11). Dynamic impact tests have been carried out on spheres of various materials such as steel (e.g. Knight et al., 1977), granite (Kawakami et al. 1990), sand-cement (Arbiter et al. 1969; Khanal et al. 2008; Tomas et al. 1999), soda-lime glass (Salman and Gorham 1997), ceramics (Andrews and Kim 1998), soils (Hadas and Wolf 1984; Newitt and Conwya-Jones 1958), glass (Andrews and Kim 1999; Cheong et al. 2003; Gorham and Salman 2005; Gorham et al. 2003) and limestone (Kapur and Fuerstenau 1967).

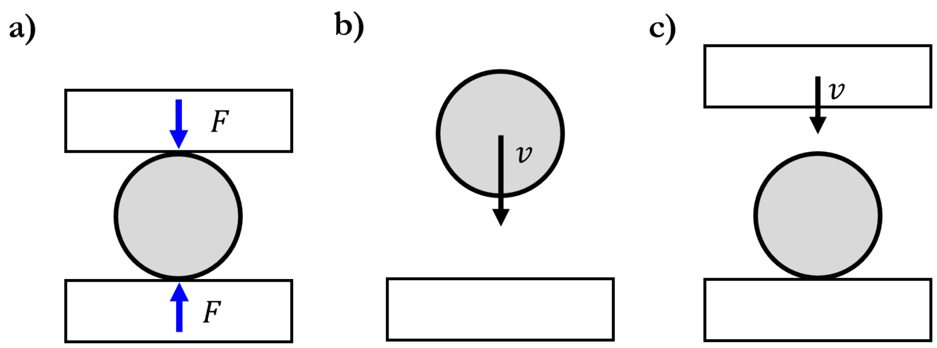

Figure 2-11: Schematics of sphere breakage tests: (a) slow compression test; (b) single impact test; (c) double impact test.

In the single impact test, a sphere (or particle) is dropped in free fall or is launched by compressed air with a certain velocity to impact on a hard surface. Single impact tests can generally be conducted in a range of loading rate between 10^0 and 10^4 s^{-1}. In the double impact test, such as drop weight test or pendulum test, the sphere is crashed by another object or by a flat surface (called drop-shatter test by Hadas and Wolf (1984)). Within these types of test, the multi-impact of the sample cannot be avoided (Huang et al. 2014b) and a loading rate of 10^4 s^{-1} is usually considered. The split Hopkinson pressure bar (SHPB) (Figure 2-12) falls within the category of double impact testing procedures and has been widely used for rock testing under dynamic conditions. The sample is sandwiched between two bars called transmission bar and incident bar. At the end of the incident bar, a stress wave is created by a sticker bar which propagates through the incident bar toward the specimen and the transmission bar. This wave is referred as incident or compression wave. A portion of this wave is reflected back into the incident bar as a tension pulse called reflected wave. Strain gauges are usually located at midpoints of the incident and transmission bar to record the stress pulse. The technique allows to conduct tests with loading rates between 10^4 and $10^6 s^{-1}$ and calculating the energy through the strain gauges located on the bars (Huang et al. 2014b; Zhang and Zhao 2014b). Table 2-3 reports a summary of dynamic loading techniques and associated loading rates.

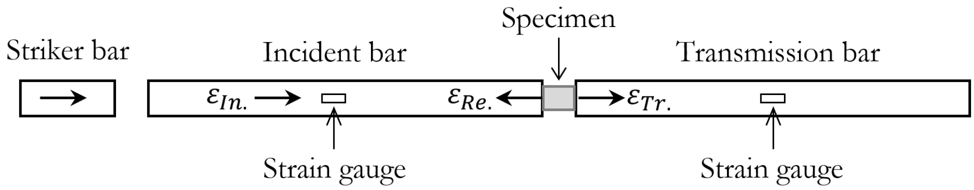

Figure 2-12 Schematic representation of a split Hopkinson pressure bar (SHPB).

Table 2-3 Classification of dynamic loading techniques to simulate the dynamic response of rock (adapted from Zhang and Zhao (2014a))

	Intermediate		Hight	
Loading rate (s^{-1})	**$10^1 – 10^3$**	**10^4**	**$10^4 – 10^6$**	**10^4 - 10^8**
Double impact	Pneumatic – hydraulic machine	Drop weight machines	Split Hopkinson pressure bar	Plate impact technique
Single impact	Drop test			
	Air compressed gun	Air compressed gun	Air compressed gun	

Rockfall impacts typically occur for impact velocities less than about 40 m/s (Wyllie 2014b) which corresponds to a maximum loading rate of 10^4. As for Table 2-3, this condition falls into the range of intermediate loading rate. Therefore, relevant studies conducted within this loading rate only are presented in the following sub-sections.

Stress field and fragmentation pattern

Theoretical and experimental studies of the failure of spheres under single impact have been conducted by Arbiter et al. (1969), Dean et al. (1952), Gan-Mor and Galili (1987), Shipway and Hutchings (1993b) and Schönert (2004). While Arbiter et al. (1969), Schönert (2004) and Wu and Chau (2006) investigated the behaviour under double impact.

Quasi-static loading and low velocity dynamic loading (in either compression or single impact) induce similar stress field, fracture pattern and shape of fragments produced at impact (Arbiter et al. 1969; Schönert 2004). However, it is generally recognised that dynamic tests require a higher energy to break a sphere compared to quasi-static condition. Chau et al. (2000) suggested an empirical correlation between the energy required to break a sphere under static compression and under double impact load, as:

$$E_k = 1.5 \cdot W_{SC} \tag{2-29}$$

where E_k and W_{SC} are the impact energy and the static compression energy required to break the sphere. A few years later, Wu and Chau (2006) proposed a new analytical solution for an elastic sphere under a double impact load that accounts for two auxiliary problems: a static solution of the applied loading (solved by using the Hiramatsu and Oka (1966) model), and the free vibration of the sphere subjected to an initial deformed shape induced by the applied load (using a Heaviside step function of time along the diameter). The solution was compared with experimental observations and it proofed to be a valuable tool to explain the fracture initiation and the fracture pattern observed in the crushing of brittle spheres or particles under double impact.

Schönert (2004) conducted experimental and theoretical investigations on the dynamic impact of spheres of Polymethylmethacrylate (PMMA) and glass. The authors showed a strong correlation between stress distribution and deformation within the contact area. In particular, he observed maximum tensile stresses around the meridional plane, determined by the pure elastic deformation of the spheres, and a non-symmetrical stress field with respect to the equatorial plane because of the development of cracks. A fairly big cone-shaped fragment is therefore created at the top of the sphere. The high stress concentration at contact, caused by the inelastic deformation, produces a stress distribution perpendicular to the meridional planes and enhances the split of the sphere in orange slice shaped fragments. The author concluded that the combination of elastic and inelastic deformations can determine the coexistence of two different fracture patterns, whose likelihood increases for increasing impact energies. The Hertz/Huber equations, combined with the Lurje solution for a sphere lying on a plate, were considered to describe the stress field and the breakage of the bottom part of the impacting sphere in elastic conditions. According to Schönert (2004), these considerations can be transferred to irregularly shaped particles. The fragmentation pattern, however, is expected to account for different fragment geometries.

Figure 2-13 shows some of the fragmentation patterns observed during the double (Figure 2-13a, b and c) and single impact (Figure 2-13d, e and f) tests. Figure 2-13a shows two cones close to the contact points, which trigger the splitting of the sphere in tensile mode along one or more meridian fracture planes. With increasing impact energy, secondary cracks begin to appear (see Figure 2-13b) up to a certain level from where several small fragments are observed. This severe fragmentation is also known as crushing (Figure 2-13c) (Chau et al. 2000; Schönert 2004; Wu and Chau 2006; Wu et al. 2004). In the single impact case, the fragmentation pattern is similar, but the top cone is not always present at low impact energies, due to the absence of impact force on the top of the sphere. However, as observed by Arbiter et al. (1969), Shipway and Hutchings (1993a), Tomas et al. (1999), Gorham et al. (2003), Salman et al. (2004), Schönert (2004) and Gorham and Salman (2005) a remaining cone can appear at the top of the sphere due to diversions of cracks as the impact energy increases (Figure 2-13d, e and f).

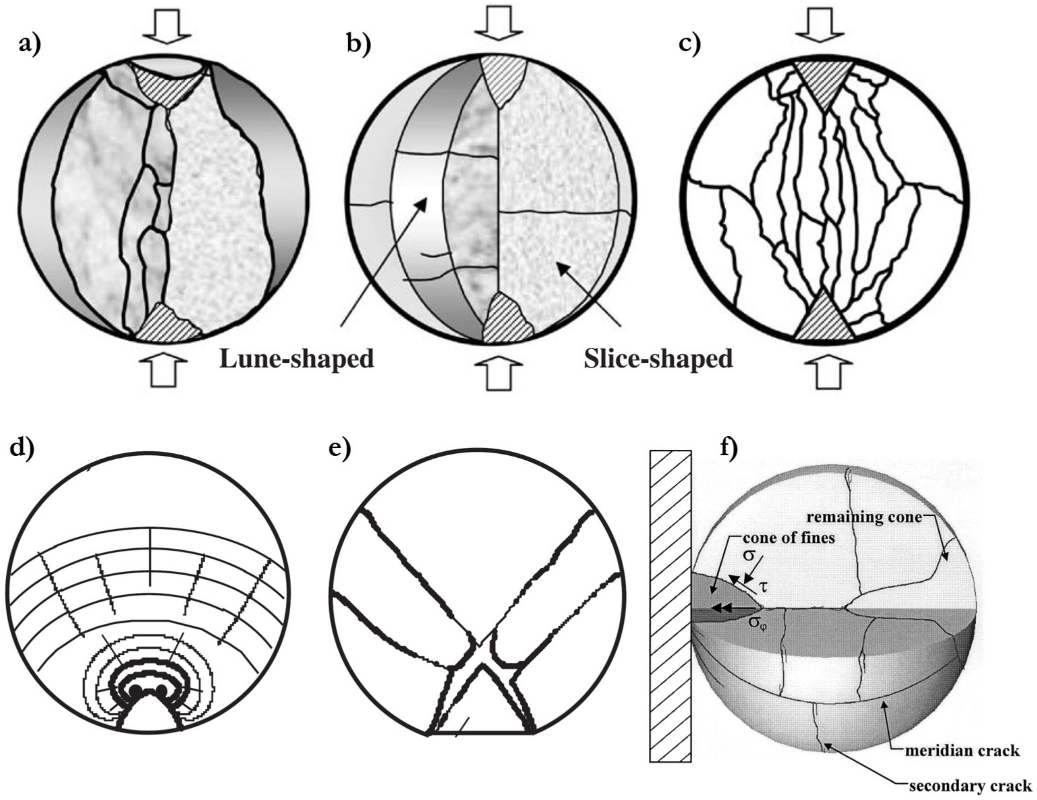

Figure 2-13: Schematic of the main form of failure for double (a, b and c) and single impact test (d, e and f): (a) double cone with meridional cracks; (b) double cone with meridional cracks and secondary cracks; (c) cross section of crushed sphere (Wu et al. 2004). (d) Single cone with meridional crack; (e) single cone with oblique fractures forming a remaining (top) cone (Gorham et al. 2003). (f) Single cone with meridian, secondary cracks and remaining (top) cone (Tomas et al. 1999).

Survival probability and parameters influencing the fragmentation occurrence

As mentioned in Chapter 1, the survival probability of spheres upon impact is of particular interest within the scope of the current research. The concept of survival probably of breakage of spheres described for quasi-static conditions can also be considered for dynamic impacts. In the case of single impact tests, due to the variability of the material, the failure of spherical samples is generally observed considering a range of impact velocities rather that a unique value of impact velocity required to break the sphere. Recent works proposed by Salman and co-workers on breakage of particles of aluminium oxide (Salman et al. 2002), glass (Cheong et al. 2003) and fertilizer granules (Maxim et al. 2006) are of particular interest in this regard.

Salman and co-workers used a compressed air gun to investigate the effect of impact velocity, impact angle, particle size, target material and target thickness on the fragmentation of small spheres (Cheong et al. 2003; Salman et al. 2002). A two-parameter cumulative

Weibull distribution was used to describe the relationship between the impact velocity and the number of unbroken particles as:

$$N_0 = 100 \cdot e^{-\left(\frac{v_{imp}}{v_{imp}^{cr}}\right)^{\mu}} \tag{2-30}$$

where N_0 is the number of unbroken particles, v_{imp} is the impact velocity, v_{imp}^{cr} is the Weibull scale parameter (also called critical velocity) and μ is the Weibull shape parameter.

The study showed how every parameter (velocity, impact angle, target material) affect the fragmentation occurrence. In particular, the survival probability of the particles decreases with the increase of impact velocity, impact angle, target thickness, target hardness and particle size.

The only attempt that can be found in the scientific literature to predict the dynamic survival probability of granules based on quasi-static compression tests, was conducted by Maxim et al. (2006). The authors proposed a model in which the maximum force expected during impact is assumed to be equal to the one experimentally measured during the quasi-static compression of the particle. The force is used to predict the critical velocity for Eq. (*2-30*). Note that no attempt to predict the Weibull shape parameter was made in Maxim's model, therefore, the experimental value estimated from the impact tests is used in the model. The results did not account for static or dynamic loading rates. Therefore, the predicted critical velocity was underestimated by a relative error higher than 20%.

2.2.2.3 In situ surveys

In situ testing has been widely performed to investigate the rockfall phenomenon and calibrate rockfall models parameters (Bourrier et al. 2009; Chau et al. 2002; Dewez et al. 2010; Dorren et al. 2006; Giacomini et al. 2009; Giacomini et al. 2010; Gili et al. 2016; Labiouse and Heidenreich 2009; Ritchie 1963; Spadari et al. 2012; Volkwein and Klette 2014). Nevertheless, only two of the cited studies focus on the experimental analysis of fragmentation in the context of rockfall: Giacomini et al. (2009) and Gili et al. (2016).

Giacomini et al. (2009) studied rock fragmentation in the context of the design of protection barriers. Two series of drop tests were performed in a quarry in Italy using granite rocks. Two high speed cameras were used to capture the impacts. The images were used to estimate the velocities of the blocks (before impact) and of the fragments upon impact (after impact). The study investigated the orientation of the rock discontinuities with respect to the impacted surface (measured from image analysis). The results showed that the angle between the discontinuities and the impacting surface (or impact angle) can significantly influence the outcome of the fragmentation (i.e. the number of fragments after impact). In addition, Giacomini et al. (2009) highlighted the complexity of defining a rockfall impact energy thresholds leading to fragmentation, as proposed by Fornaro et al. (1990), showing that the phenomenon should take into account material parameters and impact conditions affecting the potential fragmentation. An energy balance analysis was conducted for each test accounting for: (1) kinetic energy (E_k) (before and after impact) measured thought image analysis, (2) deformation energy (ΔE_d), assumed by using the coefficient of restitution (CoR_N) and (3) fragmentation energy (ΔE_{fr}). The latter was expressed as:

$$\Delta E_{fr} = E_k^b \cdot CoR_N^2 - E_k^a \tag{2-31}$$

where E_k^b is the kinetic energy just before impact; CoR_N is the normal coefficient of restitution; E_k^a is the kinetic energy after impact, defined as $E_k^a = \frac{1}{2}\sum_i m_i \cdot v_i$, where m_i is the mass of a fragment and v_i is its velocity. The results showed that the amount of fragmentation energy dissipated in fragmentation was a constant ratio on the kinetic energy before impact.

More recently, Gili et al. (2016) conducted a series of full scale rockfall tests in a quarry in Spain to investigate the rockfall fragmentation. Several slope profiles and initial falling heights were used to drop 53 rock blocks. The trajectory and the velocity of the blocks were tracked by three high-speed video cameras. An aerial photogrammetric campaign was also used to capture the full scene, including block and fragments trajectory. Similarly to Giacomini et al. 2009, the investigation did not clearly indicate an energy threshold (Fornaro et al. 1990), but showed a correlation between the number of blocks generated at breakage and the fractal dimension of the initial volumetric distribution (Ruiz-Carulla et al. 2020; Ruiz-Carulla et al. 2017).

2.2.3 *Numerical studies on fragmentation upon impact*

Over the last few decades, advanced numerical tools have also been used to investigate the fragmentation phenomenon. Numerical models are a valid alternative to difficult, time-consuming and expensive experimental research. The numerical study of the rockfall fragmentation is beyond the objectives of this research, however, given the significance of the recent numerical findings and their correlation with experimental results presented in the scientific literature, some of the main works conducted on the topic are hereby included.

Several authors numerically investigated the rockfall impact and the fragmentation mechanism by means of advanced discrete element modelling (Behera et al. 2005; Liu et al. 2010; Moreno et al. 2003; Paluszny et al. 2016; Reddish et al. 2005; Sator and Hietala 2010; Thornton et al. 1996; Wang and Tonon 2011; Wittel et al. 2008; Ye et al. 2019a; Zhao et al. 2017). Three dimensional studies resulted more realistic and highlighted the inner limitations of modelling the fragmentation process in a bi-dimensional plane (2D modelling), especially in capturing the formation of meridional cracks that determine the primary breakage mechanism.

Of particular interest is the work conducted by Wang and Tonon (2011). The authors investigated the mechanism of rock fragmentation upon impact, considering the effect of impact velocity, ground conditions and fracture proprieties. The block was modelled as an agglomerate of spherical particles impacting on top of a horizontal rigid plane. Taking into account the physical process of rockfall impact fragmentation consisting of impact-induced stress waves that propagate and create plastic zones, the ground was assumed as a half-space elastic homogenous medium. The classical 3D discrete element method (DEM) was used in the simulations. The study showed that the number of fragments increases with the impact velocity, the incidence angle (defined as the acute angle between the ground and the incident trajectory) and the ground stiffness. At an equal incidence angle, higher impact velocity generates higher impact stresses, increasing the possibility of fragmentation at impact. Instead, for a given impact velocity, a smaller incidence angle reduces the occurrence of fragmentation while producing greater angular momentum in the rock. The numerical study also showed that a variation of the incidence angle can affect the fragmentation for a given impact velocity. The normal component of the impact velocity with respect to the ground surface mainly governs the impact stresses and, hence a higher impact angle produces more fragmentation. Additionally, it was observed that a softer ground tends to extend the duration of the impact and to produce lower impact stresses with consequent less probable fragmentation at impact.

Wittel et al. (2008) and Paluszny et al. (2016) also used a 3D DEM to numerically reproduce the experimental results of brittle fragmentation of spheres. In their simulations a quite realistic representation of the fragmentation processes and the evolution of the fragmentation mechanisms, such as fragment shape and mass distribution (which was fitted with a two parameter Weibull distribution), was obtained. However, many factors that can affect the fragmentation, such as the presence of discontinuities, material heterogeneities, size effect and impact conditions were ignored.

Lisjak et al. (2010) proposed a hybrid finite-discrete element approach (FEM/DEM) to model rockfall fragmentation. In situ tests and material data (Giacomini et al. 2010) were considered to calibrate the model and account for rock deformability, damage and fragmentation. The model was applied to a case study of rockfall with fracturing along the slope. Results showed the capability of the tool to efficiently reproduce field observations for blocks breaking and fragments accumulating along the slope upon breakage. The model was applied to 2D only, and no further investigations in the three-dimensional space and accounting for materials variability were conducted.

Liu et al. (2010) investigate the breakage of agglomerates of different shape (spherical, cuboidal and cylindrical) impacting with a target wall using DEM. The results showed that cuboidal edge, cylindrical rim, and cuboidal corner impacts generate less damage than spherical agglomerate impacts. On the other hand, impact on cuboidal face, cylindrical side, and cylindrical end results into several fragments.

More recently, Ye et al. (2019a) used a 3D clumped particle method to investigate the fragmentation process of marble spheres upon impact. The authors proposed a new calibration procedure to take into account for both the quasi-static and the dynamic behaviour of the material. They successfully recreated the evolution of fragmentation pattern as a function of the impact velocity observed in the laboratory (Ye et al. 2019b). The fragment size distribution based on mass and number was fitted using a generalised extreme value law. The numerical predictions of fragmentation showed that the translational velocities of some small fragments can be significantly higher than the impact velocity due to the instant high-tensile stress wave occurring near the contact area. The results also suggested that there is no correlation between the mass of a fragment and its kinetic energy.

2.2.4 Modelling of fragmentation in rockfall engineering

To the author's knowledge, the first model accounting for fragmentation in rockfall engineering was proposed by Wang (2009). It consists of an impact fragmentation module which was integrated into the 3D rockfall code HY-STONE (Crosta et al. 2004). The module allowed performing rockfall simulation analysis by taking into account the fragmentation of a rock block upon impact and its flying fragments. The impact fragmentation model uses either an interpolation method or a neural network model based on an extensive DEM simulation database to predict the fragmentation process. The model was calibrated and validated by using both quasi-static and dynamic material behaviour obtained by laboratory tests. Several case studies were presented, and it was demonstrated that the developed fragmentation module can reasonably well predict impact fragmentation to perform risk analysis in rockfall analysis. However, the model was not able to reproduce the fragment size distribution observed in real cases. In addition, it was assumed that the velocity of the fragments can be calculated based on coefficients of restitution as no experimental data was available.

In recent years, Corominas and co-workers significantly contributed to the modelling of fragmentation in rockfall engineering. In particular, the research team proposed a "Rockfall Fractal Fragmentation Method" (RFFM) (Ruiz-Carulla and Corominas 2020; Ruiz-Carulla et al. 2020; Ruiz-Carulla et al. 2017) to obtain the rockfall block size distribution (RBSD) from in situ block size distribution (IBSD) and a GIS-based software, called RockGIS, to stochastically simulate the fragmentation of rockfall (Matas 2020; Matas et al. 2020; Matas et al. 2017).

Ruiz-Carulla et al. (2017) proposed different possible configurations to characterise the fragmentation of a block within a rockfall event to understand the predominant mechanism as disaggregation, pure breakage or both (Figure 2-14). If the initial detached mass is represented by a single block, it can remain intact (Figure 2-14a) or undergo breakage when the impact energy reaches a set energy threshold (Figure 2-14b). Alternately, if the initial block mass has major or minor structures (such as set of joints) that determine the size of further fragments at impact, the range of volume of the fragments can be characterised by the In Situ Size Distribution (IBSD). For low values of impact energy, the rock mass can simply disaggregate because of pre-existing planes of weakness (such as joints), generating a rockfall block size distribution (RBSD) similar to the original IBSD (Figure 2-14c), or a combination of breakage and disaggregation can occur (Figure 2-14b). The proposed RFFM aims to express the abovementioned scenarios (Ruiz-Carulla et al. 2017) and it is based on the generic fractal fragmentation model of Perfect (1997). Three parameters are used in the model:

1. the probability of failure, which indicate the degree of breakage of the instable identified block;
2. the survival rate, which expresses the percentage of blocks in a rock mass that will survive at impact (i.e. remaining intact);
3. the scaling factor *b,* which expresses the size ratio between the block and its fragments.

The procedure can be iterated in hierarchies. Subsequent iterations result in a progressively smaller fragment size. The fragmentation is assumed scale invariant, even though the analysis can also be conducted as scale variant. A survival rate equal to 1 reproduces the only disaggregation of the IBSD, hence the RBSD is equal to the IBSD. The model has been recently updated (Ruiz-Carulla and Corominas 2020) to meet the mass balance, and to generate both a continuous decreasing and scale variant distribution of fragment volumes.

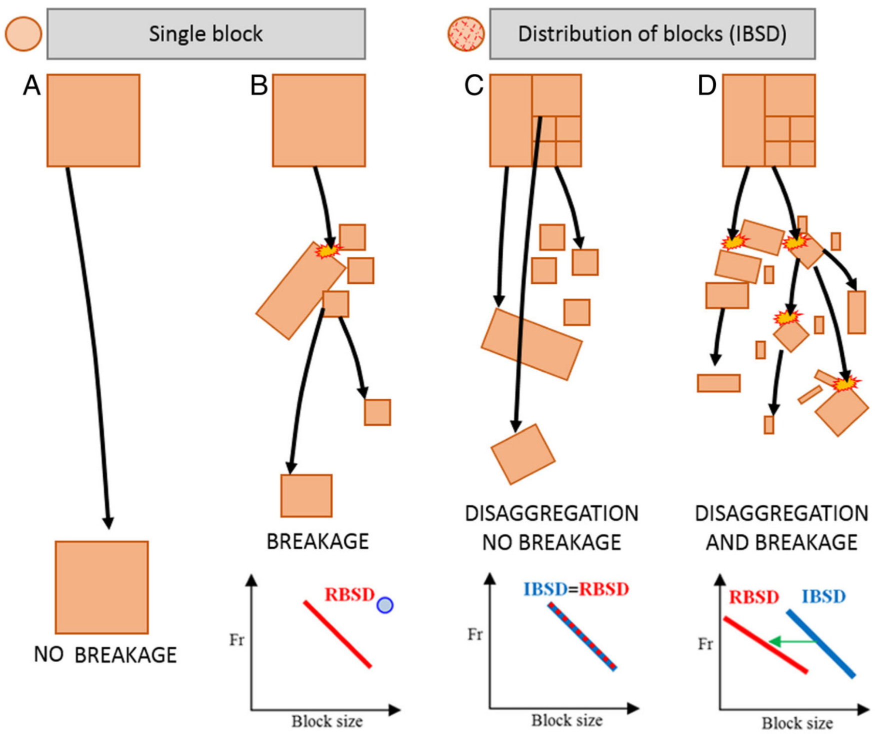

Figure 2-14: Scheme of mechanisms of fragmentation of falling rock blocks and rock masses considered by Ruiz-Carulla et al. (2017). Considered mechanisms in the. Conceptual schemes of changes in the block size distribution in the case of fragmentation by (a) lack of breakage of a single block, (b) breakage of a single block, (c) disaggregation of the rock mass through the pre-existing joints and (d) Disaggregation and breakage of the detached rock mass.

The code RockGIS (Matas et al. 2017) simulates the propagation of the blocks using a lumped mass approach in the space defined by a Digital Elevation Model and performs the rebound calculations using restitution factors according to the slope material. The fragmentation is triggered by the disaggregation of the detached rock mass through the pre-existing discontinuities just before the impact with the ground of the slope. No energy is required for the disaggregation of the IBSD. An energy threshold and a probability of brakeage are defined in order to determine whether the impacting blocks break or not. The distribution of the initial mass between a set of newly generated rock fragments is stochastically generated following a power law. The remaining energy is distributed between the fragments proportionally to their mass. The trajectories of the new fragments of rock are distributed stochastically within a cone. RockGIS has been also recently updated (Matas et al. 2020) to complement the improved Rockfall Fractal Fragmentation Method (Ruiz-Carulla and Corominas 2020). The updated RockGIS software considers the kinematic of the blocks as described in Gischig et al. (2015) and includes the rotational velocity of the blocks.

No further rockfall fragmentation models can be found in the literature as a deep understanding of how the fragmentation phenomenon occurs upon impact is not trivial.

3 Design of fragmentation cell

As part of the PhD research, an innovative experimental setup was developed to study rock fragmentation upon impact. The setup was designed to perform controlled vertical drop tests and record the following impact parameters: impact force, impulse, impact duration, translational and rotational velocities (of the block before impact and of fragments after impact) and relevant pre- and post-impact energy components. In this chapter, the experimental setup and the methodology to analyse impact data are described in detail.

3.1 Description of the setup

3.1.1 Impact testing apparatus

A hexagonal fragmentation cell (Figure 3-1) was developed in order to perform safe and controlled drop tests with detailed observation of brittle materials. The hexagonal cell consists of alternating polycarbonate and plywood panels, such that the impact in the centre of the cell can be recorded with high-speed cameras located outside the cell through the clear panels, with the painted plywood panels as background. The cell is 2.3 m high and each side is 1.2 m wide. A door on one of the plywood panels provides entry to the cell. The impact area consists of a fibre-reinforced concrete slab (1.1 m x 1.1 m x 0.2 m) having a compressive strength of 60 MPa. The test blocks are lifted using a vacuum tube (for blocks having a smooth surface) and a pulley system, suspended from the structure of the building. Blocks are released by opening the vacuum to the atmosphere. The maximum drop height is 5.1 m.

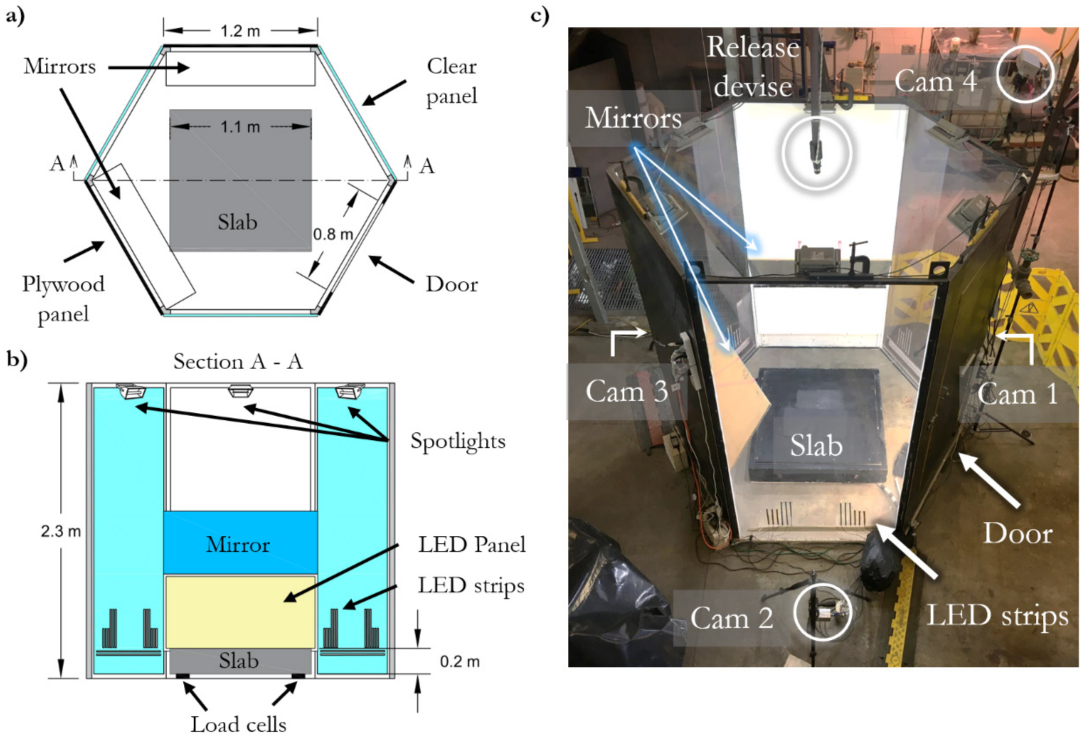

Figure 3-1: Experimental setup: (a) plan view of the fragmentation cell. (b) Section A - A of the fragmentation cell. (c) View of the fragmentation cell, release device, slab and camera positions. Cam 1 and Cam 2 are indicated with arrows because they are behind the cell and not visible.

3.1.2 Impact monitoring

Three disk-type LPX compression load cells with a capacity of 100 kN each are used to record the transmitted force at the bottom of the impact slab (Figure 3-2a and c). Note that three 10 mm thick steel plates are embedded in the underside of the slab to avoid localised concrete damage at the point of contact with the load cells (Figure 3-2c). The sum of the three measured forces, denoted F_T, is used as an indirect measurement of the impact force. An accelerometer (capacity 50g) is also mounted in a recess in the underside of the slab beneath the impact point (Figure 3-2c) to measure the acceleration during the impact along the vertical axis. Acceleration data are integrated twice with respect to time to infer the displacement of the centre of the slab. Note that the accelerometer is only used to calibrate the stiffness of the system. The load cells and the accelerometer are connected to a high frequency data logger (USB Compact DAQ system from National Instrument 9234) with a logging rate of 12,500 Hz.

A pressure measurement device (I-Scan High Speed VersaTek) is used to measure the impact duration (i.e., contact time between impacting object and the slab). The system utilises sheets of ultra-thin (0.10 mm) flexible sensors to record impact pressures and time. The sensor used in this study has 196 individual pressure sensing locations, referred to as sensels, arranged in 14 rows and 14 columns (see Figure 3-2b). The sensor is 71.1 mm square and has a spatial resolution of 3.9 sensel/cm^2. The native logging rate of the sensor is 4,000 Hz which is too low for the current application. However, the logging rate was increased to 14,000 Hz by only activating the middle four columns (highlighted in Figure 3-2b) and deactivating the peripheral columns. This modification reduces the width of the sensor to 20 mm, which compromises the measurement of the spatial pressure distribution but allows for an accurate measurement of impact duration. Note that there was no larger pressure film sensor with suitable logging rate available from the manufacturer. A sheet of aluminium foil is placed on top of the pressure sensor for each test, from which the damaged area is used to measure the size of the impact area, which can be used to back-calculate the experimental deformation of spherical blocks upon impact, from geometrical considerations.

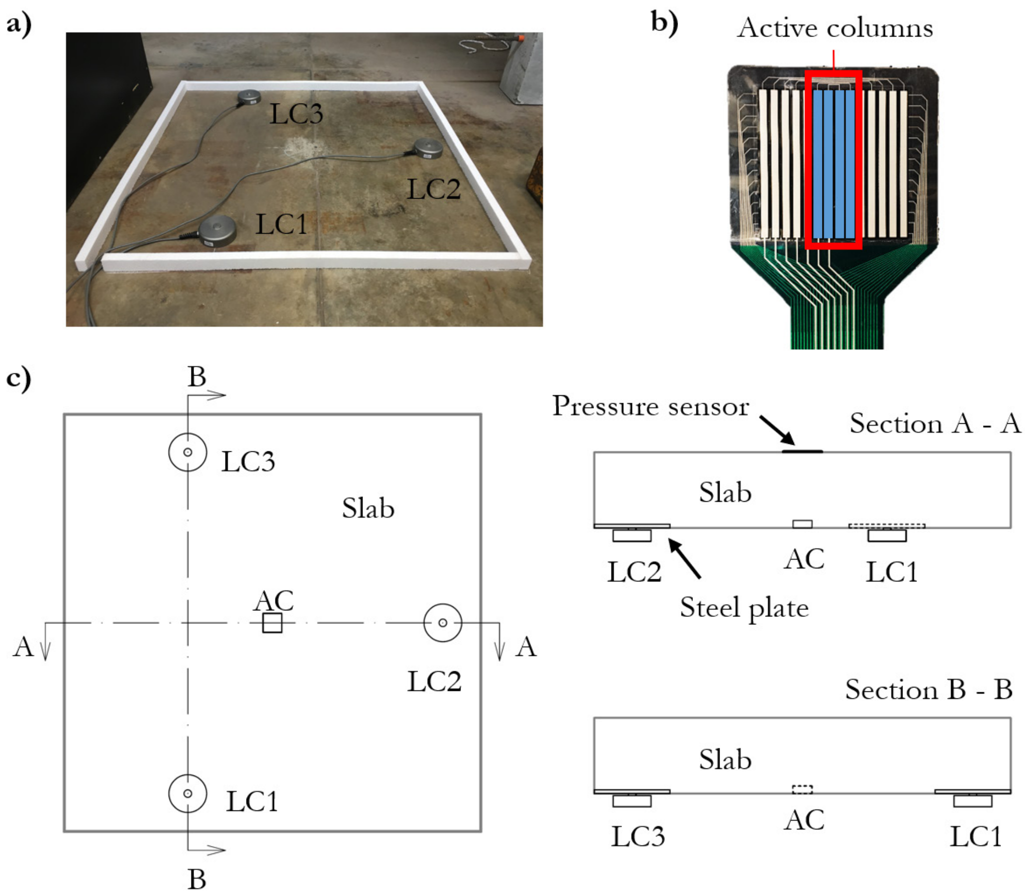

Figure 3-2: (a) Position of load cells (LCs). (b) Pressure sensor used to record the impact duration. (c) Position of load cells (LCs) and accelerometer (AC) within the slab.

3.1.3 *Motion capture*

Four high-speed cameras (referred to as Cam 1 to Cam 4) are used to capture the impact from four different positions (see Figure 3-1). Cams 1, 2 and 3 are set up at a distance of 0.6 m behind each of the transparent panels, in the same horizontal plane at 0.3 m above the floor. Cam 4 is located 3 m above the floor, in one of the corners of the cell. All four high-speed cameras are Optronics CR600x2 with a resolution of 1280x1024 pixels. Two different lenses are used depending on camera location. The three cameras behind each transparent panel (Cam 1 to Cam 3) use a Nikon AF NIKKOR 35mm f/2D lens, the camera at the top (Cam 4) has a Nikon AF NIKKOR 50mm f/2D lens. The frame rate used is 500 fps with a shutter speed of 1/3000s and an aperture of 2.8mm. All cameras are connected to a custom-build synchronisation box that serves as master controller. This assures that all cameras (slaves) are triggered simultaneously and that images from different perspectives are synchronised. A sketch of the camera connections is provided in Figure 3-3.

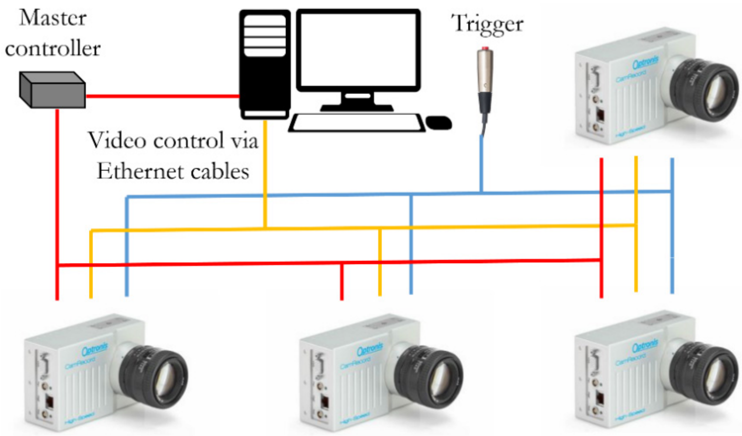

Figure 3-3: Scheme of camera connections: video (in orange), synchronisation (in red) and triggering system (in blue).

Despite using four high-speed cameras to provide four different views (V1-V4), additional views are needed to track fragments with the required accuracy (Guccione et al. 2019). An additional two views (V5 and V6) were obtained by placing tilted mirrors in front of Cam 1 and Cam 2 (see Figure 3-1 and Figure 3-4a), effectively allowing two different views to be simultaneously acquired by each camera: a direct view and an indirect view in the mirror. Note that this arrangement requires the lens focus to be adjusted to a compromised distance somewhere between d and d_1 (see Figure 3-4a) in order to see the block/fragments from both views (direct and mirrored reflection) with minimal out-of-focus blur. In the rest of this thesis, the views are named V1 to V6 according to Figure 3-4b. It should be noted that that the mirrored images from Cam 1 and Cam 2 have to be flipped before processing the images of V5 and V6 respectively (Figure 3-5).

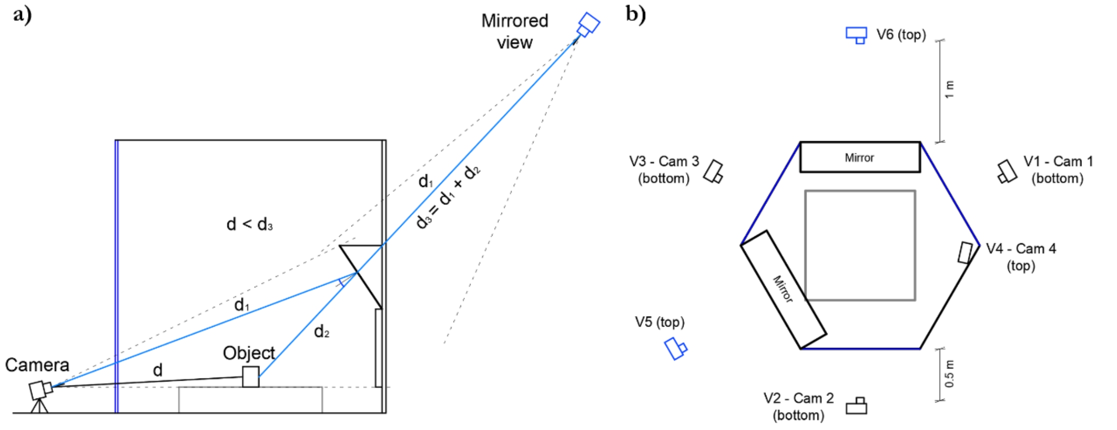

Figure 3-4: (a) Camera and mirror with effective object distances d and d_3. (b) Physical viewpoints V1 to V4 for Cam 1 to Cam 4 and virtual viewpoints V5 and V6 for the mirrored views.

Adequate lighting is crucial to be able to use high shutter speed and reduce object blur within the frame whilst retaining a reasonable depth of field and image quality. For this reason, several strips of white LED flex ribbon are installed on each clear panel and LED spotlights were mounted on the top of each side of the cell. In addition, 53-Watt LED panels (dimension 1200mm x 600mm) were attached to each plywood panel, directly opposite Cam 1, 2 and 3 (see Figure 3-1). This position allows an appropriate contrast in images taken from the bottom views (V1, V2, V3, see Figure 3-5a). To enhance contrast for the top views (V4, V5, V6), the slab was painted black (see Figure 3-1 and Figure 3-5b), noting that colour of the objects dropped is pale grey.

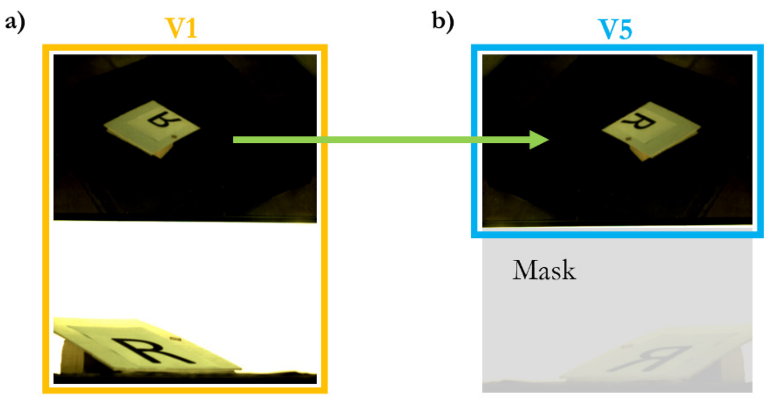

Figure 3-5: Example of an image taken with Cam 1 (a) with V1 (the whole image usable) and (b) corresponding flipped image to be used as mirrored camera with V5 (top views usable only).

3.2 Data analysis

3.2.1 *Impact data processing*

The forces recorded from the three load cells (F_1, F_2, F_3) located under the slab are first smoothed using a Python script and the Savitzky–Golay filter from SciPy (Virtanen et al. 2020) to remove noise. The three signals are then summed to obtain the total transmitted force F_T. Smoothing is conducted before summing the signals in order to avoid amplifying the noise by summation. An example of impact forces recorded during a drop test (impact velocity 2m/s) and the corresponding total transmitted force F_T is given in Figure 3-6.

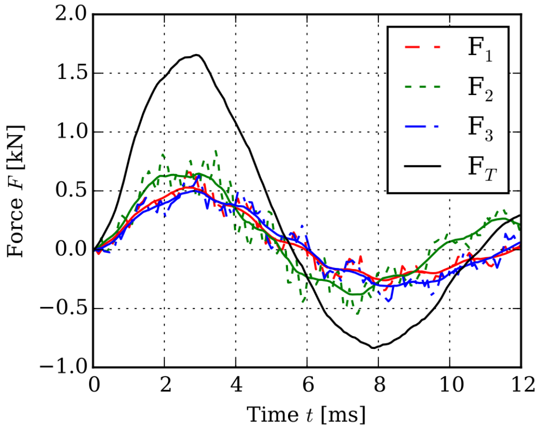

Figure 3-6: Evolution over time of the forces F_1, F_2, F_3 recorded by the bottom load cells before and after smoothing (solid lines are smoothed forces) and the total force F_T which is the sum of the three smoothed force values at any point in time.

The accelerometer response is processed by first applying a low pass filter to get rid of the noise followed by a high pass filter to remove the drift in the signal. The filtered data are then integrated twice with respect to time to get the vertical displacement (z) of the slab. Despite the filtering process on the original signal, it was found that the displacement still shows signs of being affected by a drift that has no physical cause. To mitigate such drift, the final vertical displacement is corrected by a high pass filter. This process is automated using a Python script and the Butterworth filter implemented in SciPy (Virtanen et al. 2020). Figure 3-7 illustrate the steps of the filtering process applied to the accelerometer signal.

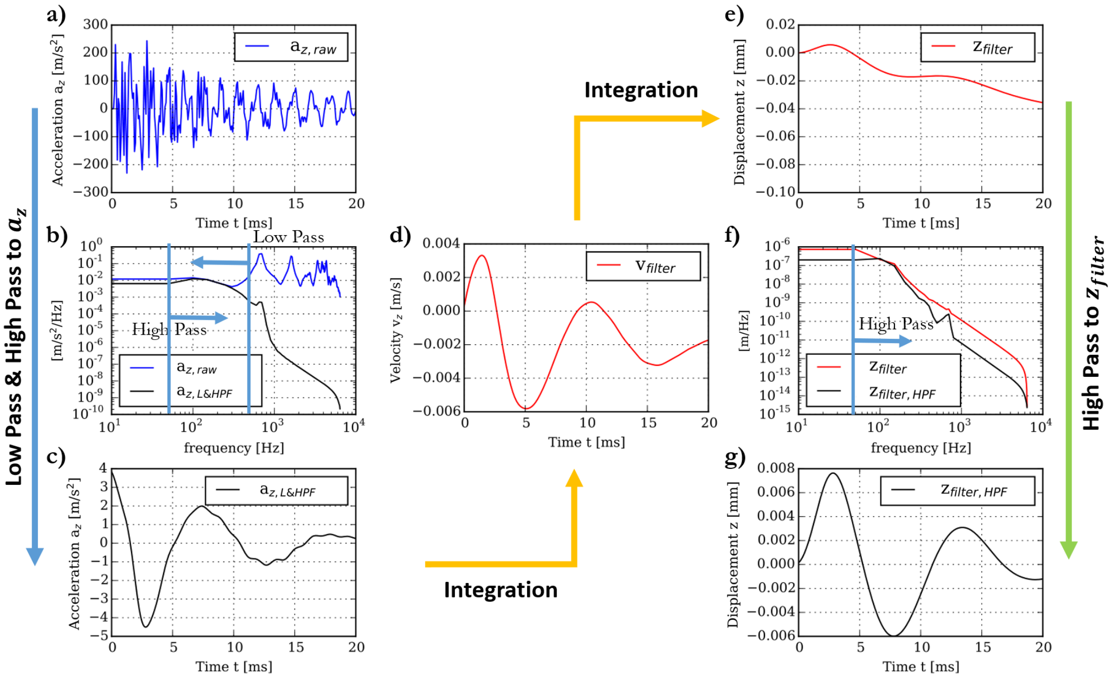

Figure 3-7: Overview of filtering and integration of accelerometer signal in order to obtain the vertical displacement of the slab. (a) Raw signal from accelerometer ($a_{z,raw}$) over time. (b) Power Spectral Density using Welch's method (Virtanen et al. 2020) for $a_{z,raw}$ and $a_{z,raw}$ after applying high and low pass filter ($a_{z,L\&HPF}$). (c) Evolution over time of the vertical slab acceleration ($a_{z,L\&HPF}$). (d) Integration of $a_{z,L\&HPF}$ to obtain the velocity of the slab after filtering (v_{filter}). (e) Integration of v_{filter} to obtain the displacement of the slab after filtering (z_{filter}) still affected by drifting. (f) Power Spectral Density using Welch's method for z_{filter} and z_{filter} after applying high pass filter ($z_{filter,HPF}$). (g) Evolution over time of the vertical slab displacement ($z_{filter,HPF}$).

Two verifications were conducted to check that the filtering process did not alter the accelerometer signal. First, the maximum filtered acceleration was multiplied by the mass of the slab to return a force. It was verified that this force is within ±10% of F_T. The second verification involved checking that the time at which the slab displacement and the transmitted force F_T return to zero after the first peak of force and displacement is the same (see Figure 3-8).

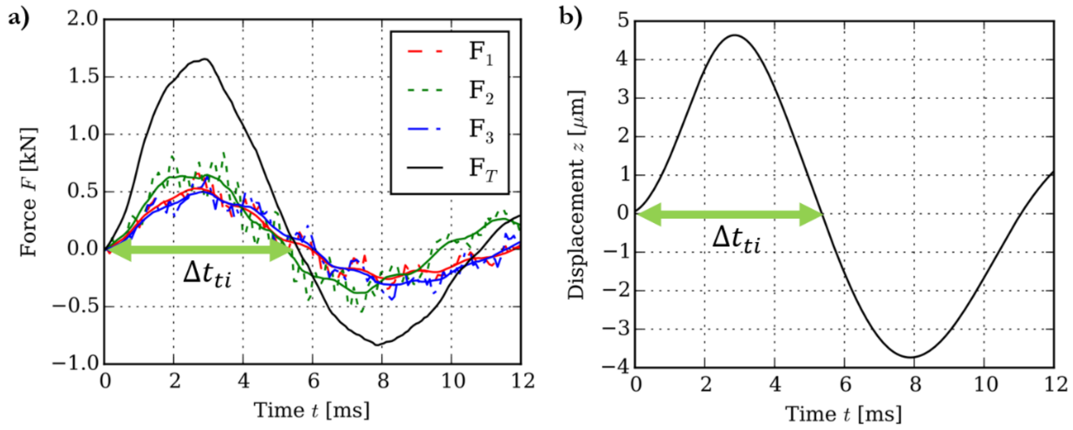

Figure 3-8: (a) Evolution over time of forces F_1, F_2, F_3 recorded by the bottom load cells and the total force F_T. (b) Evolution over time of the vertical slab displacement. Δt_{ti} represents the transmitted impact duration (equal for both signals)

As discussed in Section 3.1.2, the number of measuring cells of the I-scan pressure sensor had to be reduced to increase the logging rate, which is detrimental to an accurate measurement of impact pressure and, by integration, of impact force. To remedy this issue, an indirect estimation of the impact force is proposed by knowing:

- the transmitted force F_T recorded by load cells at the bottom of the slab,
- the relationship between the impact duration (from the I-scan pressure sensor on top of the slab) and the transmitted impact duration recorded by the bottom load cells, and
- the stiffness of the system (composed of the slab and three load cells).

The system composed of the slab and three bottom load cells can be represented by a mass-spring-damper model (Figure 3-9a). The equation of motion of the free body diagram illustrated in Figure 3-10b is:

$$m_s \ddot{z} + c\dot{z} + kz = F(t) \tag{3-1}$$

where m_s is the mass of the slab, c is the dimensional viscosity damping coefficient, k is the stiffness of the system and $\ddot{z}, \dot{z}, z$ are acceleration, velocity and displacement of the slab, respectively. $F(t)$ is the external force applied to the system at time t, i.e. the impact force F_{impact}.

The sum of the reaction forces at the base shown in Figure 3-9b must be equal to the sum of the forces recorded from the load cells (F_T). Assuming the slab is rigid, this can be written as (Thorby 2008):

$$F_T = c\dot{z} + kz \tag{3-2}$$

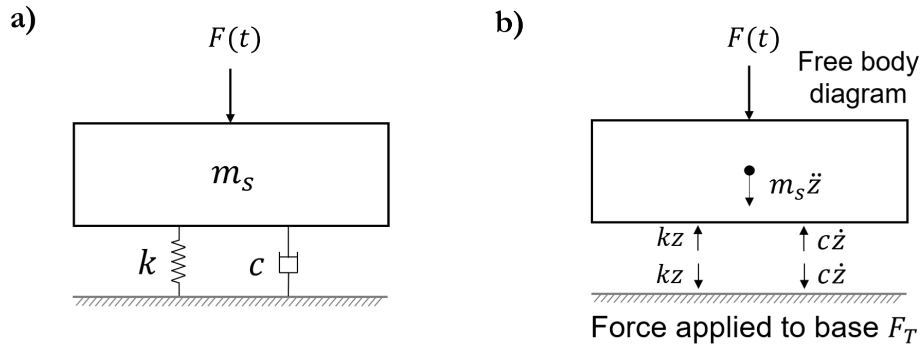

Figure 3-9: (a) Sketch of the slab-load cells system with applied force in schematic form of a mass-spring-damper and (b) corresponding free body diagram.

According to Thorby (2008), the force transmissibility is defined as ratio $|F_T|/|F_{impact}|$, the magnitude of the total reaction force divided by the magnitude of the applied force (i.e. impact force). By expressing Eqs. (3-1) and (3-2) in complex form the force transmissibility can be obtained (Thorby 2008):

$$\frac{|F_T|}{|F_{impact}|} = \sqrt{\frac{1 + (2\beta\Omega)^2}{(1 - \Omega^2)^2 + (2\beta\Omega)^2}} \tag{3-3}$$

where β is the non-dimensional viscous damping coefficient and Ω is the frequency ratio, defined as:

$$\beta = \sqrt{1 - \left(\frac{f_d}{f_n}\right)^2} \tag{3-4}$$

$$\Omega = \frac{f}{f_n} \tag{3-5}$$

with f_d being the damped natural frequency, f_n the undamped natural frequency of the system and f the impact force frequency.

From the direct measurement of the impact duration Δt_i (by the pressure sensor) and the transmitted impact duration recorded from the bottom load cells Δt_{ti}, the impact force frequency f and the damped natural frequency f_d can be obtained as:

$$f = \frac{2\pi}{2\Delta t_i} \tag{3-6}$$

$$f_d = \frac{2\pi}{2\Delta t_{ti}} \tag{3-7}$$

The undamped natural frequency f_n is determined knowing the stiffness k of the system and the mass of the slab m_s as:

$$f_n = \sqrt{\frac{k}{m_s}} \tag{3-8}$$

The stiffness k of the system in Figure 3-9b is a function of the inherent slab stiffness but also of the stiffness of the load cells. k can be estimated from the maximum force F_T (from load cells) and the corresponding maximum displacement of the slab z_{max} (from accelerometer). The estimation of the stiffness k of the system is reported in Section 6.2.2.

The total impulse generated by the impact is another important impact descriptor defined as:

$$J_{impact} = \int_0^{\Delta t_i} F(t)\, dt \tag{3-9}$$

where $F(t)$ is the impact force at instant t and Δt_i is the total impact duration. Figure 3-10 shows an example of the evolution of the impact force over time. The area under the curve showing the evolution of impact force with time can be approximated as area of a triangle having a base equal to Δt_i and height equal to the maximum value of $F(t)$, denoted F_{impact} (Figure 3-10). Hence, the total impulse of the impact can be computed using the maximum estimated impact force and the recorded impact duration (from the pressure sensor):

$$J_{impact} = \frac{1}{2} \cdot F_{impact} \cdot \Delta t_i \quad (3\text{-}10)$$

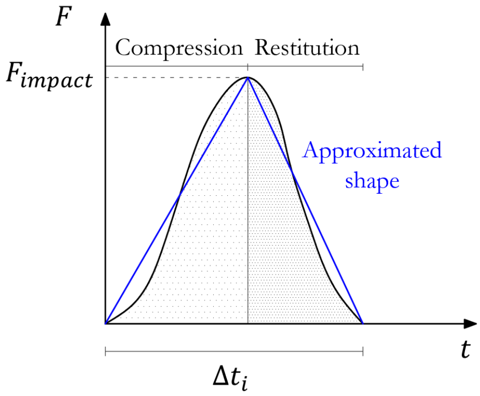

Figure 3-10: Experimental and simplified evolution of impact force in time during impact.

To summarise, the measurements of transmitted impact force and transmitted impact duration from the load cells, combined with the measurement on the impact duration from the pressure sensor allow the estimation of impact force (on top of the slab) by using Eq (3-3). The estimated impact force combined with the measured impact duration are in turn used to estimate the impulse at the impact by using Eq. (3-10).

3.2.2 Image processing

The commercial software TEMA3D (Image Systems Motion Analysis 2019) is used to process all synchronised images captured by the high-speed cameras. At the beginning of each testing day, a calibration is performed by taking a snapshot of a reference structure, the so-called calibration stick (Figure 3-11a), simultaneously with all cameras (Figure 3-11b). The images are then used to collimate all known points in all views. After the calibration, the location and orientation of each camera and the scale of the impact area are known.

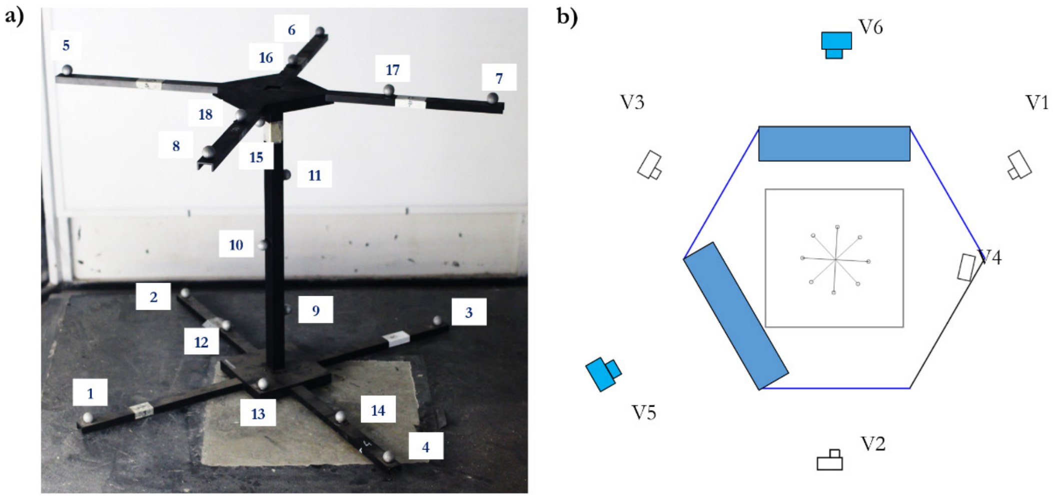

Figure 3-11: (a) Picture of the calibration stick with reference points (numbered 1 to 18); (b) position of the calibration stick with respect to the viewing points – note that V5 and V6 are mirrored views.

TEMA3D supports many different tracking algorithms, two of which were used in this study, namely feature tracking and outline tracking.

The feature tracking algorithm relies on tracking the 3D coordinates of a feature that can easily be visualised on an object. Translational velocities and accelerations of the feature or object are then estimated. To get the rotational velocity, two or more features including the centre of gravity (CofG) have to be tracked. Knowing the relative position of a feature point (here noted as P1) of the block with respect to the CofG, the angle between the vector CofG-P1 at time *i* and the same vector at time $i + \Delta t$ can be calculated. Feature tracking can be conducted from one or more viewpoints.

The outline tracking algorithm finds the outline of the object in the image (Figure 3-12) via a thresholding algorithm used to separate an object from a background, provided a good enough contrast exists between the object and the background. Satisfactory contrast is here achieved by using LED panels in the background (see Section 3.1.3). The outline is made up by a four-connective chain code, which is a sequence of up, down, left or right movements along the pixels (Anliot 2005). The chain code is complete when the sum of all movements ends up back at the starting pixel and the outline is defined.

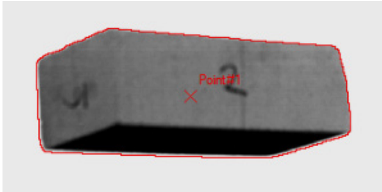

Figure 3-12: Example of outline tracking (red line) of a brick.

The outline of a view shows the silhouette of an object. The silhouette back projected to the camera creates a 3D viewing cone within which the object resides (Figure 3-13a). The intersection of all silhouette viewing cones, one from each camera view, gives an approximation of the 3D shape of the object called visual hull (VH) (Anliot 2005). The 3D visual hull is then meshed with triangles (Figure 3-14) based on a specific resolution (referred to as a VH resolution). The physical attributes of the approximated 3D mesh (such as volume, barycentre, principal axes, moment of inertia) can then be calculated.

The accuracy of the VH depends on the number of available views. Figure 3-13b and c, for example, show the concept of the VH of a cube in 3D for a case with two and three cameras respectively. It can clearly be seen that the VH is an approximation of the real shape (Figure 3-14) using a 3D surface mesh of triangular elements. The physical attributes of the approximated 3D surface mesh (i.e. volume, barycentre, principal axes, moment of inertia) can then be calculated and used to analyse trajectory and energy.

The approximation of the shape using the VH algorithm was found to be generally good enough to find the coordinates of the barycentre of the object, which is used when calculating translational velocity. However, identifying the principal axes is generally not very accurate. This is a major issue, as the principal axes are needed to compute the rotational velocity. Another limitation of the visual hull approach resides in the difficulty to track rotation of symmetric objects, such as spheres or cubes. Although this is generally not a problem for fragments that tend to be irregular, it is problematic when tracking rotation of regular objects in free fall, prior to impact and fragmentation, if they also undergo rotation. In order to address some of the current limitations and improve accuracy of rotational velocity tracking, a new post-processing algorithm was here developed (Guccione et al. 2020) with details given in the following Section 3.2.3.

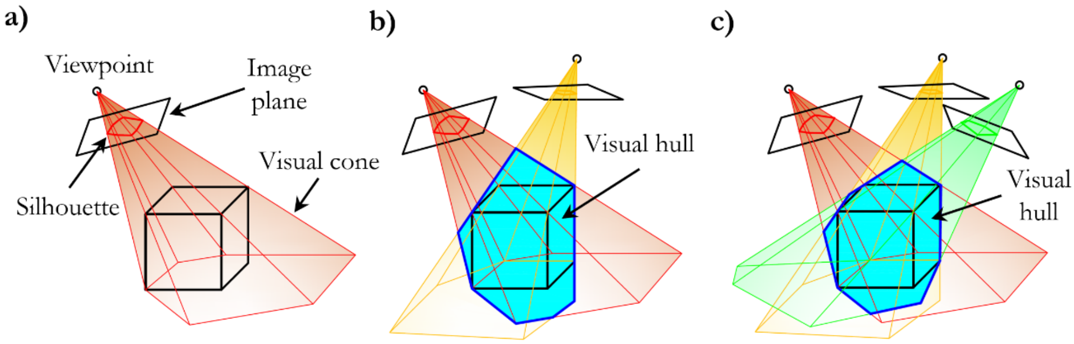

Figure 3-13: (a) Concept of silhouette and 3D cone from a viewpoint. Visual hull (in blue) based on: (2) 2 viewpoints and (c) 3 viewpoints.

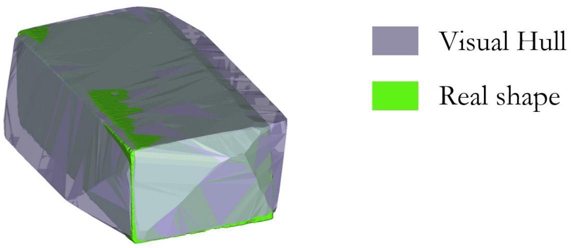

Figure 3-14: Example of visual hull (using 4 views) and real shape.

3.2.3 New post-processing algorithm

The developed post-processing algorithm relies on the knowledge of the real 3D geometry of the object, which can generally be determined before and/or after the test by an accurate photogrammetric survey or a 3D scan (Guccione et al. 2020). In this study, a structured light scanner (EinScan Pro 2X Plus) was used to reconstruct the real 3D geometry of the object. The objective is to align the 3D mesh obtained by scanning the real geometry with the approximated mesh of the VH exported from TEMA3D, at each time step, in order to calculate the orientation of the principal axes (Figure 3-15) and, hence, estimate the rotational velocity. The alignment process is performed using the iterative closest point (ICP) algorithm where points of the real geometry are automatically aligned to a sub-sampled point cloud of the VH. This step is executed within the open-source program CloudCompare (CloudCompare 2020) whereas the calculation of the principal axes is performed with the open-source library trimesh (Dawson-Haggerty 2019). This two-step process is repeated for each time step. Finally, the rotational velocity is estimated based on the orientation of the new calculated principal axes. The procedure can be summarised as follows, where all steps, except steps 1 and 2, have been implemented into a Python script:

1. Automatically export VH meshes for all time steps i from TEMA3D. Note that AutoHotkey (AutoHotkey Foundation LLC 2020) is used to automate the process of exporting the mesh, at each timestep.
2. Manually align the mesh of the real geometry with the first VH mesh (i.e. first time step $i = 0$), to assure the ICP converges to the correct solution, hence, avoiding misalignment.
3. Sub-sample all VH meshes to achieve a point density similar to that of the real geometry.
4. Automatically align the real geometry (manually aligned mesh in the first timestep i=0 and mesh from the previous timestep $i - 1$ thereafter, for $i \geq 1$) to the sub-sampled point clouds using the ICP.
5. Calculate the orientation of the principal axes using the aligned real geometry. This is done using the library trimesh. It should be noted that the calculated axes do not always represent a right-handed coordinate system. Hence, the third principal axis is always recalculated as cross product of the first two principal axes.
6. Check the orientation of the principal axes for timestep i based on the orientation in the previous timestep $i - 1$. This is necessary since the solution of the principal axes is not unique (four solutions are possible), i.e. the axes can be orientated in the positive or negative direction. Hence, changing the direction of the principal axes by 180 degrees is sometimes required.
7. Calculate the rotation between timesteps i and $i - 1$. For each timestep, the rotational increment around each axis is calculated relative to axis positions from the previous timestep. This increment is then accumulated with time increments from earlier times, to produce the total rotation around the principal axes from timestep $i = 0$.
8. Fit a linear trendline to cumulative angle increments around each principal axis, in time, to estimate the rotational velocity around each principal axis. It is assumed that the influence of air resistance on the rotational velocity is negligible, hence, a linear trendline.

The main steps of the post-processing algorithm are outlined in Figure 3-15.

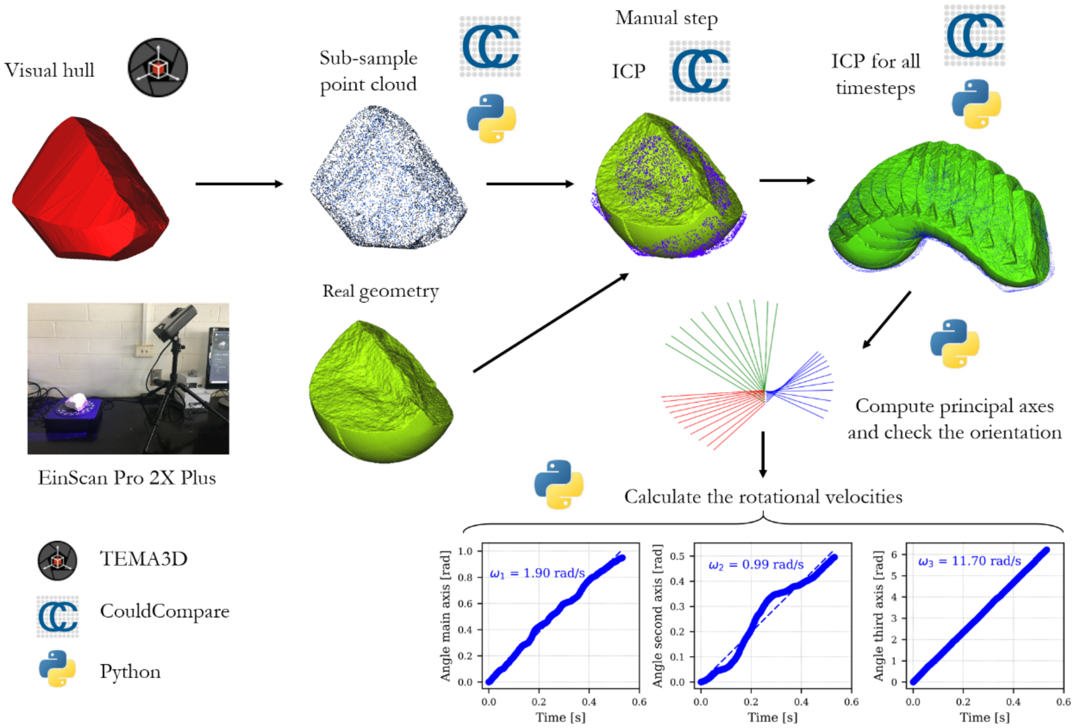

Figure 3-15: Scheme of the post-processing algorithm to calculate the rotational velocities of fragments with indication of the software or code used at each step of the process.

3.2.4 Energy balance

The experimental setup was designed to estimate the amount of energy dissipated during impact and consumed in fragmentation. This is achieved by conducting an energy balance starting with the conservation of energy (noted E), expressed as:

$$E_k^b = \Delta E_{tot} + E_k^a \tag{3-11}$$

where subscript k stands for kinetic and it is referred as the total kinetic energy (i.e. translational plus rotational); superscript b for before the impact; and superscript a for after the impact. ΔE_{tot} is the total energy loss associated with the impact.

The total kinetic energy E_k before and after impact is decomposed into a translational component E_{kt} and a rotation component E_{kr}:

$$E_k^b = E_{kt}^b + E_{kr}^b \tag{3-12}$$

$$E_k^a = E_{kt}^a + E_{kr}^a \tag{3-13}$$

Where impact results in fragmentation, the term E_k^a corresponds to the sum of the total kinetic energy (i.e. translational plus rotational) of all fragments:

$$E_{kt}^a = \sum_{i=1}^{n} E_{kt,i}^a = \sum_{i=1}^{n} \frac{1}{2} \cdot m_i \cdot v_i^2 \tag{3-14}$$

$$E_{kr}^a = \sum_{i=1}^{n} E_{kr,i}^a = \sum_{i=1}^{n} \frac{1}{2} \cdot \left(I_{I,i} \cdot \omega_{I,i}^2 + I_{II,i} \cdot \omega_{II,i}^2 + I_{III,i} \cdot \omega_{III,i}^2\right) \tag{3-15}$$

where n is the number of fragments; $E_{kt,i}^a$ is the translational kinetic energy of fragment i; m_i is the mass of fragment i; v_i is the absolute translational velocity of fragment i; $E_{kr,i}^a$ is the rotational kinetic energy of fragment i; $I_{I,i}, I_{II,i}$ and $I_{III,i}$ are the moments of inertia for the principal axes of fragment i; and $\omega_{I,i}, \omega_{II,i}$ and $\omega_{III,i}$ are the rotational velocities around the 3 principal axes of fragment i. All components of velocities are estimated from image processing as discussed in Section 3.2.2.

The equations to estimate the amount of energy dissipated by displacement, damage/fragmentation and elasto-plastic deformation are given below:

- The energy loss associated to the elastic displacement of the slab ΔE_{slab} can be estimated as:

$$\Delta E_{slab} = \frac{1}{2} \cdot F_T \cdot z_{slab} \tag{3-16}$$

  Eq. (3-16) assumes that the vertical displacement of the centre of the slab, z_{slab}, inferred from the accelerometer signal, does not include a deformation component due to bending of the slab. Given the magnitude of the impact load and the flexural stiffness of the slab, this assumption is considered valid.

- The energy loss to create the fracture surfaces ΔE_{fr} can be estimated using Eq. (3-17) (Hou et al. 2017):

$$\Delta E_{fr} = \gamma \sum_{j=1}^{n} A_j \tag{3-17}$$

A_j corresponds to the area of new surfaces generated by fragmentation. This area can be measured after the drop test by scanning each of the fragments. In this study, a high-resolution structured light scanner (EinScan Pro 2X Plus) was used. The surface energy per unit area of the rock block γ can be determined by the well-known Irwin's correlation (Zhang and Zhao 2014a):

$$\gamma = \frac{K_{Ic}^2(1 - \nu_m^2)}{Y_m} \tag{3-18}$$

where K_{Ic} is the mode I fracture toughness that can be determined using semi-circular bend specimens (Kuruppu et al. 2014), Y_m is the Young's modulus and ν_m is the Poisson's ratio of the material the block is made of (in the case of this work mortar).

Damage and fragmentation are related (i.e. fragmentation is a consequence of damage) so that Eq. (3-17) can be used to compute the energy consumed in damage and in fragmentation. However not all damage causes the formation of discrete fragments, so the difference between the two cases lies in the difficulty to estimate the extent of cracking and new surfaces within fragments, that do not lead to further fragmentation.

- The energy loss in local elastic-plastic deformation of both slab and impacting object ΔE_d can be estimated as follows:

$$\Delta E_d = E_{kt}^b \cdot (1 - CoR_d^2) \tag{3-19}$$

where CoR_d is the coefficient of restitution defined, for an elastic-perfectly plastic sphere impacting a plate (Stronge 2000), as:

$$CoR_d = \frac{v_y}{v_{imp}} \left[\frac{8}{5} \cdot \left(\frac{v_{imp}}{v_y} \right)^2 - \frac{3}{5} \right]^{\frac{3}{8}} \tag{3-20}$$

In Eq. (3-20) v_{imp} is the impact velocity and v_y is the yield velocity defined as:

$$v_y = \left(\left(\frac{4}{5} \cdot \pi\right) \left(\frac{3}{4} \cdot \pi\right)^4 \left(\frac{\vartheta_y \sigma_y}{\tilde{Y}_{mc}}\right)^4 \left(\frac{\vartheta_y \sigma_y \tilde{R}^3}{m}\right) \right)^{\frac{1}{2}} \tag{3-21}$$

where m is the mass of the impacting body; σ_y is equal to the yield stress of the impacting material (assumed equal to the compressive strength σ_c); and ϑ_y is the ratio of mean indentation pressure (assumed fully plastic) to uniaxial yield stress. ϑ_y is assumed equal to 1.61 to consider a higher failure stress compared to a uniaxial load case, as per Wang and Zhu (2013). $\tilde{Y}_{mc}$ and $\tilde{R}$ are the equivalent Young's modulus and the equivalent radius, respectively.

The equivalent radius $\tilde{R}$ is defined as:

$$\frac{1}{\tilde{R}} = \frac{1}{R_1} + \frac{1}{R_2} \tag{3-22}$$

where R_1 is the radius of the sphere and R_2 is the radius of the slab. The radius of the slab R_2 is much greater than R_1 so it can be assumed infinite and, hence, Eq. (3-22) becomes $\tilde{R} = R_1$.

The equivalent Young's modulus $\tilde{Y}_{mc}$ can be determined from Eq. (3-23):

$$\frac{1}{\tilde{Y}_{mc}} = \frac{1 - \nu_m^2}{Y_m} + \frac{1 - \nu_c^2}{Y_c} \tag{3-23}$$

where Y_m is the Young's modulus of the mortar, ν_m the Poisson's ratio of the mortar, Y_c the Young's modulus of the system slab (the combination of the concrete slab plus load cells that support it), and ν_c is the Poisson's ratio of the concreate slab.

The elastic modulus of the system Y_c is obtained by a double fitting procedure based on a non-linear least square method (Virtanen et al. 2020), where the value of Y_c is varied until a satisfactory goodness of fit is obtained between:

(1) the theoretical evolution of restitution coefficient (CoR_d) (given by Eq. (3-20)) with impact velocity and the measured coefficient of restitution ($\overline{CoR_d}$) and

(2) the theoretical evolution of impact duration (approximated by Eq. (3-24)) with impact velocity and the measured impact duration obtained from the I-scan sensor. According to Deresiewicz (1968), the theoretical impact duration Δt can be estimated as 2 times the period of the elastic compression t_c:

$$\Delta t = 2 \cdot t_c = 2 \cdot \left(1.43 \cdot \left(\frac{m^2}{\tilde{Y}_{mc}{}^2 \tilde{R} v_{imp}} \right)^{\frac{1}{5}} \right) \tag{3-24}$$

For a drop tests where the object falls without initial rotational energy and energy is dissipated in damage (or fragmentation), slab displacement and local elasto-plastic deformations, the energy balance reads:

$$E_{kt}^b = \Delta E_{slab} + \Delta E_{fr} + \Delta E_d + E_{kt}^a \tag{3-25}$$

Hence, the energy loss in elastic-plastic deformation ΔE_d is equal to:

$$\Delta E_d = E_{kt}^b - \Delta E_{slab} - \Delta E_{fr} - E_{kt}^a \tag{3-26}$$

which can further be rearranged to:

$$\Delta E_d = E_{kt}^b \left(1 - \frac{\Delta E_{slab} + \Delta E_{fr} + E_{kt}^a}{E_{kt}^b} \right) \tag{3-27}$$

Given Eq. (3-19) and (3-27), it is possible to identify the measured coefficient of restitution due to elastic-plastic deformation ($\overline{CoR_d}$) as:

$$\overline{CoR_d} = \sqrt{\frac{\Delta E_{slab} + \Delta E_{fr} + E_{k_t}^a}{E_{k_t}^b}} \tag{3-28}$$

Another possible source of energy dissipation that was considered is elastic wave propagation (through the slab and the block), which can be quantified using Zener's model (Zener 1941). The model considers the effect of stress waves on the collision between a sphere and a slab and is based on the assumption that during the normal impact, the kinetic energy of the sphere can be distributed between the generation of an elastic stress field near the contact point and a radial propagation of elastic waves into the slab. In Zener's model, the inelasticity parameter, λ , combines the parameters affecting the impact:

$$\lambda = \frac{\pi^{3/5}}{\sqrt{3}}\left(\frac{R_1}{h_s}\right)^2\left(\frac{v_{imp}}{v_p}\right)^{1/5}\left(\frac{\rho_m}{\rho_c}\right)^{3/5}\left(\frac{Y_m/(1-\nu_m^2)}{Y_m/(1-\nu_m^2)+Y_c/(1-\nu_c^2)}\right) \tag{3-29}$$

where R_1 is the radius of the sphere, h_s is the thickness of the slab, ρ_m is the density of the mortar sphere, ρ_c is the density of the concrete slab, Y_m is the Young's modulus of the sphere, ν_m is the Poisson's ratio of the mortar sphere, Y_c is the Young's modulus of the system (slab plus load cells), ν_c is the Poisson's ratio of the concrete slab, v_{imp} is the impact velocity of the mortar sphere and v_p is the propagation velocity of quasi-longitudinal waves in the slab, which is equal to:

$$v_p = \sqrt{\frac{Y_c}{\rho_c(1-\nu_c^2)}} \tag{3-30}$$

The energy lost in elastic wave propagation ΔE_w through the slab and the sphere can be estimated using a coefficient of restitution CoR_w (Zener 1941):

$$\Delta E_w = E_{k_t}^b \cdot (1 - CoR_w^2) \tag{3-31}$$

with

$$CoR_w = \frac{1-0.88\lambda}{1+0.88\lambda} \tag{3-32}$$

Due to the geometry and the material characteristics involved in this study, the coefficient of restitution CoR_w is close to 1, therefore the term $(1 - CoR_w^2$) in Eq. (3-31) is rather small. Hence, the energy loss due to the elastic wave propagation can be considered negligible. Other modes of energy dissipation such as sound and thermal components are also assumed negligible.

In conclusion, Equation (3-11) can be used to estimate the total amount of energy dissipated upon impact through the three main dissipative processes: namely, the elastic-plastic deformation of an impacting block and slab, the displacement of the slab as a whole, and fracture formation associated with damage, and ultimately, fragmentation.

3.3 Secondary setup

Based on the experimental setup described in Section 3.1 and the methodology presented in Section 3.2 a secondary setup was developed to conduct further investigation on fragment size distribution at impact velocities higher than 10 m/s (the maximum impact velocity achievable form the fragmentation cell setup described in Section 3.2).

The secondary setup was located in the stairwell beside the climbing tower at the Forum gym of the University of Newcastle (Figure 3-16). The 6-storey staircase arrangement comprises half-flights of stairs reversing in direction at small landings at either end, to form a central well with a width of 100 mm. To safely drop the spheres from different heights without interference from the adjacent stairs, the spheres were dropped through a 100 mm diameter PVC pipe that was threaded through the central well and fixed to the handrail of the stairway (Figure 3-16c), in a position so that it could be accessed at any height from the stair flights. The pipe was perforated with pairs of 20 mm holes drilled every metre and positioned diametrically across from each other to reduce the piston effect of the falling balls.

The spheres were dropped into the top of the pipe, and were delivered from the end of the pipe, 0.8m above a concrete impact slab (with the same strength as the slab described in Section 3.1 but smaller dimension of 0.8 m x 0.8 m x 0.2 m). The impact slab was again supported on 3 load cells. The same four high-speed cameras used for the other setup were installed around the impact point (see Figure 3-16a, b and d). Cam 1 was set up perpendicularly to the slab while Cams 2, 3 and 4 were arranged in order to have three top views of the impact (see Figure 3-16a, b and d). A black plastic sheet apron was placed on the floor to increase the visibility and contain the fragments.

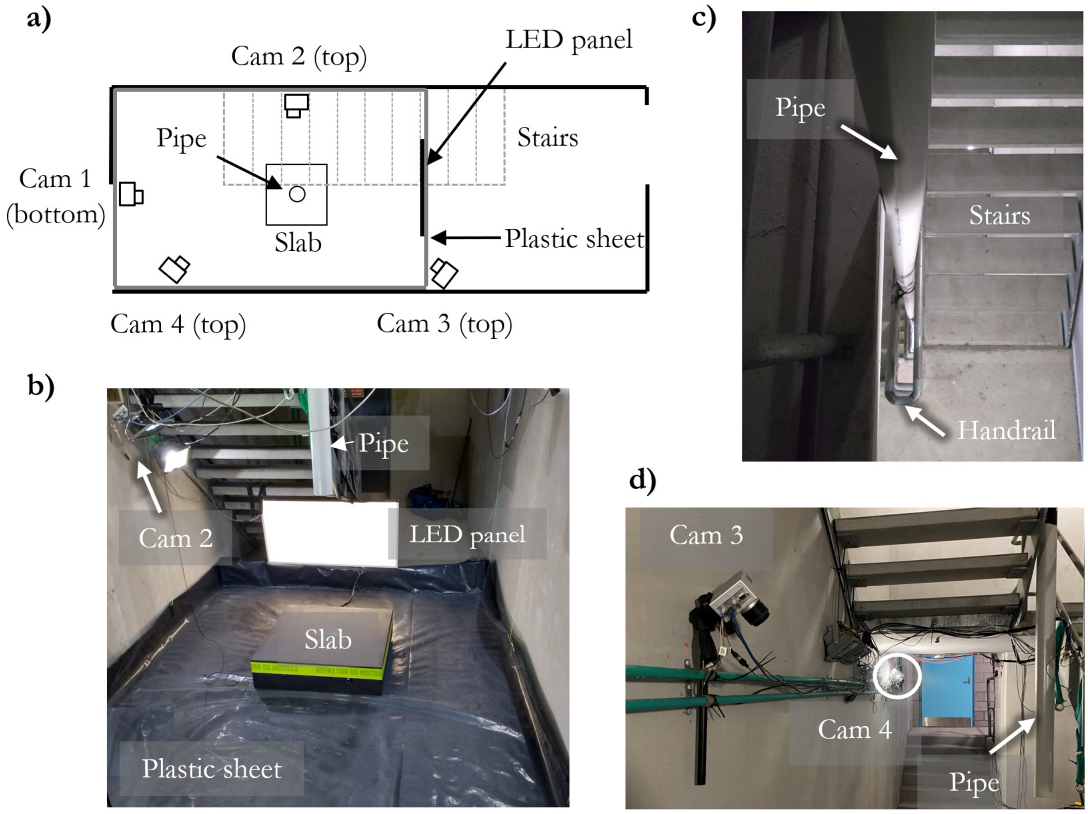

Figure 3-16: Secondary setup: (a) plan view of the secondary setup, (b) view of the slab, pipe, plastic sheet, lights and Cam 2, (c) view of pipe within the central well of the staircase, looking down, and (d) view of Cam 3 and Cam 4.

4 Derivation of predictive model for Survival probability

4.1 Rationale

The survival probability (SP) of grains or spheres subjected to compressive stress loading is commonly described using a Weibull distribution (Frossard et al. 2012; Weibull 1951):

$$SP(\sigma) = 100 \cdot e^{-\left(\frac{\sigma}{\sigma_{cr}}\right)^{\mu}} \tag{4-1}$$

where σ is the stress applied to the particles; $SP(\sigma)$ is the survival probability of the grain under stress σ; μ is the distribution shape parameter corresponding to the slope of the central part of the Weibull distribution; and σ_{cr} is the scale parameter, also called critical value of σ, corresponding to a survival probability equal to $1/e \sim 37\%$. In this study, the survival probability of a brittle sphere upon dynamic impact, here referred to as impact survival probability, is described using a Weibull distribution expressed as a function of the impact kinetic energy (E_k^b). It is suggested that for controlled specimen shape and controlled testing conditions (i.e. release and impact conditions), the impact survival probability is strongly correlated to the variability of the mechanical properties of the material, which can be assessed from the cumulative distribution of measured mechanical properties under quasi-static loading. This thesis focuses on the survival probability for each series of characterisation tests, expressed as:

$$SP(\sigma) = 1 - CD(\sigma) \tag{4-2}$$

where $CD(\sigma)$ is the value of cumulative distribution corresponding to a stress value of σ.

The rationale of the novel model is to employ shape and scale parameters to describe impact survival probability from the survival probability of specimens subjected to material characterisation tests. The shape parameter μ of the impact survival probability SP was taken as the shape parameter of the Weibull distribution of the work/energy required to fail rock specimens under indirect tension by compressive loading, which is motivated by two reasons:

- Of all characterisation tests, indirect tension tests best captures the failure pattern of brittle spheres under impact, in the range of energy that is relevant to characterise the survival probability (Arbiter et al. 1969; Asteriou et al. 2013a; Chau et al. 2000; Salman et al. 2004).
- Fragmentation upon dropping occurs as the result of an impact, the magnitude of which is quantified by an energy, and work is a measure of energy as opposed to force, strength or toughness.

Note that in the rest of this chapter, compressive loading always applies to spheres or discs, hence resulting in indirect tensile tests. The terms "compression" and "indirect tension" are hence used interchangeably. "Brazilian tests" specifically refer to a compression on a disc, not a sphere.

The work-based scale parameter of the impact survival probability (denoted $E_{k(D)}^{cr}$ in place of σ_c in Eq. (4-1)) will be estimated from the critical work required to achieve failure during Brazilian tests (noted $W_{BT(d)}^{cr}$) and three conversion factors (C_{size}, C_{shape} and C_{rate}) that account for size, shape and strain effects, respectively. Specifically:

- C_{shape} converts the work required to fail a disc of diameter d in a Brazilian test ($W_{BT(d)}$) into the work required to fail a sphere of diameter d under compressive loading ($W_{SC(d)}$);
- C_{size} converts the work required to fail a sphere of diameter d in compression ($W_{SC(d)}$) into the work required to fail a sphere of diameter D in compression ($W_{SC(D)}$); and
- C_{rate} converts the work required to fail a sphere of diameter D under quasi-static compression ($W_{SC(D)}$) to the kinetic energy to fail a sphere of diameter D under dynamic loading ($E_{k(D)}^{b}$).

Figure 4-1 provides a schematic overview of the different steps followed to predict the critical kinetic energy of spheres undergoing drop tests from the critical work of indirect tensile tests performed on discs. The derivations of the three conversion factors will be covered in the next sections. Once the two Weibull parameters have been predicted, the impact survival probability is determined by using a Weibull function or, as is shown in the in the following sections, a linear function.

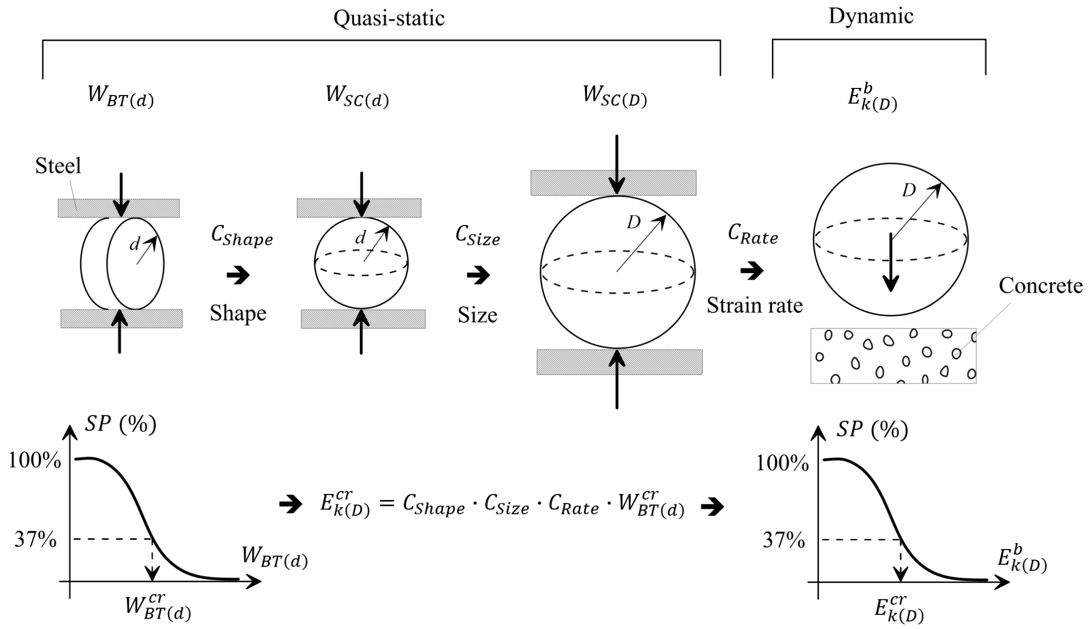

Figure 4-1: Schematic representation of the novel model to predict the critical kinetic energy for failure of a sphere upon dynamic impact. The process starts with the distribution of work required to fail a disc of diameter d under indirect tension (Brazilian test). The critical value of work $W^{cr}_{BT(d)}$ corresponding to a survival probability of 37% is converted into the critical kinetic energy $E^{cr}_{k(D)}$ of a sphere of diameter D falling on a concrete slab through application of factors C_{shape}, C_{size} and C_{rate}.

4.2 Derivation of shape conversion factor

Before delving into the derivation of all conversion factors, it is acknowledged that the applied force is assumed to evolve linearly with resulting displacement during all indirect tensile tests, and the conversion factor for work is made of two partial conversion factors: a conversion factor for the maximum force ($C_{shape-F}$) and a conversion factor for the maximum displacement ($C_{shape-\delta}$), defined in Equations (4-3) to (4-7) below. The same concept applies to the rate conversion factor in Section 4.4.

The force and displacement at failure for the sphere of diameter d ($F_{SC(d)}, \delta_{SC(d)}$) can be expressed as function of force and displacement at failure for the disc of diameter d subjected to a Brazilian test ($F_{BT(d)}, \delta_{BT(d)}$):

$$F_{SC(d)} = C_{Shape-F} \cdot F_{BT(d)} \tag{4-3}$$

$$\delta_{SC(d)} = C_{Shape-\delta} \cdot \delta_{BT(d)} \tag{4-4}$$

where $C_{Shape-F}$ and $C_{Shape-\delta}$ are shape conversion factors from disc to sphere for the force and the displacement at failure, respectively. The work $W_{SC(d)}$ required to fail a sphere of same diameter as the disc under indirect tension is:

$$\begin{gathered} W_{SC(d)} = \frac{1}{2} F_{SC(d)} \cdot \delta_{SC(d)} = \frac{1}{2}\left(C_{Shape-F} \cdot F_{BT(d)}\right) \cdot \left(C_{Shape-\delta} \cdot \delta_{BT(d)}\right) \\ \Longrightarrow W_{SC(d)} = C_{Shape-F} \cdot C_{Shape-\delta} \cdot W_{BT(d)} \end{gathered} \tag{4-5}$$

with $W_{BT(d)} = \frac{1}{2} F_{BT(d)} \cdot \delta_{BT(d)}$.

Eq. (4-5) can be re-written as:

$$W_{SC(d)} = C_{Shape} \cdot W_{BT(d)} \tag{4-6}$$

with:

$$C_{Shape} = C_{Shape-F} \cdot C_{Shape-\delta} \tag{4-7}$$

where C_{Shape} is the shape conversion factor from disc to sphere, of same diameter, for quasi-static compression.

4.2.1 *Shape conversion factor for force* $C_{Shape-F}$

The force conversion factor can be estimated from equations that give the tensile strength of a sphere (Eq. (4-8)) (Hiramatsu and Oka 1966) and disc (Eq. (4-9)) (Perras and Diederichs 2014) under indirect tensile test loading:

$$\sigma_t = \frac{0.9 \cdot F_{SC(d)}}{d^2} \tag{4-8}$$

$$\sigma_t = \frac{4 \cdot F_{BT(d)}}{\pi \cdot d^2} \tag{4-9}$$

For a sphere and a disc made of the same material and with the same diameter, equating Eq. (4-8) to Eq. (4-9) leads to $C_{Shape-F} = 1.41$

4.2.2 *Shape conversion factor for displacement* $C_{Shape-\delta}$

Hertzian contact theory (Stronge 2000) provides the total deformation when a sphere or a disc are compressed against a flat surface. In the case of steel platens, it is reasonable to consider that the total deformation occurs within the disc, providing an expression for $\delta_{BT(d)}$ (modified from Japaridze (2015))

$$\delta_{BT(d)} = \frac{4 \cdot F_{BT(d)} \cdot (1 - \nu_m^2)}{\pi \cdot Y_m \cdot h} \left[0.41 + \ln(2d) - 0.5 \cdot \ln\left(\frac{2 \cdot d \cdot F_{BT(d)}}{\pi \cdot h \cdot \tilde{Y}_{ms}} \right) \right] \tag{4-10}$$

where d and h are the diameter and thickness of the cylinder tested under indirect tensile test, respectively;· $F_{BT(d)}$ is the force required to fail the disc under indirect tension with a quasi-static loading rate; Y_m is the elastic modulus of the mortar; ν_m is the Poisson's ratio of the mortar; and $\tilde{Y}_{ms}$ is an equivalent modulus for the mortar-steel platen system defined as:

$$\frac{1}{\tilde{Y}_{ms}} = \left(\frac{1 - \nu_m^2}{Y_m} + \frac{1 - \nu_s^2}{Y_s} \right) \tag{4-11}$$

Y_m and Y_s are the elastic moduli of the mortar and steel platens, respectively; ν_m and ν_s are the Poisson's ratios of the mortar and steel platens, respectively.

For a sphere, the displacement at failure is (Stronge 2000):

$$\delta_{SC(d)} = \left(\frac{9 \cdot F_{SC(d)}^2}{d \cdot \tilde{Y}_{ms}^2}\right)^{1/3} \tag{4-12}$$

where d is the sphere diameter; $\tilde{Y}_{ms}$ is the equivalent modulus for the mortar-steel platen system as defined in Eq. (4-11); and $F_{SC(d)}$ is the force required to fail a sphere of diameter d under compression with a quasi-static loading rate.

Using Eqs. (4-4), (4-10) and (4-12), and $C_{Shape-F}$, the displacement conversion factor can be expressed as:

$$C_{Shape-\delta} = \frac{\left(\frac{9 \cdot \left(C_{Shape-F} \cdot F_{BT(d)}\right)^2}{d \cdot \tilde{Y}_{ms}^2}\right)^{1/3}}{\frac{4 \cdot F_{BT(d)} \cdot (1-\nu_m^2)}{\pi \cdot Y_m \cdot h}\left[0.41 + \ln(2d) - 0.5 \cdot \ln\left(\frac{2 \cdot d \cdot F_{BT(d)}}{\pi \cdot h \cdot \tilde{Y}_{ms}}\right)\right]} \tag{4-13}$$

Eqs. (4-10) and (4-12) are nonlinear equations, so it is not possible to obtain a closed form expression for the force and the equivalent modulus for the sphere and the disc. Consequently, the displacement conversion factor is a function of the forces required to obtain failure of the sphere and the disc.

4.2.3 Shape conversion factor C_{Shape}

Finally, the shape conversion factor C_{Shape} can be derived by inserting Eq. (4-13) in Eq. (4-7) and using $C_{Shape-F} = 1.41$ (see Section 4.2.1):

$$C_{Shape} = \frac{0.92 \cdot \pi \cdot Y_m \cdot h}{F_{BT(d)}^{1/3} \cdot \tilde{Y}_{ms}^{2/3} \cdot (1-\nu_m^2) \cdot d^{1/3} \cdot \left[0.41 + \ln(2d) - 0.5 \cdot \ln\left(\frac{2 \cdot d \cdot F_{BT(d)}}{\pi \cdot h \cdot \tilde{Y}_{ms}}\right)\right]} \tag{4-14}$$

4.3 Derivation of size conversion factor

Frossard et al. (2012) proposed a relationship to account for the size effect that affects the amount of force required to crush mineral particles. Considering the diameter d of the spheres tested in quasi-static compression and noting that D is the diameter of spheres used in the drop tests (see Figure 4-1), the relation established by Frossard et al. (2012) is expressed as:

$$F_{SC(D)} = F_{SC(d)} \left(\frac{D}{d}\right)^{2-\frac{3}{\mu_{BT-F}}} \tag{4-15}$$

where μ_{BT-F} is the Weibull distribution parameter for the distribution of crushing forces, here to be taken as force at failure for Brazilian tests on discs.

The work done to break the sphere is proportional to the force at failure and the reduction in diameter of the sphere. So, for any sphere of diameter D:

$$W \propto F_{SC(D)} \cdot \delta_{SC(D)} \tag{4-16}$$

From Eq. (4-12) it follows that:

$$\delta_{SC(D)} \propto \frac{\left(F_{SC(D)}\right)^{\frac{2}{3}}}{(D)^{\frac{1}{3}}} \tag{4-17}$$

and consequently:

$$W \propto F_{SC(D)} \cdot \frac{\left(F_{SC(D)}\right)^{\frac{2}{3}}}{(D)^{\frac{1}{3}}} = \frac{\left(F_{SC(D)}\right)^{\frac{5}{3}}}{(D)^{\frac{1}{3}}} \tag{4-18}$$

Eq. (4-18) holds for all sizes. Noting that $W_{SC(D)}$ is the work required to fail a sphere of diameter D and $W_{SC(d)}$ is the work required to fail a sphere of diameter d, and given Eq. (4-15), we get:

$$W_{SC(D)} \propto \frac{\left(F_{SC(D)}\right)^{\frac{5}{3}}}{(D)^{\frac{1}{3}}} = \frac{\left(F_{SC(d)} \left(\frac{D}{d}\right)^{2-\frac{3}{\mu_{BT-F}}}\right)^{\frac{5}{3}}}{(D)^{\frac{1}{3}}}$$

$$= \frac{\left(F_{SC(d)}\right)^{\frac{5}{3}}}{(d)^{\frac{1}{3}}} \left(\frac{D}{d}\right)^{\left(3-\frac{5}{\mu_{BT-F}}\right)}$$

$$\Rightarrow W_{SC(D)} = W_{SC(d)} \left(\frac{D}{d}\right)^{\left(3-\frac{5}{\mu_{BT-F}}\right)} \quad (4\text{-}19)$$

where the size factor C_{size} is now given by

$$C_{size} = \left(\frac{D}{d}\right)^{\left(3-\frac{5}{\mu_{BT-F}}\right)} \quad (4\text{-}20)$$

Eq. (4-20) allows to convert the work required to fail a sphere of diameter d in quasi-static compression into the work required to fail a larger sphere (of diameter D) under the same testing conditions.

4.4 Derivation of rate conversion factor

4.4.1 Estimation of the strain rate difference

All Brazilian tests were conducted under quasi static conditions, with an average time to reach failure of 30 seconds. In contrast, the average recorded duration of impact for a dropped sphere is a fraction of millisecond.

The radial strain of spheres and discs are of the same order of magnitude so that the increase in strain rate (here noted ISR) between the quasi-static testing and dynamic testing is simply taken as the ratio of loading times, assuming that half of the impact time (t_{impact}) corresponds to the compression phase, and half to the rebound phase:

$$ISR = \frac{t_{BT}}{t_{impact}/2} \quad (4\text{-}21)$$

where t_{BT} is the time to reach failure in a quasi-static Brazilian test and t_{impact} is the duration of impact (including the compression phase and restitution phase) for a drop test (cf. Figure 3-10).

4.4.2 Rate conversion factor for force C_{Rate-F}

Wu et al. (2012) conducted series of dynamic indirect tensile tests on concrete cubes. Their data was used to establish the following empirical correlation between the rate conversion factor for force and the increase in strain rate:

$$C_{Rate-F} = ISR^{0.055} \tag{4-22}$$

Hence, the dynamic force $F_{DYN(D)}$ can be calculated as:

$$F_{DYN(D)} = C_{Rate-F} \cdot F_{SC(D)} \tag{4-23}$$

4.4.3 Rate conversion factor for displacement $C_{Rate-\delta}$

As per Section 4.2.2, the dynamic displacement conversion factor is obtained from Hertzian contact theory (Stronge 2000). Under the impact force at failure, the compression displacement of a sphere of diameter D is given by Eq. (4-12) (with D instead of d). When the same sphere falls onto a flat concrete slab, generating a dynamic force $F_{DYN(D)}$, the total deformation of the mortar sphere and the concrete slab, at the point of impact, can be estimated as (Stronge 2000):

$$\delta_{DYN(D)} = \alpha \cdot \left(\frac{9 \cdot F_{DYN(D)}^2}{8 \cdot D \cdot \tilde{Y}_{mc}^2} \right)^{1/3} \tag{4-24}$$

where D is the diameter of the sphere used in drop test;· $F_{DYN(D)}$ is the force required to fail the sphere under a dynamic impact; $\tilde{Y}_{mc}$ is an equivalent modulus for the mortar-concrete slab system; and α is a factor used to estimate the part of deformation that occurs in the sphere.

In absence of an analytical solution to estimate the partition of deformation in the sphere and deformation in the slab, α has been approximated from the moduli of the sphere and the slab, noted Y_m and Y_c. Considering the sphere and the slab as materials in series, and based on the values of their moduli only, the portion of sphere deformation can be approximated as $Y_c/(Y_m + Y_c)$. However, this is not strictly correct as the reduction in diameter and the indentation of the slab depend on the size of the deformed objects. The same proportionality idea can be applied to the sphere and slab stiffness (equal to the moduli multiplied by the diameter of the sphere or the thickness of the slab), which accounts for dimensions. However, this is not totally correct either, because the deformation of the slab is localised, and the full thickness of the slab is not mobilised in compression. So, the average between the two approaches was taken as a first approximation of α.

The equivalent modulus for the mortar-concrete slab system $\tilde{Y}_{mc}$ is defined as

$$\frac{1}{\tilde{Y}_{mc}} = \left(\frac{1-\nu_m^2}{Y_m} + \frac{1-\nu_c^2}{Y_c}\right) \tag{4-25}$$

where Y_m and Y_c are the elastic moduli of the mortar and concrete slab system, respectively; ν_m and ν_c are the Poisson's ratios of the mortar and concrete slab system, respectively.

The theoretical dynamic displacement conversion factor $C_{Rate-\delta}$ can be obtained as ratio of $\delta_{DYN(D)}$ (Eq. (4-24)) over $\delta_{SC(D)}$ (Eq. (4-12)) by expressing $F_{DYN(D)}$ by Eq. (4-23) and Eq. (4-22):

$$C_{Rate-\delta} = \frac{\delta_{DYN(D)}}{\delta_{SC(D)}} = \frac{ISR^{0.0367}}{2} \cdot \alpha \cdot \left(\frac{\tilde{Y}_{ms}}{\tilde{Y}_{mc}}\right)^{2/3} \tag{4-26}$$

4.4.4 *Rate conversion factor* C_{Rate}

As for the shape conversion factor, the rate conversion factor is obtained from the product of the rate conversion factor for force and the rate conversion factor for displacement.

$$C_{Rate} = C_{Rate-F} \cdot C_{Rate-\delta} \tag{4-27}$$

Combining Eq. (4-22) and Eq. (4-26) gives:

$$C_{Rate} = \frac{ISR^{0.092}}{2} \cdot \alpha \cdot \left(\frac{\tilde{Y}_{ms}}{\tilde{Y}_{mc}}\right)^{2/3} \tag{4-28}$$

5 Experimental methods

5.1 Material and preparation of specimens

In order to eliminate some inherent complexities of natural rock and irregularly shaped blocks and to achieve a better control and repeatability of results, fragmentation was here studied using homogeneous spherical samples made of mortar. The mortar was made of silica sand, Portland cement, hydrated lime and water. Three different proportions (by mass) were used to obtain different mortar strengths. A total of four mixtures were made:

- For the first mixture (referred to as M1) the relative proportions were 3 parts of sand for 1 part of cement, 0.25 part of lime and 0.8 part of water. With this mixture a total 2 batches were made. Each batch was used to cast 30 spheres of 100 mm diameter, 5 cylinders (54 mm diameter, 135 mm height), 5 discs (54 mm diameter, 27 mm thickness) and 2 larger cylinders (100 mm diameter, 200 mm height). The two batches were subjected to a different curing process. The specimens of the first batch were cured for 8 weeks in a water bath at room temperature and then placed in a 40°C oven for 4 weeks for drying. This process led to a 90-day compressive strength of 34.4 MPa. The specimens of the second batch were cured for 12 weeks in a water bath in the same condition and subsequently dried for 4 weeks, leading to a 120-day compressive strength of 40.7 MPa. To differentiate the first batch from the second, it will be referred to as M1 and M1*, respectively. The spheres of M1 were used to investigate the energy partition at different impact energies while the spheres from M1* were used to validate the experimental setup.
- For the second mixture (referred to as M2) the relative proportions were 3 parts of sand for 1 part of cement, 0.25 part of lime and 1 part of water. This mixture has the same curing process of M1 (i.e. 8 weeks in a water bath at room temperature and then placed in a 40°C oven for 4 weeks for drying), which led to a 90-day compressive strength of 22.9 MPa. For mortar M2, a total of 4 batches were made. Each batch

was used to cast 30 spheres for each one of three diameters (50, 75 and 100 mm), 30 cylinders (54 mm diameter, 135 mm height), 30 discs (54 mm diameter, 27 mm thickness) and 10 larger cylinders (100 mm diameter, 200 mm height). This mix was used to validate the novel model to predict the impact survival probability from statistical distribution of material properties presented in Chapter 4.

- For the third mixture (referred to as M3) the proportions were 4 parts of sand for 1 part of cement, 0.25 part of lime and 1 part of water. This mixture has the same curing process of M1 and M2 (8 weeks in a water bath at room temperature and then placed in a 40°C oven for 4 weeks for drying), leading to a 90-day compressive strength of 17.3 MPa. For M3, only 30 spheres of 100 mm, 10 cylinders (54 mm diameter, 135 mm height) and 10 discs (54 mm diameter, 27 mm thickness) were made for each batch because specimens of mortar M3 were used to validate a specific aspect of the novel model (see Section 6.4.5). A total of 4 batches were also made for this mix.

The spheres were cast using 3D printed plastic (high density acrylonitrile butadiene styrene) moulds (see Figure 5-1). The moulds were designed to optimise the printing, to maximise the number of spheres per mould and to obtain an efficient alignment system of two half moulds in order to reduce the imperfections caused by the filling. The moulds were filled on a vibrating table to expel as many bubbles as possible from the mortar. Note that the filling hole of the moulds were closed with a concave plug that maintains the spherical shape (Figure 5-1b and c).

All specimens (spheres, discs and cylinders) were removed from their mould after 1 day and cured in a water bath at room temperature for 8 weeks, except for the M1* samples that were cured for 12 weeks. Following curing, all specimens were placed in a 40°C oven for 4 weeks for drying, thereby eliminating any strength variability due to differential wetness at the time of testing.

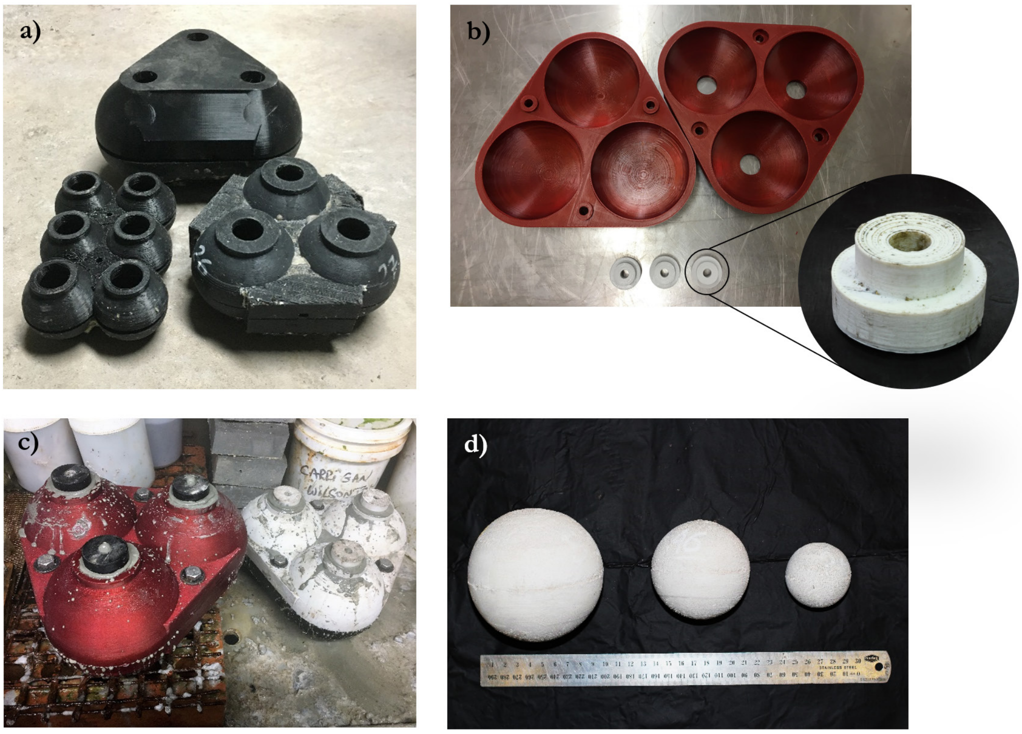

Figure 5-1: (a) 3D printed moulds used to create the spheres (assembled; filling holes unplugged); (b) example of mould open and zoom of the plug used to maintain the spherical shape; (c) moulds filled with mortar and plugged; (d) examples of the mortar spheres cast using the moulds.

5.2 Characterisation testing

The mechanical characteristics of the four mortars were assessed via the following series of material characterisation tests:

- unconfined compression tests on mortar cylinders (diameter 54 mm, height 135 mm, Figure 5-2 left) conducted according to standard ISRM 1979 (Bieniawski and Bernede 1979).
- indirect tension tests (also called Brazilian tests) on mortar discs (diameter 54 mm, thickness 27 mm, Figure 5-2centre) conducted according to standard ISRM 1978 (ISRM 1978)
- toughness tests (Mode I) on mortar half-discs (diameter 100 mm, thickness 40 mm, Figure 5-2 right) notched with a central groove (height 25 mm, thickness 1.7 mm) conducted according to standard ISRM 2014 (Kuruppu et al. 2014). The disc specimens for the toughness tests were created by cutting slices from the 100 mm diameter, 200 mm height cylinders. Each disc was then separated into two halves and a groove was precisely cut in each half.

- quasi-static compression test of mortar spheres (only for M2, diameters of 50, 75 and 100 mm) conducted under the same conditions as the indirect tension tests performed on the discs.

All these characterisation tests were conducted under quasi-static loading (loading rate ranging from 0.15 to 2.4 mm/min). The number of tests performed for each mix is reported in Table 5-1.

Table 5-1 Number and type of material characterisation tests for each mortar mix (M1, M1, M2, M3).*

	M1	M1*	M2	M3
Unconfined compression tests (UCS)	5	5	117	40
Brazilian tests on discs (BT)	5	5	119	40
Toughness tests	10	10	107	-
Compression tests on 50 mm spheres	-	-	11	-
Compression tests on 75 mm spheres	-	-	11	-
Compression tests on 100 mm spheres		-	11	-

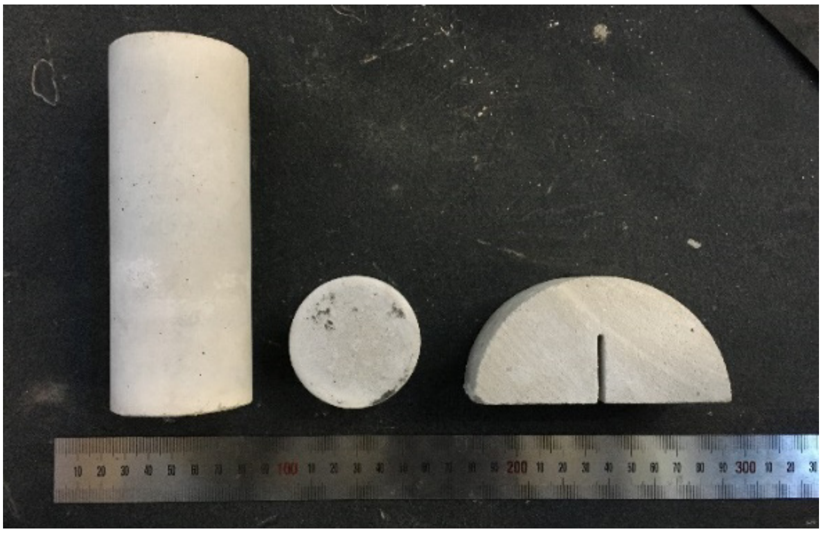

Figure 5-2: Typical specimens for the material characterisation tests: on the left, cylinder for unconfined compression test (50 mm in diameter), in the centre a disc for Brazilian test (50mm diameter) and on the right a notched half-disc (100 mm diameter) for toughness test.

As discussed in Chapter 4, it is here proposed to relate the survival probability for drop tests to the material variability highlighted from the characterisation tests. For each test, the statistical distribution of raw force at failure and processed force (i.e. strength or toughness) was determined.

5.3 Experimental program for drop tests and tracking tests

The experimental program pertaining to drop tests and tracking tests consists of four series:

- Series 1 (S1) contains all tests used to validate the experimental setup:
  - Series 1.1 (S1.1) focused on tests to assess the influence of geometry (or shape) of the tracked object, the number of viewpoints used and the method of 3D representation of the object on the accuracy of the 3D tracking outcomes.

    To investigate the ability of the algorithm to track different shapes, a brick (dimensions of 75 x 109 x 229 mm, volume 1,872 cm^3, Figure 5-3a), a disc (diameter of 100 mm, height of 49 mm, volume 385 cm^3, Figure 5-3b) and an irregular fragment from a broken 100 mm sphere (volume 130.9 cm^3, Figure 5-3c) were suspended from a string and spun around the vertical axis at a known rotational velocity. These tests are referred to as "spinning tests" in the rest of this thesis.

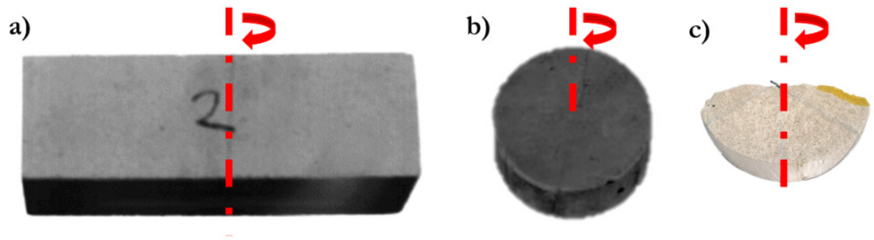

Figure 5-3: Blocks used for the spinning tests: (a) brick, (b) disc and (c) the fragment.

Also, two drop tests were conducted with a natural sandstone rock block (Figure 5-4a) and a mortar sphere (M1*, Figure 5-4b) in order assess the ability of the setup to capture the 3D trajectory of objects. The sandstone block with a mass of 2.963 kg and volume of 1,279 cm^3 was released from about 1.65 m. It had an irregular shape with a plane of discontinuity. The mortar sphere (diameter 100 mm and mass 1.002 kg) was dropped from about 3.1 m.

Figure 5-4: Natural sandstone block (a) and mortar sphere (b) used to validate the ability of the setup to capture 3D trajectories.

As previously discussed, the current setup is equipped with four cameras and two mirrors, which allow a view of the impact to be captured from six different viewpoints (see Figure 3-1 and Figure 3-4). This arrangement was found to be adequate to achieve satisfactory accuracy in tracking by following a systematic analysis of the effect of different combinations of viewpoints (V) and number of cameras, as summarised in Table 5-2.

Table 5-2 Combination of views and number of cameras used for series S1.1

Viewpoints (V)	Numbers of cameras	Arrangement
V1-V2	2	2 planar views
V3-V4	2	2 views (side-top)
V1-V2-V3	3	3 planar views
V2-V3-V4	3	3 ortho views
V1-V2-V3-V4	4	4 views
V1-V2-V3-V4-V5-V6	4 + 2 mirrors	6 views

Finally, the effect of accurately capturing the shape of the object (via the visual hull resolution and the new algorithm to identify axes of rotation) was investigated as part of series S1: VH resolution values of 1, 3, 6 and 10 were used (note: the lower the VH number, the finer the mesh used to reconstruct the object). The VH resolution strongly affects the processing time since a small value means a very fine mesh and a higher computational time. The developed post-processing algorithm (Guccione et al. 2020) was applied to the spinning tests and compared to tracking obtained with TEMA3D.

The results of this series (S1.1) are discussed in Section 6.2.1.

- Series 1.2 (S1.2) focused on the validation of the methodology to evaluate the impact force and impulse from load cells placed under the impacted surface. Spheres (using mortar M1*) were dropped onto a load cell (LPX compression disk of 50 kN capacity) placed on top of the impact slab (Figure 5-5a) providing a direct measurement of the impact force ($\overline{F_{impact}}$ where the bar denotes a measured value as opposed to F_{impact}, which is a predicted value), impact duration and impulse ($\overline{J_{impact}}$) at the point of impact, for each test. These measured parameters were compared to the estimated impact force and impulse using the methodology presented in Section 3.2.1. Seven drop heights were selected, and 3 drop tests were performed at each height for a total of 21 tests. For this series of tests, unfragmented spheres were re-used until they broke, or until they had survived 5 drops, after which they were discarded, and new spheres were used. It is here acknowledged that when surviving the impact, it is possible that the spheres have sustained some non-visible local damage (micro-cracks); however, multiple testing showed that such damage does not influence the magnitude of impact force generated by the impact.
- Series 1.3 (S1.3) focused on the validation of the methodology to evaluate the impact force and impulse from load cells placed under the impacted surface using the final setup where spheres (here for mortar M1*) were dropped onto the I-scan pressure sensor, placed directly on the impact slab (Figure 5-5b). The same seven drop heights of S1.2 were selected, and 3 drop tests were performed at each height for a total of 21 tests.

Results of S1.2 and S1.3 were used to determinate the deformability of slab and load cells system (k, Y_c). These results are reported in Section 6.2.2. The validation of the methodology to estimate impact force and impulse is discussed in Section 6.2.3.

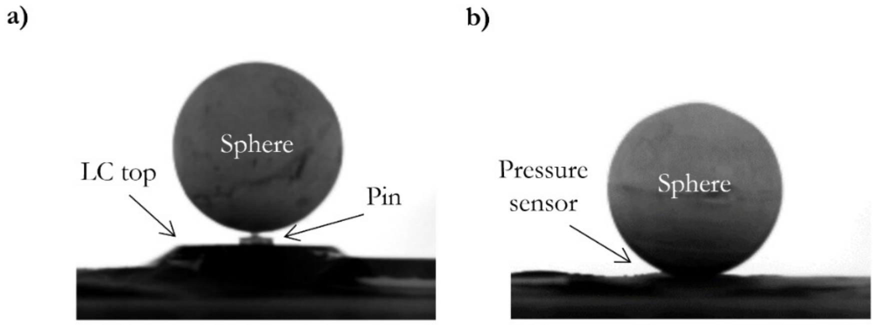

Figure 5-5: (a) Typical drop test of series S1.2 with top load cell (LC top). (b) Typical drop test of series S1.3 with pressure sensor.

- Series 2 (S2) pertains to all tests conducted to investigate the impact survival probability of artificial rock blocks and validate the novel prediction model (presented in Chapter 4) based on statistical distribution of material properties:
  - Series 2.1, 2.2 and 2.3 (using mortar M2) were conducted to establish the impact survival probability of 50, 75 and 100 mm diameter spheres, respectively. Five drop heights were selected, and 16 spheres were dropped at each height, which represents 80 drop tests per impact survival probability.
  - Series 2.4 (using mortar M3) was used to establish the impact survival probability for a mortar of different strength, for 100 mm diameter spheres only, and from the statistical information coming from a reduced number of Brazilian tests. Like other series of S2, 5 drop heights were selected, and 16 spheres were dropped at each height.

  The results of S2 are discussed in Section 6.3 and 6.4.

- Series 3 (S3) focuses on quantifying the amount of energy dissipated at impact for different values of impact energy and is made of:
  - Series 3.1 (S3.1) where 10 drop tests from series S1.3 representing three different outcomes (rebound without damage, rebound with damage and fragmentation) were analysed in detail. All energy components were estimated from the tracking and impact data with an emphasis on verifying that all significant dissipative components can be captured, and that the energy balance can be computed reliably.
  - Series 3.2 (S3.2) where 24 tests were conducted from six different drop heights. For each height, 4 spheres of 100 mm diameter (using mortar M1) were used. All energy components were estimated from the tracking and impact data with an emphasis on

the possible changes in energy partitioned between dissipation mechanisms with increasing impact energy. In this series, only cases with fragmentation were analysed. The results of these series are presented in Section 6.5.

- Series 4 (S4) focused on fragment size distribution in a range of impact velocities between 7.8 m/s and 21 m/s (drop height between 3.1 m and 22.5 m). A total of 30 tests were conducted at ten different drop heights. For each height, 3 spheres of 100 mm diameter (using mortar M1) were used. This series of tests were performed using the secondary setup described in Section 3.3. The fragments produced at each impact were counted and weighed down to a mass of 0.1 g. The results of this series are presented in Section 6.3.2

Table 5-3 summaries the test parameters of the spinning tests of S1.1, while Table 5-4 summaries the test parameters of drop tests of all the tests series.

Table 5-3 Summary of test parameters of spinning tests of S1.1.

Series	Objective of the Series	Material used	Number of tests	Reference rotational velocity [rad/s]
S1.1	Influence of number of views and object shape on 3D rotational velocity estimation	Masonry brick, mortar disc and fragment	3	11.99, 40.53, 37.46
	Influence of VH resolution and validation of the new post processing algorithm to estimate 3D rotational velocity	Masonry brick and fragment	2	11.99, 37.46

Table 5-4 Summary of test parameters of all Series except spinning tests of S1.1.

Series	Objective of testing	Material used (sphere diameter)	Number of tests	Drop height [m]	Theoretical impact velocity [ms^{-1}]
S1.1	Validation of 3D trajectory estimation	Sandstone	1	1.65	5.7
		M1* (100 mm)	1	3.06	7.8
S1.2	Validation of the impact force and impulse estimation	M1* (100 mm)	21	0.20, 0.46, 0.82, 1.27, 1.83, 2.5, 3.06	2, 3, 4, 5, 6, 7, 7.8
S1.3	Validation of the impact force and impulse estimation using the final setup	M1* (100 mm)	21	0.20, 0.46, 0.82, 1.27, 1.83, 2.5, 3.06	2, 3, 4, 5, 6, 7, 7.8
S2.1	Validation of the novel model to predict the fragmentation SP	M2 (50 mm)	80	2.15, 2.5, 2.87, 3.26 3.68	6.5, 7, 7.5, 8, 8.5
S2.2	Validation of the novel model to predict the fragmentation SP	M2 (75 mm)	80	1.54, 1.83, 2.15, 2.5, 2.87	5.5, 6, 6.5, 7, 7.5
S2.3	Validation of the novel model to predict the fragmentation SP	M2 (100 mm)	80	1.27, 1.54, 1.83, 2.15, 2.5	5, 5.5, 6, 6.5, 7
S2.4	Validation of the novel model to predict the fragmentation SP	M3 (100 mm)	80	1.19, 1.27, 1.54, 1.83, 1.94	4.83, 5, 5.5, 6, 6.17
S3.1	Validation of energy computation	M1* (100 mm)	10	0.46, 0.82, 1.27, 1.83, 2.5, 3.06	3, 4, 5, 6, 7, 7.8
S3.2	Investigation of energy partition	M1 (100 mm)	22	1.54, 1.83, 2.15, 2.5, 3.06, 5.10	5.5, 6, 6.5, 7, 7.8, 10
S4	Investigation of fragment size distribution	M1 (100 mm)	29	3.12, 4.59, 6.12, 7.92, 8.75, 12.35, 13.39, 15.93, 18.39, 22.43	7.8, 9.5, 11, 12.5, 13.1, 15.6, 16.2, 17.7, 19, 21

6 Results

6.1 Material characterisation

As mentioned in Chapter 5 (see Table 5-1), comprehensive testing was conducted to characterise the four mortar mixtures, whose key properties are reported in Table 6-1.

Table 6-1 Characteristics of mortar M1, M1, M2 and M3.*

Material	Density ρ_1 [g/cm³]	Unconfined compressive strength[1] σ_c [MPa]	Elastic modulus Y_m [MPa]	Poisson's ratio[2] ν_m	Tensile strength σ_t [MPa]	Fracture toughness K_{Ic} [MPa*m$^{0.5}$]
M1	1.947 $\pm$0.031	34.67 $\pm$1.46	7364.65 $\pm$430.67	0.20	3.59 $\pm$0.62	0.433 $\pm$0.091
M1*	1.932 $\pm$0.016	40.73 $\pm$1.00	7514.97 $\pm$166.12	0.20	3.86 $\pm$0.28	0.674 $\pm$0.087
M2	1.833 $\pm$0.024	22.90 $\pm$1.16	6055.04 $\pm$309.01	0.20	1.94 $\pm$0.24	0.436 $\pm$0.064
M3	1.852 $\pm$0.032	17.30 $\pm$1.53	6412.05 $\pm$632.34	0.20	1.81 $\pm$0.21	n.a.

Notes:
[1] Value referred to after the curing and drying process:
- **M1, M2, M3** after 12 weeks
- **M1*** after 16 weeks

[2] Presumed value

For mortars M2 and M3, a higher number of samples were used to characterise the material and highlight the material variability, since it is a key parameter of the novel model developed to predict the impact survival probability presented in Chapter 4.

The variability in mechanical properties is clearly revealed by the statistical distributions plotted in Figure 6-1 for both materials (M2 and M3). Interestingly, the variability exists despite the very meticulous preparation and curing processes applied to all specimens. There is almost a factor 2 between the lowest value and the highest value for tensile strength (obtained either from discs or spheres) and toughness (Mode I) for M2. By contrast, there is far less variability on the unconfined compressive strength. This is consistent with numerical findings of Nader et al. (2021) who showed that tensile strength was more sensitive to the presence of micro defects than the compressive strength, which seems to be closely related to the failure mechanism. It is relevant to note that, for all parameters, the survival probability tends to follow a Weibull distribution, as indicated by the very high values of goodness of fit. This is also the case for the distribution of work required to fail mortar cylinder under indirect tension, as illustrated in Figure 6-2. The value of work corresponding to a 37% survival probability (i.e. 0.663 J for M2 and 0.510 J for M3) provides the required estimate of the critical work $W_{BT(d)}^{cr}$.

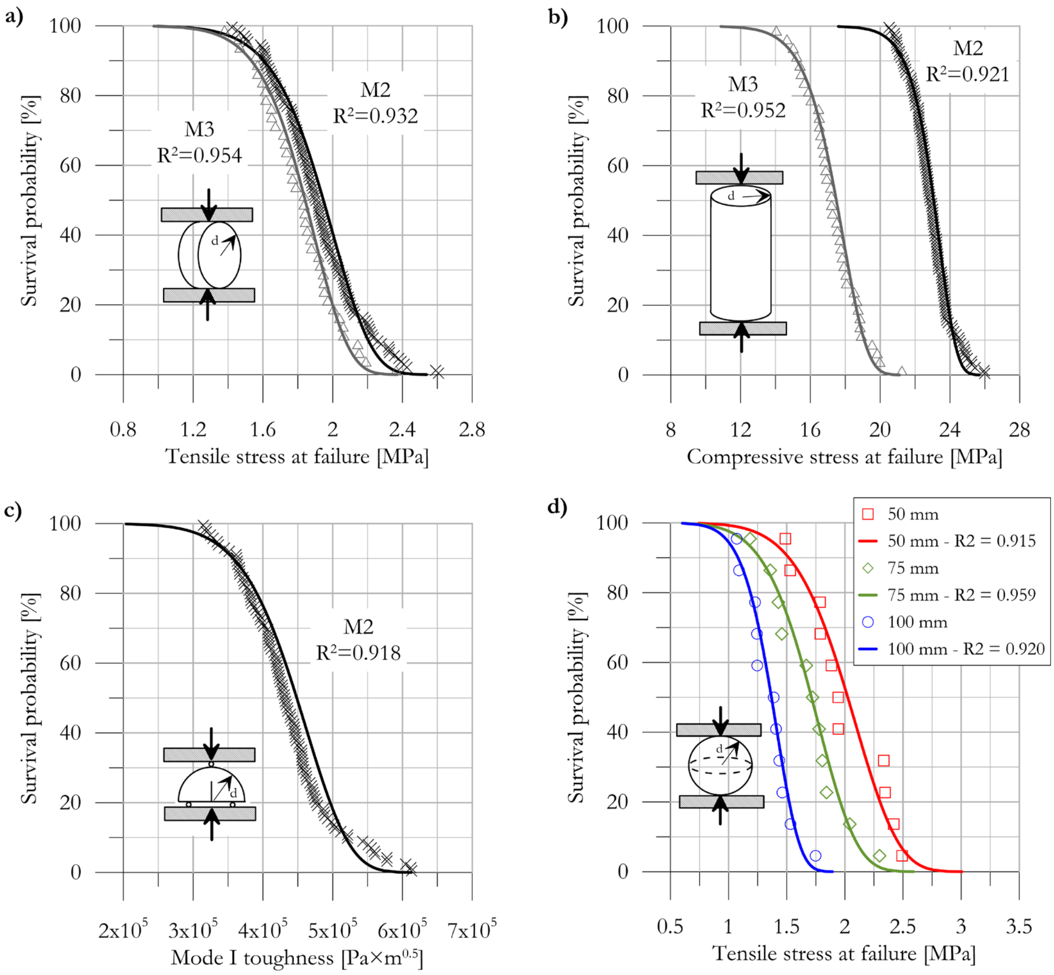

Figure 6-1: Experimental survival probability of (a) tensile stress obtained from Brazilian test on a disc (from M2 and M3), (b) unconfined compressive strength (from M2 and M3), (c) Mode I toughness (M2) and (d) tensile stress obtained from compression test on spheres of different diameters (50, 75 and 100 mm for M2). Crosses and triangles represent the experimental data of M2 and M3, respectively, while continuous lines represent the Weibull best fit (as per Eq. (4-1)) with goodness of fit indicated by the R^2 value.

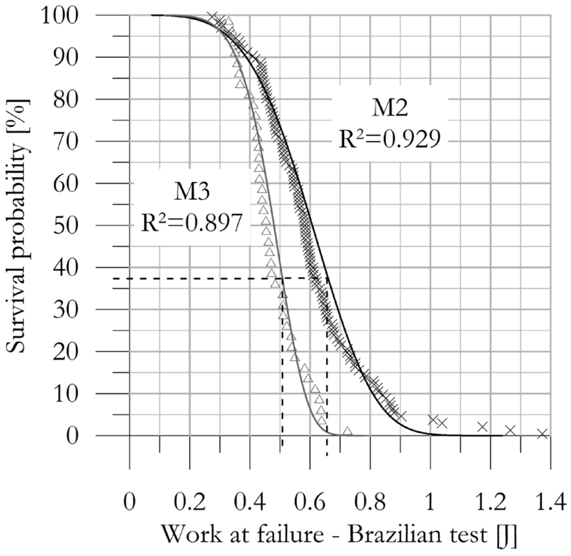

Figure 6-2: Experimental survival probability of work required to fail a cylinder under indirect tension (Brazilian test). Crosses and triangles represent the experimental data of M2 and M3, respectively, while continuous lines represent the Weibull best fit (as per Eq. (4-1)) with goodness of fit indicated by the R^2 value. The dashed lines indicate the critical work, corresponding to a survival probability of 37%.

For each test, it is possible to plot the survival probability in terms of force, stress (or toughness) and work, and to infer the corresponding shape parameter of the Weibull distribution (μ). Table 6-2 presents the values of Weibull shape parameter for all survival probabilities for both materials. A large variation of μ values appear between one type of test and another and, for a given test, between one parameter and another. However, it seems that the μ values of work are consistently lower than the μ values for force, stress or toughness and that the μ values for unconfined compression are the highest (exceeding 20 for M2), denoting a lower degree of variability, which is consistent with Figure 6-1. In contrast, the μ values for force or stress/toughness lie in the range 6.5 to 10.2. Interestingly, the Weibull shape parameter of the work distribution seems to depend on the sphere diameter: the larger the sphere, the lower μ. This would make sense for a natural material where a larger specimen might be expected to contain more defects, but it is unclear, at this stage, if the same should apply for the artificially created mortar specimens used in this study. Compared to M2, M3 presents a higher variability of unconfined compression test results but a lower variability of Brazilian tests results, which, at this stage, cannot be explained.

Table 6-2 Weibull shape parameter μ from the distribution of force, stress/toughness or work at failure for unconfined compression tests, Brazilian tests on disc, quasi-static compression on spheres and toughness tests.

Values of Weibull Shape Parameter μ	**Force at failure**		**Stress or toughness**		**Work at failure**	
	M2	**M3**	**M2**	**M3**	**M2**	**M3**
Unconfined compression tests	20.2	13.8	24.1	13.7	8.2	8.9
Brazilian tests on discs	8.9	10.2	9.8	10.3	4.2	6.2
Compression tests on 50 mm spheres	6.6	-	6.5	-	6.2	-
Compression tests on 75 mm spheres	10.1	-	10.2	-	5.2	-
Compression tests on 100 mm spheres	8.0	-	8.0	-	4.5	-
Toughness tests	8.0	-	8.3	-	4.2	-

6.2 Validation of the experimental setup

6.2.1 Tracking accuracy

The experimental setup has six different viewpoints as described in Section 3.1.3, coming from four high-speed cameras and two mirrors. Several factors can influence the tracking accuracy, the most critical being the number and location of viewpoints, the block geometry and the resolution of the visual hull for the outline tracking algorithm. In this section, the influence of these parameters, with particular attention on those influencing the calculation of the rotational velocity, is discussed.

Influence of number of views and object shape on accuracy of estimated rotational velocity

As presented in Table 5-3, in order to assess the effect of the number of views on tracking accuracy, a brick (Figure 5-3a) was rotated around an axis of rotation very close to the third axis (i.e. shortest axis) at a velocity of 11.99 rad/s and the images were processed using the different combinations of views that were presented in Table 5-2.

Figure 6-3a to c show the cumulative rotation angles around the three principal axes with time, from which the rotational velocity can be estimated by fitting a linear trend through the data points, for each principal axis.

For the first and second axis (Figure 6-3a and b), regardless of the number of views, the derived rotational velocity is low, which is consistent with the test conditions. The more views, the less rotation is inferred and the closer the recorded rotation is to the real rotation (close to zero). Notably, when using only two cameras, the position of these cameras affects the rotation recorded (see red and green lines in Figure 6-3b and c).

For this type of tests, most of the rotation occurs around the third axis and Figure 6-3c suggests that all combinations, other than 2 views in a plane perpendicular to the axis of rotation, can reasonably track the rotational velocity. However, when comparing the volume computed by TEMA3D to the real object volume (Figure 6-3d), it is clear that 6 views deliver the best outcome and the volume computed from 2 planar views gives greater fluctuation with values deviating from the real volume. Note that the fluctuations in volume come from the visual hull approach (which will always over-estimate the volume) as the intersection of silhouette cones changes with time. Both over-estimations and fluctuations in volume are exacerbated when not enough views are used (as per Figure 6-4).

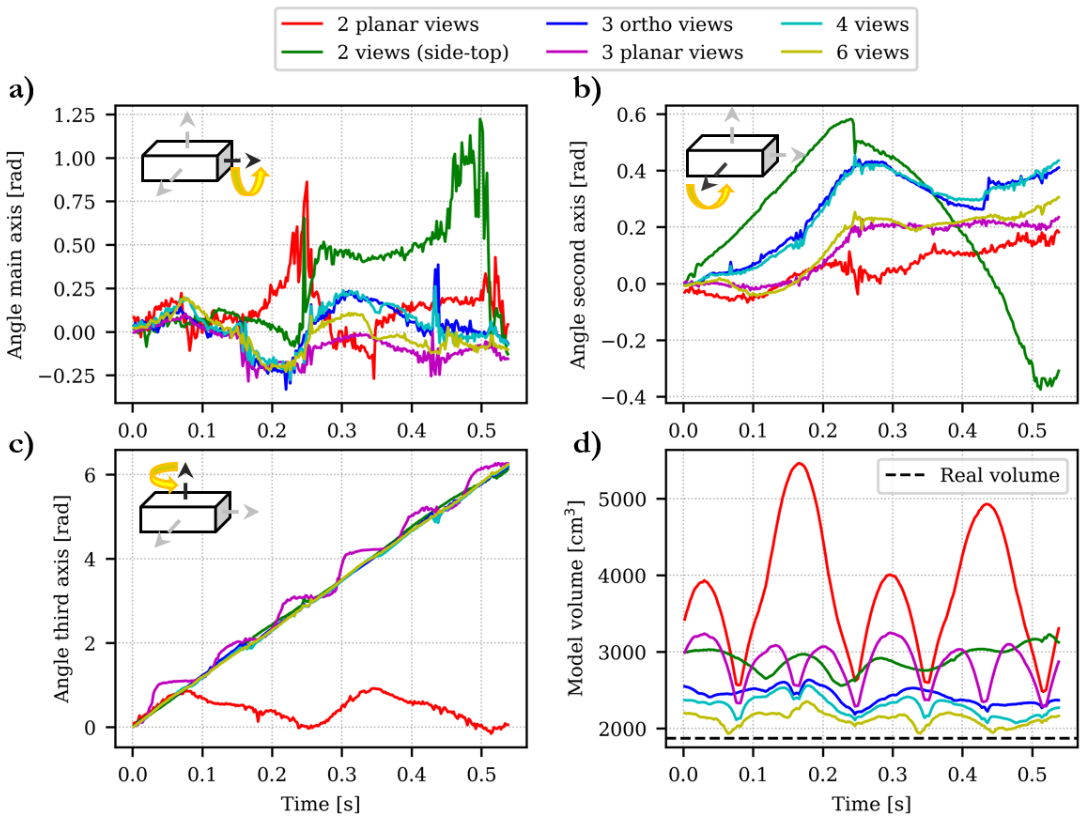

Figure 6-3: Rotating brick: influence of viewpoints on the cumulative rotation angle around (a) the main principal axes, (b) the second principal axes and (c) the third principal axes, over time. (d) the brick's volume computed by the VH algorithm as a function of time. VH resolution equal to 1 (fine mesh).

In Figure 6-4 are screenshots of the VH generated by TEMA3D using the different viewpoints, which corroborates the findings of Figure 6-3d in the sense that the shape obtained by 2 planar views (at some point of the rotation) can be very different from the real shape. In contrast, the other view combination yield a shape that is quite close to the real shape.

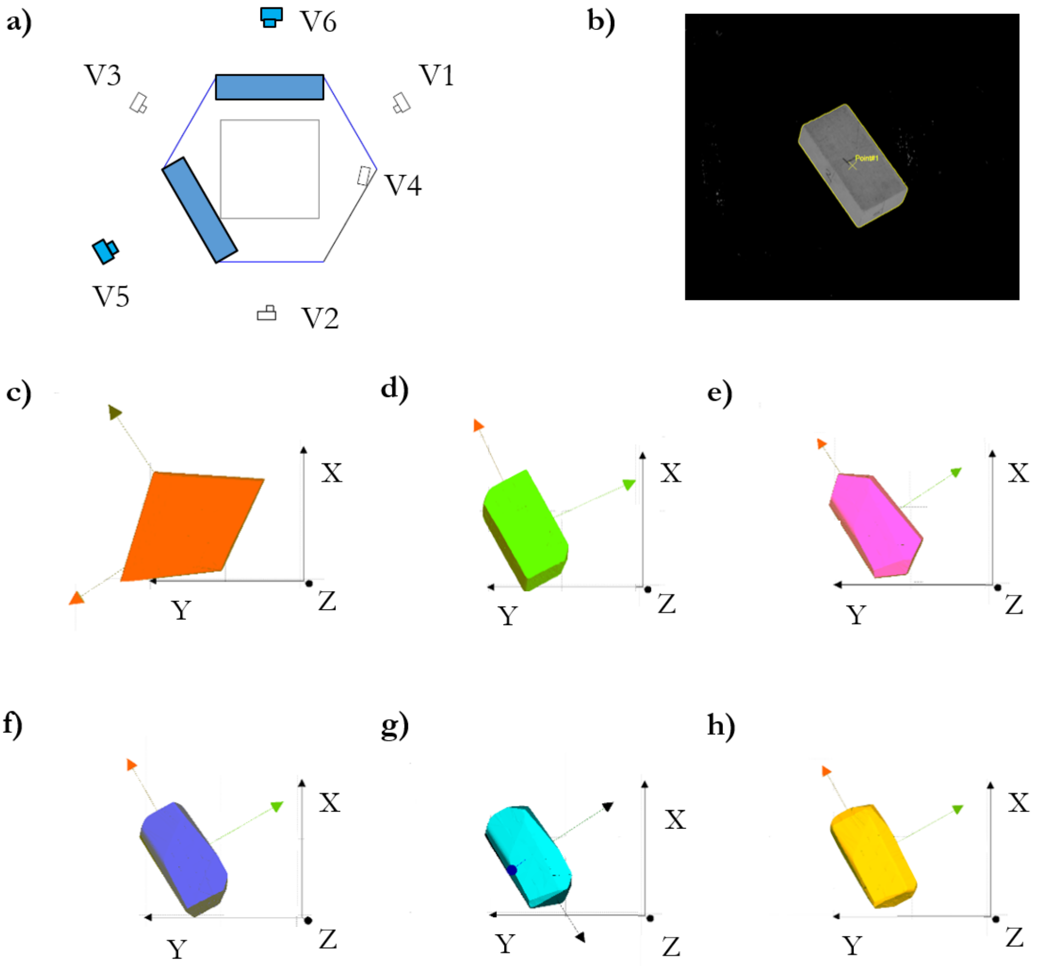

Figure 6-4: Brick influence of viewpoints: (a) physical viewpoints, (b) image of the brick taken from V4 corresponding at time 0.174s in Figure 6-3 and corresponding visual hull (VH) from a top view using (c) 2 planar views, (d) 2 views (side-top), (e) 3 planar views, (f) 3ortho views, (g) 4 views and (h) 6 views.

In another test, a disc (Figure 5-3b) was rotated around the third axis at a velocity of 41.89 rad/s. Due to the axisymmetry of the object, it was not possible to get a reliable estimation of rotational velocity using the VH algorithm (Figure 6-5) as the cumulative rotation angles around the three axes are all fluctuating around zero (Figure 6-5a to c). On the other hand, the estimation of the volume is quite accurate, because of the simple axisymmetric shape of the object. This test highlights the fact that the outline tracking algorithm is not accurate for an axisymmetric object. The feature tracking algorithm was then used to compute the rotational velocity with results shown in Figure 6-6. Tracking a feature point (P1) on the surface of the disk, and the centre of gravity, returned a rotational velocity of 40.53 rad/s, which is very close to the actual experimental value of 41.89 rad/s.

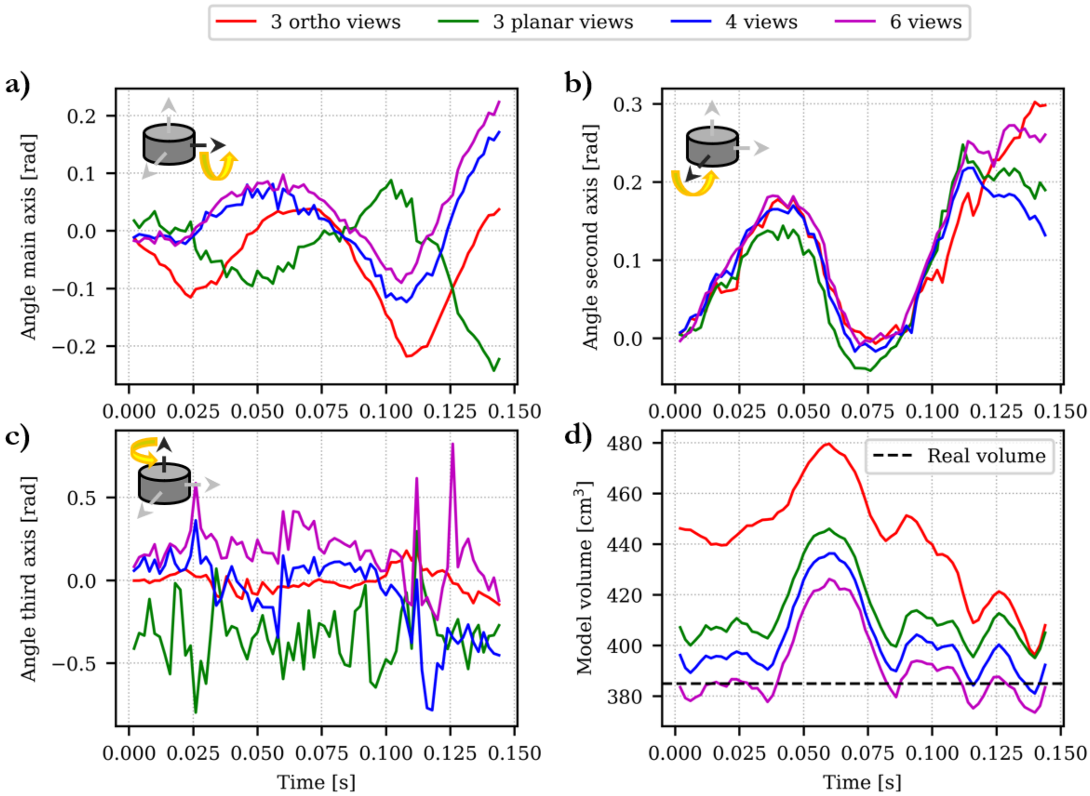

Figure 6-5: Rotating disc: influence of viewpoints on the cumulative rotation angle around (a) the main principal axes, (b) the second principal axes and (c) the third principal axes over time. (d) volume of the disc computed by the VH algorithm as a function of time. VH resolution equal to 1 (fine mesh).

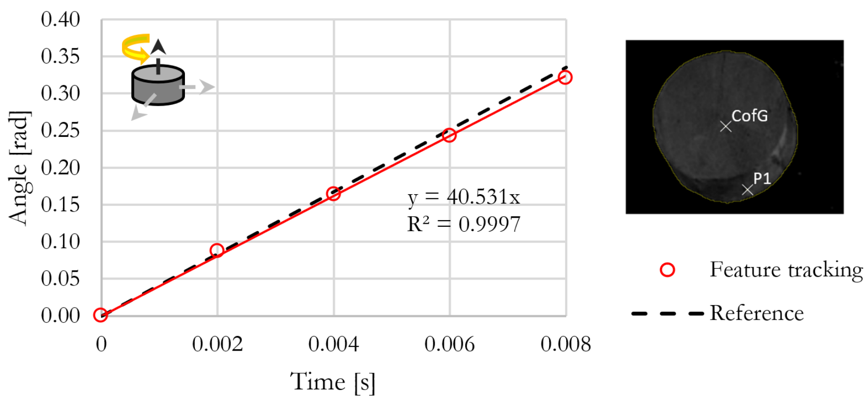

Figure 6-6: Spinning test result on disc using feature tracking. Inset shows the disc and the two tracked points: centre of gravity (CofG) in the middle, and feature point (P1) on the outer cylindrical surface.

The third object tested was a fragment of a sphere (Figure 5-3c) rotated around an arbitrary axis of rotation, close to the third axis, at a velocity of 37.46 rad/s. The results are plotted in Figure 6-7 and show that two views are clearly insufficient to estimate the main component of rotational velocity. It takes at least three views to obtain a realistic estimate of rotational velocity. However, looking at the estimation of volume (Figure 6-7d), it is clear that six views are required if one needs an accurate estimate of both rotational velocity and volume.

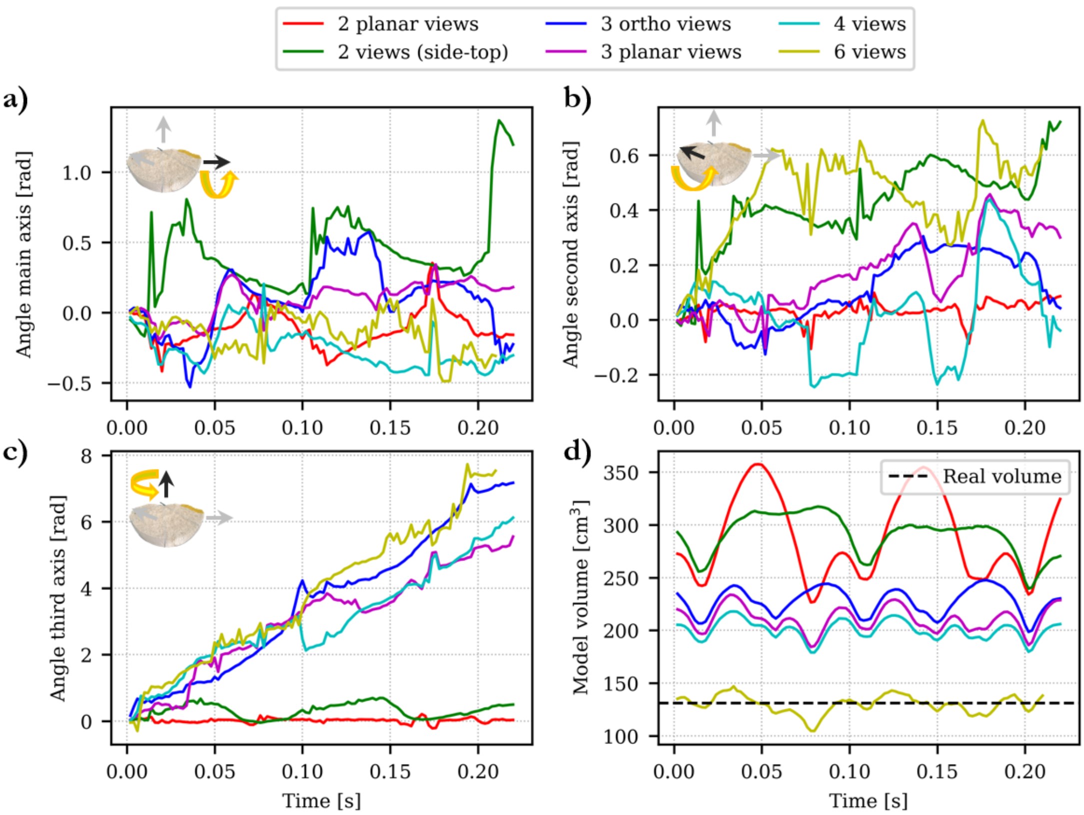

Figure 6-7: Rotating sphere fragment: influence of viewpoints on the cumulative rotation angle around (a) the main principal axes, (b) the second principal axes and (c) the third principal axes over time. (d) volume of the sphere fragment computed by the VH algorithm as a function of time. VH resolution equal to 1 (fine mesh).

Based on the results of this section, it was decided that all drop tests in the fragmentation cell would be conducted with six views made of four cameras and two mirrors.

Influence of Visual Hull resolution on accuracy of estimated rotational velocity

As discussed above, the tests conducted for this part of the study all use six views. Figure 6-8 to Figure 6-11 compare the outcomes of volumes derived from VHs meshed to different resolutions (VH01 corresponds to highest resolution whereas VH10 to lowest). Figure 6-8 and Figure 6-9 pertain to the brick while Figure 6-10 and Figure 6-11 pertain to the sphere fragment.

Figure 6-8a to c show the evolution of cumulative rotation angle with time around the three axes while Figure 6-8d shows the evolution of the volume computed form the visual hull algorithm with time. Because of the large dimension and the regular shape of the brick, there is no influence of the VH resolution on the outcome of the test, which is corroborated by the visual hulls presented in Figure 6-9. The number of mesh elements (triangles) seem to affect the textural appearance of the object (compare texture of Figure 6-9a to Figure 6-9d) but not the volume (Figure 6-8d).

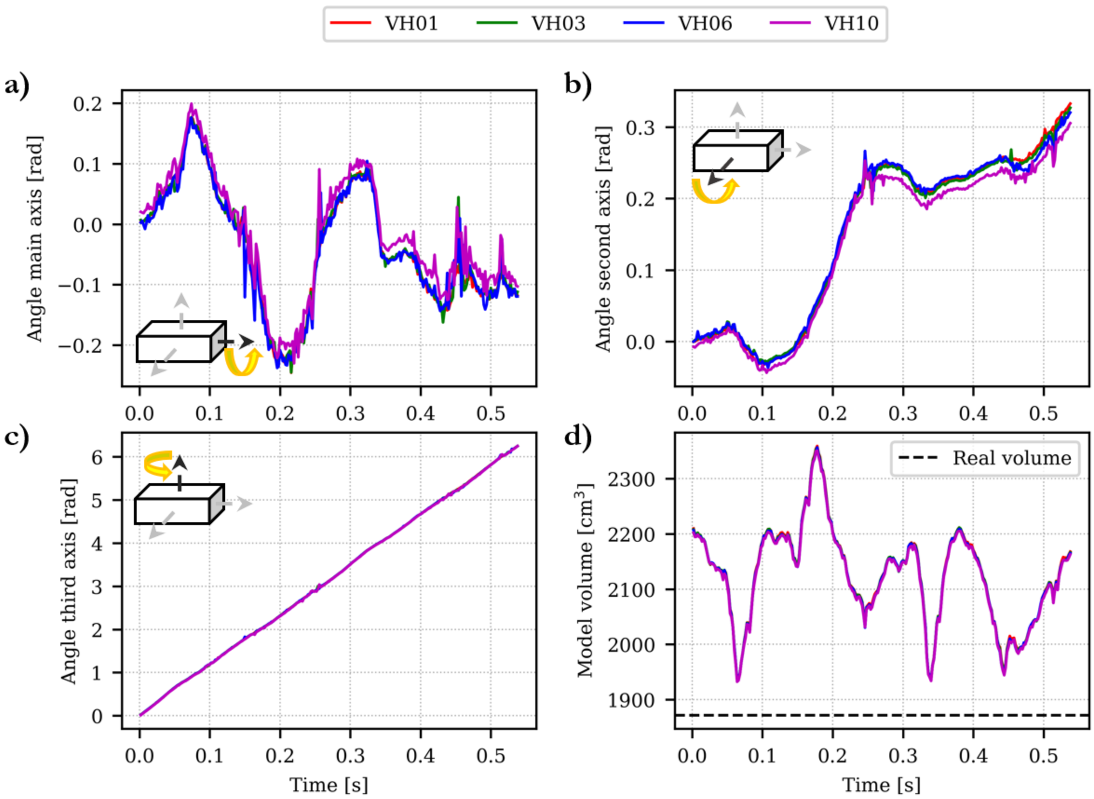

Figure 6-8: Rotating brick - 6 views: influence of VH resolution on the cumulative rotation angle around (a) the main principal axes, (b) the second principal axes and (c) the third principal axes over time. (d) Volume of brick computed by the VH algorithm as a function of time.

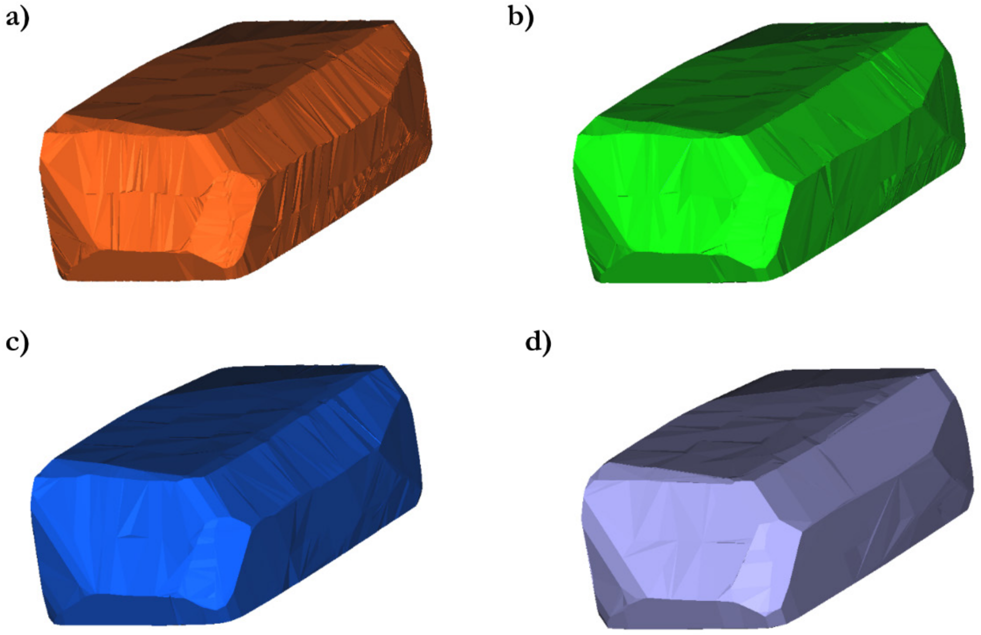

Figure 6-9: Brick influence of VH resolution: (a) VH01 (highest), (b) VH03, (c) VH06 and (d) VH10 (lowest).

Unlike for the brick, the sphere fragment has an irregular shape and Figure 6-10 shows that the VH resolution now clearly affects the accuracy of the rotational velocity (Figure 6-10a to c) and, in particular, no reliable estimation of rotational velocity can be obtained by using VH06 and V10. Like for the brick, the VH resolution still has little effect on the computed volume (Figure 6-10 d), which is corroborated by Figure 6-11, illustrating the scanned fragment shape and its VH approximations (VH01, VH03, VH06 and VH10). In conclusion, VH01 will be used to a better estimation of rotational velocities for small fragments.

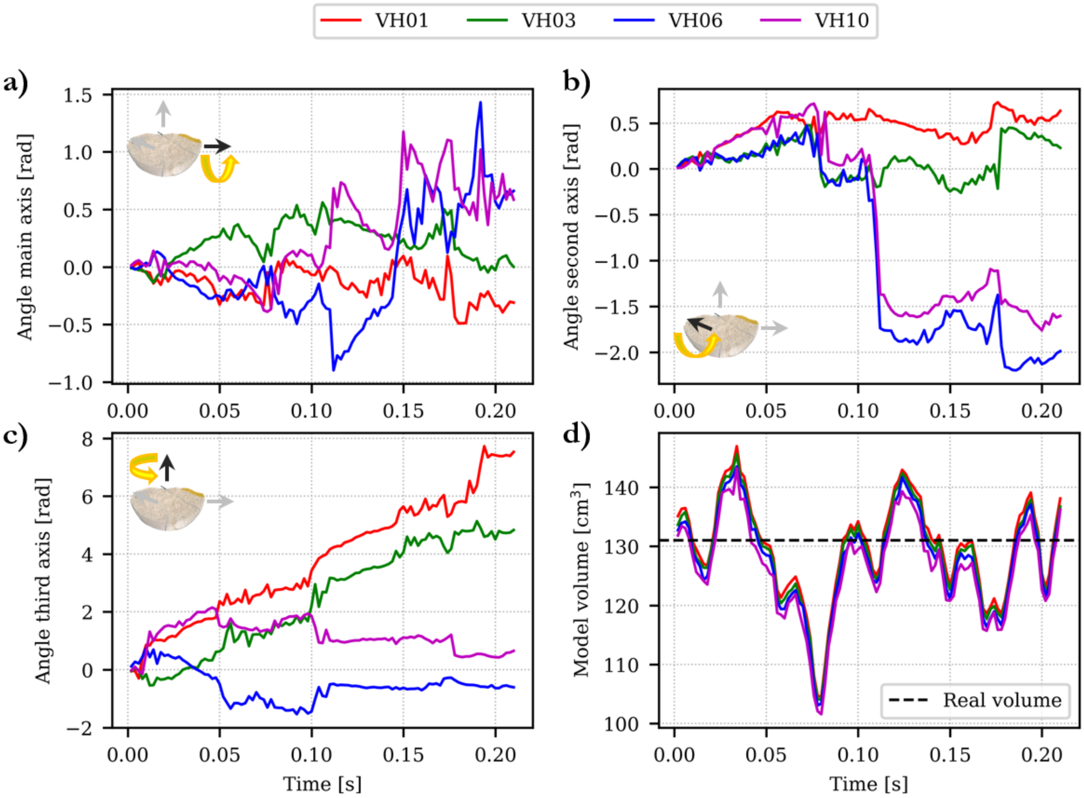

Figure 6-10: Rotating sphere fragment - 6 views: influence of VH resolution on the cumulative rotation angle around (a) the main principal axes, (b) the second principal axes and (c) the third principal axes over time. (d) volume of sphere fragment computed by the VH algorithm as a function of time.

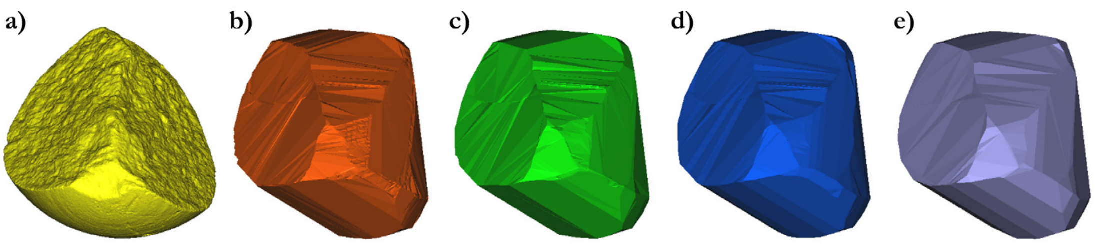

Figure 6-11: Influence of VH resolution on inferred volume of sphere fragment i: (a) scanned shape, (b) VH01, (c) VH03, (d)VH06 and (e) VH10.

Influence of new post processing algorithm on accuracy of estimated rotational velocity

The validation of the new post processing algorithm (Guccione et al. 2020), implemented to improve the calculation of rotational velocities, was also evaluated using the spinning tests of the brick and the fragment. Although it was previously concluded that six views should be used for all fragmentation tests, it is very likely that fragments will overlap in certain views, making those views unusable. Consequently, in this section, the new algorithm developed to track rotational velocity was compared to TEMA3D, both for four views and six views, in terms of evolution of cumulative rotational angle with time for the three principal axes.

Figure 6-12a to f pertain to the brick while Figure 6-13a to f pertain to the fragment. In each case, sub-figures a to c correspond to four views while sub-figures d to f correspond to six views. Also, each sub-figures a to c correspond to one axis of rotation. As previously, rotation mainly occurs around the third axis with much smaller rotation around the first and second axes.

When comparing the new post-processing method with the results from TEMA3D, we can observe more stable trends (i.e. less noise and less fluctuation) with the new post-processing algorithm. This is especially so when the rotation velocity is low, around the first and second axes. There is no significant difference between four views and six views for a regularly shaped object like the brick.

Table 6-3 summarises the computed rotational velocities around the main axes ($\omega_I, \omega_{II}, \omega_{III}$), the absolute rotational velocity (ω) and the relative error (computed as $1 - \omega/\omega_{ref}$). The new method shows estimated velocities closer (i.e. lower relative error) to the reference value, compared to the TEMA3D estimation for both four views and six views.

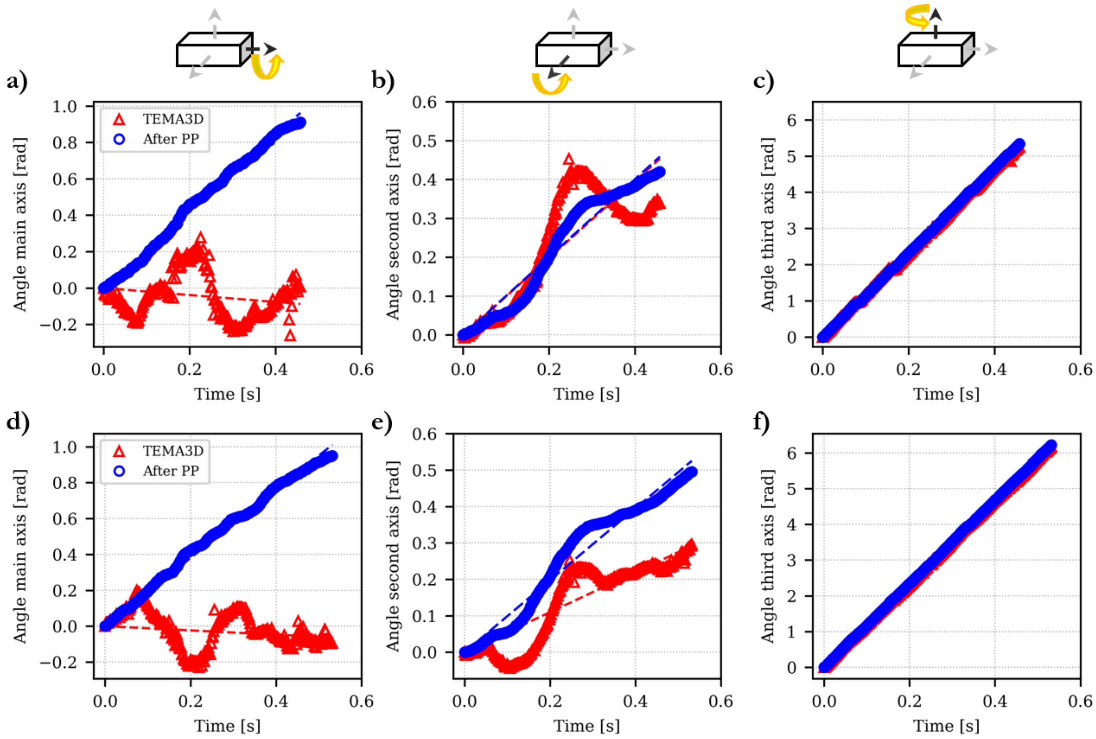

Figure 6-12: Rotating brick: comparison between the cumulative rotation angles around the principal axes calculated using TEMA3D and the new post-processing (PP) algorithm developed by Guccione et al. (2020). (a), (b) and (c) using 4 views and (d), (e) and (f) using 6 views.

Table 6-3 Results of spinning brick (ω_{ref} = 11.99 rad/s)

		$\boldsymbol{\omega_I}$ **[rad/s]**	$\boldsymbol{\omega_{II}}$ **[rad/s]**	$\boldsymbol{\omega_{III}}$ **[rad/s]**	$\boldsymbol{\omega}$ **[rad/s]**	**Relative error**
4 views	TEMA	-0.19	0.99	11.58	11.62	-3.06%
	After PP	2.10	1.00	11.65	11.88	-0.93%
6 views	TEMA	-0.12	0.55	11.63	11.64	-2.88%
	After PP	1.90	0.99	11.70	11.89	-0.81%

For an irregular shape, it is again clear that the new post-processing algorithm provides a better estimate of rotational velocities (Figure 6-13). In particular, the error after post-processing of four views reduces by a factor of four (from 29.32% to 7.64%). This is a very important finding as in most of the cases not all six views will be available. A part from that it can be seen that, this time, there is an influence of the number of views with six views yielding more accurate values of rotational velocities (Table 6-4).

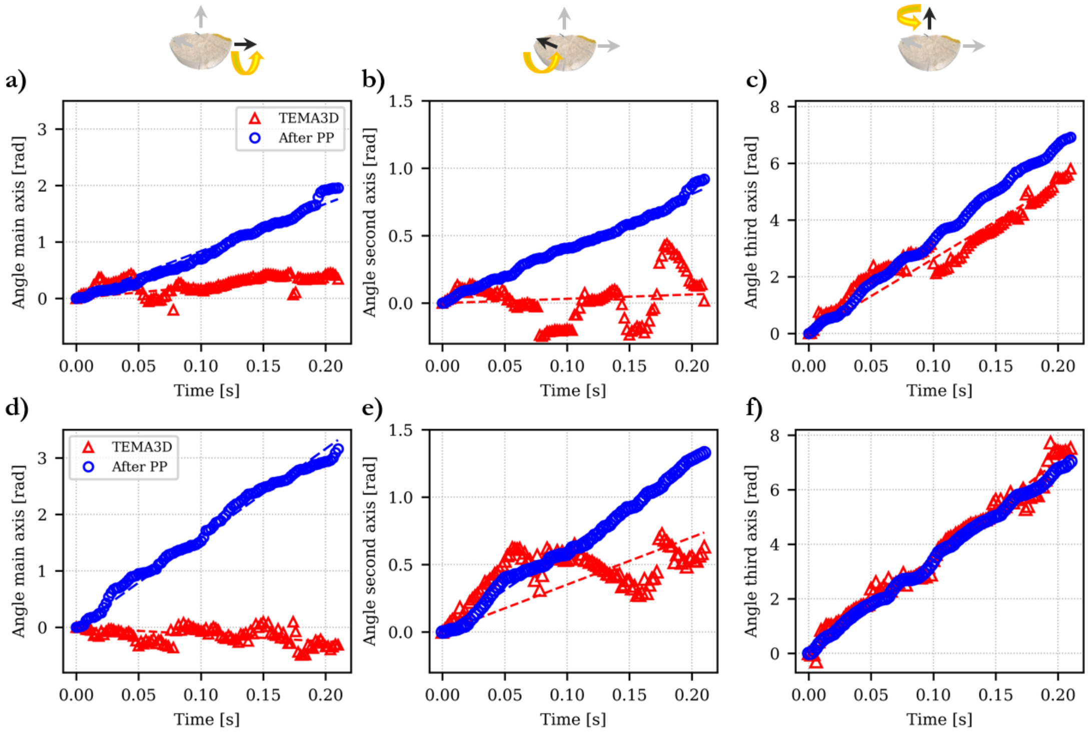

Figure 6-13: Rotating sphere fragment: comparison between the cumulative rotation angles around the principal axes calculated using TEMA3D and the new post-processing (PP) algorithm developed by Guccione et al. (2020). (a), (b) and (c) using 4 views and (d), (e) and (f) using 6 views.

Table 6-4 Results of rotating sphere fragment (ω_{ref} = 37.46 rad/s)

		$\boldsymbol{\omega_I}$ **[rad/s]**	$\boldsymbol{\omega_{II}}$ **[rad/s]**	$\boldsymbol{\omega_{III}}$ **[rad/s]**	$\boldsymbol{\omega}$ **[rad/s]**	**Relative error**
4 views	TEMA	2.13	0.32	26.39	26.47	-29.32%
	After PP	8.37	4.04	33.32	34.59	-7.64%
6 views	TEMA	-1.26	3.51	35.35	35.55	-5.09%
	After PP	15.80	6.22	33.89	37.91	1.21%

In conclusion, the proposed post-processing method seems to provide more accurate results, especially if less than six views are used, and will be employed to process all tracking results.

Preliminary tracking of trajectory pre- and post-impact

To validate the tracking methodology, two preliminary drop tests were conducted: one using a sandstone block and one using a mortar sphere (M1*) (see Figure 5-4 and Table 5-4). The reconstructed 3D trajectories were compared to theoretical trajectories: a free-fall (of known initial position and initial velocity) pre-impact; and a parabolic trajectory, contained in a single vertical plane, after impact.

The sandstone block was dropped from a height of 1.65 m and did not break upon impact. Both translational and rotational components of trajectory post-impact were computed using six viewpoints. Figure 6-14 shows a sequence of images recorded from viewpoint V3 during that drop test (Figure 6-14a-c) and the corresponding processed data indicating the 3D trajectory and the estimated shape (Figure 6-14d-f). The coordinates of the centre of gravity (X,Y,Z) exported from the tracking are expressed in the global reference system represented in Figure 6-14d-f (X and Y are horizontal directions and Z is vertical) and are plotted in Figure 6-15. A linear fitting is used to determine the X and Y components of the translational velocity, whereas a second order polynomial (i.e. parabola) is used for the Z component. The R^2 values reported on the figure represent the goodness of fit between the reconstructed trajectories (free fall and rebound) and the theoretical trajectories (parabola or straight line). It can be seen that R^2 values are very close to 1, hence the measured trajectory of the block respects the expected physics motion laws.

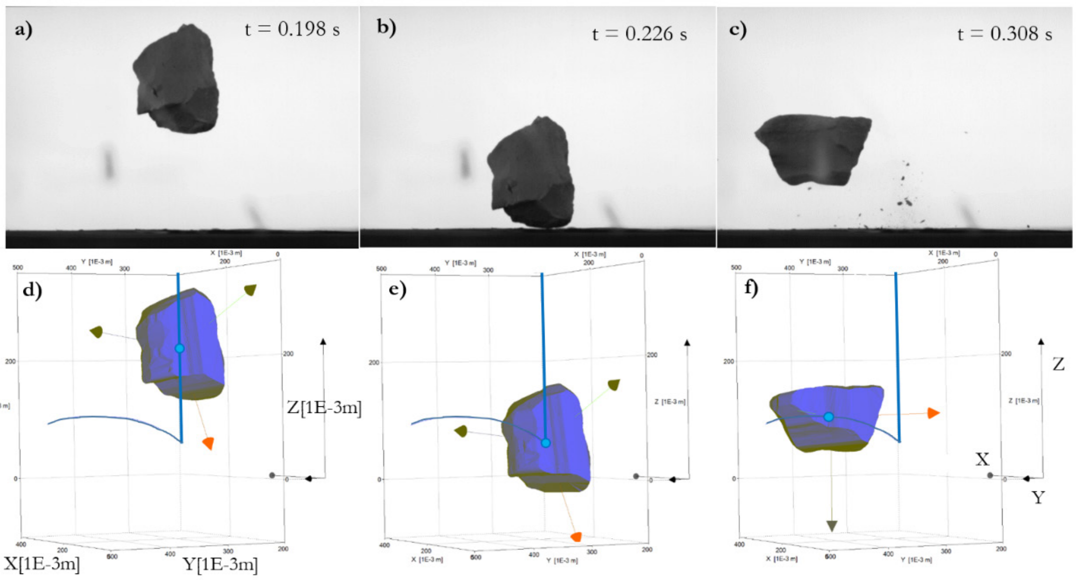

Figure 6-14: Drop test sandstone block (drop height 1.65 m, impact velocity 5.7 m/s). Sequence of images from V3: (a) free fall, (b) impact, (c) rebound and corresponding tracking results (d), (e) and (f) in 3D.

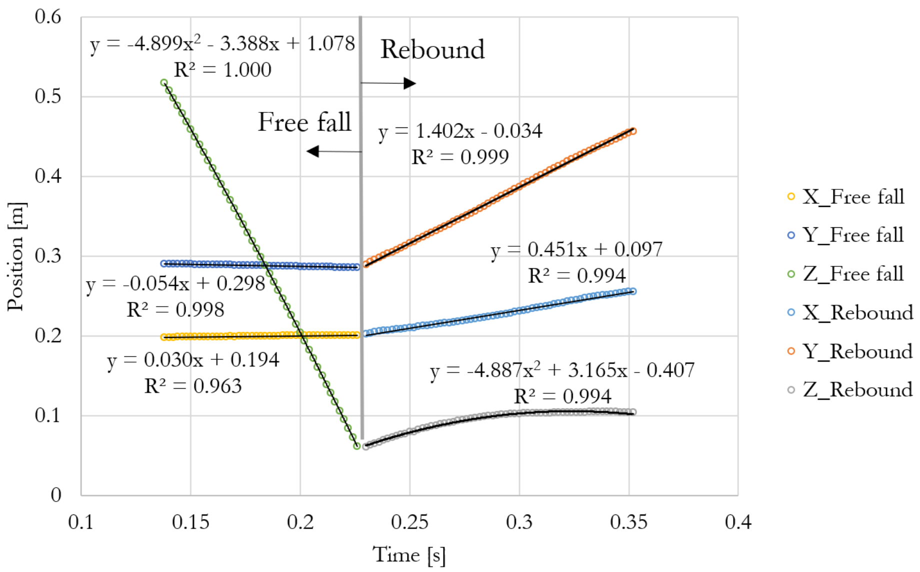

Figure 6-15: Tracking of drop test sandstone block: X,Y,Z components of the centre of gravity vs. time.

The mortar sphere (specimen M1*) was dropped from a height of 3.1 m. Upon impact, the sphere broke into three fragments. Figure 6-16a shows an image of the sphere at the end of the free-fall recorded just before impact, with Cam 2 including view V2 and mirrored view V6. The corresponding VH of the sphere and the measured trajectory are shown in Figure 6-16b (in a vertical plane) and Figure 6-16c (in a horizontal plane). The free-fall trajectory does follow a vertical line, as expected. The R^2 values reported on the figures represent the goodness of fit between the reconstructed trajectories (or their projection on the vertical and horizontal planes on Figure 6-16) and the theoretical trajectories (parabola or straight line).

Figure 6-16d shows an image of the fragments after impact, recorded with Cam 2 including view V2 and mirrored view V6. The corresponding VH of these fragments and the measured trajectories are shown in Figure 6-16e (in a vertical plane) and Figure 6-16f (in a horizontal plane). In the side view (Figure 6-16e), the recorded trajectories were fitted with a parabolic equation returning R^2 values of 0.999. Similarly, high values were computed and reflect the fact that each fragment trajectory is contained in a vertical plane (Figure 6-16f).

Tracking the fragments confirmed the conclusion drawn after tracking the sphere: the methodology developed in this thesis allows for accurate capture of 3D trajectories of regular and irregular objects, in translation and rotation.

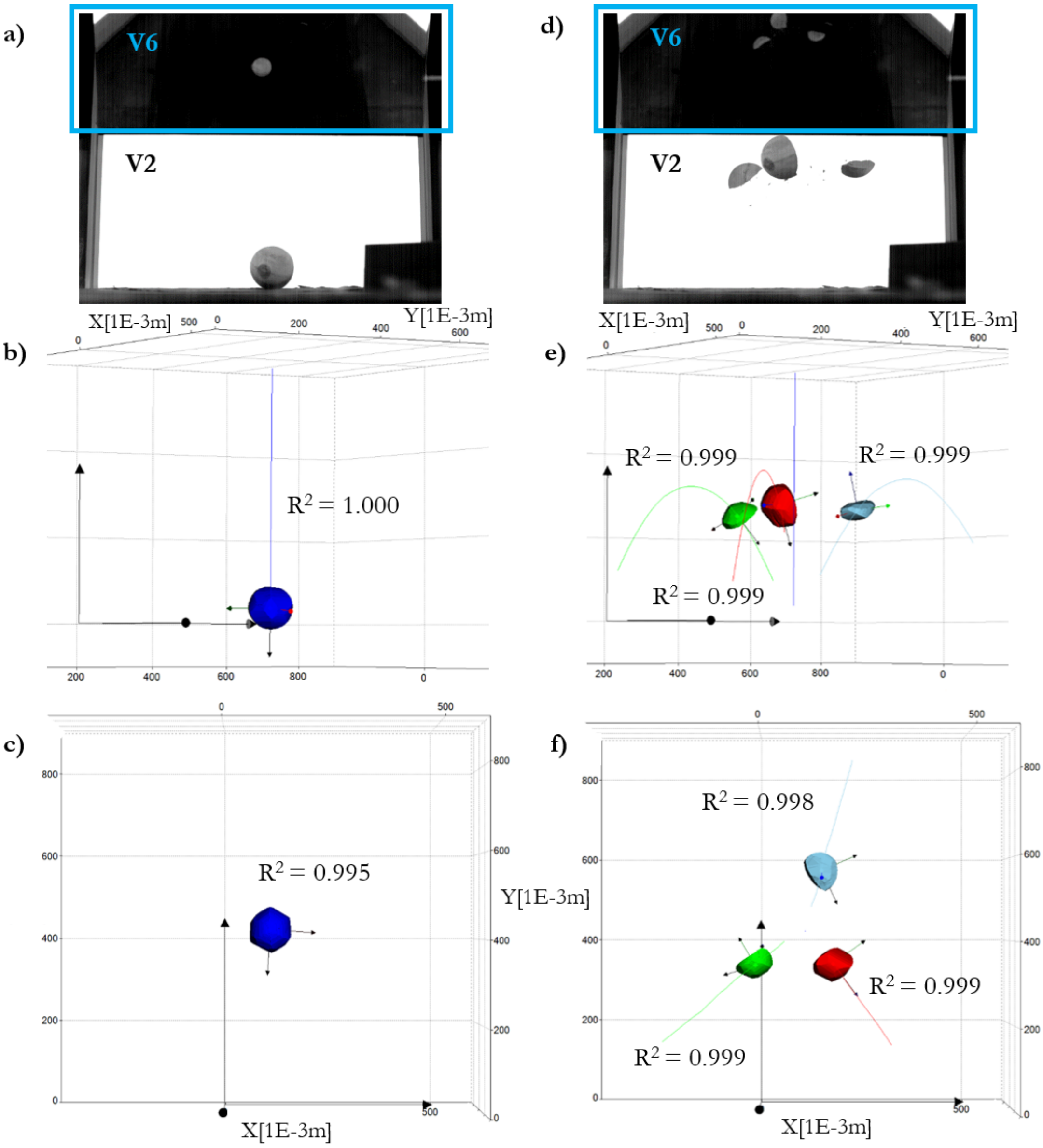

Figure 6-16: Results of trajectory tracking for drop test with mortar sphere (M1). (a): Image of V2/V6 just before the impact with (b) corresponding tracking analysis and (c) visual hull from side view in vertical plane and top view in horizontal plane. (d): Image of V2/V6 after the impact with corresponding tracking analysis and (e) visual hulls from the side view in vertical plane; and (f) top view in horizontal plane. The R^2 in (b) and (e) represents the coefficient of determination of a parabola fit of the trajectory in a vertical plane. R^2 in (c) and (f) represents an average coefficient of determination of a linear fit of the trajectory projected on a horizontal plane.*

6.2.2 *Determination of the deformability of slab and load cells system*

Before elaborating on the results, recall that the concrete slab rests on three load cells. The system deformability can be inferred by plotting the slab reaction force (measured by the three bottom load cells) against slab displacement (inferred from the accelerometer), as per Figure 6-17. The relationship between force and displacement can be reasonably fitted as linear, with the slope of the trend equal to the stiffness of the system (slab plus load cells), here $k = 3.653 \times 10^8$ N/m. Data from both series S1.2 and S1.3 have been used for the linear fitting.

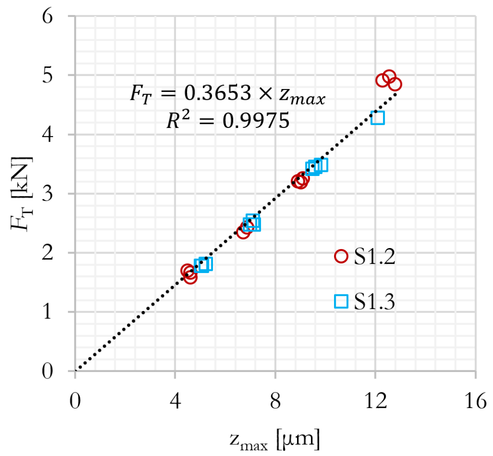

Figure 6-17: Values of impact force measured under the slab, and corresponding slab displacement for the two series of drop tests S1.2 and S1.3

The elastic modulus of the system slab plus load cells (denoted Y_c) was calibrated using the procedure described in Section 3.2.4 using the drop tests of series S1.3 where the sphere did not sustain any damage. In absence of damage and referring to Eq. (3-28), the experimental value of restitution coefficient is computed from energy terms as:

$$\overline{CoR_d} = \sqrt{\frac{\Delta E_{slab} + E_{k_t}^a}{E_{k_t}^b}} \tag{6-1}$$

Note that in absence of damage $\overline{CoR_d}$ is equal to $\overline{CoR_E}$.

The experimental value of impact duration was obtained directly by the pressure sensor located on the slab and the theoretical evolutions of coefficient of restitution and impact durations are given by Eqs. (3-18) and (3-24), respectively.

Figure 6-18 shows the evolution of the goodness of fit (R^2) for the two equations as a function of Y_c. The trend is non-linear and values of modulus comprised between 11.6 GPa and 13.3 GPa yield R^2 in excess of 0.9 and 0.55 for Eq. (3-20) and Eq.(3-24) respectively. Here, it was deemed that 11.6 GPa is an adequate value for the modulus of the system.

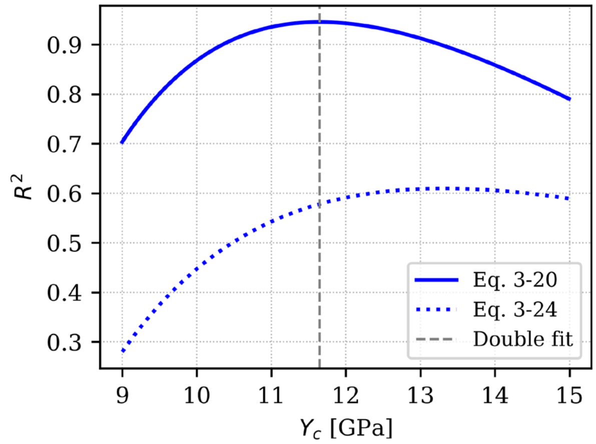

Figure 6-18: Evolution of the goodness of fit (R^2) for the two equations as a function of Y_c and value of Y_c by a double fitting procedure using a non-linear least square fitting (Virtanen et al. 2020).

Figure 6-19 shows both theoretical and experimental values of coefficient of restitution and impact duration with impact velocity to confirm that the fitting is adequate. Note that the impact times shown in Figure 6-19b are average values (of three tests) with the error bars representing precision of the measurements, calculated for the number tests shown in Figure 6-19a.

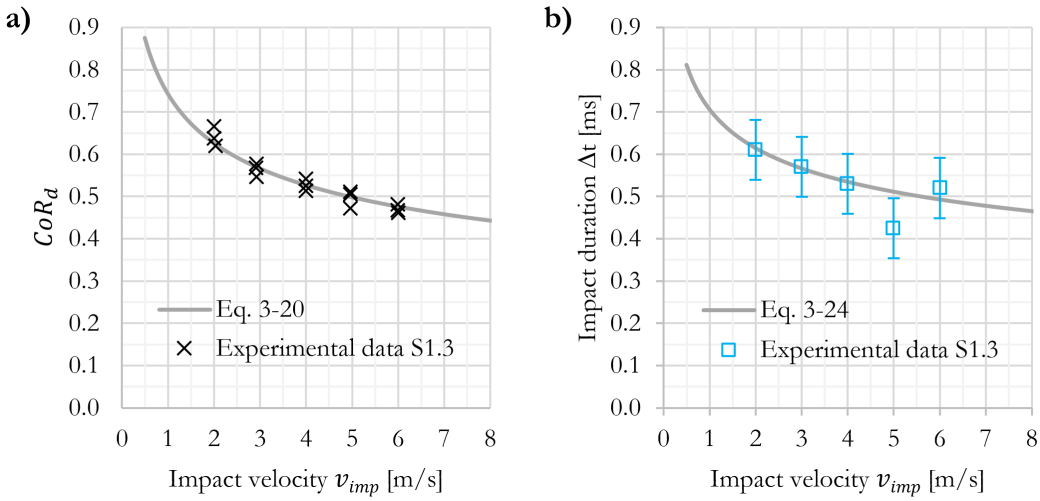

Figure 6-19: (a) Measured values of coefficient of restitution $\overline{CoR_d}$ as a function of impact velocity v_{imp}. The grey line represents the relationship of Eq. (3-20). (b) Average impact duration measured from I-scan sensor Δt_i and relationship given by Eq. (3-24).

6.2.3 *Estimation of impact force and total impulse*

Because the load cells are placed under the slab, the impact force and duration between the sphere and the slab (F_{Impact}, Δt_i) differ from the force and time recorded under the slab (F_T, Δt_{ti}), as shown in Figure 6-20. Note that the duration of impact is required to estimate the impact impulse.

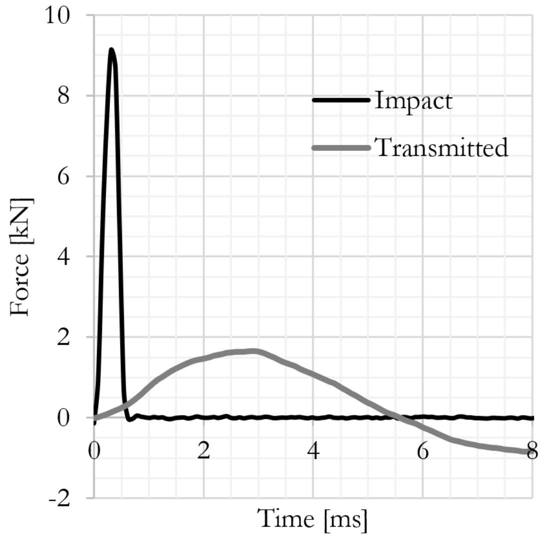

Figure 6-20: Temporal evolution of impact force recorded from a load cell placed on the slab and directly impacted by a falling sphere (F_{impact}) and total transmitted force (F_T) recoded from the load cells under the slab.

Figure 6-21 summarises the results of the impact analysis of series S1. Figure 6-21a shows the evolution of the transmitted force measured under the slab (F_T) as a function of impact velocity, ranging from 2 to 7.8 m/s. It can be seen that the trend for the transmitted forces is linear. Tests repeated with the same impact velocity give very similar results except for impact velocities greater than 6 m/s, which is a transition zone to fragmentation.

In Section 3.2.1, a theoretical relationship was established to predict the impact force from the transmitted force (Eq. (3-3)). To apply Eq. (3-3), one needs to know the duration of both the impact (here recorded by the load cell top) and the transmitted impact (recorded by the load cells under the slab), which are noted $\Delta t_{i,LC}$ and Δt_{ti}, respectively. Figure 6-21b shows the impact duration and transmitted impact duration with impact velocity, ranging from 2 to 7.8 m/s.

The impact force (F_{impact}) was estimated using the measured transmitted force (F_T) and the force ratio given by Eq. (3-3). The predicted impact force F_{impact} was then compared to the impact force measured by the load cell placed on top of the slab ($\overline{F_{impact}}$). Results are presented in Figure 6-21c where the grey dashed lines correspond to a relative error of ±20%. For 85% of the tests, the relative error is less than 11%, which suggests that the impact force can satisfactorily be estimated from the recorded value of transmitted force.

The predicted impact force can then be combined with the recorded impulse duration to compute the impulse generated by the impact (using Eq. (3-10)). Figure 6-21d compares the measured impulse ($\overline{J_{impact}}$) to the estimated impulse (J_{impact}). For 80% of the tests, the relative error is less than 12%.

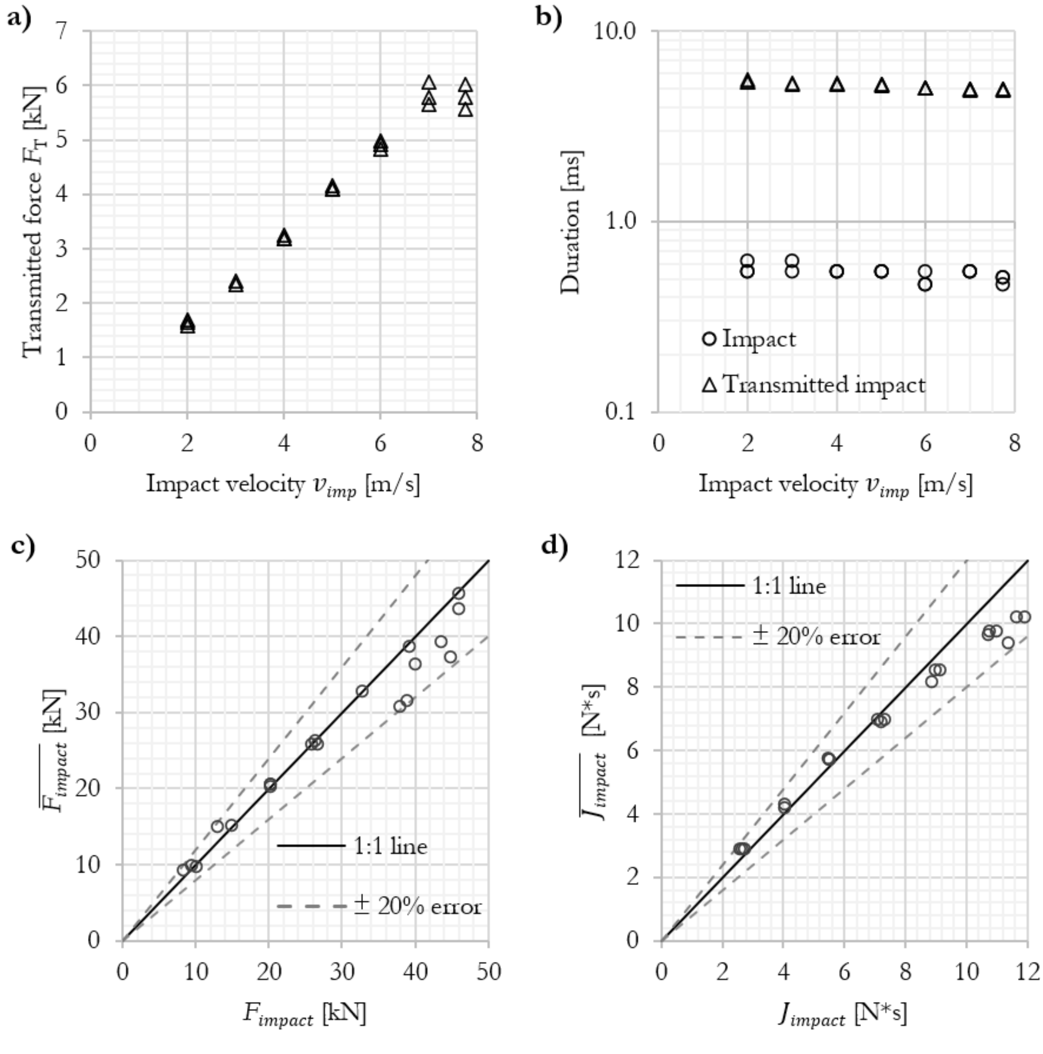

Figure 6-21: (a) Evolution of experimental values of transmitted force F_T with impact velocity v_{imp}. (b) Experimental values of impact impulse duration $\Delta t_{i,LC}$ and transmitted impulse duration Δt_{ti}. (c) Comparison of measured impact force ($\overline{F_{impact}}$) and impact force calculated with Eq. (3-3) (F_{impact}). (d) Comparison of measured impact impulse ($\overline{J_{impact}}$) and impact impulse calculated with Eq. (3-10) (J_{impact}).

It is now possible to drop mortar spheres on a pressure film sensor (used to record the impact duration) and estimate the impact force (between the sphere and the slab) and the impact impulse (between the sphere and the slab) from the transmitted force, transmitted impact duration and direct impact duration. This is illustrated in Figure 6-22 where the results of series S1.3 are superimposed on to the estimated impact force and impulse of series S1.2. Note that tests of series S1.3 were conducted with a pressure sensor film without a direct measurement of impact force so the direct comparison to an impact force is not possible. This is why the predicted force values are compared to results of series S1.2 to assess whether the predicted results are acceptable. A good agreement can be observed between measured and estimated results.

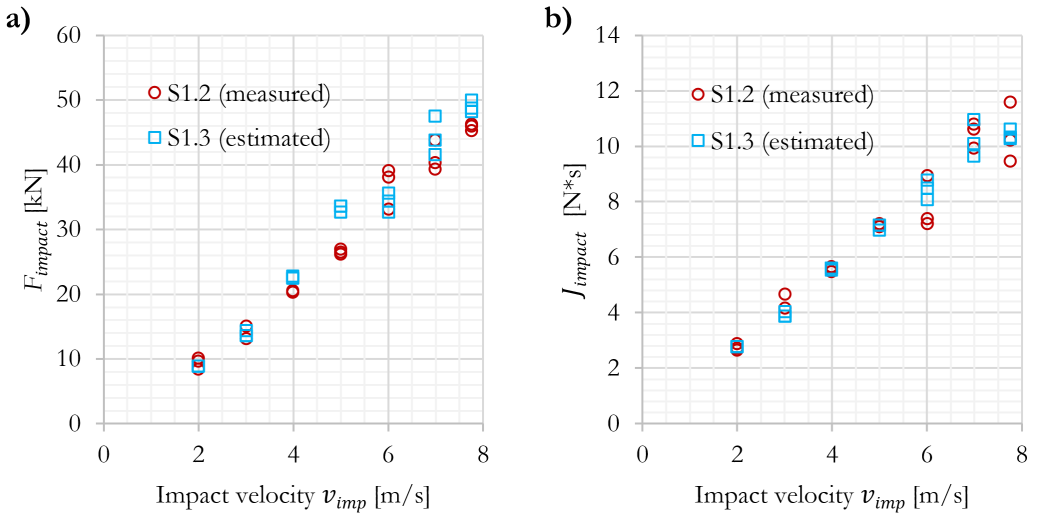

Figure 6-22: Comparison between S1.2 and S1.3 for (a) the estimated impact force (F_{impact}) calculated with Eq. (3-3), and (b) the estimated impact impulse (J_{impact}) calculated with Eq. (3-10).

6.3 Experimental outcomes of fragmentation

6.3.1 Impact survival probabilities

A drop test can have three possible outcomes: the falling object (here a sphere) can remain intact (case referred to as survival without damage), sustain some damage (referred to as damage, Figure 6-23a) or break into fragments (referred to as fragmentation, Figure 6-23b). For all drop tests, the impact survival probability (SP) was computed from the total number of drop tests (N) and the number of tests resulting in fragmentation (N_f) as:

$$SP = \frac{N - N_f}{N} \tag{6-2}$$

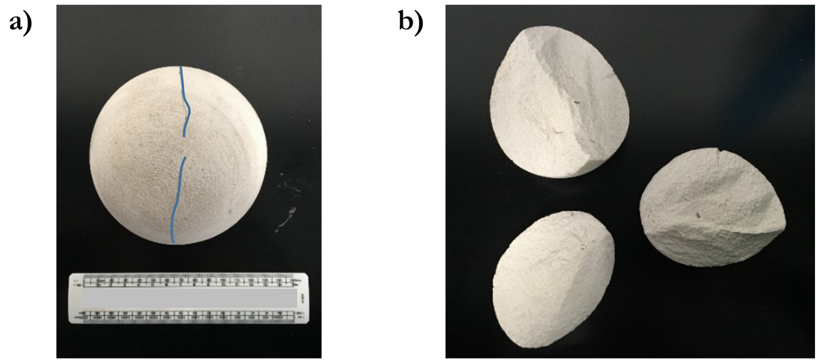

Figure 6-23: (a) Sphere with damage (fracture) indicated with a blue line on the sphere without fragmentation; (b) typical fragmentation of the sphere into 3 fragments.

Before investigating the impact survival probability of mortar spheres, it is important to ascertain the number of tests required to obtain a reliable estimate of survival probability. Figure 6-24 shows how, for a given diameter and impact velocity, the impact survival probability evolves with the number of tests. Starting from either 0% or 100%, it took about 10 tests (for the 50 and 100 mm spheres) for the survival probability to reach a point where it fluctuates around a stable value: for the data shown, about 50% for the 100 mm spheres and about 35% for the 50 mm spheres. For the 75 mm, it took more drops to reach a suitably stable value of about 50%. Based on these results, it was decided to conduct 16 drops, per drop height, in order to obtain a reliable value of survival probability, regardless of the sphere diameter.

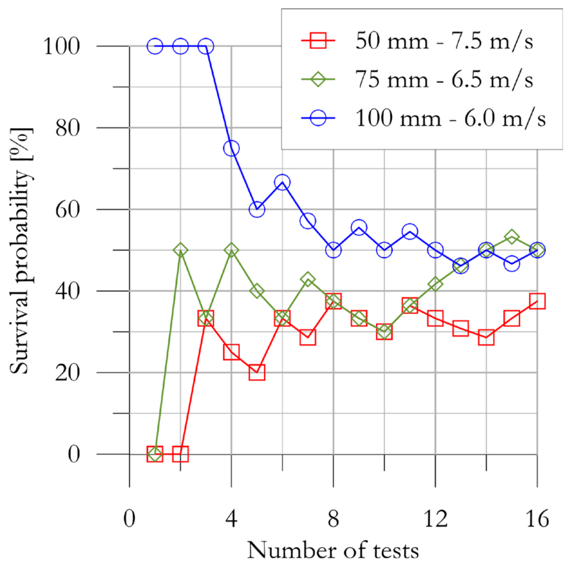

Figure 6-24: Evolution of impact survival probability as a function of the number of drop tests performed. For each sphere diameter (50, 75 and 100 mm for M2), 16 drop tests were performed, at the impact velocity indicated in the legend.

Although 16 drop tests can be considered satisfactory from a practical testing point of view, it is a relatively small number of tests from a statistical point of view. Consequently, when fitting the experimental survival probability data with a Weibull distribution, the procedure described in Fischer-Cripps (2007) was followed, in order to account for the relatively small number of tests. In this procedure, a correction factor of 0.5 is used to compute the probability of failure, and the survival probability is then taken as one minus the probability of failure:

$$SP_{fit} = 1 - \frac{(N_f - 0.5)}{N} \tag{6-3}$$

By applying such a correction when fitting the experimental data, the effect of a small and finite number of tests is accounted for.

Figure 6-25 presents the experimental impact survival probability data for mortar M2 (Figure 6-25a and b) and for mortar M3 (Figure 6-25c and d). For both materials, the survival probability is expressed in terms of kinetic energy and impact velocity. It can be observed that, although it is possible to fit the data with a Weibull distribution (parameters provided in Table 6-5, for all distributions), it seems that a linear trend offers a better goodness of fit. In particular, there is a clear divergence between experimental data and the Weibull function, at 0% and 100% survival probability. Also, it can be observed that the diameter of the sphere affects the position of the survival probability, both in terms of kinetic energy and impact velocity (see Figure 6-25a and b): the larger the sphere, the higher the critical kinetic energy and the lower the critical impact velocity.

Also, it appears that the larger the sphere, the flatter the central part of the survival probability, which is visible in Figure 6-25 and in Table 6-5 from the μ_E and μ_v values. Note that the size effect on the μ values is not fully understood and cannot be captured via the size conversion factor presented in Section 4.3. Consequently, different μ_E and μ_v values are used for different sphere diameters, where possible. It is interesting to note, from Table 6-5, that across the experimental data, $\mu_v \sim 2 \cdot \mu_E$. The factor of 2 derives from Eq. (4-1) and the fact that, for a given diameter, the kinetic energy is proportional to the square of the velocity.

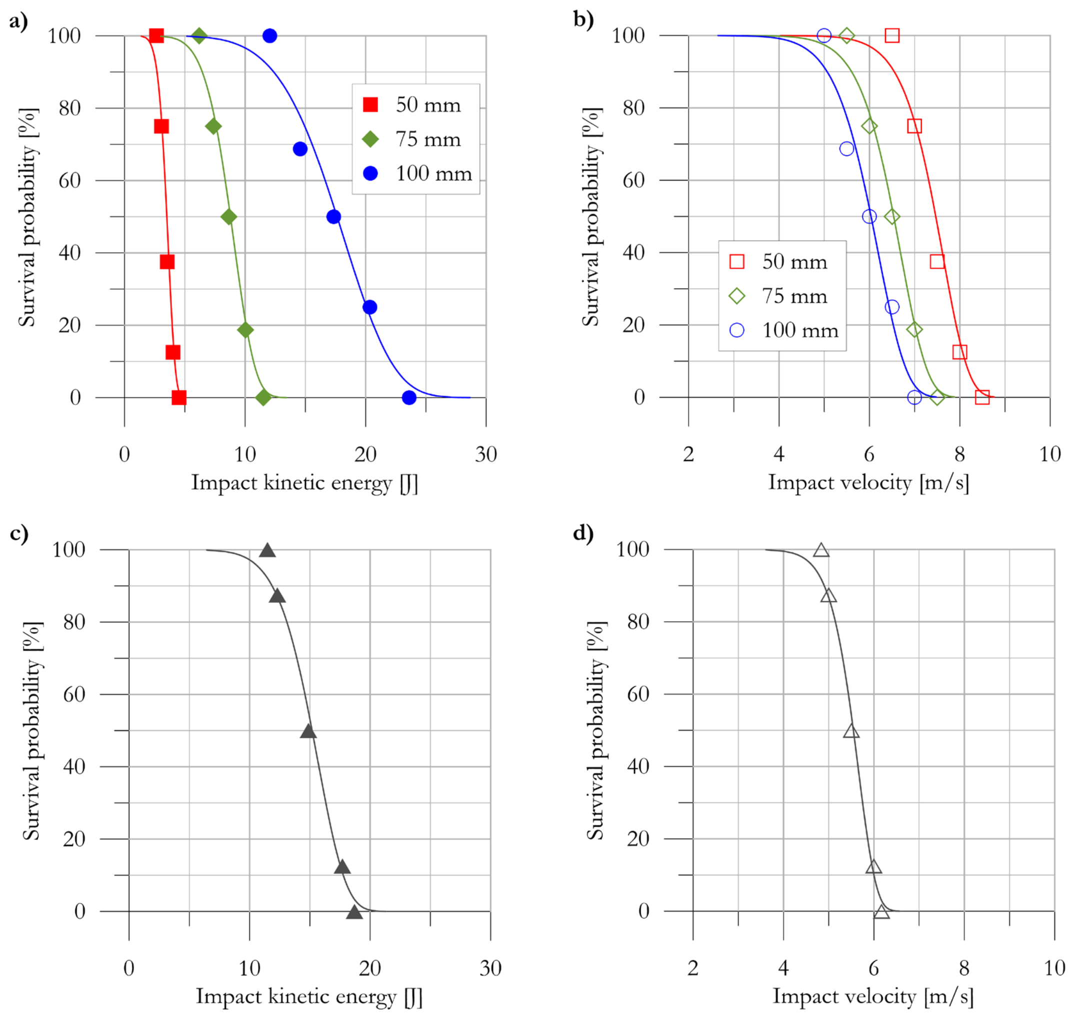

Figure 6-25: Experimental impact survival probability of mortar spheres for M2 (diameter of 50, 75 and 100 mm) (a and b) and M3 (diameter 100mm) (c and d). Symbols represent the experimental data, while continuous lines represent the Weibull best fit (as per Eq. (4-1)). Each data point corresponds to 16 drop tests.

Table 6-5 Parameters of the Weibull distribution fitting the experimental survival probabilities. The critical kinetic energy and critical velocity are the scale parameters while μ_E and μ_v are the shape parameters.

Sphere diameter (material)		50 mm (M2)	75 mm (M2)	100 mm (M2)	100 mm (M3)
Kinetic Energy	$E_{k(D)}^{cr}$ [J]	3.68	9.28	18.79	15.93
	μ_E	7.05	6.09	5.32	7.64
Impact Velocity	$v_{imp(D)}^{cr}$ [m/s]	7.66	6.74	6.24	5.68
	μ_v	14.36	12.25	10.74	15.24

6.3.2 *Fragment size distribution*

In this section, the evolution of the number of fragments as a function of impact velocities is first discussed, with particular focus on the range of velocity corresponding to an impact survival probability between 100% and 0% (series S2.1, S2.2, S2.3, S2.4). Then, the cumulative number of fragments is presented as a function of fragment mass, for the series of drop tests at "high velocities" (from 7.8 to 21 m/s, S4).

Figure 6-26 presents the average number of large and small fragments for mortars M2 (Figure 6-26a, b and c) and M3 (Figure 6-26d) with the corresponding experimental impact survival probability. For each velocity, 16 tests were conducted. Large and small fragments were arbitrarily defined as those having a mass larger and smaller than 5% of the initial sphere mass, respectively. For completeness of data and despite the fact they are insignificant as a hazard, fragments as small as 0.1 g in mass were accounted for. The error bars in Figure 6-26 represents the minimum and the maximum number of fragments (large or small) observed at each velocity. Figure 6-26 shows similar trends for all series, regardless of size and strength of spheres: the average number of fragments goes from two, for high impact survival probability (i.e. when the fragmentation of the sphere can be observed only for a small number of tests), to a maximum of five for survival probability of 0% (i.e. all the spheres will break at that impact velocity). Figure 6-26 also shows that the number of small fragments in the range of velocity considered is very low.

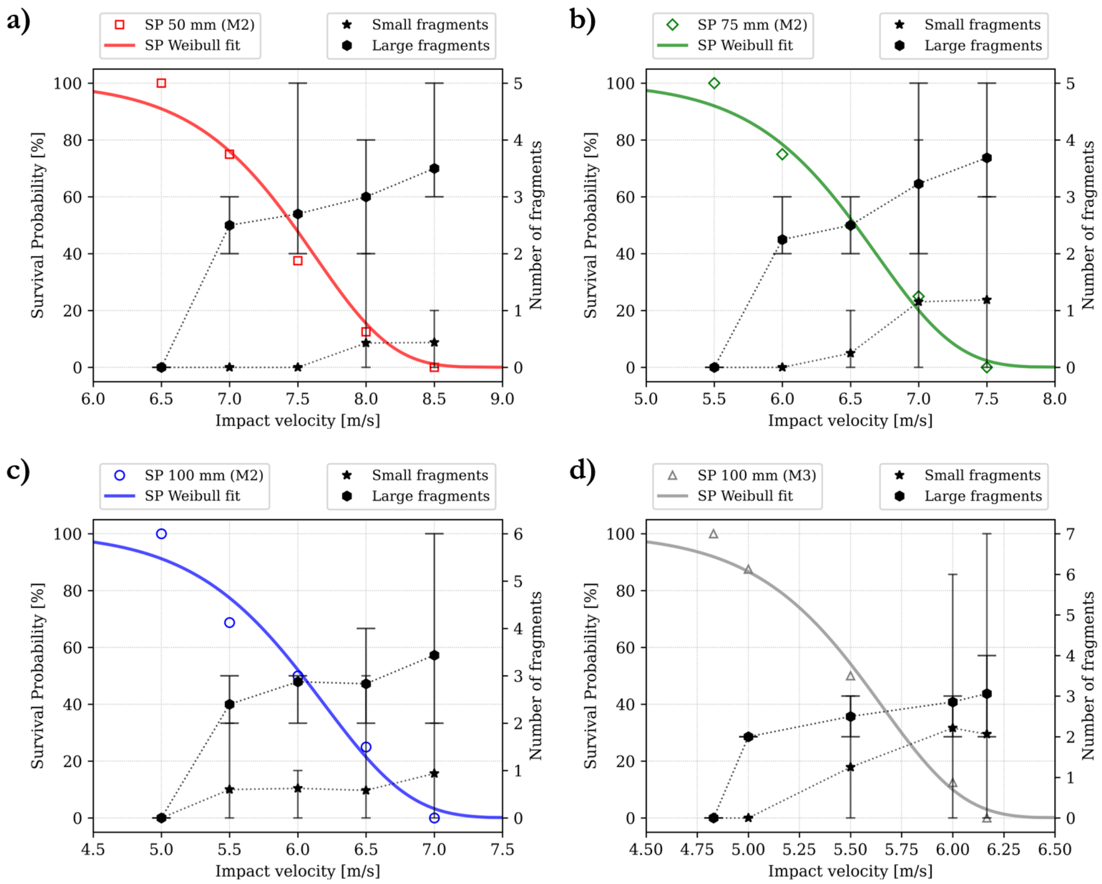

Figure 6-26: Average number of large (mass > 5% of initial mass) and small (mass < 5% of initial mass) fragments as a function of impact velocity for M2 spheres (diameter of 50, 75 and 100 mm) (a, b and c) and M3 spheres (diameter 100bmm) (d). The error bars on the number of fragments represent the minimum and maximum value recorded at that specific impact velocity. The experimental survival data and survival probability functions (Weibull) are also plotted.

A similar trend can be seen for mortar M1 (Figure 6-27a) in the range of impact velocity corresponding to 0%-100% of survival probability. Interestingly, it can be seen that increasing the impact velocity further results in an average number of small fragments exceeding the average number of large fragments. This change in trend is possibly the reflection of a change in breakage mechanism with more crushing and localised damage creating small fragments, as the impact velocity increases. This phenomenon was further investigated using Series S4 of mortar M1 (Figure 6-27b and Figure 6-29).

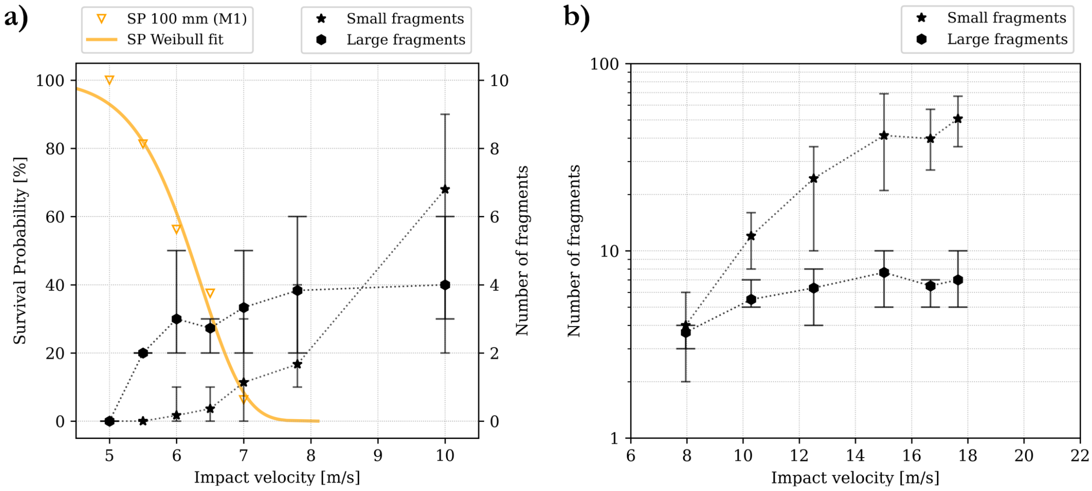

Figure 6-27: Average number of large (mass > 5% of initial mass) and small (mass < 5% of initial mass) fragments as a function of impact velocity for 100 mm spheres for M1, for (a) series S3.2 with low impact velocities, and (b) series S4 with higher impact velocities. The error bars on the number of fragments represent the minimum and maximum value recorded at that specific impact velocity. The experimental survival data and survival probability functions (Weibull) are also plotted. Note that, for series S3.2, 16 tests were performed at each velocity between 5 m/s and 7 m/s and 4 tests for impact velocity equal to 7.8 m/s and 10 m/s. For series S4 only, tests were grouped according to the measured impact velocity (see Table 6-6).

Figure 6-27b and Figure 6-29 report the results of drop tests conducted at "high velocity" (S4, see Section 5.3) and focusing on fragment size distribution. Note these tests of spheres of 100 mm diameter (using mortar M1) were conducted using the secondary setup. Due to the different dropping device (see Figure 3-16), the impact velocity of these tests was less controlled than it was for the other series conducted in the fragmentation cell (see Figure 6-28). In addition, Figure 6-28 shows that the terminal velocity of spheres delivered through the pipe was approached. For this reason, tests with similar impact velocity measured were grouped as per Table 6-6.

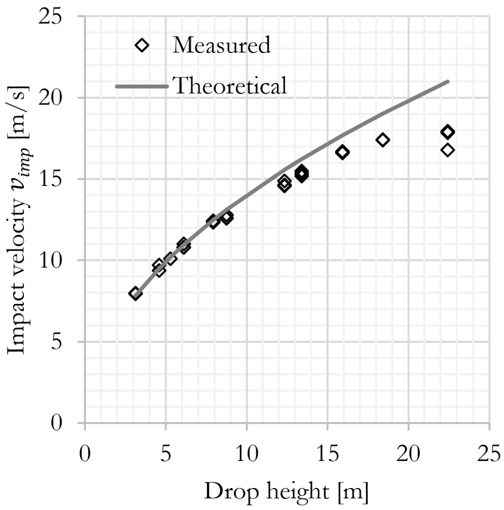

Figure 6-28: Difference between theoretical and measured impact velocity as function of the drop height for series S4.

Table 6-6 Number of tests from a given height and corresponding average impact velocity for series S4.

Average impact velocity (measured) [m/s]	# of tests
8.8	3
10.3	6
12.5	6
15.0	6
16.7	4
17.6	4

Figure 6-27b shows that, for values of impact velocity larger than that corresponding to 0% survival probability (i.e. 7.8 m/s), the average number of small fragments is larger than the average number of large fragments and that the number of small fragments increases with the impact velocity, up to 15m/s. Then, between 15 m/s and 17.6 m/s, the number of large and small fragments both seem to reach a plateau. This observation could suggest that the same fragmentation mechanism prevails in that range, leading to similar numbers of small and large fragments. However, further analysis of the drop test results, presented hereafter, will show that it is not the case.

Results of drop tests were then plotted in terms of mass distribution rather than fragment numbers (Figure 6-29) for all drop tests, under impact velocities ranging from 8 m/s and 17.6 m/s.

Figure 6-29a shows that the fragment size distributions (FSD) under 8 m/s and 17.6m/s are very different and that progressively increasing the impact velocity leads to a progressive change in the shape of the distribution. The FSD under 8 m/s contains three parts: a steep increase of large fragments (mass > 100 g), a relatively flat central part (0.5 g < mass < 100 g) and a steep part showing an accumulation of very small fragments (mass < 0.5 g). Such a distribution reflects the presence of 4 to 5 large fragments (mass > 100 g), 1 medium size fragment (mass around 10 g) and some very small fragments. On the other end, the FSD under 17.6 m/s is more well graded with 3 large fragments (mass > 100g) and many fragments in the mass range from 1 to 100 g, leading to a continuous increase of cumulative number of fragments.

Unlike in Figure 6-26b, it is here possible to see a difference between tests conducted at 15 m/s and those at 17.6 m/s: the increase of velocity leads to a steepening of the central part of the FSD (masses below 100 g), and upward shift of the curve due to the fact that the largest fragments (mass > 100 g) produced under 17.6m/s tend to be of similar size (resulting in a steep start of the FSD) as opposed to three fragments of different sizes (resulting in a flatter start of the FSD).

Interestingly, the FSD obtained here are not linear in a logarithmic scale, which accords with in situ observations by Corominas and co-workers (Ruiz-Carulla et al. 2015) but contradicts the idea of a scale invariant fractal distribution of fragments (Ruiz-Carulla et al. 2017). Ruiz-Carulla and Corominas (2020) updated the fractal fragmentation model using the formulation proposed by Perfect (1997) for scale variant fragmentation, which would result in a better fit of our experimental data.

To summarise, mortar spheres were found to fragment into less than five large and a few small fragments for impact velocities corresponding to a 100%-0% range of survival probability, while for higher values of impact velocities, increasing fragment numbers are produced and the size of the largest fragments progressively decreases with increasing velocity.

a)

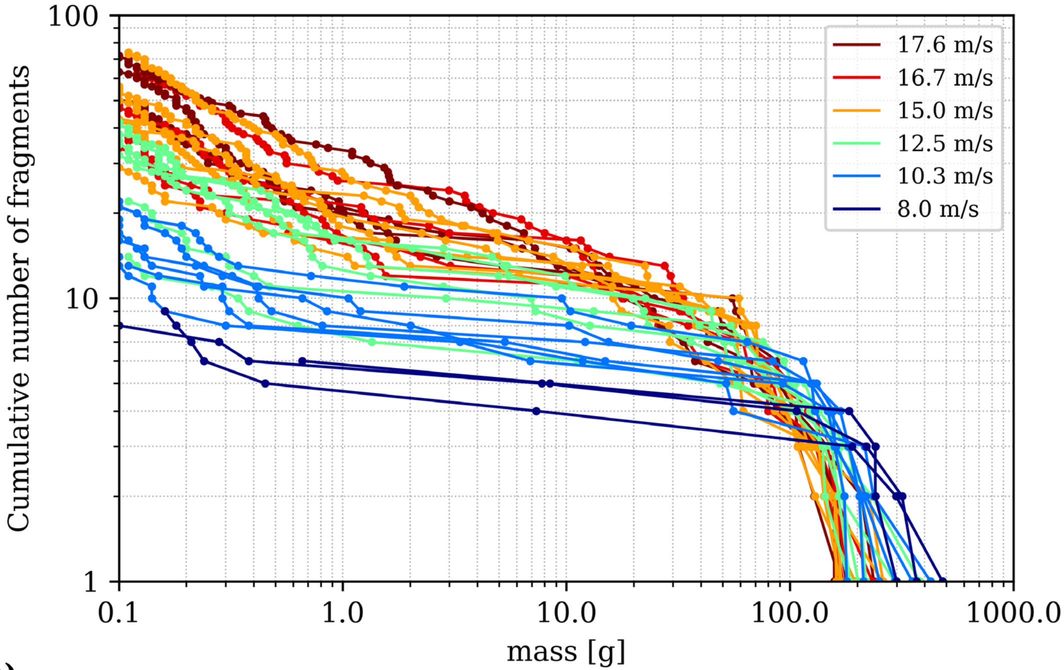

b)

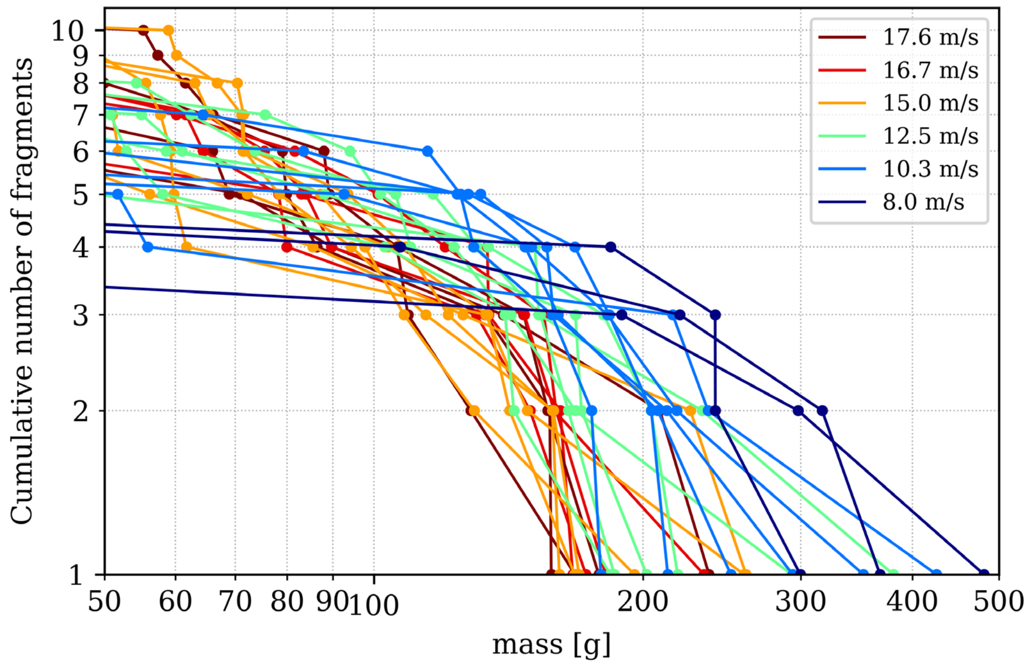

Figure 6-29: Cumulative number of fragments as function of the fragment mass for series S4 (mortar M1): (a) all data and (b) close up of Figure 6-28a for fragment masses in excess of 50 g.

6.4 Prediction of survival probability

As discussed in Section 4.1, the Weibull impact survival probability is described by the predicted shape parameter (μ_E or μ_v) and the calculated scale parameter (i.e. critical kinetic energy $E_{k(D)}^{cr}$ or critical impact velocity $v_{imp(D)}^{cr}$).

6.4.1 Experimental and predicted values of values of conversion factors

The experimental data collected during this study allowed the determination of experimental conversion factors and predicted conversion factors, derived in Sections 4.2, 4.3 and 4.4. Comparing the experimental and predicted values constitutes a first step towards the validation of the novel model to predict the survival probability of the mortar spheres upon dynamic impact.

To determine C_{Size}, the critical work required to fail the spheres under compression was measured and plotted as a function of sphere diameter. The data was then fitted with a power law, the exponent of which was compared to the exponent of the proposed size conversion factor, (see Eq. (4-20) and Figure 6-30): $3 - 5/\mu_{BT-F}$. The factor μ_{BT-F} is obtained by fitting a Weibull curve to the distribution force at failure for all Brazilian tests on discs of a given mortar. The conversion factor C_{rate} was determined using experimental values of C_{Rate-F} and $C_{Rate-\delta}$:

- C_{Rate-F} was obtained, for each sphere diameter, by dividing the critical impact force for all drop tests by the critical force at failure for all sphere compression tests. Note: the critical force is the value corresponding to 37% probability when expressing the results of a test in terms of survival distribution, as per Eq. (*4-1*).
- $C_{Rate-\delta}$ was calculated, for each sphere diameter, by dividing the critical dynamic reduction in diameter of the spheres (back-calculated from the impact mark left on the aluminium foil on the impact surface, see Section 3.1.2) by the measured critical reduction in diameter at failure for spheres under compression.

Finally, C_{Shape} was back-calculated for each sphere diameter, from the experimental values of the size conversion factor (C_{Size}), of the critical work required to fail the 54 mm disc ($W_{BT(d)}^{cr}$) under indirect tension (Brazilian test) and of the critical work required to fail spheres of diameter *D* in compression ($W_{SC(D)}^{cr}$), owing to the following relationship:

$$W_{SC(D)}^{cr} = C_{shape} \cdot C_{size} \cdot W_{BT(d)}^{cr} \tag{6-4}$$

Equations (4-14), (4-20) and (4-28) provide the formulation of the different conversion factors required to predict the critical value of kinetic energy for the drop tests. The inputs used to calculate these factors are given in Table 6-7. Note the following details regarding the inputs:

- The Young's modulus of steel and Poisson's ratio of mortar, concrete and steel are presumptive values.
- For the mortar, a series of UCS tests were conducted and for each test the secant modulus (between the initiation of specimen loading and failure) was determined. An average value, computed from all UCS test results, was used as an input for Eq. (4-14) and Eq. (4-28).
- The Young's modulus of the system slab plus load cells was back-calculated from measurements upon impact, as detailed in Section 6.2.2.
- Given the variability of force required to fail the mortar discs during the Brazilian test, the critical value of $F_{BT(d)}^{cr}$ was used as an input in Eq. (4-14).

Figure 6-30 below shows the increase of critical work required to fail the mortar spheres in compression with increasing sphere diameter for M2. The data are fitted with a power law whose exponent (equal to 2.36), is the exponent of the experimental size conversion factor (as discussed before and utilised as per Eq. (4-20)).

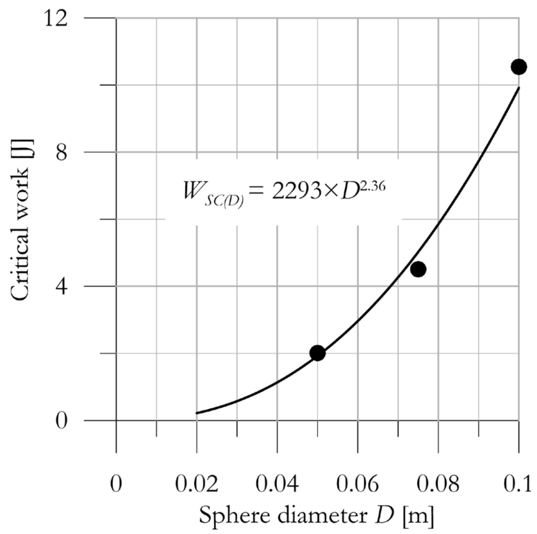

Figure 6-30: Evolution of critical work of sphere compression tests (M2) as function of their diameter. The continuous line is a power law fitting.

Table 6-7 Input parameters for the calculation of predicted and experimental conversion factors.

Parameter	M2				M3
	Brazilian tests	50 mm Sphere	75 mm Sphere	100 mm Sphere	Brazilian tests
$\boldsymbol{D}$ [mm]	54	50	75	100	54
$\boldsymbol{h}$ [mm]	27	n/a	n/a	n/a	27
m [kg]	0.116	0.125	0.409	0.964	0.118
$\boldsymbol{Y_m}$ [GPa]	4.40				4.57
$\boldsymbol{Y_c}$ [GPa]	11.70				
$\boldsymbol{Y_s}$ [GPa]	210				
$\boldsymbol{\nu_m}$	0.20				0.20
$\boldsymbol{\nu_c}$	0.15				
$\boldsymbol{\nu_s}$	0.29				
$\boldsymbol{F^{cr}_{BT(d)}}$ [N]	4849	n/a	n/a	n/a	4487
$\boldsymbol{F^{cr}_{SC(D)}}$ [N]*	n/a	5909	9132	15924	n/a
$\boldsymbol{F^{cr}_{DYN(D)}}$ [N]*	n/a	10274	17788	27900	n/a
$\boldsymbol{\delta^{cr}_{SC(D)}}$ [mm]*	n/a	0.80	1.16	1.49	n/a
$\boldsymbol{\delta^{cr}_{DYN(D)}}$ [mm]*	n/a	0.70	0.91	1.15	n/a
$\boldsymbol{W^{cr}_{BT(d)}}$ [J]	0.663	n/a	n/a	n/a	0.510
$\boldsymbol{W^{cr}_{SC(D)}}$ [J]*	n/a	2.01	4.51	10.54	n/a
$\boldsymbol{\alpha}$	0.8				0.8
$\boldsymbol{t_{BT}}$[s]	30	n/a	n/a	n/a	20
$\boldsymbol{t_{impact}}$ [ms]	n/a	0.24	0.38	0.52	0.51
$\boldsymbol{\mu_{BT-F}}$	8.90	n/a	n/a	n/a	10.25

*: experimental values used to compute the experimental conversion factors for M2 only.

Table 6-8 Predicted and experimental conversion factors with associated relative error.

Sphere diameter (Material)		50 mm (M2)	75 mm (M2)	100 mm (M2)	100 mm (M3)
$\boldsymbol{C_{Shape}}$	Predicted	4.16			4.70
	Experimental	3.64	3.13	3.70	n/a
	Relative error	*12.6%*	*24.8%*	*11.0%*	*n/a*
$\boldsymbol{C_{Size}}$	Predicted	0.83	2.23	4.49	4.28
	Experimental	0.83	2.18	4.30	n/a
	Relative error	*-0.5%*	*2.3%*	*4.3%*	*n/a*
$\boldsymbol{C_{Rate}}$	Predicted	1.54	1.48	1.43	1.39
	Experimental	1.51	1.54	1.35	n/a
	Relative error	*2.0%*	*-4.2%*	*6.5%*	*n/a*

6.4.2 *Prediction of Weibull scale parameters*

The critical work and critical force determined from the series of Brazilian tests are 0.663 J and 4,849 N for M2 and 0.520 J and 4,487 N for M3, respectively (see Table 6-7). Applying the predicted values of conversion factors (C_{Shape}, C_{Size}, C_{Rate}) of Table 6-8 to the critical work yields the values of critical kinetic energy and critical velocity reported in Table 6-9 and plotted in Figure 6-31.

Table 6-9 Predicted and experimental values of critical kinetic energy and critical impact velocity (Weibull scale parameters) with relative error.

Sphere diameter (Material)		50 mm (M2)	75 mm (M2)	100 mm (M2)	100 mm (M3)
$E_{k(D)}^{cr}$ [J]	Predicted	3.52	9.06	17.75	14.26
	Experimental	3.68	9.28	18.79	15.93
	Relative error	*-4.4%*	*-2.4%*	*-5.5%*	*-10.5%*
$v_{imp(D)}^{cr}$ [m/s]	Predicted	7.49	6.65	6.07	5.38
	Experimental	7.66	6.74	6.24	5.68
	Relative error	*-2.2%*	*-1.2%*	*-2.8%*	*-5.2%*

The error between the measured and predicted critical kinetic energy ranges from about -2.4% to -11% while the error between the measured and predicted critical impact velocity is less than -5.2%. Note that Table 6-9 reports the error between the predicted Weibull parameters against the parameters of the Weibull distribution that has been fitted against the experimental data. It is not a direct comparison with the experimental data, which will be presented later (see Section 6.4.4).

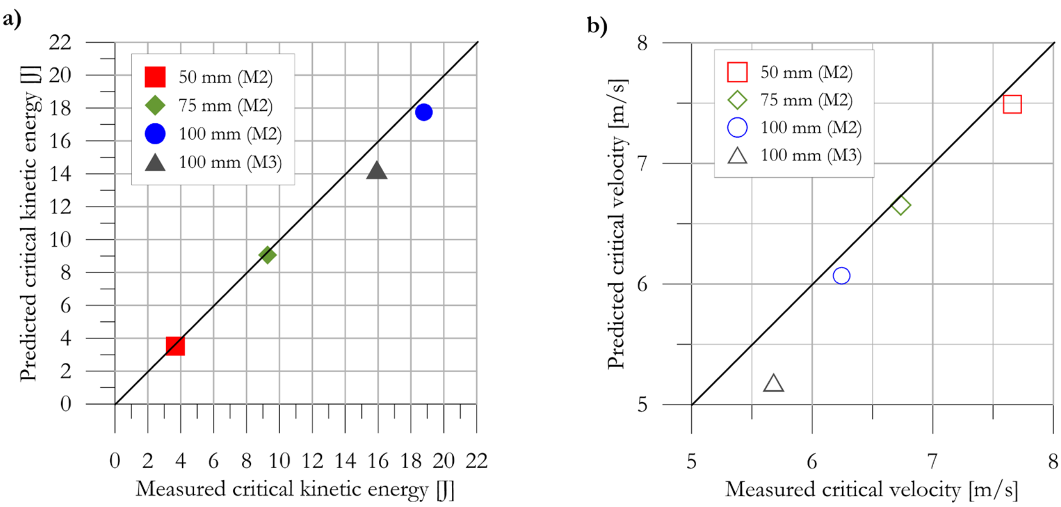

Figure 6-31: Comparison of predicted and measured critical kinetic energy (a) and critical velocity (b) for the three sphere diameters, for both M2 and M3 mortars.

6.4.3 *Prediction of Weibull shape parameters*

There are many strength characterisation tests (refer to Table 6-2) in which samples are tested to failure, and which might serve as a proxy for the impact strength of a sphere. This presents a dilemma of which test to adopt to give the Weibull shape parameter for the impact survival probability. To be consistent with an impact survival probability expressed in kinetic energy and the shape of the falling object, it is first proposed to use the Weibull shape parameter of the distribution of the critical work required to fail the mortar spheres in quasi-static compression:

$$\mu_E = \mu_{SC-W} \tag{6-5}$$

As discussed in Section 6.3.1, for a given sphere diameter, kinetic energy is proportional to the square of impact velocity, which for a Weibull distribution translates into $\mu_v = 2 \cdot \mu_E$. So, considering Eq. (6-5), we get:

$$\mu_v = 2 \cdot \mu_{SC-W} \tag{6-6}$$

Given Eq. (6-5) and Eq. (6-6) and the Weibull shape parameters of Table 6-2, the μ_E and μ_v values of Table 6-10 were used for the prediction of impact survival probability.

Table 6-10 Values of Weibull shape parameter for the prediction of impact survival probability of mortar spheres (M2).

Sphere diameter	50 mm	75 mm	100 mm
μ_E	6.2	5.2	4.5
μ_v	12.4	10.4	9

Note that using Eq. (6.6) and (6.7) allows the size effect on the Weibull shape parameter as observed in Section 6.3.1 to be captured.

6.4.4 *Impact survival probability function and prediction accuracy*

Figure 6-32 shows the impact survival probability (in terms of kinetic energy in Figure 6-32a and impact velocity in Figure 6-32b) predicted from the Weibull formulation shape and scale parameters reported in Table 6-9 and Table 6-10. The experimental data are also reported in Figure 6-32 for comparison. The predicted curves fall very close to the experimental data and the size effect is adequately captured. This is consistent with the prediction of critical kinetic energy and impact velocity reported in Table 6-9 and confirms the excellent predictive ability of the novel model.

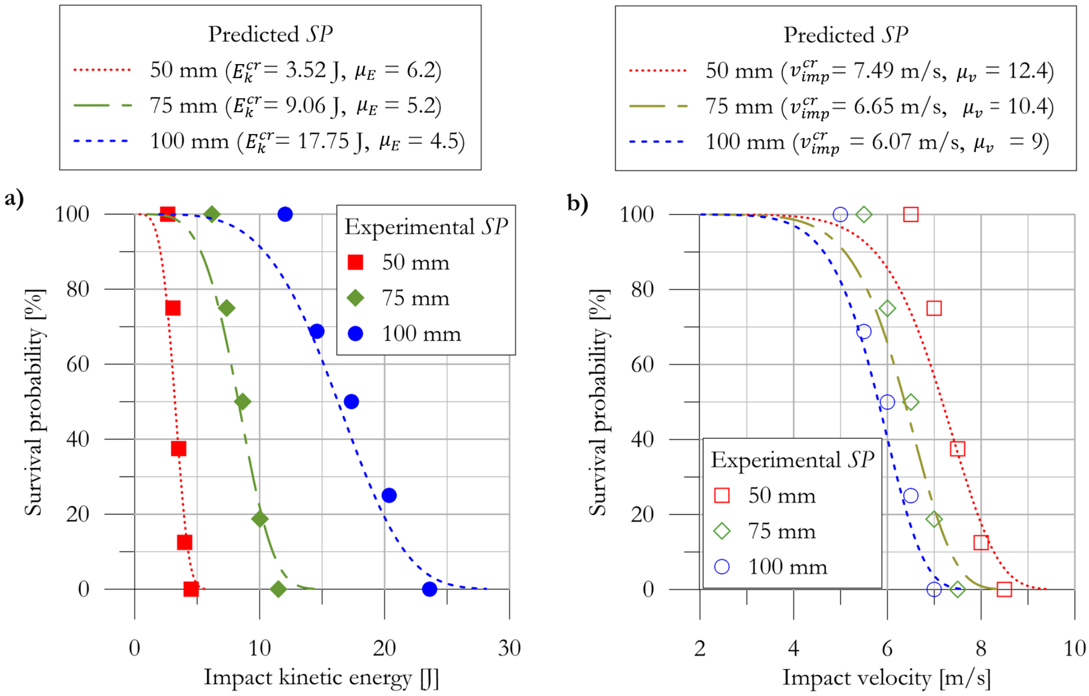

Figure 6-32: Experimental and predicted survival probability (SP) in terms of (a) kinetic energy and (b) velocity for mortar spheres subjected to dynamic impact (diameter of 50, 75 and 100 mm, mortar M2). A Weibull function is used to describe the survival probability. Prediction made using parameters of Table 6-9 and Table 6-10.

Figure 6-33 reports the error between the prediction and the actual experimental data (5 data points per survival probability). The relative error was estimated for the kinetic energy and for the impact velocity for given values of survival probability. As mentioned in Section 6.3.1, the error is relatively large at 0% and 100% survival probability, which is due to the difference in basic shape between the Weibull distribution and the experimental trend, which seems to be almost linear. Note that the suitability of a linear function will be considered in more detail in Section 6.4.5. For all other values of survival probability, the prediction is made with a relative error of less than 10%.

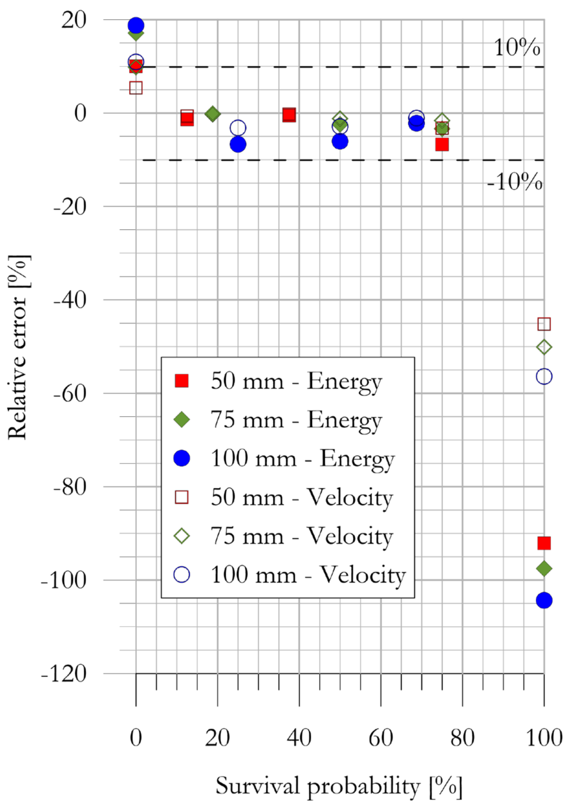

Figure 6-33: Evolution of relative error on predicted kinetic energy and impact velocity for given values of survival probability and for three sphere diameters (mortar M2). The error is computed relative to the experimental data.

6.4.5 *Evaluation of the outcomes of this model*

It is pertinent to discuss the accuracy of prediction using the model developed here in the context of rockfall engineering. As a preface to this, it is first acknowledged that the treatment of spheres has limited direct application and that the effects of block shape, discontinuities and impacted surface properties (among others) all need to be captured for the prediction of impact survival probability to be realistic, but this constitutes future research.

For the sake of the discussion, however, consideration will be limited to spherical falling rocks. The prediction method presented is a rigorous academic exercise that relies on extensive material characterisation testing, including a series of compression tests on spherical specimens having different diameters, to obtain a diameter specific shape parameter for the impact survival probability (μ_E and μ_V, see Table 6-10). Obtaining a very large number of identical spherical rock specimens to test in practice would be expensive, time consuming and impractical, if not impossible. For the approach described here to be applied in practice, it is essential to reduce the volume of testing required and obtain the statistical information from tests for which specimen preparation is not difficult and expensive, such as the Brazilian tests. In addition, for practical reasons, it is reasonable to consider that all specimens would be cored from blocks to have a standard diameter.

Consequently, it is appropriate here to assess the quality of survival predictions for spheres of any diameter when the shape parameter μ of the impact survival probability function (i.e. $\mu_E = \mu_{BT-W}$) is based solely on the statistical information from a series of Brazilian tests conducted on specimens of standard diameter (around 50 mm). Note that the corresponding value of $E^{cr}_{k(D)}$ is unchanged as it does not rely on any statistical information coming from the compression tests on spheres. The Weibull shape and scale parameters used for such practical prediction are given in Table 6-11.

Table 6-11 Weibull parameters used for prediction of impact survival probability of spheres having different diameter and using statistical information from Brazilian tests only.

Weibull Parameters of prediction	**Sphere diameter (material)**			
	50 mm (M2)	**75 mm (M2)**	**100 mm (M2)**	**100 mm (M3)**
$\boldsymbol{\mu_E}$	4.2			6.2
$\boldsymbol{E^{cr}_{k(D)}}$ **[J]**	3.52	9.06	17.75	14.26

Given that the Weibull shape parameter of Table 6-11 is lower than the Weibull shape parameters of the previous prediction from M2 (see Table 6-9, Figure 6-32 and Figure 6-33), which, in turn, are lower than the experimental shape parameters (Table 6-5), the relative error can be expected to increase. In order to obtain a better-quality prediction and be more consistent with the experimental observations, it is proposed to describe the impact survival probability as a linear function rather than a Weibull function. The linear function is still defined from the Weibull scale and shape parameters as (see derivations in Appendix A) as:

$$E^{b}_{k(D)} = E^{cr}_{k(D)}\left(1 - \frac{\left(SP\left(E^{b}_{k(D)}\right) - 37\right)\cdot e}{100\cdot \mu_E}\right) \tag{6-7}$$

Figure 6-34 shows the predicted impact survival probability based on a linear function and the relative error, with respect to the experimental data for both materials. Overall, a very good match is observed between the data and the prediction, which is made only from material properties derived from standard Brazilian tests. The maximum relative error is around 27% but for two thirds of the predicted points, the relative error is less than 12%. Most of the errors are negative, indicating that the model tends to slightly underestimate the kinetic energy associated to a given survival probability.

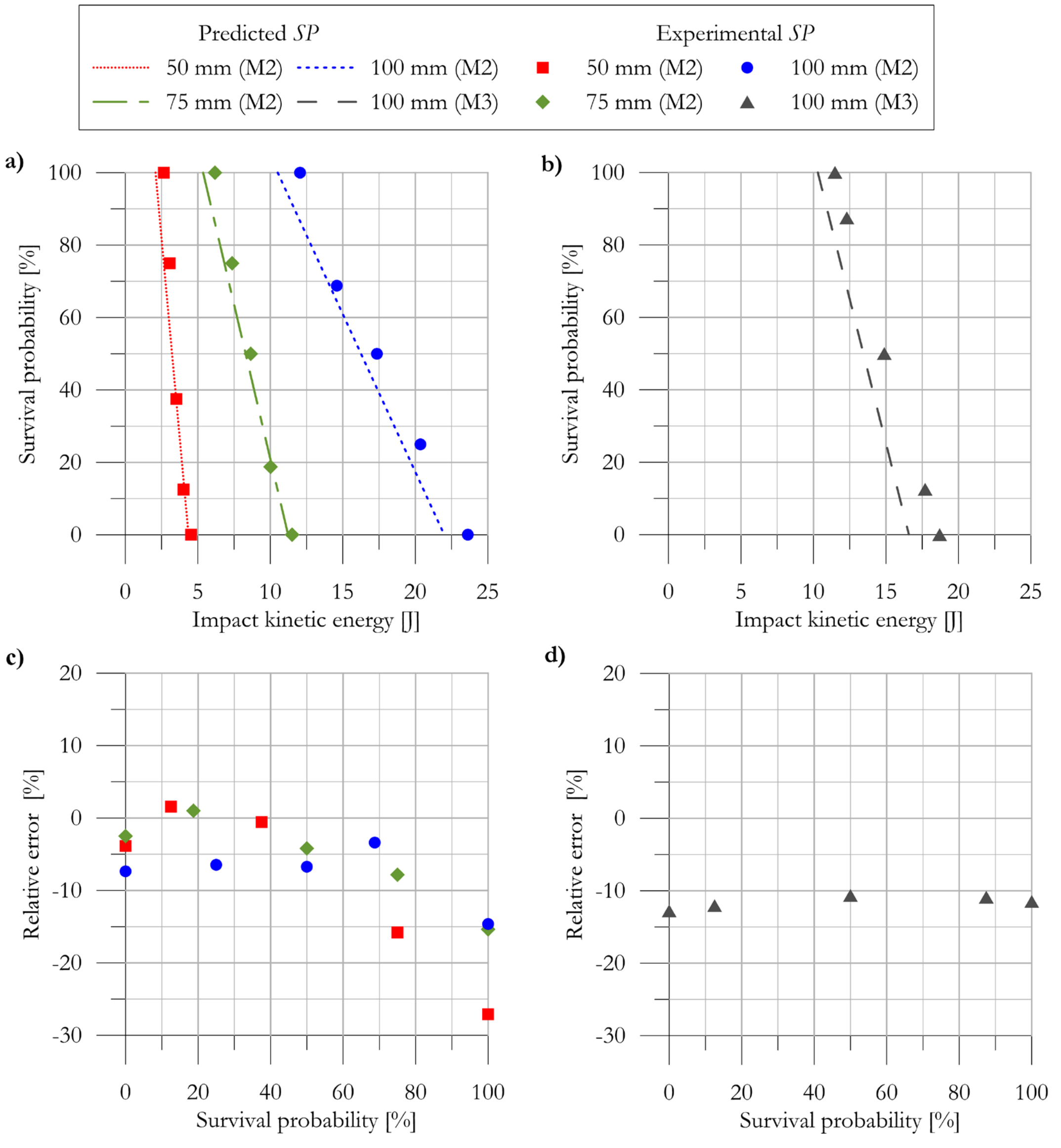

Figure 6-34: Experimental and predicted impact survival probability; (a) expressed in terms of kinetic energy for M2 (diameter of 50, 75 and 100 mm) and (b) for M3 (diameter 100 mm). Evolution of relative error on predicted kinetic energy for given values of survival probability for M2 (c) and M3 (d). All predictions were made using the parameters of Table 6-11.

6.5 Energy partition and tracking of fragments

As stated in the introduction of this thesis, many aspects of rockfall fragmentation are still poorly understood and, when it comes to the energy balance, the following questions still remain unanswered:

- Question 1: Is it possible to approximate the energy consumed in fragmentation as a surface energy per unit area multiplied by the total area of fragment surface (Eq. (3-17))? Although Eq. (3-17) provides the amount of energy to form a new fracture surface, in the context of rockfall, not all cracks produced during an impact lead to the creation of a fragment surface (some remain internal and are not visible) and hence cannot be accounted for. Also, the impacted materials can be subjected to some crushing in addition to cracking.
- Question 2: Is the ratio of amount of energy consumed in fragmentation over kinetic energy at impact constant?
- Question 3: Is there a clear relationship between energy of fragments post-impact and their mass?

In this section, the result of series S3.1 and S3.2 will be presented to provide elements of answer to these questions. As mentioned in Section 5.3, in Series S3.1 (impact velocity from 2.9 to 7.8 m/s), all energy components were estimated from the tracking and impact data with an emphasis on verifying that all significant dissipative components can be captured and that the energy balance can be computed reliably. Ten drop tests from series S1.3 representing three different outcomes (rebound without damage, rebound with damage and fragmentation) were analysed in detail and the results are presented in this section. In Series S3.2 (impact velocity from 5.5 to 10 m/s), all energy components were estimated from the tracking and impact data with an emphasis on the possible change in energy partition between various dissipation mechanisms with increasing impact energy. In this series, 22 tests with fragmentation were analysed.

6.5.1 Validation of the energy balance

The experimental setup presented in Chapter 3 was designed so that the most significant components of energy could be accurately computed, before and after impact. Ten drop tests of series S1.3 (mortar M1*) were first used to introduce and compute the different components of energy, one at a time. These tests correspond to:

- 4 cases of rebound without damage (tests referred to as S1.3-I1, S1.3-I2, S1.3-I3 and S1.3-I4, "I" standing for intact);
- 2 cases of rebound with damage (S1.3-D1 and S1.3-D2, "D" standing for damage) (see Figure 6-23a);
- 4 cases of fragmentation (S1.3-F1, S1.3-F2, S1.3-F3 and S1.3-F4, "F" standing for fragmentation) (see Figure 6-23b).

Note that damage refers to the creation of cracks within the mortar spheres without creation of fragments. Fragmentation is only observed when sufficient cracks extend or coalesce across the sphere.

For all drop tests, the total kinetic energy before impact (E_k^b) is the sum of total energy loss (ΔE_{tot}) plus the total kinetic energy after impact (E_k^a). In addition, because all spheres were dropped without rotation, the rotational energy component pre-impact is nil ($E_{kr}^b = 0$). For each test, the relevant energy dissipation mechanisms were identified and the energy losses were computed, as per Section 3.2.4. The results, expressed in Joules and in % of kinetic energy before impact, are reported in Table 6-12.

Analysis of tests without damage

Tests S1.3-I1, S1.3-I2, S1.3-I3 and S1.3-I4 were conducted at impact velocities of 2.91, 4.00, 4.98, and 6.00 m/s, respectively, and no fragmentation or damage was observed. The analysis of energy transformation components is as follows:

- ΔE_{slab} : the energy lost in displacing the slab only represents 0.2% of the total kinetic energy at impact and can be considered negligible.
- ΔE_d: between 67% and 77% of the kinetic energy at impact is dissipated by deformation of the sphere and the slab at the site of the impact.
- ΔE_{fr}: the fragmentation or damage energy component is nil.
- E_k^a: as a consequence of the increasing energy loss at impact, the translational kinetic energy after the impact decrease from 32% to 21% of the total kinetic energy at impact.

The sum of all energy components is very close to 100%.

Table 6-12: Result of energy balance computation for drop tests of series S1.3. Each energy component is expressed in absolute value (in J) and in relative value (percentage of the total kinetic energy before impact).

			TESTS									
		Unit	**S1.3 -I1**	**S1.3 -I2**	**S1.3 -I3**	**S1.3 -I4**	**S1.3 -D1**	**S1.3 -D2**	**S1.3 -F1**	**S1.3 -F2**	**S1.3 -F3**	**S1.3 -F4**
Impact velocity $\boldsymbol{v_{imp}}$		m/s	2.91	4.00	4.98	6.00	7.06	7.07	7.06	7.79	7.80	7.81
Energy component	$\boldsymbol{E_k^b}$ (1)	J	4.23	7.97	12.56	18.21	25.49	25.25	25.20	30.59	30.57	30.92
	$\boldsymbol{\Delta E_{slab}}$ (2)	J	0.01	0.02	0.03	0.04	0.05	0.06	0.05	0.06	0.05	0.05
		%	*0.2*	*0.2*	*0.2*	*0.2*	*0.2*	*0.2*	*0.2*	*0.2*	*0.2*	*0.2*
	$\boldsymbol{\Delta E_d}$ (3)	J	2.85	5.76	9.44	14.09	20.17	19.97	19.93	24.50	24.49	24.78
		%	*67.5*	*72.2*	*75.1*	*77.3*	*79.1*	*79.1*	*79.1*	*80.1*	*80.1*	*80.1*
	$\boldsymbol{\Delta E_{fr}}$ (4)	J	0.00	0.00	0.00	0.00	0.91	1.11	1.22	1.38	1.38	1.39
		%	*0.0*	*0.0*	*0.0*	*0.0*	*3.6*	*4.4*	*4.9*	*4.5*	*4.5*	*4.5*
	$\boldsymbol{\Delta E_{tot}}$ (5)	J	2.86	5.78	9.46	14.12	21.13	21.14	21.20	25.94	25.92	26.22
		%	*67.7*	*72.5*	*75.3*	*77.5*	*82.9*	*83.7*	*84.1*	*84.8*	*84.8*	*84.8*
	$\boldsymbol{E_{kt}^a}$ (6)	J	1.36	2.20	3.14	3.91	4.51	6.69	3.49	3.72	3.26	3.37
		%	*32.2*	*27.5*	*25.0*	*21.4*	*17.7*	*26.5*	*13.8*	*12.2*	*10.6*	*10.9*
	$\boldsymbol{E_{kr}^a}$ (7)	J	0.00	0.00	0.00	0.00	0.00	0.00	0.07	0.02	0.03	0.06
		%	*0.0*	*0.0*	*0.0*	*0.0*	*0.0*	*0.0*	*0.3*	*0.1*	*0.1*	*0.2*
	$\boldsymbol{E_k^a}$ (8)	J	1.36	2.20	3.14	3.91	4.51	6.69	3.56	3.74	3.28	3.43
		%	*32.2*	*27.5*	*25.0*	*21.4*	*17.7*	*26.5*	*14.1*	*12.2*	*10.7*	*11.1*
	$\boldsymbol{E_k^b - E_k^a}$	J	2.87	5.78	9.43	14.30	20.99	18.56	21.64	26.85	27.29	27.50
		%	*67.8*	*72.5*	*75.0*	*78.6*	*82.3*	*73.5*	*85.9*	*87.8*	*89.3*	*89.0*
	$\boldsymbol{E_{tot}}$ (9)	J	4.22	7.97	12.60	18.02	25.64	27.83	24.76	29.68	29.2	29.64
		%	*99.9*	*100.0*	*100.3*	*99.0*	*100.6*	*110.2*	*98.3*	*97.0*	*95.5*	*95.9*

Notes:

(1) Total kinetic energy before impact, measured from mass and impact velocity;
(2) Energy loss in displacement of the slab, estimated by Eq. (3-16);
(3) Energy loss by deformation of the sphere and the slab, estimated by Eq. (3-19);
(4) Energy loss to create the fracture surfaces, estimated by Eq; (3-17);
(5) Total energy loss associated with the impact: $\boldsymbol{\Delta E_{tot} = \Delta E_{slab} + \Delta E_d + \Delta E_{fr}}$;
(6) Total translational kinetic energy of all the fragments, estimated by Eq. (3-14);
(7) Total rotational kinetic energy of all the fragments, estimated by Eq. (3-15);
(8) Total kinetic energy after impact, estimated by Eq. (3-13);
(9) Total energy after impact: $\boldsymbol{E_{tot} = \Delta E_{tot} + E_k^a}$.

Analysis of tests with damage but no fragmentation

For the two damage tests, S1.3-D1 and S1.3-D2 (impact velocity of 7 m/s), the spheres presented visible damage (cracks) but did not produce fragments at the first impact (see Figure 6-23a). As such, energy was lost in displacement of the slab, deformation of the slab and the sphere and damage within the sphere. The analysis of energy transformation components is as follows:

- ΔE_{slab}: the energy dissipated by displacing the slab is again negligible (0.2% of total kinetic energy at impact).
- ΔE_{d}: about 79% of total kinetic energy at impact is dissipated by deformation of the sphere and the slab.
- ΔE_{fr}: for test S1.3-D2, the sphere broke at the second impact of the first drop (after the first rebound). Therefore, it was possible to scan a fracture area (see Figure 6-35c) that was initiated at the first impact. For test S1.3-D1, it was assumed that the fracture would split the sphere in two halves (as per test S1.3-D2 and other results reported in the literature, e.g. Asteriou et al. (2013a), Salman et al. (2004)). Table 6-12 shows that for test S1.3-D1 and S1.3-D2, about 3.6% and 4.4% of total kinetic energy at impact is consumed by damage, respectively.
- E_k^a: the two tests showed different translational kinetic energy after impact: 17.7% and 26.5% of the total kinetic energy at impact, for S1.3-D1 and S1.3-D2 respectively.

For S1.3-D1, the sum of all energy components adds up to 100.6%, which is considered acceptable, given a relative error estimated to be around ±5%. In contrast, a total of 110% is achieved for test S1.3-D2, which indicates quite a large error. Analysing in more detail the different energy components pertaining to test S1.3-D2 revealed that the translational kinetic energy after impact is much higher than that of test S1.3-D1: 26.5% against 17.7%. Such anomaly is also confirmed by the experimental value of $\overline{CoR_E}$ computed as square root of the ratio between the experimental total kinetic energy after and before impact (see Figure 6-36). The computation of energy balance relies on the prediction of CoR_d as a function of impact velocity as per Eq. (3-20) (represented by the grey line in Figure 6-36a). For some unexplained reason, sphere S1.3-D2 bounced more than predicted, resulting in less dissipation of energy and, hence, an overestimation of the energy balance (110% instead of 100%). This unexpected result only constitutes one case out of 21 drops over the two series and is considered an outliner.

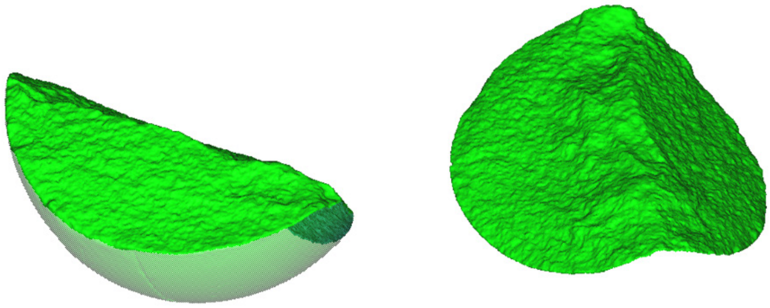

Figure 6-35: Example of a scanned fragment showing the fracture surface created by fragmentation.

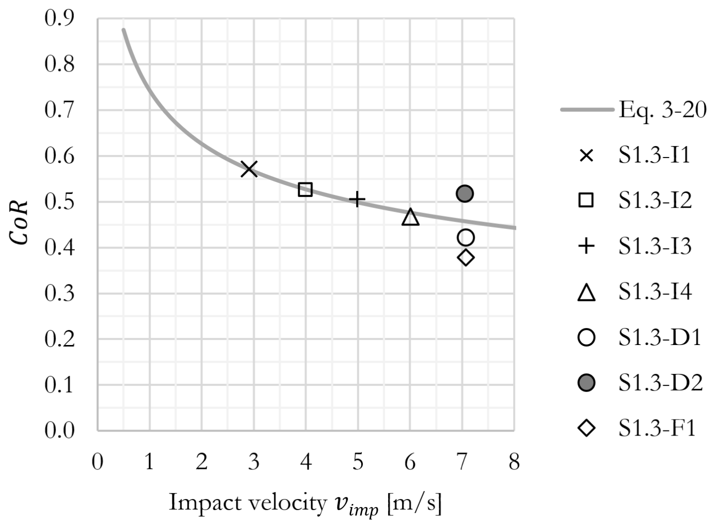

Figure 6-36: Coefficient of restitution $\overline{CoR_E}$ for tests S1.3-I1, S1.3-I2, S1.3-I3, S1.3-I4, S1.3-D1, S1.3-D2 and S1.3-F1.

Analysis of tests with fragmentation

The impact velocity for the fragmentation tests was 7m/s for test S1.3-F1 and 7.8m/s for tests S1.3-F2, S1.3-F3 and S1.3-F4. Sphere S1.3-F1 broke into 2 pieces, while the other 3 spheres fragmented into 3 pieces upon the first impact. S1.3-F1 and S1.3-F4 each had a fragment that further split in two pieces at the second impact with the slab, due to the presence of a fracture created at the first impact. Therefore, it was possible to scan the actual fracture areas initiated at the first impact for these two tests. All relevant fragment characteristics are reported in Table 6-13. For these tests, all three energy dissipation components (displacement, deformation, fragmentation) prevail. The analysis of energy transformation components is as follows:

- ΔE_{slab}: the energy dissipated by displacing the slab is negligible for all tests (0.2% of total kinetic energy at impact).
- ΔE_d: the energy lost in slab/sphere deformation accounts for around 80% of the total kinetic energy at impact (see in Table 6-12).
- ΔE_{fr}: between 4.5% and 4.9% of the total kinetic energy at impact is consumed in fragmentation. The slightly higher value of energy dissipated in fragmentation for test S1.3-F1 is related to a slightly higher fracture area (see in Table 6-12). Indeed, the energy dissipated in fragmentation is directly proportional to the fracture area (see Eq. (3-17)).
- E_k^a: the translational kinetic energy after impact is around 14% to 11% of the total kinetic energy at impact. A small amount of rotational kinetic energy was computed for the fragments post impact. For a drop test of a sphere without initial rotation, less than 1% of the total kinetic energy at impact is transferred into rotation of fragments.

The sum of all energy dissipation components and residual kinetic energy was found to represent 95.5% to 98.2% of the total kinetic energy at impact, which is considered acceptable, given a relative error estimated around ±5%.

Results in Table 6-12 also show that overall, as the impact energy (E_k^b) increases, more energy is dissipated at impact (ΔE_{tot}), which is associated to an increasing development of cracks up to the creation of fragments.

The energy balance of in Table 6-12 was further processed to compare the energy lost at impact defined as the difference of kinetic energy before and after impact ($E_k^b - E_k^a$) and the energy lost at impact defined as the sum of all dissipative energy components (i.e., total energy loss ΔE_{tot}). The comparison is presented in Figure 6-37 with an estimate of experimental error (assessed as ± 5%). All data points plot on or very close to the 1:1 line, which suggests that all relevant dissipative components have been captured and that the energy balance has been computed properly. The two main dissipative components of the impact pertain to the deformation of the sphere and slab upon impact and the creation of cracks, leading to fragmentation.

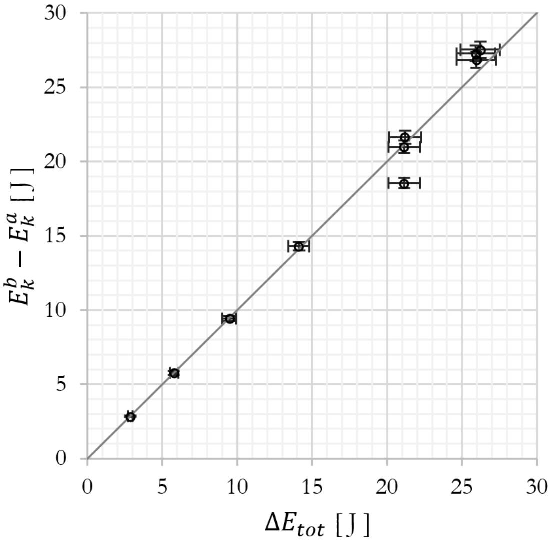

Figure 6-37: Difference between kinetic energy before and after impact vs the sum of all the energy loss. The error bars indicate the maximum experimental error (about 5% in ΔE_{tot} and 2% in the difference of the kinetic energies).

So to answer Question 1, on the basis of Figure 6-37, it is possible to estimate the energy consumed in fragmentation as the surface energy per unit area multiplied by the total area of fragment surface (Eq. (3-17)).

Table 6-13 Fragment characteristics for tests S1.3-F1, S1.3-F2, S1.3-F3 and S1.3-F4.

		Mass [g]	Volume [cm^3]	Fracture area [m^2]	v_{xy} [m/s]	v_z [m/s]	v [m/s]	E_{kt}^{a} [J]	I_I [kg*m^2]	I_{II} [kg*m^2]	I_{III} [kg*m^2]	ω_I [rad/s]	ω_{II} [rad/s]	ω_{III} [rad/s]	E_{kr}^{a} [J]
S1.3-F1	Frag 1	283.1	146.51	7.61E-03	0.31	2.70	2.72	1.05	1.10E-04	1.54E-04	2.16E-04	11.109	6.207	4.456	0.01
	Frag 2*	642.9	332.72	1.35E-02	0.37	2.73	2.75	2.44	5.55E-04	6.05E-04	7.72E-04	3.961	2.131	12.143	0.06
S1.3-F2	Frag 1	267.0	138.18	7.73E-03	0.37	2.67	2.69	0.97	9.36E-05	1.47E-04	1.92E-04	3.727	5..006	2.772	0.00
	Frag 2	525.9	272.17	9.29E-03	0.22	2.72	2.73	1.96	3.04E-04	3.86E-04	4.97E-04	4.964	5.470	4.828	0.02
	Frag 3	214.2	110.85	6.84E-03	0.42	2.57	2.61	0.83	6.40E-05	1.04E-04	1.39E-04	5.386	1.522	1.094	0.00
S1.3-F3	Frag 1	222.1	114.94	6.89E-03	0.96	2.47	2.65	0.78	6.55E-05	1.17E-04	1.48E-04	5.246	8.858	4.636	0.01
	Frag 2	536.2	277.50	9.72E-03	0.71	2.46	2.56	1.75	3.31E-04	4.45E-04	4.99E-04	4.328	1.609	3.246	0.01
	Frag 3	245.7	127.16	7.12E-03	0.94	2.42	2.60	0.73	8.30E-05	1.38E-04	1.84E-04	11.912	7.196	5.843	0.01
S1.3-F4	Frag 1	104.9	54.29	4.79E-03	0.57	2.41	2.47	0.32	1.75E-05	3.57E-05	4.57E-05	7.712	11.162	6.591	0.00
	Frag 2	576.7	298.46	8.92E-03	0.43	2.54	2.57	1.91	1956.21	2192.34	3051.39	7.101	9.751	8.122	0.05
	Frag 3*	330.4	170.99	1.02E-02	0.33	2.60	2.62	1.14	1.24E-04	2.10E-04	2.51E-04	2.829	6.310	3.864	0.01

Notes:

* Fragment split at second impact. Geometric information and velocities in table are referred to the fragment at first impact (before splitting). The fracture area is the sum of the fracture areas of the fragments after splitting.

6.5.2 *Energy partition during impact*

In this section, results of test series S3.2 are presented. 22 spheres of mortar M1 were dropped from six different drop heights and the components of kinetic energy and energy dissipation were computed. All results are reported in Table 6-14 with tests sorted in increasing values of impact velocity (from 5.3 m/s to 9.9m/s) and all fragment characteristics required to compute the energy components are listed in Table B-1 in Appendix B. Note that only fragments with significant motion ($v_{imp} > 1$ m/s) were analysed.

The results of Table 6-14 show that the total amount of energy lost at impact slightly increases with increasing impact velocity, from about 83% at 5.3m/s to about 88% at 9.9m/s.

It is also clear that the proportion of total kinetic energy after impact decreases with increasing impact velocity: from about 18% at 5.3m/s to about 9% at 9.9m/s. Less than 1% of the total kinetic energy at impact is transferred into rotation of fragments, which is largely due to the fact that the spheres impacted without initial rotation.

As for series S1.3, the energy associated to the different energy transformation mechanisms was estimated and the following was observed:

- ΔE_{slab}: the energy dissipated by displacing the slab is negligible for all tests (0.2% of total kinetic energy at impact), consistent with results of Section 6.5.1.
- ΔE_{d}: the energy lost in slab/sphere deformation accounts for around 80% to 85% of the total kinetic energy at impact (see in Table 6-14).
- ΔE_{fr}: about 3% of the total kinetic energy at impact is consumed in fragmentation (see in Table 6-14), which is slightly less than for series S1.3 (Section 6.5.1).
- E_k^a: the translational kinetic energy after impact is between 20% and 7% of the total kinetic energy at impact (see in Table 6-14).

Figure 6-38 shows values of energy normalised by the initial kinetic energy as a function of impact velocity (Figure 6-38a) and kinetic energy before impact (Figure 6-38b). It is relevant to remember that the range of impact velocity of 5.3 to 9.9 m/s covers the range of 0%-100% survival probability (see Figure 6-27).

As mentioned previously, the energy dissipated by displacing the slab is negligible. Interestingly, although the impact velocity is almost doubled (from 5.3m/s to 9.9 m/s), covering the full survival probability (from 100% to 0%), the trends of normalised energy are almost constant with only very small changes. Figure 6-27 shows that the number of fragments increases from 2 to 5, for an impact velocity increasing from 5.5 m/s to 10 m/s, hence almost tripling the amount of fragmentation energy (see Table 6-14) but the normalised value of fragmentation energy remains approximately constant. This is consistent with findings form Giacomini et al. (2009) but should be investigated over a larger range of impact velocity.

So, to answer Question 2: under the conditions of the limited data obtained in this thesis, it seems that, in the range of energy including 0-100% of the survival probability, the energy consumed in fragmentation can be considered a constant fraction of the total kinetic energy at impact. As the impact energy increases, more fragments are created, leading to more energy dissipated in fragmentation and a constant ratio of fragmentation energy over impact energy. The reason for this ratio being constant is not yet explained. More research is needed to explain it and verify whether this observation holds for a wider range of impact velocities and other block shapes.

The fact that energy is dissipated in fragmentation results in less kinetic energy post-impact and less rebound. Figure 6-39 shows the theoretical coefficient of restitution CoR_d (Eq. (3-20)) not accounting for fragmentation and the $\overline{CoR_E}$ computed as square root of the ratio between the experimental total kinetic energy after and before impact. It can be seen that the experimental $\overline{CoR_E}$ is lower than the theoretical CoR_d, which is due to increasing degree of damage and fragmentation in the spheres (Ye et al. 2019a).

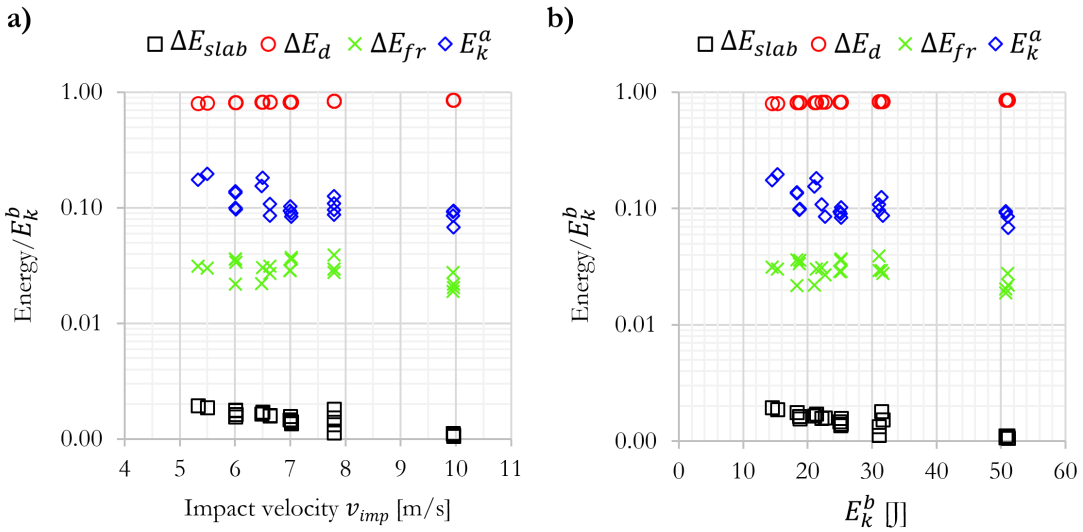

Figure 6-38: Normalised value of energy loss at impact and (a) the total kinetic energy after impact as function of impact velocity and (b) kinetic energy before impact (Series S3.2).

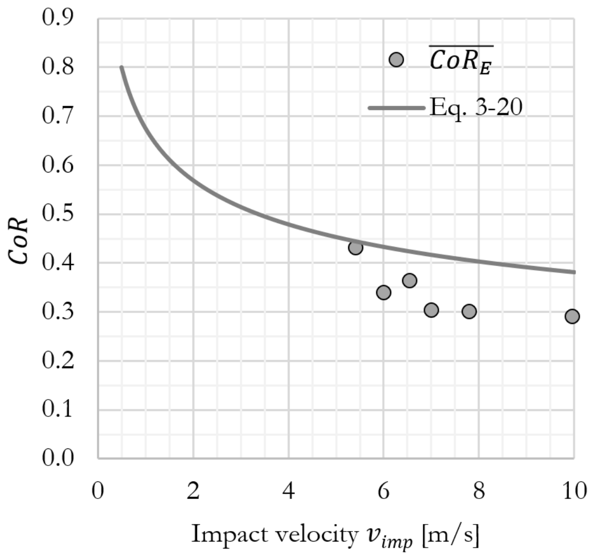

Figure 6-39: Theoretical and experimental values of coefficient of restitution as function of impact velocity. CoR_d is obtained from Eq.(3-20) and does not account for damage. $\overline{CoR_E}$ is the experimental value defined as the square root of total kinetic energy after impact over total kinetic energy before impact.

Table 6-14 Result of energy balance computation for drop tests of series S3.2. Each energy component is expressed in absolute value (in J) and in relative value (percentage of the total kinetic energy before impact).

Test	Before impact		Dissipation at impact								Sum of the energy of the fragments (after impact)						E_{tot}	
	v_{imp}	E_k^b	ΔE_{slab}		ΔE_d		ΔE_{fr}		ΔE_{tot}		E_{kt}^a		E_{kr}^a		E_k^a			
	m/s	J	J	%	J	%	J	%	J	%	J	%	J	%	J	%	J	%
1	5.33	14.49	0.03	*0.2*	11.62	*80.1*	0.45	*3.1*	12.10	*83.5*	2.53	*17.5*	0.06	*0.4*	2.60	*17.9*	14.70	*101.4*
2	5.49	15.29	0.03	*0.2*	12.30	*80.4*	0.46	*3.0*	12.79	*83.7*	3.01	*19.7*	0.03	*0.2*	3.04	*19.9*	15.84	*103.5*
3	6.01	18.76	0.03	*0.2*	15.25	*81.3*	0.67	*3.6*	15.95	*85.0*	1.87	*10.0*	0.06	*0.3*	1.93	*10.3*	17.87	*95.3*
4	6.01	18.33	0.03	*0.2*	14.90	*81.3*	0.66	*3.6*	15.60	*85.1*	2.47	*13.5*	0.02	*0.1*	2.49	*13.5*	18.09	*98.7*
5	6.01	18.35	0.03	*0.2*	14.92	*81.3*	0.40	*2.2*	15.35	*83.7*	2.54	*13.8*	0.00	*0.0*	2.54	*13.9*	17.89	*97.5*
6	6.02	18.74	0.03	*0.2*	15.24	*81.3*	0.63	*3.4*	15.90	*84.8*	1.82	*9.7*	0.01	*0.1*	1.83	*9.8*	17.73	*94.6*
7	6.49	21.05	0.03	*0.2*	17.26	*82.0*	0.46	*2.2*	17.76	*84.4*	3.26	*15.5*	0.02	*0.1*	3.27	*15.6*	21.03	*99.9*
8	6.50	21.32	0.04	*0.2*	17.49	*82.0*	0.65	*3.0*	18.17	*85.2*	3.89	*18.2*	0.00	*0.0*	3.89	*18.3*	22.07	*103.5*
9	6.63	22.20	0.04	*0.2*	18.25	*82.2*	0.69	*3.1*	18.98	*85.5*	2.41	*10.8*	0.09	*0.4*	2.49	*11.2*	21.47	*96.7*
10	6.63	22.72	0.04	*0.2*	18.68	*82.2*	0.61	*2.7*	19.33	*85.1*	1.94	*8.5*	0.05	*0.2*	1.99	*8.8*	21.32	*93.8*
11	6.99	25.00	0.04	*0.1*	20.67	*82.7*	0.80	*3.2*	21.50	*86.0*	2.35	*9.4*	0.09	*0.4*	2.45	*9.8*	23.87	*95.5*
12	7.00	25.20	0.04	*0.2*	20.84	*82.7*	0.72	*2.9*	21.60	*85.7*	2.58	*10.3*	0.05	*0.2*	2.63	*10.4*	24.23	*96.2*
13	7.02	25.12	0.03	*0.1*	20.77	*82.7*	0.90	*3.6*	21.71	*86.4*	2.26	*9.0*	0.20	*0.8*	2.46	*9.8*	24.17	*96.2*
14	7.02	25.19	0.04	*0.1*	20.83	*82.7*	0.93	*3.7*	21.80	*86.5*	2.11	*8.4*	0.09	*0.4*	2.20	*8.7*	24.00	*95.3*
15	7.80	31.09	0.04	*0.1*	25.99	*83.6*	1.22	*3.9*	27.25	*87.6*	3.38	*10.9*	n.a.	*n.a.*	3.38	*10.9*	30.63	*98.5*
16	7.79	31.46	0.06	*0.2*	26.29	*83.6*	0.93	*2.9*	27.27	*86.7*	3.95	*12.5*	n.a.	*n.a.*	3.95	*12.5*	31.22	*99.2*
17	7.79	31.68	0.05	*0.2*	26.47	*83.6*	0.88	*2.8*	27.40	*86.5*	2.75	*8.7*	n.a.	*n.a.*	2.75	*8.7*	30.15	*95.2*
18	7.80	31.05	0.04	*0.1*	25.95	*83.6*	0.91	*2.9*	26.89	*86.6*	2.99	*9.6*	n.a.	*n.a.*	2.99	*9.6*	29.89	*96.3*
19	9.95	50.73	0.06	*0.1*	43.36	*85.5*	0.96	*1.9*	44.37	*87.5*	4.68	*9.2*	n.a.	*n.a.*	4.68	*9.2*	49.05	*96.7*
20	9.94	51.08	0.06	*0.1*	43.66	*85.5*	1.41	*2.8*	45.12	*88.3*	4.35	*8.5*	n.a.	*n.a.*	4.35	*8.5*	49.48	*96.9*
21	9.96	51.12	0.05	*0.1*	43.70	*85.5*	1.12	*2.2*	44.87	*87.8*	3.48	*6.8*	n.a.	*n.a.*	3.48	*6.8*	48.35	*94.6*
22	9.95	50.73	0.05	*0.1*	43.36	*85.5*	1.03	*2.0*	44.45	*87.6*	4.80	*9.5*	n.a.	*n.a.*	4.80	*9.5*	49.25	*97.1*

Notes:
Note that a very small rotational motion was observed for tests at higher impact velocity (7.8 and 10 m/s). Hence, the rotational velocity was not computed for these tests. The rotational kinetic energy is very small compared to the initial kinetic energy (<1%) and has a negligible influence on the energy balance for this type of impact condition.

The rockfall literature lacks experimental fragmentation data, especially with comprehensive estimates of energy components. As highlighted in the beginning of Section 6.5, the distribution of energy among fragments is not well understood. In one of the few fragmentation models (Matas et al. 2020), it is assumed that the energy is distributed throughout fragments proportionally to their mass. Such assumptions will be tested using the fragmentation data produced in this thesis (results of series S3.2).

Figure 6-40a presents the velocity of fragments normalised by the impact velocity of the sphere they formed from (v_i/v_{imp}) as a function of fragment mass. Each data point corresponds to one fragment. Figure 6-40a shows the absence of a clear relationship between normalised velocity and fragment mass. 95% of data points are contained between a lower bound of 19% and an upper bound of 42%.

Figure 6-40b then presents fragment kinetic energy normalised by total kinetic energy before impact ($E_{k,i}^a/E_k^b$) as a function of fragment mass. Again, each data point corresponds to one fragment. With a R^2 value of 0.95, Figure 6-40b suggests that a trend may exist between normalised energy and fragment mass. However, it can be shown that the normalised energy is equal to:

$$\frac{E_{k,i}^a}{E_k^b} = \frac{m_i}{m}\left(\frac{v_i}{v_{imp}}\right)^2 \tag{6-8}$$

where $E_{k,i}^a$, is the total kinetic energy after impact of the fragment i, E_k^b is the total kinetic energy before impact, m_i and m are the masses of the fragment i and the impacting sphere, respectively, v_i is the absolute velocity of the fragment i after impact and v_{imp} is the impact velocity. Figure 6-40a shows that, for 95% of the data the bounds of normalised velocity are 0.19 and 0.42, so the bounds of the squared normalised velocity are 0.19^2 and 0.42^2, i.e. 0.036 and 0.176. Data of Figure 6-40b are proportional to these two bounds (0.036 and 0.176) weighted by the relative mass of fragment (m_i/m), as per Eq. (6-8). The implication of this is that on the right-hand side of Figure 6-38b, where m_i/m~1, the scattering of Figure 6-38a largely remains; but on the left hand side where $m_i/m \ll 1$, the scattering is much smaller, leading to high values of R^2. So, the high goodness of fit of Figure 6-38b comes from the small fragments but significant scattering still exists for large fragments, i.e. those posing a high risk.

a)

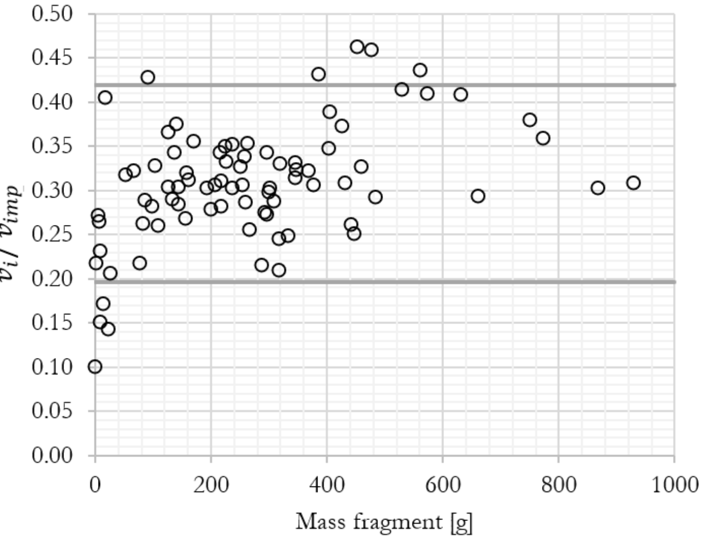

b)

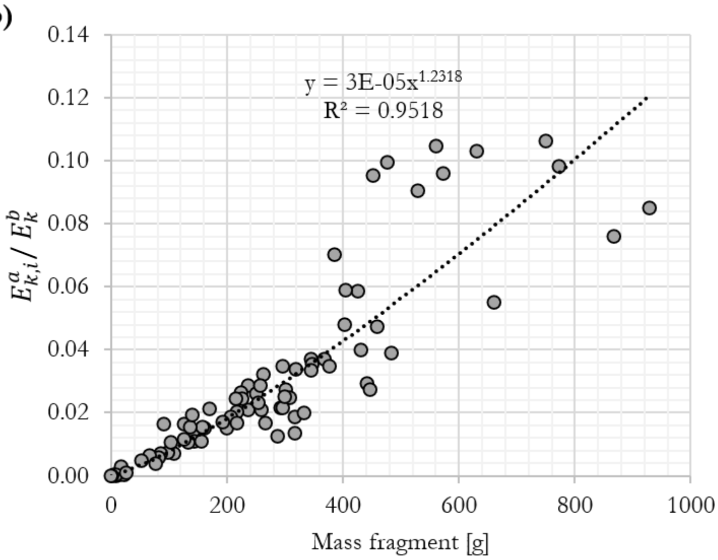

Figure 6-40: (a) Fragment velocity over impact velocity (v_i/v_{imp}) as a function of fragment mass. Horizontal lines represent the 95% confidence interval. (b) Total kinetic energy of fragments over kinetic energy before impact ($E^a_{k,i}/E^b_k$) as a function of fragment mass.

In the following, the error made when assigning kinetic energy to fragments proportionally to their mass is assessed. To do so, the two main dissipative components considered are plastic deformation (ΔE_d) and fragmentation (ΔE_f), for which experimental values are used, for each fragment. In a real rockfall prediction exercise, one could predict the fragment size distribution using the fractal fragmentation model (Ruiz-Carulla et al. 2017), and get the fragmentation energy from the surface energy; the energy dissipated by plastic deformation can be computed from the theoretical coefficient of restitution.

With ΔE_d and ΔE_f known, it is possible to compute the total kinetic energy after impact:

$$E_k^a = E_k^b - \Delta E_d - \Delta E_f \tag{6-9}$$

Assuming that the total kinetic energy will be distributed to all fragments proportionally to their mass, the kinetic energy of fragment i $E_{k,i}^a$ can be expressed as:

$$E_{k,i}^a = \frac{m_i}{m} \cdot E_k^a \tag{6-10}$$

where m_i is the mass of the fragment i, m is the initial mass of the sphere and E_k^a is the total kinetic energy after impact.

Figure 6-41a shows a comparison between the kinetic energy predicted using Eq. (6-10) and the experimental values of kinetic energy for all fragments, while Figure 6-41b presents the cumulative distribution of relative error, calculated as 100 x (predicted value-experimental value)/experimental value. Positive values of relative error reflect an overestimation of energy and vice versa.

Consistent with Figure 6-40, Figure 6-41a shows a significant amount of scattering. The predicted values form a cloud around the one-to-one line with the largest scattering for the biggest fragments. This poor quality of prediction is corroborated by Figure 6-41b where 30% of predictions have a relative error of less than 20%; 60% of predictions have a relative error of less than 50%; and 10% of predictions have a relative error of higher than 150%. Although the maximum relative error is as high as 1200%, it is only for small fragments, with very low values of kinetic energy and low significance from a risk point of view.

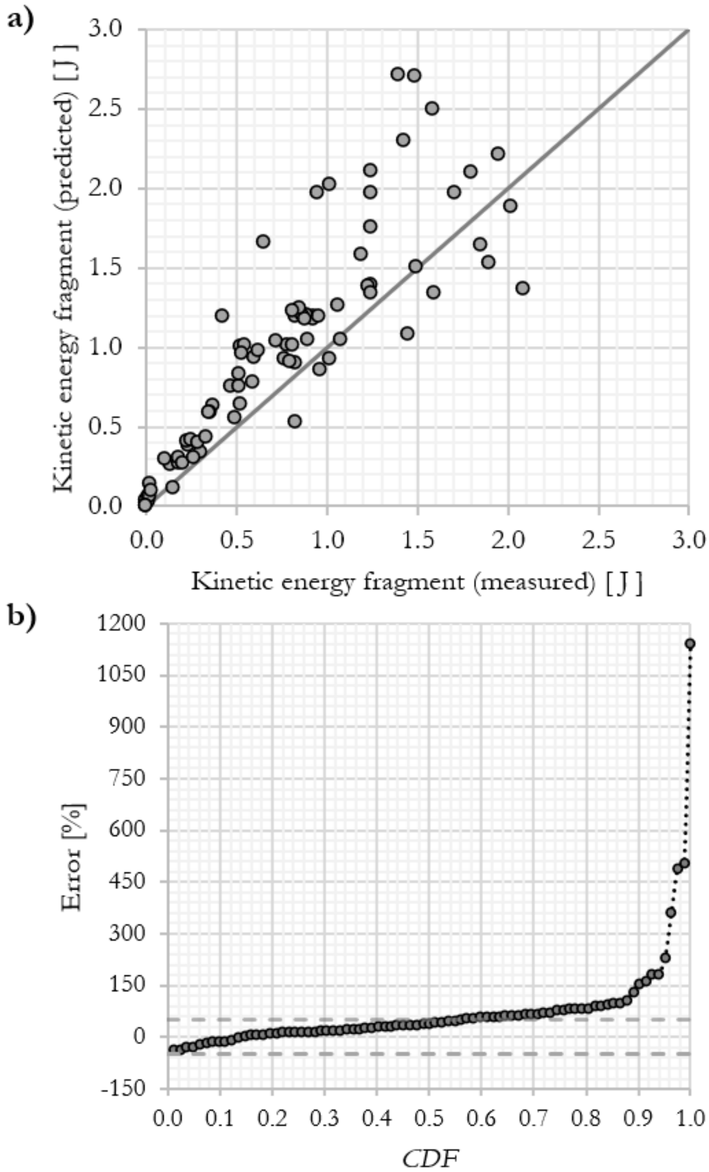

Figure 6-41: (a) Predicted kinetic energy (using Eq. (6-10)) vs measured kinetic energy for all fragments of series S3.2. (b) Cumulative distribution of the relative error on the prediction of kinetic energy for all fragments. Dashed horizontal lines represent ±50% of error.

So, to answer Question 3: from the limited data obtained in this study, it seems that assigning kinetic energy to fragments based on their mass can lead to significant error in rockfall modelling. However, at this stage, there does not seem to be a superior alternative approach and more research is required.

The last aspect that will be discussed in this section is the velocity of fragments and, in particular, how the vertical and horizontal components of velocity change with increasing impact velocity. Figure 6-42 illustrates the evolution of the absolute velocity of fragments normalised by the impact velocity (v_i/v_{imp}), with impact velocity. As for previous observations, the scattering is quite large and increasing with the impact velocity. The upper bound of values seems approximatively constant (around 0.45) but the lower bound decreases progressively. This evolution reflects the fact that under increasing impact velocity, more fragments of different sizes are produced, leading to a broader range of velocities post-impact.

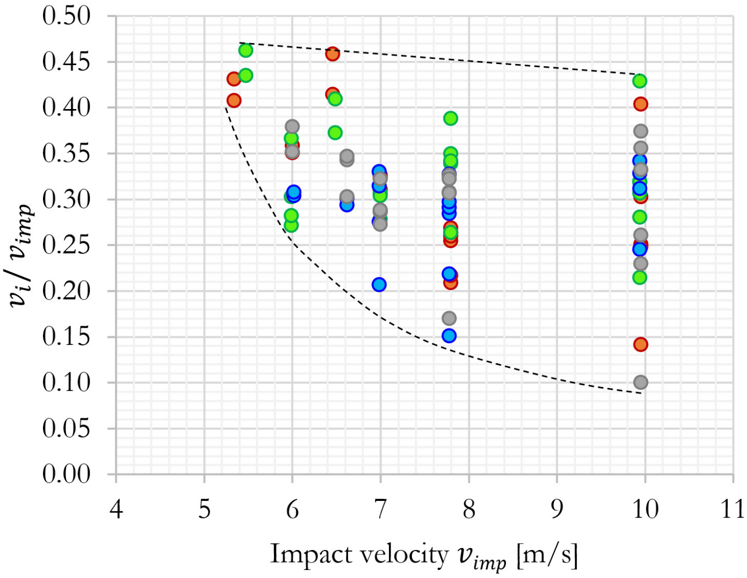

Figure 6-42: Absolute velocity of the fragment i over impact velocity (v_i/v_{imp}) vs. impact velocity. Points with the same colour (red, green, blue and grey) at each impact velocity represent fragments of the same test at a particular value of impact velocity.

Increasing the impact velocity also changes the trajectory of fragments post-impact, as shown in Figure 6-43, which presents the ratio of the vertical component of velocity to the horizontal component of velocity, for each fragment (Figure 6-43a shows all data while Figure 6-43b shows the average value at each impact velocity). High values of $v_{z,i}/v_{xy,i}$ correspond to a high rebound (launch angle close to 90° from horizontal), while low values correspond to fragments travelling parallel to the impacted surface.

Under low impact velocity, the fragments tend to bounce but, as the impact velocity increases, they tend to be ejected sideways. Such observation is very relevant in order to realistically model trajectory of fragments.

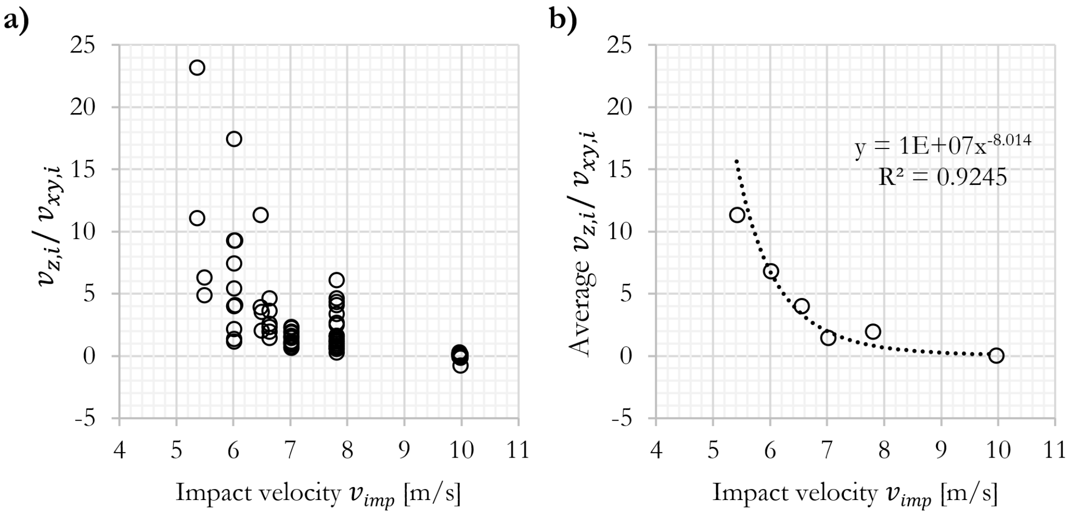

Figure 6-43: Ratio of vertical ($v_{z,i}$) and horizontal ($v_{xy,i}$) component of velocity for all fragments as function of impact velocity: (a) all data, (b) average values.

In conclusion, in the range of impact energy analysed, the ratio of energy consumed in fragmentation over kinetic energy before impact seems constant (between 3% and 5% of the kinetic energy before impact, considering data of M1 and M1*, respectively). There does not seem to be a clear relationship between total kinetic energy of fragments and their mass, and when trying to assign kinetic energy to fragments based on their mass significant relative errors were obtained. Lastly, there is a correlation between the trajectory of the fragments and the initial impact velocity of the block: at "low velocity" (between 5.5 m/s and 6.5 m/s) the main component of the fragment velocity is the vertical component (v_z), while with the increasing of impact velocity (and number of fragments) the main component of the velocity become the horizontal velocity (v_{xy}). All of these observations are relevant for rockfall modelling.

7 Conclusions and future research

Although rock fragmentation has been frequently observed during rockfalls, it is rarely considered in rockfall analysis and for the design of rockfall protection structures. This can be attributed to the complexity and lack of understanding of the physical process. Indeed, experimental and numerical studies showed that many factors influence the occurrence and outcomes of fragmentation in a rockfall event. More research is hence required to better understand the fragmentation process and adequately model it.

In this PhD research, a specifically-designed apparatus was built and validated to record and study the complex phenomenon of fragmentation of rocks upon impact. This experimental setup comprises a custom-made hexagonal fragmentation cell in which natural or artificial rock blocks can be dropped in a safe and controlled way onto an instrumented concrete slab to simulate the impact with a rock slope. The impact can be recorded with four high-speed cameras and two mirrors, offering six unique viewpoints. In order to eliminate some inherent complexities of natural rock and irregularly shaped blocks, and to achieve better control and repeatability of results, mortar spheres were used. During the validation process, attention was focused on devising a method to evaluate the impact force and impulse on the sphere from the measurement of forces under the slab. Another aspect given close attention was 3D tracking accuracy, with an emphasis on the influence that object shape, number of viewpoints and 3D object representation have on the calculation of rotational velocity. Results showed the apparatus and methods developed in this thesis allow for accurate capture of 3D trajectories of regular and irregular objects, in translation and/or rotation, and reliable prediction of the magnitude of impulse at impact.

Four series of drop tests were conducted using mortars of four different strengths and spheres of three diameters, in order to produce high-quality data that can be used to advance knowledge of rockfall fragmentation.

The main conclusions to be drawn from the 360 drop tests carried out are:

- In the range of impact velocities corresponding to a 100%-0% range of survival probability, less than five large and a few small fragments can be expected independently by the size and the strength of the mortar sphere, while for higher values of impact velocities, more and more fragments are produced and the size of largest fragments progressively decreases with increasing velocity. The fragment size distributions (FSD) obtained in this research are not linear in a logarithmic scale, hence it is in contrast with a scale invariant fractal distribution of fragments.
- Fragmentation survival probability can be approximated as a linear function of the kinetic energy or impact velocity and is both material strength dependent and sphere diameter dependent. The existence of a survival probability confirms the fact that fragmentation is not a threshold phenomenon.
- The total normalised amount of energy loss during the impact increases with impact velocity, consequently the total kinetic energy after impact decreases. Although the quantity of damage and fragments increases with impact velocity, the energy loss to create the fracture surfaces is a constant fraction of the kinetic energy before impact and it can be estimated using Eq. (3-17). There is absence of a clear relationship between normalised velocity and fragment mass.
- The trajectories of fragments are related to the impact velocity. At low impact velocity, the fragments tend to bounce but, as the impact velocity increases, they tend to be ejected sideways. No high-flying fragments were observed.

A significant contribution of this research to the field of rockfall is the development and validation of a novel model that can predict the impact survival probability of brittle homogenous spheres, to serve as a basis for further development. The rationale of the novel model is that (1) the impact survival probability can be entirely defined by the Weibull shape and scale parameters and (2) it is possible to predict these two parameters from the statistical variability of mechanical properties of the material measured under quasi static loading. Of particular importance is the response of the material in indirect tension (Brazilian tests). The prediction process also involves three theoretically-derived conversion factors that account for size, shape and strain rate effects, two of which are based on Hertz's elastic contact theory, assuming elastic deformations of the bodies in contact.

Extensive material testing was first conducted in order to assess the statistical variability in material properties in terms of force, stress, toughness and work required to reach failure. The measured mechanical properties of the mortar were found to generally follow Weibull distributions. Then, the predicted conversion factors were first validated against their experimental counterparts, with a maximum relative error of 25%. The impact survival probabilities were then predicted using both a Weibull function and a linear function, with the latter option being considered to improve the prediction at the 0% and 100% survival probability limits. For a Weibull function, the model can predict the impact survival probability with a maximum error of 10% but this is only possible by using statistical information from compression tests on spheres of different diameters, which is not very practical. The possibility to predict the impact survival probability (in a linear form) from Brazilian tests was then assessed. The motivation for this follows from a view that the Brazilian tests are an easy and less time-consuming type of test that could be readily performed in practice. The maximum relative error was found to be around 27% but about two thirds of the data points were predicted with an error of less than 12%, which demonstrates an excellent predictive ability of the novel model. Such a predictive model is the first step towards predicting whether, in a given geological setting, a rock is likely to fragment upon impact or not. It has to be borne in mind that there is currently no method or model in the literature that can be used to predict the survival probability of brittle spheres, let alone natural blocks.

The outcomes of this PhD thesis constitute a significant step forward in the understanding of fragmentation in the context of rockfall but the specific findings strictly apply to mortar spheres under normal impact without rotation, which is quite restrictive. Consequently, more research is required to understand the influence of rotational energy, irregular block shape, presence and properties of discontinuities and angle of impact. All these parameters are representative of realistic rockfall conditions. It would also be useful to conduct the energy analysis on the fragmentation tests at higher energy to obtain validation of the idea that the energy dissipated in fragmentation is approximately a constant fraction of the impact energy and to identify the conditions leading to high-flying fragments. It is finally suggested that the robustness of the survival probability prediction model should be tested by comparing predictions and experimental data for a greater range of mortar strength and larger spheres and ultimately real rocks.

References

Agliardi F, Crosta GB. (2003). High resolution three-dimensional numerical modelling of rockfalls. *International Journal of Rock Mechanics and Mining Sciences 40*:455-471. doi:http://dx.doi.org/10.1016/S1365-1609(03)00021-2

Alizadeh E, Bertrand F, Chaouki J. (2013). Development of a granular normal contact force model based on a non-Newtonian liquid filled dashpot. *Powder Technology 237*:202-212. doi:https://doi.org/10.1016/j.powtec.2013.01.027

Anderson TL. (2017). *Fracture mechanics: fundamentals and applications.* CRC press,

Andrews EW, Kim KS. (1998). Threshold conditions for dynamic fragmentation of ceramic particles. *Mechanics of Materials 29*:161-180. doi:https://doi.org/10.1016/S0167-6636(98)00014-3

Andrews EW, Kim KS. (1999). Threshold conditions for dynamic fragmentation of glass particles. *Mechanics of Materials 31*:689-703. doi:https://doi.org/10.1016/S0167-6636(99)00024-1

Anliot M. (2005). *Volume Estimation of Airbags: A Visual Hull Approach.* Master's thesis, Linköping University, Sweden.

Ansari MK, Ahmad M, Singh R, Singh TN. (2015). Correlation between Schmidt hardness and coefficient of restitution of rocks. *Journal of African Earth Sciences 104*:1-5. doi:https://doi.org/10.1016/j.jafrearsci.2015.01.005

Antonyuk S, Tomas J, Heinrich S, Mörl L. (2005). Breakage behaviour of spherical granulates by compression. *Chemical Engineering Science 60*:4031-4044. doi:https://doi.org/10.1016/j.ces.2005.02.038

Arbiter N, Harris CC, Stramboltzis GA. (1969). Single fracture of brittle spheres. *Transaction of AIME 244*:118-133

Asteriou P, Saroglou H, Tsiambaos G. (2012). Geotechnical and kinematic parameters affecting the coefficients of restitution for rock fall analysis. *International Journal of Rock Mechanics and Mining Sciences 54*:103-113. doi:https://doi.org/10.1016/j.ijrmms.2012.05.029

Asteriou P, Saroglou H, Tsiambaos G. *Rockfall: scaling factors for the coefficient of restitution*. In: ISRM International Symposium-EUROCK 2013, 2013a. International Society for Rock Mechanics and Rock Engineering,

Asteriou P, Saroglou H, Tsiambaos G. (2013b). Rockfalls: influence of rock hardness on the trajectory of falling rock blocks. *Bulletin of the Geological Society of Greece 47*:1684. doi:https://doi.org/10.12681/bgsg.11033

Asteriou P, Tsiambaos G. (2018). Effect of impact velocity, block mass and hardness on the coefficients of restitution for rockfall analysis. *International Journal of Rock Mechanics and Mining Sciences 106*:41-50. doi:https://doi.org/10.1016/j.ijrmms.2018.04.001

Atkinson BK. (1987). *Fracture Mechanics of Rock*. Elsevier,

AutoHotkey Foundation LLC. (2020). AutoHotkey. https://www.autohotkey.com. Accessed 1 May 2020

Azimi C, Desvarreux P. (1977). *Calcul de Chutes de Blocs et Vérification sur Modèle Réduit*. Paper presented at the Association pour le développement des recherches sur les glissements de terrain, Grenoble,

Azimi C, Desvarreux P, Giraud A, Martin-Cocher J. (1982). Méthode de calcul de la dynamique des chutes de blocs - Application à l'étude du versant de la montagne de La Pale (Vercors). *Bull de Liaison Labo P et Ch 122*:93-102

Azzoni A, De Freitas MH. (1995). Experimentally gained parameters, decisive for rock fall analysis. *Rock Mechanics and Rock Engineering 28*:111-124. doi:https://doi.org/10.1007/BF01020064

Azzoni A, La Barbera G, Zaninetti A. (1995). Analysis and prediction of rockfalls using a mathematical model. *International Journal of Rock Mechanics and Mining Sciences & Geomechanics Abstracts 32*:709-724. doi:https://doi.org/10.1016/0148-9062(95)00018-C

Azzoni A, Rossi PP, Drigo E, Giani GP, Zaninetti A. *In situ observation of rockfall analysis parameters*. In: Sixth International Symposium of Landslides, 1992. pp 307-314

Backers T, Fardin N, Dresen G, Stephansson O. (2003). Effect of loading rate on Mode I fracture toughness, roughness and micromechanics of sandstone. *International Journal of Rock Mechanics and Mining Sciences 40*:425-433. doi:https://doi.org/10.1016/S1365-1609(03)00015-7

Bažant ZP, Planas J. (1997). *Fracture and size effect in concrete and other quasibrittle materials*. vol 16. CRC press,

Bažant ZP, Shang-Ping B, Ravindra G. (1993). Fracture of rock: Effect of loading rate. *Engineering Fracture Mechanics 45*:393-398. doi:https://doi.org/10.1016/0013-7944(93)90024-M

Behera B, Kun F, McNamara S, Herrmann HJ. (2005). Fragmentation of a circular disc by impact on a frictionless plate. *Journal of Physics: Condensed Matter 17*:S2439

Bennett JG. (1936). Broken coal. *J Inst Fuel 10*:22-39

Berger F, Dorren LKA. (2006). Objective comparison of rockfall models using real size experimental data. *Disaster Mitigation of Debris Flows, Slope Failures and Landslides*:245-252

Bergstrom BH, Sollenberger CL. (1961). Kinetic energy effect in single particle crushing. *Transaction of AIME 220*:373-379

Bergstrom BH, Sollenberger CL, Mitchell W. *Energy and size distribution aspects of single particle crushing.* In: Rock Mechanics. Proceedings of the 5th symposium on rock Mechanics, 1962. pp 155-172

Bieniawski ZT, Bernede MJ. (1979). Suggested methods for determining the uniaxial compressive strength and deformability of rock materials. *International Journal of Rock Mechanics and Mining Sciences & Geomechanics Abstracts 16*:137-140. doi:https://doi.org/10.1016/0148-9062(79)91451-7

Bourrier F. (2008). *Modélisation de l'impact d'un bloc rocheux sur un terrain naturel, application à la trajectographie des chutes de blocs, Ph.D. Thesis.* Ph.D. Thesis,

Bourrier F, Dorren L, Nicot F, Berger F, Darve F. (2009). Toward objective rockfall trajectory simulation using a stochastic impact model. *Geomorphology 110*:68-79. doi:https://doi.org/10.1016/j.geomorph.2009.03.017

Bourrier F, Nicot F, Darve F. (2008). Physical processes within a 2D granular layer during an impact. *Granular Matter 10*:415-437. doi:https://doi.org/10.1007/s10035-008-0108-0

Bozzolo D, Pamini R. (1986). Simulation of rock falls down a valley side. *Acta Mechanica 63*:113-130. doi:https://doi.org/10.1007/bf01182543

Bozzolo D, Pamini R, Hutter K. (1988). Rockfall analysis - a mathematical model and its test with field data. *Landslides Proc 5th symposium, Lausanne 1*:555-560

Brake MR. (2012). An analytical elastic-perfectly plastic contact model. *International Journal of Solids and Structures 49*:3129-3141. doi:https://doi.org/10.1016/j.ijsolstr.2012.06.013

Brake MRW. (2015). An analytical elastic plastic contact model with strain hardening and frictional effects for normal and oblique impacts. *International Journal of Solids and Structures 62*:104-123. doi:https://doi.org/10.1016/j.ijsolstr.2015.02.018

Breval E, Jennings J, Komarneni S, Macmillan N, Lunghofer E. (1987). Microstructure, strength and environmental degradation of proppants. *Journal of materials science 22*:2124-2134

Broili L. *Relations between scree slope morphometry and dynamics of accumulation processes*. In: Meeting on Rockfall dynamics and protective works effectiveness, 1977. pp 11-23

Buzzi O, Giacomini A, Spadari M. (2012). Laboratory investigation on high values of restitution coefficients. *Rock Mechanics and Rock Engineering 45*:35-43. doi:https://doi.org/10.1007/s00603-011-0183-0

Cadoni E. (2010). Dynamic Characterization of Orthogneiss Rock Subjected to Intermediate and High Strain Rates in Tension. *Rock Mechanics and Rock Engineering 43*:667-676. doi:https://doi.org/10.1007/s00603-010-0101-x

Camponuovo GF. (1977). ISMES experience on the model of St. Martino. *Proc Meet Rockfall Dynamics Protective Works Effectiveness 90*:25-38

Carmona HA, Wittel FK, Kun F, Herrmann HJ. (2008). Fragmentation processes in impact of spheres. *Physical Review E 77*:051302. doi:https://doi.org/10.1103/PhysRevE.77.051302

Chang WR, Etsion I, Bogy DB. (1987). An Elastic-Plastic Model for the Contact of Rough Surfaces. *Journal of Tribology 109*:257-263. doi:https://doi.org/10.1115/1.3261348

Chau KT, Chan LCP, Wu JJ, Liu J, Wong RHC, Lee CF. (1998a). Experimental studies on rockfall and debris flow. *Proc Seminar on Planning, Design and Implementation of Debris Flow and Rockfall Hazards Mitigation Measures*:115-128

Chau KT, Wei XX. (1999). Spherically isotropic, elastic spheres subject to diametral point load strength test. *International Journal of Solids and Structures 36*:4473-4496. doi:https://doi.org/10.1016/S0020-7683(98)00202-9

Chau KT, Wei XX, Wong RHC, Yu TX. (2000). Fragmentation of brittle spheres under static and dynamic compressions: experiments and analyses. *Mechanics of Materials 32*:543-554. doi:https://doi.org/10.1016/S0167-6636(00)00026-0

Chau KT, Wong RHC, Lee CF. (1998b). Rockfall problems in Hong Kong and some new experimental results for coefficients of restitution. *International Journal of Rock Mechanics and Mining Sciences 35*:662-663

Chau KT, Wong RHC, Liu J, Wu JJ, Lee CF. *Shape effects on the coefficient of restitution during rockfall impacts*. In: 20th Century Lessons, 21st Century Challenges., 1999a. pp 541-544

Chau KT, Wong RHC, Wu JJ. (2002). Coefficient of restitution and rotational motions of rockfall impacts. *International Journal of Rock Mechanics and Mining Sciences 39*:69-77. doi:https://doi.org/10.1016/S1365-1609(02)00016-3

Chau KT, Wu JJ, Wong RH, Lee CF. (1999b). The coefficient of restitution for boulders falling onto soil slopes with various values of dry density and water content. *Proc Int Symp on Slope Stability Engineering: Geotechnical and Geoenvironmental Aspects 2*:1355-1360

Chen EP, Sih GC. (1977). *Elastodynamic Crack Problems*. Noordhoff 1983,

Cheong YS, Salman AD, Hounslow MJ. (2003). Effect of impact angle and velocity on the fragment size distribution of glass spheres. *Powder Technology 138*:189-200. doi:https://doi.org/10.1016/j.powtec.2003.09.010

Christen M, Bartelt P, Gruber U. (2007). RAMMS - A modeling system for snow avalanches, debris flows and rockfalls based on IDL. *PFG Photogrammetrie Fernerkundung Geoinformation 4*:289-292

CloudCompare. (2020). version 2.12.alpha. https://www.danielgm.net/cc/. Accessed 17 Dicember 2020

Corominas J, Matas G, Ruiz-Carulla R. (2019). Quantitative analysis of risk from fragmental rockfalls. *Landslides 16*:5-21. doi:https://doi.org/10.1007/s10346-018-1087-9

Costin LS, Grady DE. (1984). *Dynamic fragmentation of brittle materials using the torsional Kolsky bar*. Conference: 3. meeting on liquid metal in energy applications, Oxford, UK, 9 Apr 1984; Other Information: Paper copy only, copy does not permit microfiche production. ; Sandia National Labs., Albuquerque, NM (USA),

Crosta GB, Agliardi F, Frattini P, Imposimato S. (2004). A three-dimensional hybrid numerical model for rockfall simulation. *Geophysical Research Abstracts 6*

Cundall PA. (1971). A computer model for simulating progressive large scale movements in blocky rock systems. *Proceedings of the Symposium of the International Society of Rock Mechanics*:129-136

Curran DR, Seaman L, Shockey DA. (1977). Dynamic failure in solids. *Physics Today 30*:46

Darvell B. (1990). Uniaxial compression tests and the validity of indirect tensile strength. *Journal of Materials Science 25*:757-780

Dawson-Haggerty ea. (2019). Trimesh. 3.2.0 edn.,

Dean WR, Sneddon IM, Parsons HW. (1952). Distribution of stress in a deccelerating elastic sphere. *Selected Government Research Reports: Strength and Testing of Materials: Part II: Testing Methods and Test Results*:212-234

Deresiewicz H. (1968). A note on Hertz's theory of impact. *Acta Mechanica 6*:110-112

Descoeudres F. (1997). Aspects géomécaniques des instabilités de falaises rocheuses et des chutes de blocs. *Publications de la Société Suisse de Mécanique des Sols et des Roches 135*:3-11

Descoeudres F, Zimmermann T. (1987). Three-dimensional dynamic calculation of rockfalls. *Proc 6th Congress International Society for Rock Mechanics, Montreal, 1987 Vol 1*:337-342

Dewez T et al. (2010). OFAI: 3D block tracking in a real-size rockfall experiment on a weathered volcanic rocks slope of Tahiti, French Polynesia. *Rock Slope Stability*

Dimnet E. (2002). *Mouvement et collisions de solides rigides ou déformables, Ph.D. Thesis*. Ph.D. Thesis,

Dimnet E, Fremond M. *Instantaneous collisions of solids*. In: European Congress on Computational Methods in Applied Sciences and Engineering, ECCOMAS 2000, 2000.

Dorren LKA. (2003). A review of rockfall mechanics and modelling approaches. *Progress in Physical Geography 27*:69-87. doi:https://doi.org/10.1191/0309133303pp359ra

Dorren LKA, Berger F, Putters US. (2006). Real-size experiments and 3-D simulation of rockfall on forested and non-forested slopes. *Natural Hazards and Earth System Sciences 6*:145-153. doi:https://doi.org/10.5194/nhess-6-145-2006

Dorren LKA, Maier B, Putters US, Seijmonsbergen AC. (2004). Combining field and modelling techniques to assess rockfall dynamics on a protection forest hillslope in the European Alps. *Geomorphology 57*:151-167. doi:https://doi.org/10.1016/S0169-555X(03)00100-4

Effeindzourou A, Thoeni K, Giacomini A, Wendeler C. (2017). Efficient discrete modelling of composite structures for rockfall protection. *Computers and Geotechnics 87*:99-114. doi:https://doi.org/10.1016/j.compgeo.2017.02.005

Evans SG, Hungr O. (1993). The assessment of rockfall hazard at the base of talus slopes. *Canadian Geotechnical Journal 30*:620-636. doi:https://doi.org/10.1139/t93-054

Falcetta JL. (1985). Un nouveau modèle de calcul de trajectoires de blocs rocheux. *Revue Francaise de Geotechnique 30*:11-17

Ferrari F, Giacomini A, Thoeni K. (2016). Qualitative Rockfall Hazard Assessment: A Comprehensive Review of Current Practices. *Rock Mechanics and Rock Engineering 49*:2865-2922. doi:https://doi.org/10.1007/s00603-016-0918-z

Ferrari F, Giani G, Apuani T. (2013). Why can rockfall normal restitution coefficient be higher than one? *Rendiconti Online Societa Geologica Italiana 24*:122-124

Fischer-Cripps AC. (2007). *Introduction to contact mechanics*. vol 101. Springer,

Fornaro M, Peila D, Nebbia M. (1990). Block falls on rock slopes. Application of a numerical simulation program to some real cases. *Proceedings of the 6th International Congress IAEG*:2173-2180

Frémond M. (1995). Rigid bodies collisions. *Physics Letters A 204*:33-41. doi:https://doi.org/10.1016/0375-9601(95)00418-3

Frossard E, Hu W, Dano C, Hicher P-Y. (2012). Rockfill shear strength evaluation: a rational method based on size effects. *Géotechnique 62*:415-427. doi:https://doi.org/10.1680/geot.10.P.079

Gan-Mor S, Galili N. (1987). Model for failure and plastic-flow in dynamic loading of spheres. *Transactions of the ASAE 30*:1506-1511

Gaudin AM, Meloy TP. (1962). Model and a comminution distribution equation for single fracture. *Transaction of AIME 223*:40-50

Ghaednia H, Marghitu DB, Jackson RL. (2014). Predicting the Permanent Deformation After the Impact of a Rod With a Flat Surface. *Journal of Tribology 137*. doi:https://doi.org/10.1115/1.4028709

Giacomini A, Buzzi O, Renard B, Giani GP. (2009). Experimental studies on fragmentation of rock falls on impact with rock surfaces. *International Journal of Rock Mechanics and Mining Sciences 46*:708-715. doi:http://dx.doi.org/10.1016/j.ijrmms.2008.09.007

Giacomini A, Spadari M, Buzzi O, Fityus SG, Giani GP. *Rockfall motion characteristics on natural slopes of eastern australia.* In: Rock Mechanics in Civil and Environmental Engineering - Proceedings of the European Rock Mechanics Symposium, EUROCK 2010, 2010. pp 621-624

Giacomini A, Thoeni K, Lambert C, Booth S, Sloan SW. (2012). Experimental study on rockfall drapery systems for open pit highwalls. *International Journal of Rock Mechanics and Mining Sciences 56*:171-181. doi:https://doi.org/10.1016/j.ijrmms.2012.07.030

Giani GP. (1992). *Rock slope stability analysis.* CRC Press, Balkera

Giani GP, Giacomini A, Migliazza M, Segalini A. (2004). Experimental and Theoretical Studies to Improve Rock Fall Analysis and Protection Work Design. *Rock Mechanics and Rock Engineering 37*:369-389. doi:https://doi.org/10.1007/s00603-004-0027-2

Gili JA et al. *Experimental study on rockfall fragmentation: In situ test design and first results.* In: Landslides and Engineered Slopes. Experience, Theory and Practice, 2016. pp 983-990

Gilvarry JJ. (1961). Fracture of brittle solids. I. Distribution function for fragment size in single fracture (theoretical). *Journal of Applied Physics 32*:391-399

Gilvarry JJ, Bergstrom BH. (1961a). Fracture and comminution of brittle solids (theory and experiment). *Transaction of AIME 220*:380-389

Gilvarry JJ, Bergstrom BH. (1961b). Fracture of Brittle Solids. II. Distribution Function for Fragment Size in Single Fracture (Experimental). *Journal of Applied Physics 32*:400-410. doi:https://doi.org/10.1063/1.1736017

Giokari S, Pavlos A, Saroglou H, Tsiambaos G. (2015). *Rockfalls: Experimental Investigation of the Effect of Surface Weathering on the Coefficients of Restitution*. doi:https://doi.org/10.1007/978-3-319-09057-3_363

Gischig VS, Hungr O, Mitchell A, Bourrier F. (2015). Pierre3D: a 3D stochastic rockfall simulator based on random ground roughness and hyperbolic restitution factors. *Canadian Geotechnical Journal 52*:1360-1373. doi:https://doi.org/10.1139/cgj-2014-0312

Goldsmith W. (1960). *Impact: The Theory and Physical Behaviour of Colliding Solids*. Edward Arnold Publishers, Dover

Gorham DA, Salman AD. (2005). The failure of spherical particles under impact. *Wear 258*:580-587. doi:https://doi.org/10.1016/j.wear.2004.09.012

Gorham DA, Salman AD, Pitt MJ. (2003). Static and dynamic failure of PMMA spheres. *Powder Technology 138*:229-238. doi:https://doi.org/10.1016/j.powtec.2003.09.008

Grady DE. (1981). Fragmentation of solids under impulsive stress loading. *Journal of Geophysical Research: Solid Earth 86*:1047-1054

Grady DE. (1982). Local inertial effects in dynamic fragmentation. *Journal of Applied Physics 53*:322-325. doi:https://doi.org/10.1063/1.329934

Grady DE, Benson DA. (1983). Fragmentation of metal rings by electromagnetic loading. *Experimental Mechanics 23*:393-400. doi:https://doi.org/10.1007/bf02330054

Grady DE, Kipp ME. (1980). Continuum modelling of explosive fracture in oil shale. *International Journal of Rock Mechanics and Mining Sciences & Geomechanics Abstracts 17*:147-157. doi:https://doi.org/10.1016/0148-9062(80)91361-3

Grady DE, Kipp ME. (1985). Geometric statistics and dynamic fragmentation. *Journal of Applied Physics 58*:1210-1222

Grady DE, Kipp ME. (1987). Dynamic rock fragmentation. In: *Fracture mechanics of rock*. vol 10. p 429

Griffith AA. (1920). The phenomena of flow and rupture in solids *Phil Trans Roy Soc Lond Ser A 221*:163-198

Guccione DE, Thoeni K, Fityus S, Buzzi O, Giacomini A. (2019). *Development of an apparatus to track rock fragment trajectory in 3D*. Paper presented at the Rock Mechanics for Natural Resources and Infrastructure Development-Full Papers: Proceedings of the 14th International

Congress on Rock Mechanics and Rock Engineering (ISRM 2019), September 13-18, 2019, Foz do Iguassu, Brazil,

Guccione DE, Thoeni K, Giacomini A, Buzzi O, Fityus S. (2020). Efficient multi-view 3D tracking of arbitrary rock fragments upon impact. *International Archives of the Photogrammetry, Remote Sensing and Spatial Information Sciences XLIII-B2-2020*:589-596. doi:https://doi.org/10.5194/isprs-archives-XLIII-B2-2020-589-2020

Guzzetti F, Crosta G, Detti R, Agliardi F. (2002). STONE: a computer program for the three-dimensional simulation of rock-falls. *Computers & Geosciences 28*:1079-1093. doi:https://doi.org/10.1016/S0098-3004(02)00025-0

Hadas A, Wolf D. (1984). Soil Aggregates and Clod Strength Dependence on Size, Cultivation, and Stress Load Rates 1. *Soil Science Society of America Journal 48*:1157-1164

Heidenreich B. (2004). *Small- and half-scale experimental studies of rockfall impacts on sandy slopes, Ph.D Thesis.* Ph.D Thesis,

Hertz HR. (1882). Uber die Beruhrung fester elastischer Korper und Uber die Harte. *Verhandlung des Vereins zur Beforderung des GewerbefleiBes, Berlin*:449

Hiramatsu Y, Oka Y. (1966). Determination of the tensile strength of rock by a compression test of an irregular test piece. *International Journal of Rock Mechanics and Mining Sciences & Geomechanics Abstracts 3*:89-90. doi:https://doi.org/10.1016/0148-9062(66)90002-7

Hoek E. (1987). Rockfall: a computer program for prediction rockfall trajectors. *ISRM News Journal 2*:4-16

Hoek E, Bieniawski Z. (1965). Brittle fracture propagation in rock under compression. *International Journal of Fracture Mechanics 1*:137-155

Hou T-x, Xu Q, Xie H-q, Xu N-w, Zhou J-w. (2017). An estimation model for the fragmentation properties of brittle rock block due to the impacts against an obstruction. *Journal of Mountain Science 14*:1161-1173. doi:https://doi.org/10.1007/s11629-017-4398-8

Huang J, Xu S, Yi H, Hu S. (2014a). Size effect on the compression breakage strengths of glass particles. *Powder Technology 268*:86-94. doi:https://doi.org/10.1016/j.powtec.2014.08.037

Huang S, Liu H, Xia K. (2014b). A dynamic ball compression test for understanding rock crushing. *Review of Scientific Instruments 85*:123902. doi:https://doi.org/10.1063/1.4902836

Huber MT. (1904). Zur theorie der Berührung fester elastischer Körper. *Annalen der Physik 319*:153-163

Hungr O, Evans SG. (1988). Engineering evaluation of fragmental rockfall hazards. *Landslides Proc 5th symposium, Lausanne, 1988 Vol 1*:685-690

Image Systems Motion Analysis. (2019). TEMA3D. http://www.imagesystems.se/tema/. Accessed 28 February 2020

Imre B, Räbsamen S, Springman SM. (2008). A coefficient of restitution of rock materials. *Computers & Geosciences 34*:339-350. doi:https://doi.org/10.1016/j.cageo.2007.04.004

Irwin G. (1958). Fracture. Encyclopaedia of Physics, Vol. VI. *Springer-Verlag 1*:168

ISRM. (1978). Suggested methods for determining tensile strength of rock materials. *International Journal of Rock Mechanics and Mining Sciences & Geomechanics Abstracts 15*:99-103. doi:https://doi.org/10.1016/0148-9062(78)90003-7

Jaboyedoff M, Dudt JP, Labiouse V. (2005). An attempt to refine rockfall hazard zoning based on the kinetic energy, frequency and fragmentation degree. *Natural Hazards and Earth System Sciences 5*:621-632

Jackson RL, Green I, Marghitu DB. (2010). Predicting the coefficient of restitution of impacting elastic-perfectly plastic spheres. *Nonlinear Dynamics 60*:217-229. doi:https://doi.org/10.1007/s11071-009-9591-z

Jaeger JC. (1967). Failure of rocks under tensile conditions. *International Journal of Rock Mechanics and Mining Sciences & Geomechanics Abstracts 4*:219-227. doi:https://doi.org/10.1016/0148-9062(67)90046-0

Japaridze L. (2015). Stress-deformed state of cylindrical specimens during indirect tensile strength testing. *Journal of Rock Mechanics and Geotechnical Engineering 7*:509-518. doi:https://doi.org/10.1016/j.jrmge.2015.06.006

Ji Z-M, Chen Z-J, Niu Q-H, Wang T-J, Song H, Wang T-H. (2019). Laboratory study on the influencing factors and their control for the coefficient of restitution during rockfall impacts. *Landslides 16*:1939-1963. doi:https://doi.org/10.1007/s10346-019-01183-x

Jones CL, Higgins JD, Andrew RD. (2000). Colorado Rockfall Simulation Program Users Manual for Version 4.0. Denver: Colorado Department of Transportation. *Colorado Rockfall Simulation Program Version 40*

Kamijo A, Onda S, Masuya H, Tanaka Y. (2000). Fundamental test on restitution coefficient and frictional coefficient of rock fall. *5th Symposium on Impact Problems in Civil Engineering*:83-86

Kapur PC, Fuerstenau DW. (1967). Dry strength of pelletized spheres. *Journal of the American Ceramic Society 50*:14-18

Kawahara S, Muro T. (1999). Effect of soil slope gradient on motion of rockfall. *International Symposium on Slope Stability Engineering 2*:1343-1348

Kawakami S, Kanaori Y, Fujiwara A. (1990). Microcracks induced in granite spheres by projectile impact at velocities ranging from 2.3 to 3.6 km/s. *Rock Mechanics and Rock Engineering 23*:39-51. doi:https://doi.org/10.1007/bf01020421

Khanal M, Schubert W, Tomas J. (2008). Compression and impact loading experiments of high strength spherical composites. *International Journal of Mineral Processing 86*:104-113. doi:https://doi.org/10.1016/j.minpro.2007.12.001

Kipp ME, Grady DE, Chen EP. (1980). Strain-rate dependent fracture initiation. *International Journal of Fracture 16*:471-478

Kirkby MJ, Statham I. (1975). Surface stone movement and scree formation. *Journal of Geology 83*:349-362

Kobayashi Y, Harp EL, Kagawa T. (1990). Simulation of rockfalls triggered by earthquakes. *Rock Mechanics and Rock Engineering 23*:1-20. doi:https://doi.org/10.1007/BF01020418

Kolmogorov AN. *On the degeneration of isotropic turbulence in an incompressible viscous fluid.* In: Dokl. Akad. Nauk SSSR, 1941. pp 319-323

Kschinka BA, Perrella S, Nguyen H, Bradt RC. (1986). Strengths of glass spheres in compression. *Journal of the American Ceramic Society 69*:467-472

Kuruppu MD, Obara Y, Ayatollahi MR, Chong KP, Funatsu T. (2014). ISRM-Suggested Method for Determining the Mode I Static Fracture Toughness Using Semi-Circular Bend Specimen. *Rock Mechanics and Rock Engineering 47*:267-274. doi:https://doi.org/10.1007/s00603-013-0422-7

Kuwabara G, Kono K. (1987). Restitution Coefficient in a Collision between Two Spheres. *Japanese Journal of Applied Physics 26*:1230-1233. doi:https://doi.org/10.1143/jjap.26.1230

Kuznetsov VM, Faddeenkov NN. (1975). Fragmentation schemes. *Combustion, Explosion and Shock Waves 11*:541-548. doi:https://doi.org/10.1007/bf00744924

Labiouse V, Descoeudres F. *Possibilities and difficulties in predicting rockfall trajectories.* In: Proc. of the Joint Japan-Swiss Scientific Seminar on Impact Load by Rock Falls and Design of Protection Structures, Kanazawa, Japan, 1999. pp 29-36

Labiouse V, Heidenreich B. (2009). Half-scale experimental study of rockfall impacts on sandy slopes. *Natural Hazards and Earth System Sciences 9*:1981-1993. doi:https://doi.org/10.5194/nhess-9-1981-2009

Labous L, Rosato AD, Dave RN. (1997). Measurements of collisional properties of spheres using high-speed video analysis. *Physical review E 56*:5717

Langefors U, Kihlström B. (1978). *The modern technique of rock blasting*. Wiley,

Lied K. (1977). Rockfall problems in Norway. *Rockfall Dynamics and Protective Work Effectiveness 90*:51-53

Lienau CC. (1936). Random fracture of a brittle solid. *Journal of the Franklin Institute 221*:769-787

Lisjak A, Spadari M, Giacomini A, Grasselli G. (2010). *Numerical modelling of rock falls using a combined finite-discrete element approach*. Paper presented at the In Proceedings of the symposium rock slope stability, Paris, France,

Liu L, Kafui KD, Thornton C. (2010). Impact breakage of spherical, cuboidal and cylindrical agglomerates. *Powder Technology 199*:189-196. doi:https://doi.org/10.1016/j.powtec.2010.01.007

Lurje AI. (1963). *Räumliche Probleme der Elastizitätstheorie*. Akademie-Verlag, Berlin

Masuya H, Ihara T, Onda S, Kamijo A. (2001). Experimental study on some parameters for simulation of rock fall on slope. *Fourth Asia-Pacific Conf on Shock and Impact Loads on Structures*:63-69

Matas G. (2020). *Modelling fragmentation in rockfalls*. Department of Civil and environmental engineering. Universitat Politècnica de Catalunya (UPC-BarcelonaTech).

Matas G, Lantada N, Corominas J, Gili J, Ruiz-Carulla R, Prades A. (2020). Simulation of Full-Scale Rockfall Tests with a Fragmentation Model. *Geosciences 10*:168

Matas G, Lantada N, Corominas J, Gili JA, Ruiz-Carulla R, Prades A. (2017). RockGIS: a GIS-based model for the analysis of fragmentation in rockfalls. *Landslides 14*:1565-1578. doi:https://doi.org/10.1007/s10346-017-0818-7

Maxim RE, Salman AD, Hounslow MJ. (2006). Predicting dynamic failure of dense granules from static compression tests. *International Journal of Mineral Processing 79*:188-197. doi:https://doi.org/10.1016/j.minpro.2006.02.003

McDowell GR, Amon A. (2000). The Application of Weibull Statistics to the Fracture of Soil Particles. *Soils and Foundations 40*:133-141. doi:https://doi.org/10.3208/sandf.40.5_133

Melosh HJ. (1984). Impact ejection, spallation, and the origin of meteorites. *Icarus, International Journal of the Solar System 59*:234-260

Meyers MA, Meyers PP. (1983). Compressive strength of iron-ore agglomerates. *Transactions of the Society of Mining Engineers of AIME 274*:1875-1884

Mock WJ, Holt WH. (1983). Fragmentation behavior of Armco iron and HF-1 steel explosive-filled cylinders. *Journal of Applied Physics 54*:2344-2351

Moreno R, Ghadiri M, Antony SJ. (2003). Effect of the impact angle on the breakage of agglomerates: a numerical study using DEM. *Powder Technology 130*:132-137. doi:https://doi.org/10.1016/S0032-5910(02)00256-5

Mott NF, Linfoot EH. (1943). A Theory of Fragmentation, Extra-Mural Research No. *F72/80, Ministry of Supply, AC 3348*

Murata S, Shibuya H. (1997). Measurement of impact loads on the rockfall prevention walls and speed of falling rocks using a middle size slope model. *2nd Asia-Pacific Conference on Shock & Impact Loads on Structures*:383-393

Nader F, Thoeni K, Giacomini A, Fityus S, Buzzi O. (2021). Numerical investigation of the strength variability of rock using DEM. Accepted at the 16th International Conference of the International Association for Computer Methods and Advances in Geomechanics – IACMAG. Turin, Italy

Nakata AFL, Hyde M, Hyodo H, Murata H. (1999). A probabilistic approach to sand particle crushing in the triaxial test. *Géotechnique 49*:567-583

Newitt DM, Conwya-Jones JM. (1958). A contribution to the theory and practice of granulation. *Transactions of the Institution of Chemical Engineers 36*:422-442

Newton I. (1687). *Philosophiae naturalis principia mathematica*. Cambrige University Press, Cambrige

O'Keefe JD, Ahrens TJ. *Impact ejecta on the moon*. In: Lunar and Planetary Science Conference Proceedings, 1976. pp 3007-3025

Ovalle C, Frossard E, Dano C, Hu W, Maiolino S, Hicher P-Y. (2014). The effect of size on the strength of coarse rock aggregates and large rockfill samples through experimental data. *Acta Mechanica 225*:2199-2216. doi:https://doi.org/10.1007/s00707-014-1127-z

Paluszny A, Tang X, Nejati M, Zimmerman RW. (2016). A direct fragmentation method with Weibull function distribution of sizes based on finite- and discrete element simulations. *International Journal of Solids and Structures 80*:38-51. doi:https://doi.org/10.1016/j.ijsolstr.2015.10.019

Paronuzzi P. (2009). Field evidence and kinematical back-analysis of block rebounds: The lavone rockfall, Northern Italy. *Rock Mechanics and Rock Engineering 42*:783-813. doi:https://doi.org/10.1007/s00603-008-0021-1

Peila D, Ronco C. (2009). Design of rockfall net fences and the new ETAG 027 European guideline. *Natural Hazards and Earth System Sciences 9*:1291

Perfect E. (1997). Fractal models for the fragmentation of rocks and soils: a review. *Engineering Geology 48*:185-198. doi:http://dx.doi.org/10.1016/S0013-7952(97)00040-9

Perras MA, Diederichs MS. (2014). A Review of the Tensile Strength of Rock: Concepts and Testing. *Geotechnical and Geological Engineering 32*:525-546. doi:http://dx.doi.org/10.1007/s10706-014-9732-0

Pfeiffer TJ, Bowen TD. (1989). Computer simulation of rockfalls. *Bulletin - Association of Engineering Geologists 26*:135-146

Piteau D, Clayton R. *Discussion of paper Computerized design of rock slopes using interactive graphics for the input and output of geometrical databy Cundall, P.* In: Proceedings of the 16th Symposium on Rock Mechanics, Minneapolis, USA, 1977. pp 62-63

Reddish DJ, Stace LR, Vanichkobchinda P, Whittles DN. (2005). Numerical simulation of the dynamic impact breakage testing of rock. *International Journal of Rock Mechanics and Mining Sciences 42*:167-176. doi:https://doi.org/10.1016/j.ijrmms.2004.06.004

Ritchie AM. (1963). Evaluation of rockfall and its control. *Highway Research Record 17*:13-28

Rochet L. (1987). Application des modèles numériques de propagation a l'étude des éboulements rocheux. *Bulletin de liaison des laboratoires des ponts et chaussèes 150-151*:84-95

Rosin P, Rammler E. (1933). Regularities in the distribution of cement particles. *J Inst Fuel 7*:29-33

Ruiz-Carulla R, Corominas J. (2020). Analysis of Rockfalls by Means of a Fractal Fragmentation Model. *Rock Mechanics and Rock Engineering 53*:1433-1455. doi:https://doi.org/10.1007/s00603-019-01987-2

Ruiz-Carulla R et al. (2020). Analysis of Fragmentation of Rock Blocks from Real-Scale Tests. *Geosciences 10*:308

Ruiz-Carulla R, Corominas J, Mavrouli O. (2015). A methodology to obtain the block size distribution of fragmental rockfall deposits. *Landslides 12*:815-825. doi:https://doi.org/10.1007/s10346-015-0600-7

Ruiz-Carulla R, Corominas J, Mavrouli O. (2017). A fractal fragmentation model for rockfalls. *Landslides 14*:875-889. doi:https://doi.org/10.1007/s10346-016-0773-8

Russell A, Schmelzer J, Müller P, Krüger M, Tomas J. (2015). Mechanical properties and failure probability of compact agglomerates. *Powder Technology 286*:546-556. doi:https://doi.org/10.1016/j.powtec.2015.08.045

Salman AD, Biggs CA, Fu J, Angyal I, Szabó M, Hounslow MJ. (2002). An experimental investigation of particle fragmentation using single particle impact studies. *Powder Technology 128*:36-46. doi:https://doi.org/10.1016/S0032-5910(02)00151-1

Salman AD, Gorham DA. (1997). The fracture of glass spheres under impact loading. *Powders & Grains 97*

Salman AD et al. (2004). Descriptive classification of the impact failure modes of spherical particles. *Powder Technology 143-144*:19-30. doi:https://doi.org/10.1016/j.powtec.2004.04.005

Santurbano R. (1994). *An experimental and analytical study of the mechanics of rock particle fragmentation during impact crushing*. PhD dissertation, University of Minnesota, USA.

Sator N, Hietala H. (2010). Damage in impact fragmentation. *International Journal of Fracture 163*:101-108. doi:https://doi.org/10.1007/s10704-009-9406-8

Schönert K. (2004). Breakage of spheres and circular discs. *Powder Technology 143-144*:2-18. doi:https://doi.org/10.1016/j.powtec.2004.04.004

Schubert H. (1975). Tensile strength of agglomerates. *Powder Technology 11*:107-119. doi:https://doi.org/10.1016/0032-5910(75)80036-2

Scioldo G. (2006). User guide ISOMAP & ROTOMAP-3D surface modelling and rockfall analysis. http://www.geoandsoft.com/manuali/english/rotomap.pdf.

Seifried R, Schiehlen W, Eberhard P. (2005). Numerical and experimental evaluation of the coefficient of restitution for repeated impacts. *International Journal of Impact Engineering 32*:508-524. doi:https://doi.org/10.1016/j.ijimpeng.2005.01.001

Shen W-G, Zhao T, Crosta GB, Dai F. (2017). Analysis of impact-induced rock fragmentation using a discrete element approach. *International Journal of Rock Mechanics and Mining Sciences 98*:33-38. doi:http://dx.doi.org/10.1016/j.ijrmms.2017.07.014

Shinohara K, Capes CE. (1979). Effect of distributed loading on stress patterns in discoidal agglomerates during the diametral compression test. *Powder Technology 24*:179-186. doi:https://doi.org/10.1016/0032-5910(79)87035-7

Shipway PH, Hutchings IM. (1993a). Attrition of brittle spheres by fracture under compression and impact loading. *Powder Technology 76*:23-30. doi:https://doi.org/10.1016/0032-5910(93)80037-B

Shipway PH, Hutchings IM. (1993b). Fracture of brittle spheres under compression and impact loading. I. Elastic stress distributions. *Philosophical Magazine A 67*:1389-1404

Shipway PH, Hutchings IM. (1993c). Fracture of brittle spheres under compression and impact loading. II. Results for lead-glass and sapphire spheres. *Philosophical Magazine A 67*:1405-1421

Shockey DA, Curran DR, Seaman L, Rosenberg JT, Petersen CF. (1974). Fragmentation of rock under dynamic loads. *International Journal of Rock Mechanics and Mining Sciences & Geomechanics Abstracts 11*:303-317. doi:https://doi.org/10.1016/0148-9062(74)91760-4

Sikong L, Hashimoto H, Yashima S. (1990). Breakage behavior of fine particles of brittle minerals and coals. *Powder Technology 61*:51-57. doi:https://doi.org/10.1016/0032-5910(90)80065-7

Spadari M, Giacomini A, Buzzi O, Fityus S, Giani GP. (2012). In situ rockfall testing in New South Wales, Australia. *International Journal of Rock Mechanics and Mining Sciences 49*:84-93. doi:https://doi.org/10.1016/j.ijrmms.2011.11.013

Statham I. (1979). A simple dynamic model of rockfall: Some theoretical principles and field experiments. *International Colloquium on Physical and Geomechanical Models*:237-258

Statham I, Francis S. (1986). Hillslope processes. *Influence of Scree Accumulation and Weathering on the Development of Steep Mountain Slopes*

Sternberg E, Rosenthal F. (1952). The elastic sphere under concentrated loads. *Journal of Applied Mechanics-Transactions of the ASME 19*:413-421

Stevens W. (1998). *Rockfall: A tool for probabilistic analysis, design of remedial measures and prediction of rockfalls, Master's Thesis.* Master's Thesis, University of Toronto.

Stronge WJ. (2000). *Impact Mechanics.* Cambridge University Press, Cambridge. doi:https://doi.org/10.1017/CBO9780511626432

Teraoka M, Iguchi H, Ichikawa T, Nishigaki Y, Sakurai S. (2000). Analysis of motion for rock falling on a natural slope by using digital video image. *5th Symposium on Impact Problems in Civil Engineering*:87-90

Thoeni K, Giacomini A, Lambert C, Sloan SW, Carter JP. (2014). A 3D discrete element modelling approach for rockfall analysis with drapery systems. *International Journal of Rock Mechanics and Mining Sciences 68*:107-119. doi:https://doi.org/10.1016/j.ijrmms.2014.02.008

Thorby D. (2008). *Structural dynamics and vibration in practice.* Elsevier,

Thornton C. (1997). Coefficient of Restitution for Collinear Collisions of Elastic-Perfectly Plastic Spheres. *Journal of Applied Mechanics 64*:383-386. doi:https://doi.org/10.1115/1.2787319

Thornton C, Yin KK, Adams MJ. (1996). Numerical simulation of the impact fracture and fragmentation of agglomerates. *Journal of Physics D: Applied Physics 29*:424

Tomas J, Schreier M, Gröger T, Ehlers S. (1999). Impact crushing of concrete for liberation and recycling. *Powder Technology 105*:39-51. doi:https://doi.org/10.1016/S0032-5910(99)00116-3

Turner AK, Schuster RL. (2013). *Rockfall characterization and control*. Transportation Research Board, Washington, D.C.

Urciuoli G. (1996). *Giornata di Studio Su la Protezione Contro la Caduta Massi Dai Versanti Rocciosi*. Torino, Italy,

Ushiro T, Shinohara S, Tanida K, Yagi N. (2000). A study on the motion of rockfalls on slopes. *Proceedings of the 5th Symposium on Impact Problems in Civil Engineering*:91-96

Varnado SG, Stoller HM. (1978). Geothermal drilling and completion technology development. Sandia Labs., Albuquerque, NM (USA),

Virtanen P et al. (2020). SciPy 1.0: Fundamental Algorithms for Scientific Computing in Python. *Nature Methods*. doi:https://doi.org/10.1038/s41592-019-0686-2

Volkwein A, Gerber W, Klette J, Spescha G. (2019). Review of Approval of Flexible Rockfall Protection Systems According to ETAG 027. *Geosciences 9*:49

Volkwein A, Klette J. (2014). Semi-Automatic Determination of Rockfall Trajectories. *Sensors 14*:18187-18210

Volkwein A et al. (2011). Rockfall characterisation and structural protection - a review. *Natural Hazards and Earth System Sciences 11*:2617-2651. doi:https://doi.org/10.5194/nhess-11-2617-2011

Wang QJ, Zhu D. (2013). Contact Yield. In: Wang QJ, Chung Y-W (eds) *Encyclopedia of Tribology*. Springer US, Boston, MA, pp 559-566. doi:https://doi.org/10.1007/978-0-387-92897-5_503

Wang Y. (2009). *Three-dimensional rock-fall analysis with impact fragmentation and fly-rock modeling*. PhD Thesis, The University of Texas at Austin.

Wang Y, Dan W, Xu Y, Xi Y. (2015). Fractal and morphological characteristics of single marble particle crushing in uniaxial compression tests. *Advances in Materials Science and Engineering 2015*. doi:https://doi.org/10.1155/2015/537692

Wang Y, Tonon F. (2011). Discrete Element Modeling of Rock Fragmentation upon Impact in Rock Fall Analysis. *Rock Mechanics and Rock Engineering 44*:23-35. doi:https://doi.org/10.1007/s00603-010-0110-9

Warpinski NR, Schmidt RA, Cooper PW, Walling HC, Northrop DA. *High-energy gas frac: multiple fracturing in a wellbore*. In: 20th US Symposium on Rock Mechanics (USRMS), 1979. American Rock Mechanics Association, Wei XX, Chau KT. (1998). Spherically isotropic spheres subject to diametral point load test: Analytic solutions. *International Journal of Rock Mechanics and Mining Sciences 35*:623-624. doi:https://doi.org/10.1016/S0148-9062(98)00022-9

Weibull W. (1951). A statistical distribution function of wide applicability. *J Appl Mech 18*:290-293

Weimer RJ, Rogers HC. (1979). Dynamic fracture phenomena in high-strength steels. *Journal of Applied Physics 50*:8025-8030

Wittel FK, Carmona HA, Kun F, Herrmann HJ. (2008). Mechanisms in impact fragmentation. *International Journal of Fracture 154*:105-117. doi:https://doi.org/10.1007/s10704-008-9267-6

Wong JY, Laurich-McIntyre SL, Khaund AK, Bradt RC. (1987). Strengths of green and fired spherical aluminosilicate aggregates. *Journal of the American Ceramic Society 70*:785-791

Wong RH, Ho K, Chau KT. (1999). Experimental study for rockfall simulation. *Construction Challenges into the Next Century*:92-97

Wong RHC, Ho KW, Chau KT. *Shape and mechanical properties of slope material effects on the coefficient of restitution of rockfall study*. In: 4th North American Rock Mechanics Symposium, 2000. American Rock Mechanics Association,

Wu S-S. (1985). Rockfall evaluation by computer simulation. *Transportation Research Record*:1-5

Wu S, Chen X, Zhou J. (2012). Tensile strength of concrete under static and intermediate strain rates: Correlated results from different testing methods. *Nuclear Engineering and Design 250*:173-183. doi:https://doi.org/10.1016/j.nucengdes.2012.05.004

Wu SZ, Chau KT. (2006). Dynamic response of an elastic sphere under diametral impacts. *Mechanics of Materials 38*:1039-1060. doi:https://doi.org/10.1016/j.mechmat.2005.08.005

Wu SZ, Chau KT, Yu TX. (2004). Crushing and fragmentation of brittle spheres under double impact test. *Powder Technology 143-144*:41-55. doi:https://doi.org/10.1016/j.powtec.2004.04.028

Wyllie DC. (2014a). Calibration of rock fall modeling parameters. *International Journal of Rock Mechanics and Mining Sciences 67*:170-180. doi:https://doi.org/10.1016/j.ijrmms.2013.10.002

Wyllie DC. (2014b). *Rock fall engineering*. CRC Press,

Wynnyckyj JR. (1985). The correlation between the strength factor and the true tensile strength of agglomerate spheres. *The Canadian Journal of Chemical Engineering 63*:591-597

Yang M, Fukawa T, Ohnishi Y, Nishiyama S, Miki S, Hirakawa Y, Mori S. (2004). The application of 3-dimensional dda with a spherical rigid block for rockfall simulation. *International Journal of Rock Mechanics and Mining Sciences 41*:2B 25 21-26. doi:https://doi.org/10.1016/j.ijrmms.2004.03.108

Yashima S, Kanda Y, Sano S. (1987). Relationships between particle size and fracture energy or impact velocity required to fracture as estimated from single particle crushing. *Powder Technology 51*:277-282. doi:http://dx.doi.org/10.1016/0032-5910(87)80030-X

Ye Y, Thoeni K, Zeng Y, Buzzi O, Giacomini A. (2019a). Numerical Investigation of the Fragmentation Process in Marble Spheres Upon Dynamic Impact. *Rock Mechanics and Rock Engineering*. doi:https://doi.org/10.1007/s00603-019-01972-9

Ye Y, Zeng Y. (2017). A size-dependent viscoelastic normal contact model for particle collision. *International Journal of Impact Engineering 106*:120-132. doi:https://doi.org/10.1016/j.ijimpeng.2017.03.020

Ye Y, Zeng Y, Thoeni K, Giacomini A. (2019b). An Experimental and Theoretical Study of the Normal Coefficient of Restitution for Marble Spheres. *Rock Mechanics and Rock Engineering 52*:1705-1722. doi:https://doi.org/10.1007/s00603-018-1709-5

Yoshida H. (1998). Movement of boulders on slope and its simulation, Recent studies on rockfall control in Japan. *Tech Rep*

Yoshikawa H, Sata T. (1960). Measurement of tensile strength of granular brittle materials. *Scientific papers of the Institute of Physical and Chemical Research 54*:389 - 393

Zener C. (1941). The Intrinsic Inelasticity of Large Plates. *Physical Review 59*:669-673

Zhang QB, Zhao J. (2014a). Quasi-static and dynamic fracture behaviour of rock materials: phenomena and mechanisms. *International Journal of Fracture 189*:1-32. doi:https://doi.org/10.1007/s10704-014-9959-z

Zhang QB, Zhao J. (2014b). A Review of Dynamic Experimental Techniques and Mechanical Behaviour of Rock Materials. *Rock Mechanics and Rock Engineering 47*:1411-1478. doi:https://doi.org/10.1007/s00603-013-0463-y

Zhao T, Crosta GB, Utili S, De Blasio FV. (2017). Investigation of rock fragmentation during rockfalls and rock avalanches via 3-D discrete element analyses. *Journal of Geophysical Research: Earth Surface 122*:678-695. doi:https://doi.org/10.1002/2016JF004060

Appendix A

An impact survival probability following a Weibull distribution and expressed in terms of kinetic energy is written as:

$$SP(E^b_{k(D)}) = 100 \cdot e^{-\left(\frac{E^b_{k(D)}}{E^{cr}_{k(D)}}\right)^{\mu_E}} \tag{A-1}$$

with $SP(E^b_{K(D)})$ in percent and $E^b_{k(D)}$ in joules.

The slope of the central part of the Weibull distribution can be approximated as the gradient G of the cumulative Weibull curve at the critical value of energy, which is written:

$$G = \left.\frac{dSP\left(E^b_{k(D)}\right)}{dE^b_{k(D)}}\right|_{E^b_{k(D)}=E^{cr}_{k(D)}} = \frac{-100 \cdot \mu_E}{e \cdot E^{cr}_{k(D)}} \tag{A-2}$$

The linear evolution of $SP(E_{K(D)})$ with $E_{K(D)}$ can hence be formulated as:

$$SP\left(E_{K(D)}\right) = \frac{-100 \cdot \mu_E}{e \cdot E^{cr}_{K(D)}} \cdot E_{K(D)} + b \tag{A-3}$$

Since for $E^b_{k(D)} = E^{cr}_{k(D)}$, $SP\left(E^{cr}_{k(D)}\right) = 37\%$, we can identify b:

$$b = 37 + \frac{100 \cdot \mu_E}{e} \tag{A-4}$$

Consequently, the linear function $SP(E^b_{k(D)})$ can be written as:

$$SP\left(E^b_{k(D)}\right) = 37 + \frac{100 \cdot \mu_E}{e} \cdot \left(1 - \frac{E^b_{k(D)}}{E^{cr}_{k(D)}}\right) \tag{A-5}$$

In order to predict the kinetic energy for a given survival probability Eq. (A-5) needs to be re-formulated as:

$$E_{k(D)}^{b} = E_{k(D)}^{cr}\left(1 - \frac{\left(SP\left(E_{k(D)}^{b}\right) - 37\right) \cdot e}{100 \cdot \mu_E}\right) \tag{A-6}$$

Eq. (A-6) can also be applied to the impact velocity:

$$v_{imp(D)} = v_{imp(D)}^{cr}\left(1 - \frac{\left(SP\left(v_{imp(D)}\right) - 37\right) \cdot e}{100 \cdot \mu_V}\right) \tag{A-7}$$

Appendix B

Table B-1 Characteristics of fragments with significant motion for all tests of S3.2.

		Mass [g]	Volume [cm³]	Fracture area [m²]	v_{xy} [m/s]	v_z [m/s]	v [m/s]	E_{kt}^a [J]	I_I [kg*m²]	I_{II} [kg*m²]	I_{III} [kg*m²]	ω_I [rad/s]	ω_{II} [rad/s]	ω_{III} [rad/s]	E_{kt}^a [J]
1	Frag 1	632.9	325.02	8.12E-03	0.20	2.17	2.17	1.50	4.49E-04	4.73E-04	6.69E-04	2.91	2.16	4.09	0.01
	Frag 2	386.5	198.49	8.10E-03	0.10	2.30	2.30	1.02	1.96E-04	2.22E-04	3.36E-04	11.94	5.80	15.01	0.06
2	Frag 1	560	287.59	8.23E-03	0.48	2.34	2.39	1.60	3.67E-04	3.79E-04	5.51E-04	2.49	3.25	1.83	0.00
	Frag 2	452.8	232.53	8.27E-03	0.40	2.50	2.53	1.45	2.75E-04	2.95E-04	4.54E-04	6.60	11.00	2.68	0.03
3	Frag 1*	774.4	397.69	1.67E-02	0.12	2.15	2.16	1.80	3.00E-04	4.27E-03	4.06E-04	2.01	1.94	3.91	0.01
	Frag 2	237	121.71	7.01E-03	0.38	2.07	2.11	0.53	8.38E-05	1.11E-04	1.63E-04	8.51	1.79	3.75	0.00
4	Frag 1	4.8	2.47	6.48E-04	1.05	1.24	1.63	0.01	7.34E-08	2.13E-07	2.32E-07	1.08	11.19	34.94	0.00
	Frag 2	126.7	65.07	5.32E-03	1.31	1.76	2.20	0.31	3.30E-05	4.21E-05	6.77E-05	11.05	34.37	5.06	0.03
	Frag 3	97.1	49.87	4.74E-03	0.70	1.54	1.69	0.14	1.49E-05	3.40E-05	4.16E-05	4.36	11.15	6.86	0.00
	Frag 4*	868.7	446.12	1.33E-02	0.19	1.80	1.81	1.43	7.79E-04	8.55E-04	8.82E-04	1.80	3.77	6.12	0.02
5	Frag 1	144.2	74.05	5.53E-03	0.43	1.78	1.83	0.24	3.36E-05	5.44E-05	7.69E-05	5.08	11.36	3.21	0.00
	Frag 2*	928.8	476.98	1.70E-02	0.20	1.84	1.85	1.59	9.15E-04	9.91E-04	1.05E-03	2.88	1.93	1.66	0.01
6	Frag 1	264.2	135.68	7.12E-03	0.51	2.06	2.12	0.59	1.02E-04	1.33E-04	1.98E-04	2.11	3.29	1.84	0.00
	Frag 2	750.9	385.62	7.16E-03	0.30	2.26	2.28	1.95	5.81E-04	6.14E-04	7.98E-04	1.91	0.73	0.98	0.00
7	Frag 1	477.49	245.21	8.34E-03	0.26	2.95	2.96	2.10	2.69E-04	3.01E-04	4.32E-04	1.20	3.77	2.28	0.00
	Frag 2*	530.91	272.65	1.48E-02	0.66	2.59	2.68	1.90	8.12E-05	1.75E-04	1.83E-04	1.13	0.17	1.25	0.00
8	Frag 1	424.88	218.20	8.33E-03	1.04	2.18	2.42	1.24	3.88E-04	4.02E-04	5.82E-04	6.55	2.49	1.18	0.01
	Frag 2	574.41	294.99	8.26E-03	0.71	2.55	2.65	2.02	2.47E-04	2.71E-04	4.14E-04	2.41	7.86	0.98	0.01
9	Frag 1	236.9	121.66	7.32E-03	0.77	1.84	2.00	0.47	7.09E-05	1.23E-04	1.54E-04	8.63	9.93	8.65	0.01
	Frag 2	660.7	339.30	9.18E-03	0.40	1.90	1.94	1.25	4.52E-04	5.05E-04	6.67E-04	3.42	7.71	3.98	0.02
	Frag 3	132.6	68.10	5.43E-03	1.09	1.59	1.92	0.25	2.87E-05	5.03E-05	6.90E-05	30.15	8.37	7.24	0.02
10	Frag 1	301.6	154.89	7.92E-03	0.90	1.79	2.00	0.60	1.18E-04	1.68E-04	2.26E-04	6.18	10.76	3.83	0.01
	Frag 2	297.2	152.63	8.38E-03	0.59	2.19	2.27	0.77	1.02E-04	1.81E-04	2.14E-04	7.06	15.49	8.78	0.03
	Frag 3	404.8	207.88	8.40E-03	0.80	2.15	2.29	1.06	1.98E-04	2.50E-04	3.47E-04	9.60	14.62	5.40	0.04

		Mass [g]	Volume [cm^3]	Fracture area [m^2]	v_{xy} [m/s]	v_z [m/s]	v [m/s]	E_{kt}^{a} [J]	I_I [kg*m^2]	I_{II} [kg*m^2]	I_{III} [kg*m^2]	ω_I [rad/s]	ω_{II} [rad/s]	ω_{III} [rad/s]	E_{kt}^{a} [J]
11	Frag 1	217.9	111.90	7.89E-03	0.98	1.94	2.17	0.51	5.46E-05	1.28E-04	1.37E-04	6.67	3.30	5.33	0.00
	Frag 2	348.5	178.97	8.60E-03	1.05	2.00	2.26	0.89	1.49E-04	2.12E-04	2.82E-04	4.72	6.80	3.71	0.01
	Frag 3*	458.5	235.46	9.36E-03	0.92	2.09	2.28	1.19	2.49E-04	2.86E-04	4.14E-04	3.99	14.94	1.98	0.03
12	Frag 1	199.6	102.50	7.49E-03	1.23	1.51	1.95	0.38	4.63E-05	1.05E-04	1.15E-04	11.71	13.99	12.34	0.02
	Frag 2	309	158.69	8.05E-03	1.46	1.37	2.01	0.62	1.19E-04	1.71E-04	2.29E-04	8.28	15.39	8.02	0.03
	Frag 3	377.7	193.97	9.92E-03	0.84	1.97	2.14	0.87	1.52E-04	2.73E-04	3.04E-04	3.17	13.54	3.52	0.03
	Frag 4*	126.5	64.96	7.89E-03	1.16	1.78	2.13	0.29	2.19E-05	5.80E-05	6.39E-05	9.95	15.16	5.70	0.01
13	Frag 1	345.7	177.53	8.25E-03	1.30	1.91	2.31	0.92	1.39E-04	2.00E-04	2.64E-04	7.22	20.13	7.83	0.05
	Frag 2	345.9	177.64	8.08E-03	1.52	1.58	2.20	0.83	1.48E-04	1.98E-04	2.74E-04	3.39	13.77	5.03	0.02
	Frag 3*	293.8	150.88	9.34E-03	1.26	1.46	1.92	0.54	1.07E-04	1.56E-04	2.07E-04	3.39	13.77	5.03	0.02
	Frag 4	27.1	13.92	2.82E-03	0.78	1.22	1.44	0.03	2.49E-06	2.89E-06	2.99E-06	4.94	4.71	4.91	0.00
14	Frag 1*	367.9	188.93	9.71E-03	1.52	1.66	2.25	0.93	1.68E-04	2.05E-04	2.90E-04	12.58	28.09	5.57	0.10
	Frag 2	259.9	133.47	7.73E-03	1.61	1.19	2.00	0.52	8.31E-05	1.38E-04	1.75E-04	18.86	8.24	14.54	0.04
	Frag 3	296.6	152.32	9.96E-03	0.99	1.63	1.91	0.54	9.57E-05	2.13E-04	2.25E-04	8.08	7.15	18.20	0.05
	Frag 4	86.2	44.27	4.81E-03	1.64	1.17	2.02	0.18	1.09E-05	3.35E-05	3.76E-05	27.02	11.72	19.92	0.01
15	Frag 1	266.7	136.96	7.69E-03	1.62	1.14	1.99	0.53	n.a.	n.a.	n.a.	n.a.	n.a.	n.a.	n.a.
	Frag 2	109.4	56.18	5.37E-03	1.61	1.23	2.03	0.22	n.a.	n.a.	n.a.	n.a.	n.a.	n.a.	n.a.
	Frag 3	317.6	163.10	1.28E-02	0.60	1.52	1.63	0.42	n.a.	n.a.	n.a.	n.a.	n.a.	n.a.	n.a.
	Frag 4*	83.1	42.68	7.04E-03	1.31	1.58	2.05	0.18	n.a.	n.a.	n.a.	n.a.	n.a.	n.a.	n.a.
	Frag 5	156.8	80.52	5.96E-03	1.61	1.33	2.09	0.34	n.a.	n.a.	n.a.	n.a.	n.a.	n.a.	n.a.
	Frag 6	77.6	39.85	4.60E-03	1.43	0.91	1.69	0.11	n.a.	n.a.	n.a.	n.a.	n.a.	n.a.	n.a.
16	Frag 1	6.5	3.34	8.56E-04	0.33	2.03	2.06	0.01	n.a.	n.a.	n.a.	n.a.	n.a.	n.a.	n.a.
	Frag 2	224.3	115.19	9.74E-03	0.64	2.65	2.72	0.83	n.a.	n.a.	n.a.	n.a.	n.a.	n.a.	n.a.
	Frag 3	257.8	132.39	7.55E-03	1.54	2.14	2.64	0.90	n.a.	n.a.	n.a.	n.a.	n.a.	n.a.	n.a.
	Frag 4	138.2	70.97	5.95E-03	1.36	2.29	2.66	0.49	n.a.	n.a.	n.a.	n.a.	n.a.	n.a.	n.a.
	Frag 5	405.5	208.24	8.95E-03	0.84	2.91	3.03	1.86	n.a.	n.a.	n.a.	n.a.	n.a.	n.a.	n.a.
17	Frag 1	9.8	5.03	9.48E-04	0.26	1.15	1.18	0.01	n.a.	n.a.	n.a.	n.a.	n.a.	n.a.	n.a.
	Frag 2	144	73.95	6.18E-03	1.52	1.61	2.21	0.35	n.a.	n.a.	n.a.	n.a.	n.a.	n.a.	n.a.
	Frag 3	482.9	247.99	9.40E-03	1.17	1.95	2.27	1.24	n.a.	n.a.	n.a.	n.a.	n.a.	n.a.	n.a.
	Frag 4	3	1.54	1.11E-03	0.59	1.59	1.70	0.00	n.a.	n.a.	n.a.	n.a.	n.a.	n.a.	n.a.
	Frag 5	104.2	53.51	5.27E-03	1.53	2.05	2.56	0.34	n.a.	n.a.	n.a.	n.a.	n.a.	n.a.	n.a.
	Frag 6	299.8	153.96	8.35E-03	1.26	1.95	2.32	0.81	n.a.	n.a.	n.a.	n.a.	n.a.	n.a.	n.a.

		Mass [g]	Volume [cm^3]	Fracture area [m^2]	v_{xy} [m/s]	v_z [m/s]	v [m/s]	E_{kt}^a [J]	I_I [kg*m^2]	I_{II} [kg*m^2]	I_{III} [kg*m^2]	ω_I [rad/s]	ω_{II} [rad/s]	ω_{III} [rad/s]	E_{kt}^a [J]
18	Frag 1	14.9	7.65	2.57E-03	0.28	1.30	1.33	0.01	n.a.	n.a.	n.a.	n.a.	n.a.	n.a.	n.a.
	Frag 2	250.2	128.49	7.49E-03	2.22	1.24	2.54	0.81	n.a.	n.a.	n.a.	n.a.	n.a.	n.a.	n.a.
	Frag 3	432	221.85	1.03E-02	1.55	1.83	2.40	1.24	n.a.	n.a.	n.a.	n.a.	n.a.	n.a.	n.a.
	Frag 4	254.8	130.85	8.23E-03	1.81	1.55	2.38	0.72	n.a.	n.a.	n.a.	n.a.	n.a.	n.a.	n.a.
	Frag 5	66.5	34.15	4.01E-03	2.40	0.73	2.51	0.21	n.a.	n.a.	n.a.	n.a.	n.a.	n.a.	n.a.
19	Frag 1	23.59	12.11	3.76E-03	1.14	-0.83	1.41	0.02	n.a.	n.a.	n.a.	n.a.	n.a.	n.a.	n.a.
	Frag 2	447.72	229.93	8.50E-03	2.49	0.27	2.50	1.40	n.a.	n.a.	n.a.	n.a.	n.a.	n.a.	n.a.
	Frag 3	18.99	9.75	2.17E-03	4.01	-0.36	4.03	0.15	n.a.	n.a.	n.a.	n.a.	n.a.	n.a.	n.a.
	Frag 4*	194.25	99.76	8.92E-03	2.97	0.50	3.01	0.88	n.a.	n.a.	n.a.	n.a.	n.a.	n.a.	n.a.
	Frag 5*	333.71	171.38	1.67E-02	2.44	0.38	2.47	1.02	n.a.	n.a.	n.a.	n.a.	n.a.	n.a.	n.a.
20	Frag 1	205.88	105.73	7.01E-03	3.01	0.47	3.05	0.95	n.a.	n.a.	n.a.	n.a.	n.a.	n.a.	n.a.
	Frag 2*	288.67	148.25	1.60E-02	2.03	0.64	2.13	0.66	n.a.	n.a.	n.a.	n.a.	n.a.	n.a.	n.a.
	Frag 3	157.65	80.96	8.55E-03	3.03	0.96	3.18	0.80	n.a.	n.a.	n.a.	n.a.	n.a.	n.a.	n.a.
	Frag 4*	91.77	47.13	5.43E-03	4.24	0.49	4.26	0.83	n.a.	n.a.	n.a.	n.a.	n.a.	n.a.	n.a.
	Frag 5	217.13	111.51	4.77E-03	2.77	0.35	2.79	0.85	n.a.	n.a.	n.a.	n.a.	n.a.	n.a.	n.a.
	Frag 6	53.01	27.22	6.04E-03	3.12	0.50	3.16	0.26	n.a.	n.a.	n.a.	n.a.	n.a.	n.a.	n.a.
21	Frag 1	162.53	83.47	8.08E-03	3.09	-0.19	3.10	0.78	n.a.	n.a.	n.a.	n.a.	n.a.	n.a.	n.a.
	Frag 2	317.87	163.24	8.06E-03	2.43	0.28	2.44	0.95	n.a.	n.a.	n.a.	n.a.	n.a.	n.a.	n.a.
	Frag 3	214.85	110.34	7.44E-03	3.40	0.09	3.40	1.24	n.a.	n.a.	n.a.	n.a.	n.a.	n.a.	n.a.
	Frag 4	319.03	163.84	1.06E-02	3.20	0.68	3.27	1.71	n.a.	n.a.	n.a.	n.a.	n.a.	n.a.	n.a.
22	Frag 1	441.1	226.53	1.01E-02	2.60	0.12	2.60	1.49	n.a.	n.a.	n.a.	n.a.	n.a.	n.a.	n.a.
	Frag 2	225.82	115.97	7.44E-03	3.31	-0.06	3.31	1.24	n.a.	n.a.	n.a.	n.a.	n.a.	n.a.	n.a.
	Frag 3	9.67	4.97	1.79E-03	2.22	0.57	2.29	0.03	n.a.	n.a.	n.a.	n.a.	n.a.	n.a.	n.a.
	Frag 4	0.22	0.11	2.50E-03	0.96	0.27	0.99	0.00	n.a.	n.a.	n.a.	n.a.	n.a.	n.a.	n.a.
	Frag 5*	139.94	71.87	8.45E-03	3.72	0.18	3.72	0.97	n.a.	n.a.	n.a.	n.a.	n.a.	n.a.	n.a.
	Frag 6	170.98	87.81	6.65E-03	3.54	0.03	3.54	1.07	n.a.	n.a.	n.a.	n.a.	n.a.	n.a.	n.a.

Note:

* Fragment split at second impact. Geometric information and velocities in table are referred to the fragment at first impact (before splitting). The fracture area is the sum of the fracture areas of the fragments after splitting.

- Note that a very small rotational motion was observed for tests at higher impact velocity (7.8 and 10 m/s). Hence, the rotational velocity was not computed for these tests. The rotational kinetic energy is very small compared to the initial kinetic energy (<1%) and has a negligible influence on the energy balance for this type of impact condition.